



HAL
open science

New approaches to study the architecture and dynamics of the sealing zone in osteoclasts

Marion Portes

► **To cite this version:**

Marion Portes. New approaches to study the architecture and dynamics of the sealing zone in osteoclasts. Biochemistry, Molecular Biology. Université Paul Sabatier - Toulouse III, 2019. English. NNT : 2019TOU30294 . tel-02535262v2

HAL Id: tel-02535262

<https://laas.hal.science/tel-02535262v2>

Submitted on 11 Jan 2021

HAL is a multi-disciplinary open access archive for the deposit and dissemination of scientific research documents, whether they are published or not. The documents may come from teaching and research institutions in France or abroad, or from public or private research centers.

L'archive ouverte pluridisciplinaire **HAL**, est destinée au dépôt et à la diffusion de documents scientifiques de niveau recherche, publiés ou non, émanant des établissements d'enseignement et de recherche français ou étrangers, des laboratoires publics ou privés.



THÈSE

En vue de l'obtention du

DOCTORAT DE L'UNIVERSITÉ DE TOULOUSE

Délivré par :

Université Toulouse 3 Paul Sabatier (UT3 Paul Sabatier)

Présentée et soutenue par :

Marion PORTES

le 8 novembre 2019

Titre :

Nouvelles approches pour l'étude de l'architecture et la dynamique de la sealing zone des ostéoclastes

École doctorale et discipline ou spécialité :

ED BSB : Biologie cellulaire

Unité de recherche :

IPBS et LAAS - CNRS, Toulouse

Directeur/trice(s) de Thèse :

Renaud POINCLOUX et Christophe THIBAUT

Jury :

Mme Anne BLANGY, Rapporteur

Mme Alessandra CAMBI, Rapporteur

M. Olivier DESTAING, Rapporteur

M. Christophe VIEU, Examineur

M. Renaud POINCLOUX, Directeur de thèse

M. Christophe THIBAUT, Co-directeur de thèse



THÈSE

En vue de l'obtention du

DOCTORAT DE L'UNIVERSITÉ DE TOULOUSE

Délivré par : *l'Université Toulouse 3 Paul Sabatier (UT3 Paul Sabatier)*

Présentée et soutenue le 08/11/2019 par :

MARION PORTES

New approaches to study the architecture and dynamics of the sealing zone in osteoclasts

JURY

ALESSANDRA CAMBI	Professor and Chair, Radboudumc	Rapportrice
ANNE BLANGY	Directrice de recherches, CRBM	Rapportrice
OLIVIER DESTAING	Chargé de recherches, IAB	Rapporteur
CHRISTOPHE VIEU	Professeur des universités, LAAS/INSA Toulouse	Examineur
RENAUD POINCLOUX	Ingénieur de recherche, IPBS	Directeur de thèse
CHRISTOPHE THIBAUT	Maître de conférences, LAAS/INSA Toulouse	Co-directeur de thèse
CHRISTEL VÉROLLET	Chargée de recherche, IPBS	Invitée

École doctorale et spécialité :

BSB : Biologie cellulaire

Unité de Recherche :

*Institut de Pharmacologie et Biologie Structurale (UMR 5089) & Laboratoire
d'Analyse et d'Architecture des Systèmes (UPR 8001)*

Directeur(s) de Thèse :

Renaud POINCLOUX et Christophe THIBAUT

Rapporteurs :

Alessandra CAMBI, Anne BLANGY et Olivier DESTAING

This PhD work has been financially supported by:



Acknowledgements

First things first, I am grateful to Anne Blangy, Alessandra Cambi, Olivier Destaing and Christophe Vieu for accepting to review my manuscript and be part of the jury, and for their fruitful scientific discussion during my defense.

I would also like to send my thanks to both my supervisors Renaud Poincloux and Christophe Thibault. Renaud, thank you for putting up with my 1.000 dabs/minute and my weird vocabulary choices. Christophe, thank you for always being philosophical about my ups and downs (especially my downs, though) and for giving me the occasion to teach at INSA for two years.

Thank you to both research team members (past and present) at IPBS and LAAS for welcoming me during these three eventful years, and allowing me to discover the daily life in a biology lab and in a micro/nanotechnology lab. A special thanks to the TEAM team at LAAS for introducing me to the micro/nano world, and for showing many new things in the clean room with your never-ending patience and thoroughness. And thank you to Thomas Mangeat for allowing me to try out his ever-evolving RIM on my challenging samples.

A big shout-out to those who have been there for some time now, and so rarely seem to get tired of me (congrats for that): my family, my friends from high school and from ENSTA and my bad bitches poney crew. Thank you for being amazing persons, keep up the good work! Last but not least, this tender thought goes to Adrien, even if I don't need so many words to tell you how grateful I am for you being you, by my side.

Résumé

L'os forme un environnement cellulaire complexe, et est sujet à un renouvellement constant tout au long de l'existence. Son remodelage dépend de trois types cellulaires : les ostéoblastes, les ostéoclastes et les ostéocytes. Le rôle des ostéoblastes consiste en la construction de la nouvelle matrice osseuse, tandis que les ostéoclastes sont responsables de sa dégradation. Tout ceci se fait sous la régulation des ostéocytes. Afin de pouvoir efficacement dissoudre les parties minérales et organiques de l'os, les ostéoclastes mettent en place une polarisation spécifique de leur membrane plasmique afin de créer un microenvironnement confiné, favorable à la résorption. Ce confinement des sites de résorption est dû à la présence d'une zone de scellement ou « sealing zone ». Cette structure à forte densité d'actine a été caractérisée à la fin des années 80, et une vingtaine d'années plus tard des sous-unités ressemblant à des podosomes ont été identifiées à l'intérieur de cette entité. Pourtant, l'organisation interne de la zone de scellement reste encore aujourd'hui peu décrite à petite échelle.

Au cours de cette étude, une première caractérisation quantitative à l'échelle nanométrique de la zone de scellement des ostéoclastes humains a été proposée. A l'aide d'une technique de microscopie de super-résolution de pointe, les cœurs d'actine ont pu être identifiés comme des sites de remodelage intense de l'actine. De plus, le traitement des signaux associés a permis de mettre en évidence que ces événements dynamiques avaient lieu de manière synchrone entre cœurs voisins, et l'analyse de la localisation de protéines majeures de la zone de scellement a suggéré que les cœurs d'acteurs étaient organisés en îlots de taille variable, encerclés de complexes d'adhérence.

Les mécanismes cellulaires permettant à cette superstructure d'adhérence de reconnaître les propriétés de surface de la matrice osseuse sont encore méconnus. Ainsi, les travaux menés au cours de cette thèse se sont aussi concentrés sur le développement de substrats compatibles avec l'étude de ces fonctions. Un protocole pour produire des lamelles de verre présentant une couche de polyacrylamide de quelques centaines de nanomètres a été mis au point. Ces supports pourront également permettre à l'avenir d'évaluer des forces appliquées à l'échelle nanométrique. De plus, l'utilisation de ressources de micro- et nanotechnologies a permis de développer des substrats spécialement mis en forme pour l'étude des réponses cellulaires aux nano-topographies. Des lamelles de verres ont été traitées par photolithographie et gravure chimique pour présenter des lignes micrométriques, de hauteur nanométrique, caractérisées grâce à la microscopie de force atomique.

De manière générale, les travaux présentés dans ce manuscrit décrivent de nouvelles approches pour caractériser les propriétés structurales et dynamiques de la sealing zone. Du fait de leur polyvalence, ces outils pourront également s'inscrire dans une recherche plus globale concernant les structures d'adhérence cellulaires.

Mots clés : Ostéoclastes - Sealing zone - Podosomes - Os - Microscopie de super-résolution - Mécanobiologie - Micro/nanotechnologie.

Abstract

Bone is a complex biological environment, and a living tissue under constant renewal throughout life. Its remodeling process is orchestrated by three different cell types: osteoblasts, osteoclasts and osteocytes. While osteoblasts are in charge of the generation of new bone matrix, the main function of osteoclasts is to degrade it, and both activities are under the regulation of osteocytes. In order to efficiently dissolve both mineralized and organic bone components, osteoclasts compartmentalize their plasma membrane to create a resorption microenvironment. In particular, osteoclasts form a superstructure called the sealing zone, which confines the digestion site. The sealing zone has been identified in the late 80s as a dense actin structure, then in the late 2000s as composed of podosomal subunits. However, little is still known about the precise inner organization of this specific cytoskeletal arrangement. This study proposed a quantitative characterization at the nanoscale of the organization and dynamics of the sealing zone in human osteoclasts. State-of-the-art super-resolution microscopy confirmed that single cores were tightly packed in a complex filament network, and time-lapse imaging revealed that they consisted in preferential sites of intense actin remodeling. In addition, signal processing yielded that these subunits display a synchronous behavior at the local scale. Further analysis of the organization showed that actin cores are arranged in groups encircled by adhesion complexes, and of various sizes.

The mechanisms used by the sealing zone to probe the stiffness and the topography of bone have been but poorly investigated. Thus, this work also aimed at developing new substrates compatible with super-resolution microscopy to investigate the mechanisms of rigidity and topography sensing. First, a protocol to create gels of polyacrylamide of only a few hundreds of nanometers was developed. Such substrates will pave the way for the investigation of forces at the nanoscale. In addition, micro- and nanotechnological resources have been applied to the development of new substrates to assess topography sensing at the nanoscale. Micron-sized lines presenting nanoscale heights were directly shaped on glass coverslips thanks to photolithography and chemical etching, and their characterization was carried out with atomic force microscopy.

Overall, the work presented in this manuscript describes new technological approaches to characterize the structural and dynamical properties of the sealing zone. The versatility of the presented tools and techniques will allow their use in various other contexts, such as individual podosomes or focal adhesions.

Keywords: Osteoclasts - Sealing zone - Podosomes - Bone - Super-resolution microscopy - Cell mechanics - Micro/nanotechnology.

Contents

Introduction (in French)	1
Introduction	5
1. Literature review	7
1.1. Bone homeostasis	7
1.1.1. Bone as a complex biological environment	8
1.1.2. Bone remodeling process	12
1.1.3. Bone resorption by osteoclasts	19
1.2. Individual podosomes	23
1.2.1. Podosome molecular composition and regulation	23
1.2.2. Podosomes as dynamic, matrix-probing structures	29
1.3. The sealing zone - towards a molecular representation	38
1.3.1. Architecture of the osteoclast actin cytoskeleton	38
1.3.2. Regulation of the sealing zone	52
1.3.3. Scale-dependent dynamics of the sealing zone	58
1.4. Conclusions and perspectives	65
2. Nanoscale architecture and dynamics of the sealing zone	67
2.1. Abstract	68
2.2. Introduction	68
2.3. Results	70
2.3.1. Nanoscale organization of actin cores in the sealing zones formed by human osteoclasts	70
2.3.2. Local synchrony of sealing zone actin cores	72
2.3.3. Sealing zone podosome cores are organised into islets surrounded by adhesion complexes	73
2.3.4. Three-dimensional nanoscale organization of the podosome belt	77
2.4. Discussion	80
2.5. Materials and methods	83
2.5.1. Differentiation and culture of primary monocyte-derived osteoclasts	83
2.5.2. Cleaning of precision glass coverslips	84
2.5.3. Primary antibodies	84
2.5.4. Immunofluorescence	84
2.5.5. Scanning Electron Microscopy imaging	84
2.5.6. Analysis of SEM images	85
2.5.7. RIM 2D super-resolution imaging	85
2.5.8. Analysis of RIM images of fixed samples	86
2.5.9. Analysis of RIM live acquisitions	87

2.5.10. DONALD 3D super-resolution imaging	88
2.5.11. Analysis of DONALD 3D super-resolution images	89
2.5.12. Statistical analysis	89
3. Developing new substrates for the characterization of podosome mechanical properties and topography sensing with super-resolution microscopy	91
3.1. Introduction	92
3.1.1. Mechanical sensing of ECM	92
3.1.2. Probing ECM geometric characteristics	94
3.1.3. ECM proteins interactions with associated integrins	94
3.2. Towards the development of a 3D super-resolved traction force microscopy setup	96
3.2.1. Characterization of cell adhesion forces	96
3.2.2. Towards a super-resolved 3D TFM setup	109
3.2.3. Trying to meet the requirements specification point by point	118
3.2.4. Possible improvement strategies	142
3.3. Designing nanoscale 2.5D glass substrates for assessing of macrophage topography sensing	147
3.3.1. Characterization of cell topography sensing	147
3.3.2. Generation of wet-etched glass coverslips to study topography sensing	156
3.3.3. Main results	162
3.3.4. Discussion	169
3.4. Discussion	172
Conclusions	173
Appendices	179
A. Appendix to chapter 2	181
A.1. Details of the analysis workflow for the geometric characterization of actin cores with RIM technique	182
A.2. Details of the analysis workflow for the 2D localization of proteins relative to actin cores with RIM technique	183
A.3. Details of the analysis workflow for the 3D localization of proteins relative to actin cores with DONALD technique	184
A.4. Proposition for the 2D localization of proteins relative to actin cores within the sealing zone	185
A.5. Proposition for the 3D localization of proteins relative to actin cores, and dynamic processes within the sealing zone	186
B. Appendix: Annex publication	187
Bibliography	193

List of Figures

1.1. Hierarchical structural organization of bone.	9
1.2. Structural organization of osteons.	10
1.3. Bone cells involved in the bone remodeling process.	11
1.4. The main stages of the bone remodeling process.	14
1.5. The capillary network within cortical bone.	15
1.6. Systemic and growth factor regulation of bone remodeling.	16
1.7. Evolution of bone erosion in the course of rheumatoid arthritis.	18
1.8. Direct bone effect of HIV.	18
1.9. Schematic view of a bone resorbing osteoclast.	20
1.10. Remodeling is initiated within basic multicellular units at points beneath the canopy of cells lining trabecular bone and within cortical bone Haversian canals.	21
1.11. Matching resorption patterns generated by OCs <i>in vitro</i> and <i>in vivo</i>	22
1.12. Podosome architecture and composition.	24
1.13. Schematic showing a model for the organization of proteins in a single podosome.	26
1.14. Summary of the signaling hierarchy involved in the regulation of podosomes.	28
1.15. Schematic view of signaling pathways that lead to actin organization at podosomes.	30
1.16. Force and actin synchrony between close neighbors.	31
1.17. Interplay between microtubules, myosin IIA filaments and integrin adhesions.	33
1.18. Established functions of podosomes in ECM sensing.	35
1.19. Model of ring protein organization and podosome force generation.	36
1.20. Podosomes in monocytic cells display various global organizations.	37
1.21. Schematics of the different actin structures observed along osteoclast differentiation and activation.	39
1.22. Observation of osteoclast ventral membrane on bone with scanning electron microscopy.	40
1.23. Replica images of podosomes decorated with myosin S1 in osteoclasts.	42
1.24. Schematics displaying integrin structure and activation.	43
1.25. Schematic view showing the major integrin-ligand combinations, using hypothetical cell surfaces.	44
1.26. Localization of total and "activated" $\alpha v\beta 3$ in resorbing osteoclasts.	45
1.27. OC podosome belt is composed of two F-actin domains specifically associated with CD44 and the $\beta 3$ integrin subunit.	47
1.28. Schematic view of the sealing zone components at the podosome scale, in a bone resorbing osteoclast.	47
1.29. Signaling pathways involved in the regulation of the sealing zone components.	53
1.30. Myosin X is positioned between microtubules and actin of forming podosome belts and sealing zone.	57
1.31. Osteoclasts adhering to different bone topographies differ in the size of their sealing zone rings.	60

List of Figures

1.32. Podosome ring expansion and osteoclast migration are correlated.	61
1.33. Expanding podosome rings are formed inside podosome clusters and grow larger as differentiation progresses.	63
1.34. Schematic view of the dynamic regulation of actin filament length by the severing activity of gelsolin.	65
2.1. Nanoscale organization of actin cores in the sealing zones formed by human osteoclasts.	71
2.2. Comparison between epi-fluorescence and RIM super-resolution microscopy.	72
2.3. Nanoscale analysis of the dynamics of the sealing zone with RIM technique.	74
2.4. Localization in the sealing zone of cortactin, α -actinin 1, filamin A and vinculin with RIM technique.	76
2.5. 3D nanoscopy of vinculin and talin-C in the podosome belt.	78
2.6. 3D nanoscopy of F-actin, cortactin, α -actinin1, filamin A and paxillin in the podosome belt.	79
2.7. Model of the organization of the sealing zone into islets.	80
3.1. Cell responses to physical cues that are transduced through the mechanical properties, the architecture of fibrous structural proteins and receptor-binding peptides contained within the native ECM.	93
3.2. Summary of the most relevant techniques for cell mechanical characterization.	97
3.3. Schematic diagram of a TFM substrate.	102
3.4. Main steps in TFM analyses and associated influential factors.	104
3.5. Outline of STED-TFM.	105
3.6. Schematic of the confocal reference-free TFM set-up and involved techniques.	106
3.7. Configuration of the 3D TFM mathematical problem.	107
3.8. Basic principles of super-resolution microscopy.	110
3.9. Inherent trade-offs in super-resolution microscopy.	115
3.10. Far and near field emission components.	118
3.11. Direct optical nanoscopy with axially localized detection setup and data analysis.	119
3.12. Main steps for the preparation of PAA-coated coverslips for a TFM experiment.	120
3.13. Comparison of two polyacrylamide coating roughness with AFM.	122
3.14. Polyacrylamide thickness measurements by profilometry, corresponding to the deposition of a decreasing solution volume.	124
3.15. Polyacrylamide thickness measurements performed by either profilometry or DONALD.	124
3.16. Polyacrylamide thickness measurements depending on the applied pressure with NANONEX machine.	126
3.17. Polyacrylamide thickness measurements depending on the nano-imprint conditions with NANONEX machine.	126
3.18. Polyacrylamide thickness measurements depending on the thermal nano-imprint conditions with NANONEX machine, and the deposition of a decreasing solution volume.	127
3.19. Schematic representation of Alexa Fluor 488-coupled Fluoronanogold particle, and Alexa Fluor 647-coupled Fluoronanogold particle.	128
3.20. Analysis of particle distribution before and after transfer on polyacrylamide gels, for two dilutions of AF488-coupled Fluoronanogold particles.	129
3.21. Median photon number corresponding to EPI signal, and UAF signal, depending on the exposure time of polyacrylamide gels coated with various fluorescent markers.	130
3.22. Median photon number corresponding to EPI signal, and UAF signal, depending on the time exposure of polyacrylamide gels coated with AF488-coupled cadaverine.	131

List of Figures

3.23. Measurements of 3T3 fibroblast cell area and circularity, depending on the coating conditions of PAA gels coated with AF488-coupled cadaverine and ECM protein.	133
3.24. Quantification of useful observables for TFM imaging, depending on AF488-coupled cadaverine-coating conditions and observation medium, at room temperature.	135
3.25. Quantification of useful observables for TFM imaging, depending on AF488-coupled cadaverine-coating conditions and observation medium, at 37°C.	138
3.26. Multiscale hierarchy of different representative tissues and representative synthetic substrates sharing the same topography lengthscale.	148
3.27. Most representative micro/nanofabrication methods represented in terms of range resolution and compared with natural systems at different scales of organizational levels.	149
3.28. Examples of different type of topographies used to mimic the extracellular matrix of tissues: pillars; pits; grooves/gratings; tubes; fibers; wires and roughness.	152
3.29. Three scenarios of a cell interfacing with an adhesive substratum containing spatially graded topographic features and the corresponding topotaxis directionality.	153
3.30. A schematic graphic model of the topotaxis in invasive and non-invasive cells, controlled by PI3-kinase and ROCK signaling pathways.	154
3.31. Correlation between size of substratum topography and cellular sensing organelles.	155
3.32. Main steps of the optimized process to fabricate nano-topographies.	158
3.33. Creation of a merged image to visualize actin-rich cores and ring proteins with epifluorescence, with respect to the topographic features observed with light transmission.	160
3.34. Creation of masks based on actin fluorescence image.	161
3.35. The binary mask allows for cell area evaluation estimation by scanning the image from top to bottom and storing the mean intensity value for each scan line.	161
3.36. Optical microscope observation of the center of the coverslip, sample exposed with a dose of 50 mJ.cm ⁻² , 10x magnification.	162
3.37. Optical microscope observation of the center of the coverslip, sample exposed with a dose of 100 mJ.cm ⁻² , 10x magnification.	163
3.38. Optical microscope observation of the center of the coverslip, sample exposed with a dose of 100 mJ.cm ⁻² and developed for 75 seconds, 10x magnification.	163
3.39. Optical microscope observation of the center of the coverslip, sample exposed with a dose of 100 mJ.cm ⁻² and developed for 60 seconds, 10x magnification.	164
3.40. Optical microscope observation of the center of the coverslip, sample exposed with a dose of 100 mJ.cm ⁻² in hard contact and developed for 60 seconds, 10x magnification.	164
3.41. Scanning electron microscopy observation of the topographic features after wet etching.	165
3.42. Estimation of the etching rate of borosilicate glass by a buffered hydrofluoric acid (7:1) solution	166
3.43. Characteristic aspect of an etching defect observed with AFM tapping mode.	167
3.44. Human macrophages on a coverslip displaying 16 nm high topographies, showing podosomes lacking from the top othe motifs.	168
3.45. Human macrophages on a coverslip displaying 16 nm high topographies, showing podosome accumulation on the edge of motifs.	168
3.46. Preferential localization of actin cores relative to the motifs, depending on the topography heights.	169
A.1. Analysis worklow for the geometric characterization of actin cores with RIM technique.	182
A.2. Analysis worklow for the 2D localization of proteins relative to actin cores with RIM technique.	183

List of Figures

A.3. Analysis workflow for the 3D localization of proteins relative to actin cores with DON-ALD technique.	184
A.4. Schematics of the proposed in-plane localization of proteins relative to actin cores within a sealing zone.	185
A.5. Schematics of the proposed dynamics and axial localization of proteins relative to actin cores within a sealing zone.	186

List of Tables

3.1. Roughness (nm) analysis of polyacrylamide gels with Young's modulus value of 10 kPa or 40 kPa.	123
3.2. Thickness (nm) analysis of polyacrylamide gels shaped with NANONEX machine, with varying process conditions.	127
3.3. Thickness (nm) analysis of polyacrylamide gels shaped with NANONEX machine, with varying process temperature and solution volume.	128
3.4. Area (μm^2) analysis for 3T3 fibroblasts plated on polyacrylamide gels, depending on the gel coating conditions.	133
3.5. Circularity analysis for 3T3 fibroblasts plated on polyacrylamide gels, depending on the gel coating conditions.	134
3.6. Median EPI photon number analysis for observation conditions at room temperature	136
3.7. Median UAF photon number analysis for observation conditions at room temperature	136
3.8. Fluorescent marker density (μm^{-2}) analysis for observation conditions at room temperature	137
3.9. Mean inter-marker distance (nm) analysis for observation conditions at room temperature	137
3.10. Median EPI photon number analysis for observation conditions at $37^\circ C$	139
3.11. Median UAF photon number analysis for observation conditions at $37^\circ C$	139
3.12. Fluorescent marker density (μm^{-2}) analysis for observation conditions at $37^\circ C$	140
3.13. Mean inter-marker distance (nm) analysis for observation conditions at $37^\circ C$	140
3.14. Synthesis of 3D super-resolution TFM development main challenges and the proposed optimal solution according to this study	143
3.15. AFM characterization results of etched coverslips subsequently used for cell plating	166

List of abbreviations

2D	Two dimensions, bidimensional
3D	Three dimensions, tridimensional
AFM	Atomic force microscopy
DNA	Deoxyribonucleic acid
DONALD	Direct optical nanoscopy with axially localized detection
DVC	Digital volume correlation
ECM	Extracellular matrix
F-actin	Filamentous actin, actin monomers assembled in a microfilament
FEM	Finite element method
FN	Fibronectin
FRAP	Fluorescence recovery after photobleaching
FTTC	Fourier transform traction cytometry
G-actin	Globular actin, actin free monomers
GFP	Green fluorescent protein
M-CSF	Macrophage colony stimulating factor
PAA	Polyacrylamide
PAINT	Point accumulation for imaging in nanoscale topography
PALM	Photoactivated localization microscopy
PBS	Phosphate buffered saline
PDMS	Polydimethylsiloxane
PEG	Polyethylene glycol
PFM	Protrusion force microscopy
PIV	Particle image velocimetry
PSF	Point spread function
PTV	Particle tracking velocimetry
RANK-L	Receptor activator of nuclear factor κ -B ligand
RGD	Arg-Gly-Asp peptide
RIM	Random illumination microscopy
ROI	Region of interest
SAF	Supercritical angle fluorescence
SEM	Scanning electron microscopy
SIM	Structured illumination microscopy
SMLM	Single molecule localization microscopy
SNR	Signal to noise ratio
STED	Stimulated emission depletion

List of Tables

STORM	Stochastic optical reconstruction microscopy
TEM	Transmission electron microscopy
TFM	Traction force microscopy
TIRF	Total internal reflection fluorescence
UAF	Under-critical angle fluorescence
UV	Ultraviolet

Introduction (in French)

L'os est un tissu vivant, dont le remodelage constant est soumis à la régulation de sa microstructure par les différentes cellules osseuses. Leurs actions coordonnées permettent notamment la croissance du squelette, la réparation des fractures, l'adaptation aux contraintes musculosquelettiques, et participent à l'homéostasie calcique. Les cycles successifs de résorption par les ostéoclastes et de formation de la nouvelle matrice par les ostéoblastes contribuent au renouvellement osseux, mais c'est surtout l'équilibre entre ces deux fonctions cellulaires opposées qui est caractéristique des conditions physiologiques. En effet, même un déséquilibre mineur peut entraîner des effets majeurs se répercutant sur l'intégrité osseuse.

Une des pathologies les plus connues résultant de ce déséquilibre consiste en une perte accrue de densité osseuse : l'ostéoporose. Cette maladie a des impacts socio-économiques dramatiques, avec environ 3,5 millions de personnes de plus de 50 ans touchées en France, et presque 150000 fractures associées chaque année.

Mais les problèmes osseux ne concernent pas uniquement les personnes âgées, et sont souvent aussi couplés à des maladies inflammatoires chroniques telles que la polyarthrite rhumatoïde. De plus, ils peuvent aussi apparaître en tant que complications secondaires d'autres pathologies, telles que le cancer avec la présence de métastases osseuses, ou également de maladies infectieuses, notamment dans le cas d'infection par le VIH.

Les traitements actuels visant à limiter la perte de densité osseuse comptent notamment l'utilisation des bisphosphonates, dont l'action avérée est d'inhiber la dégradation osseuse en perturbant la différenciation et la survie des ostéoclastes. Pourtant, ces cellules jouent un rôle majeur dans la régulation de tout le cycle de remodelage osseux, et mettent en place des voies de signalisation nécessaires aux fonctions ostéoblastiques. Ainsi, le fait d'essayer de limiter la résorption osseuse induit également une formation de la nouvelle matrice osseuse moins efficace. Il est donc crucial d'explorer de nouvelles stratégies thérapeutiques, ciblant principalement l'activité de dégradation tout en préservant l'intégrité cellulaire.

Dans ce contexte, une connaissance pointue et la plus complète possible du dispositif cellulaire permettant la dégradation osseuse constitue la première étape vers l'identification d'opportunités thérapeutiques alternatives.

Les ostéoclastes détruisent les composants tant minéraux qu'organiques de l'os au niveau d'un domaine spécifique de leur membrane plasmique présentant d'importantes convolutions. Pour instaurer un milieu favorable à la dégradation, un microenvironnement acide est isolé du milieu extracellulaire

à l'aide d'un contact étroit entre la matrice et la membrane entourant la zone de résorption. Ce confinement est médié par la présence d'une structure riche en actine : la zone de scellement, ou « sealing zone ».

Les recherches concernant la zone de scellement ont débuté dans les années 80, et ses propriétés ultrastructurales ont été mises à jour pour la première fois à la fin des années 2000. Elle composée de cœurs d'actine, connectés à la fois à la membrane plasmique sous-jacente et à leurs proches voisins, à l'aide d'un réseau complexe de filaments d'actine. Cette organisation est très proche de celle retrouvée dans les podosomes individuels, les structures d'adhérence caractéristiques des cellules d'origine hématopoïétique. De plus, des protéines majeures impliquées dans l'arrangement spatial et la jonction entre les filaments d'actine ont également été observées dans la zone de scellement. Cependant, leur localisation au sein de cette structure n'a été que qualitative jusqu'à maintenant.

La présence de telles protéines liées au réarrangement des filaments d'actine témoigne d'une activité intense de remodelage de ces filaments à l'intérieur de la zone de scellement. Toutefois, l'aspect dynamique de la zone de scellement n'a été étudié que très rarement à une échelle aussi petite. Ses variations globales dans des contextes de migration ont, elles, été plus souvent décrites dans la littérature.

Par ailleurs, les cycles de polymérisation et dépolymérisation de l'actine aux sites des cœurs de podosomes individuels ont été associés à une application périodique de forces protrusives par les cellules. Ces événements sont notamment supposés faire partie des stratégies cellulaires pour sonder les propriétés de leurs substrats. Dans le cadre des ostéoclastes, étant donné le rôle de confinement de la zone de scellement, il est plausible que ces oscillations aient également un rôle mécanique dans le maintien de contact étroit. Cependant, aucun outil n'est actuellement disponible pour permettre de valider ou infirmer cette hypothèse. L'étude de la migration des ostéoclastes sur des substrats reproduisant la biochimie de l'os ont également mis en évidence la dépendance de la motilité des cellules vis-à-vis de l'état de surface, et notamment dans le cas de variations de leur topographie. La question de la relation entre ces modifications globales et des relocalisations probables des protéines de liaison de l'actine à l'échelle locale n'a pas encore été abordée.

Ce manque actuel d'informations à l'échelle sousmicron à propos de la zone de scellement a conduit les travaux de cette thèse à se concentrer sur le développement d'outils et de nouvelles approches basées sur des nanotechnologies de pointe. Ces méthodes permettront l'étude tant de l'architecture interne que de la dynamique des sous-unités de la zone de scellement. Pour cela, des ostéoclastes humains, différenciés à partir de monocytes sanguins, ont été imagés avec de nouvelles techniques de microscopie afin de dégager des informations quantitatives à l'échelle nanométrique sur la zone de scellement. Ces résultats représentent la première description à une telle échelle de l'organisation et la dynamique interne de cette structure cellulaire. De plus, l'utilisation de ressources de micro- et nanotechnologies ont permis de mettre au point des substrats destinés à l'étude future des propriétés de mécanosensibilité en trois dimensions, ainsi que les réponses cellulaires aux nano-topographies.

Pour permettre de présenter l'intégralité de mes travaux de thèse liés à cette étude, le manuscrit a été organisé comme suit :

- Le premier chapitre présente une revue de la littérature en trois parties. La première partie

se concentre sur le concept général de l'homéostasie osseuse. La structure de l'os y est décrite selon différentes échelles, rendant compte de la complexité tant biologique que physique de cet environnement cellulaire. Les différentes cellules osseuses : ostéoblastes, ostéoclastes et ostéocytes y sont présentées, ainsi que leur rôle dans les étapes majeures du remodelage osseux. Enfin, les mécanismes impliqués dans l'activité de résorption osseuse, tant physiologique que pathologique, sont brièvement évoqués. La deuxième partie de ce chapitre aborde le sujet des podosomes, structures d'adhérence majeures des cellules d'origine hématopoïétique. Leur organisation à l'échelle nanométrique y est décrite à l'aide des études de cette dernière décennie, ainsi que leurs mécanismes de régulation. De plus, leurs propriétés dynamiques, en tant que structures mécanosensibles, y sont résumées. La dernière partie du chapitre 1 consiste en une revue de littérature plus poussée sur les différents aspects de la zone de scellement. En premier lieu, il y est fait état des connaissances actuelles quant à son organisation et ses différents composants. Ensuite, les principaux régulateurs de la composition de la sealing zone sont présentés à l'aide des différentes études s'étant intéressé aux ostéoclastes. Enfin, les propriétés dynamiques à différentes échelles y sont décrites. Cette partie est destinée à donner lieu à la publication d'une revue.

- Le deuxième chapitre présente les résultats majeurs de mes travaux de thèse sur la caractérisation à l'échelle nanométrique de l'architecture et la dynamique interne de la sealing zone, à l'aide de techniques de microscopie de super-résolution de pointe et de microscopie électronique à balayage. Nous avons montré que la nouvelle technique de microscopie à illumination aléatoire permet d'identifier et d'imager en temps réel les sous-unités de la zone de scellement des ostéoclastes humains. L'analyse des signaux temporels associés à l'actine a démontré qu'il existe un degré de synchronie locale entre voisins, et non à l'échelle globale de la structure. De plus, la localisation de protéines de liaison de l'actine a permis d'identifier des groupe de plusieurs cœurs d'actine, chacun entouré d'un anneau d' α -actinine, délimités par des complexes d'adhérence comprenant notamment la vinculine. Ainsi, ces travaux ont permis de mettre en lumière pour la première fois que la sealing zone est composée d'îlots de cœurs d'actine synchrones, participant au confinement de la zone de résorption. Ces résultats sont en cours de finalisation, pour donner lieu à une publication dont je serai le premier auteur.
- Le troisième chapitre présente les étapes de mise au point et les résultats préliminaires de deux projets réalisés au cours de ma thèse. Le premier projet visait initialement à développer des substrats compatibles avec la mesure de forces en trois dimensions à l'aide de techniques de microscopie de super-résolution. A l'issue de ce projet, les substrats mis au point ne permettaient pas encore d'atteindre cet objectif, néanmoins ils pourront permettre à court terme d'étudier l'organisation à l'échelle nanométrique et en trois dimensions des structures d'adhérence dans un contexte d'étude des propriétés de mécanosensibilité. Le second projet présenté dans ce chapitre consiste en les travaux d'une stagiaire que j'ai aidé à encadrer lors de son stage de fin d'études à l'INSA de Toulouse. Son étude s'est porté sur la mise au point d'un protocole pour produire des lamelles de verre présentant des topographies de l'ordre de la dizaine à la centaine de nanomètres, et compatibles avec l'observation par microscopie de super-résolution.

Ces substrats permettront également d'analyser l'organisation à l'échelle nanométrique et en trois dimensions des structures d'adhérence cellulaires.

Au cours de mes travaux de thèse, j'ai donc pu mettre en place diverses techniques et méthodes compatibles avec l'étude à l'échelle nanométrique de la zone de scellement des ostéoclastes tant au niveau architectural que dynamique. De plus, la polyvalence de ces outils leur permettra d'être utilisés dans de nombreux contextes étudiant les structures d'adhérence cellulaires, telles que les podosomes individuels ou les adhérences focales.

En annexe de ce manuscrit figure également une publication dont j'ai participé à l'écriture au cours de ma thèse (BOUSSOU et al., 2018). Cette publication décrit par écrit et en vidéo le protocole pour mettre en place une expérience type de microscopie à force de protrusion, qui a été développé lors des travaux de thèse d'une étudiante précédente, Anna Labernadie. Cette méthode permet de quantifier les déformations axiales causées par la présence de podosomes, sur un film fin de Formvar observé à l'aide de microscopie à force atomique. Cet article a été publié en 2018, dans le journal intitulé « Journal of Visualized Experiments ».

Introduction

In the context of bone remodeling, bone cells play a crucial role in regulating the microstructure of the bone tissue. Their synergized actions allow for skeletal growth, fracture healing, adaptation to musculoskeletal loads and calcium homeostasis. Sequential resorption by osteoclasts and formation by osteoblasts, and most importantly the balance between these contrasting functions are required for the constant renewal of bone matrix. Indeed, slight variations from this balance can have dramatic effects on bone integrity.

One of the most frequent results from this imbalance is the loss of bone density, namely osteoporosis. This bone disease leads to major socio-economic impacts, with approximately 3.5 million persons over 50 with osteoporotic diagnostic in France and approximately 150 thousand fractures per year, due to related bone weakness. Bone defect is not only an elderly issue, but it is also associated with chronic inflammatory diseases, such as rheumatoid polyarthritis. Moreover, it can consist in a major complication in the context of cancer, especially in the case of bone metastases, or of infectious diseases like AIDS.

Recent treatments against bone density loss include bisphosphonate administration, which inhibit osteolytic activity by interfering with osteoclast differentiation and viability. Yet, osteoclasts are required to take part in the intricate signal pathways also regulating osteoblastic activity. Therefore, by attempting to prevent bone resorption, bone formation ends up also being impaired. It appears paramount to research new therapeutic strategies, mainly targeting the resorption activity at the cellular level while preserving the cell integrity.

Hence, gathering the most precise and exhaustive description of the degradation apparatus of osteoclasts is a crucial first step towards identifying alternative therapeutic opportunities.

Osteoclasts digest bone mineralized and organic components at a specific plasma membrane domain: the ruffled border. To facilitate the digestion, an acidic microenvironment is established below the ruffled border, and is isolated from the extracellular medium through a tight contact between the surrounding plasma membrane and the matrix. This close contact is allowed by the presence of a dense actin structure: the sealing zone.

The sealing zone has been intensively researched from the late 80s, and its ultrastructural properties have first been reported in the late 2000s. It is composed of single actin cores, which are both connected to the plasma membrane and to each other *via* an intricate network of actin filaments. This actin organization is very similar to the architecture of individual podosomes, submicron adhesion structures found in hematopoietic cells. In addition, major actin crosslinker proteins, also associated with podosomes, have been identified as involved in the sealing zone. However, their identification have mainly been combined with only a qualitative localization in this structure.

The presence of such proteins involved in the rearrangement of actin filaments is a hallmark of intense actin dynamics within the structure. Yet, the sealing zone dynamics has rather been studied in macroscopic contexts, such as migration.

Furthermore, actin cyclic polymerization and depolymerization events have been related to the periodic application of probing forces in individual podosomes. And considering the confinement role of the sealing zone, it is conceivable that forces are also applied below this superstructure. Nevertheless, no tool has yet been proposed to characterize this mechanical aspect of the sealing zone. Investigations of osteoclast migration on bone-mimicking substrates have also pointed out its dependence on surface conditions, notably on variations of topography. Whether this global alteration of the cell movement might be locally regulated by changes in localization of actin-binding proteins is an issue yet to be tackled.

In this context, the main aim of this work was focused on developing tools and new approaches based on nanotechnologies to help the investigation of the sealing zone architecture and dynamic properties. Human osteoclasts differentiated from blood monocytes were observed with state-of-the-art microscopy techniques to assess quantitative characteristics of the sealing zone. This resulted in the first description of both sealing zone inner architecture and dynamics at the nanoscale.

In addition, the use of micro- and nanotechnological resources have allowed for the design of substrates to facilitate future studies in three dimensions of cell mechanics and cell responses to substrate nanotopographies.

To set up the general context of this study, the main manuscript sections have been organized as follows:

- the first chapter presents a literature review focusing on bone homeostasis general concept, introducing the major podosome characteristics, and a detailed state of knowledge concerning the sealing zone. The third section of this chapter will likely be used as a draft for the future redaction of a review;
- the second chapter consists in the report of the main results acquired when researching the sealing zone architecture and inner actin dynamics at the nanoscale. This chapter is aimed at leading to a publication in an international journal;
- the third chapter outlines the main stages and associated results of the development of two substrates aimed at measuring 3D forces applied by adhesion structures or at assessing their organization in the presence of topographies, at the nanoscale. The second part of this chapter is based on the work of an intern, whose project was integrated in the global frame of my PhD project.

In addition, a publication describing the protocol for protrusion force microscopy has been appended in annex of this manuscript (Bouissou et al., 2018). This method proposes to quantify the axial deformations induced by podosomes on thin Formvar films *via* atomic force microscopy measurements. It was developed by the works of a previous PhD student, Anna Labernadie, and I participated in the redaction of this publication during my PhD.

Chapter 1.

Literature review

This chapter introduces the general concepts of bone homeostasis and podosomes. The third section consists in a thorough examination of the current knowledge about the sealing zone in osteoclasts, and will lead to the publication of a review article in 2020.

Contents

1.1. Bone homeostasis	7
1.1.1. Bone as a complex biological environment	8
1.1.2. Bone remodeling process	12
1.1.3. Bone resorption by osteoclasts	19
1.2. Individual podosomes	23
1.2.1. Podosome molecular composition and regulation	23
1.2.2. Podosomes as dynamic, matrix-probing structures	29
1.3. The sealing zone - towards a molecular representation	38
1.3.1. Architecture of the osteoclast actin cytoskeleton	38
1.3.2. Regulation of the sealing zone	52
1.3.3. Scale-dependent dynamics of the sealing zone	58
1.4. Conclusions and perspectives	65

1.1. Bone homeostasis

Bones are living, active tissues that are constantly being remodeled through life. This permanent adaptation of both structure and architecture of bone tissue results in an inner microstructure displaying heterogeneous mechanical and mineral properties. The functions of bones can be listed as follows: mechanical support of soft tissues, levers for muscle action, protection of the central nervous system, release of calcium and other ions for the maintenance of a constant ionic environment in the extracellular fluid, and housing and support of haematopoiesis. The structure and amount of bone, both at the macroscopic and microscopic level, are determined by the genetic blueprint and by regulatory factors that help carry out bone functions.

Bone matrix degradation and *de novo* formation relies on the conjugated and tightly regulated actions of the different types of bone cells, that maintain a homeostatically controlled amount of bone mass. Especially, impairments in bone degradation have been identified as involved in many bone diseases, such as osteoporosis, leading to acute fracture risks and skeleton weaknesses. Thus, the mechanisms modulating the resorption of bone have been under thorough scrutiny for the past few decades, making them prime targets in the development of new therapeutic treatments.

1.1.1. Bone as a complex biological environment

Bones display multiple anatomic functions spanning from structurally supporting the body, providing anchorage for skeletal muscles, to protecting vital organs. They also provide an environment for bone marrow, from where blood cells originate, and they act as a storage area for minerals, especially calcium. It comprises an extracellular matrix (ECM) which is composed of both organic materials and mineral components, blood vessels and nerves, and hosts three major types of bone cells: osteoblasts, osteoclasts and osteocytes.

Structure of the bone matrix

Bone has a varied arrangement of material structures at many length scales that work in concert to perform diverse mechanical, biological and chemical functions. Scale is of importance in discussing bone architecture as the structure is hierarchical and complex. Indeed, each of its component phases is associated with specific material properties, and all are linked *via* a structural relationship at the various levels of hierarchical structural organization (Weiner et al., 1992; Landis, 1995). These levels and structures are (Fig. 1.1):

- the macrostructure: cancellous and cortical bone;
- the microstructure (from 1 to 500 μm): Haversian systems, osteons, single trabeculae, lamellas;
- the nanostructure (from a few hundred nanometers to 1 μm): fibrillar collagen and embedded mineral, non-collagenous organic proteins.

This hierarchically organized structure has an inhomogeneous, yet optimized, arrangement and orientation of the components, making the material of bone heterogeneous and anisotropic.

The macrostructure - At the macrostructure level, bone is distinguished into the cortical (or compact) and cancellous (or trabecular) types (Carter et al., 1977; Gibson, 1985; Rho et al., 1993). In cross-section, the end of a long bone such as the femur displays a dense cortical shell with a porous internal part. Flat bones such as the calvaria have a sandwich structure: dense cortical layers on the outer surfaces and a thin, reinforcing cancellous structure within.

In general, cancellous bone material is much more active metabolically, is remodeled more often than cortical bone, and is therefore ‘younger’ on average than cortical bone (Fernández et al., 2006). It is composed of bony trabecular struts and marrow-filled cavities, and displays high anisotropy, even though a preferential orientation of the struts can be defined thanks to Wolff’s law (Wolff, 1892; Van Rietbergen et al., 1996; Odgaard et al., 1997). Furthermore, its microstructure is characterized

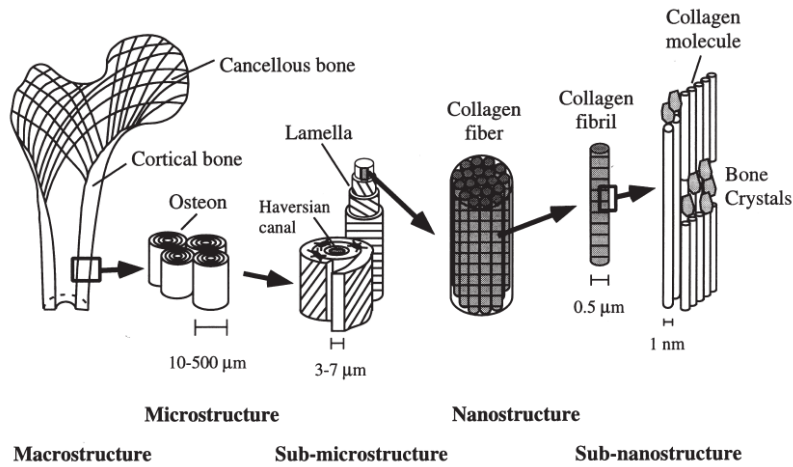


Figure 1.1.: Hierarchical structural organization of bone: (a) cortical and cancellous bone; (b) osteons with Haversian systems; (c) lamellae; (d) collagen fiber assemblies of collagen fibrils; (e) bone mineral crystals, collagen molecules, and non-collagenous proteins. Adapted from Rho et al., 1998.

by irregular and sinuous convolutions of lamellae. Typically, its porosity percent ranges from 5 % to 95 %.

In contrast, cortical bone shows lesser regional heterogeneity, which might be the result of the lower turnover rate. Its microstructure is distinguished by regular and cylindrically-shaped structure, called osteons (Wheater, 2006). Both types of bone are most easily distinguished by their degree of porosity and density, but also upon histological evaluation of their specific microstructure.

The microstructure - Collagen fibers arrange into planar layouts when they are mineralized, and form what is called lamellae. Lamellae can be categorized into thin or thick lamellae, depending on their degree of homogeneity in collagen fiber orientations and on their compactness.

A few of these can wrap in concentric layers around a central canal to establish an approximately 200 μm wide Haversian system, composed of an osteon with its Haversian canal (Fig. 1.2). Osteons have been shown to have their major axis roughly parallel to the long axis of the bone (Bullough et al., 1984). What is more, the major orientation of collagen fibers within lamellae can either be longitudinal - coplanar with osteon long axis - or alternating, which confers them different mechanical strengths depending on the loading mode (Ascenzi et al., 1967; Ascenzi et al., 1968; Ascenzi et al., 1990; Ascenzi et al., 1994). The spacing between two lamellae composing an osteon displays numerous small cavities, which are called lacunae and host osteocytes. These lacunae are interconnected *via* micron-sized channels, namely canaliculi, radiating from each lacuna and eventually reaching the central Haversian canal. Blood vessels and nerve fibers are contained within the Haversian canal, and also run transverse to osteon major axis in Volkmann's canals, ensuring the transport of nutrients and cells from the periosteum to the endosteum and back (Eriksen et al., 1994; Wheeler, 2006).

Osteons represent the essential brick of cortical bone.

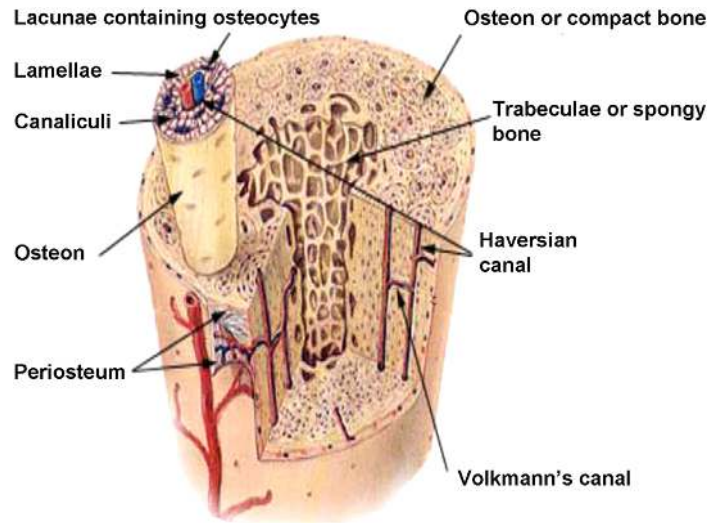


Figure 1.2.: Structural organization of osteons in the epiphysis of a long bone. There are two basic systems: the Haversian canals within osteons, which run near longitudinally, and the Volkmann canals, which run nearly radially. The two systems are intimately anastomosed to each other. Canaliculi serve to connect osteocytic processes. Adapted from Cowin et al., 2015.

In contrast, cancellous bone is made of an interconnecting framework of trabeculae, plates and rod-like elements ranging from 50 to 500 μm in diameter. They have been showed to align towards the major mechanical load distribution within long bones and some short bones (Gdyczynski et al., 2014).

The nanostructure - In contrast to all other physiological extracellular matrices, bone matrix displays the particularity of being mineralized. It is mostly composed of type I collagen fibers assembled from single collagen fibrils, in which collagen molecules and hydroxyapatite crystals alternate in a periodic fashion (Glimcher, 1989). Mature hydroxyapatite crystals are plate-shaped, and occur within the discrete spaces within collagen fibrils, thus forcing their discontinuous distribution. They display a specific crystalline orientation, with their vertical axis - c axis - aligning with collagen fibril long axis (Kuhn-Spearing et al., 1996). Collagen molecules self-assemble into fibrils with a specific tertiary structure, displaying a 67 nm periodicity and 40 nm gaps between each molecule.

Bone cells involved in the bone remodeling process

Both bone tissue growth during development phase and bone repair and remodeling through life are coordinated processes controlled by the specific functions of three types of bone cells (Fig. 1.3). Osteoblasts form new bone matrix and osteoclasts resorb bone, while osteocytes are in charge of generally maintaining bone tissue integrity.

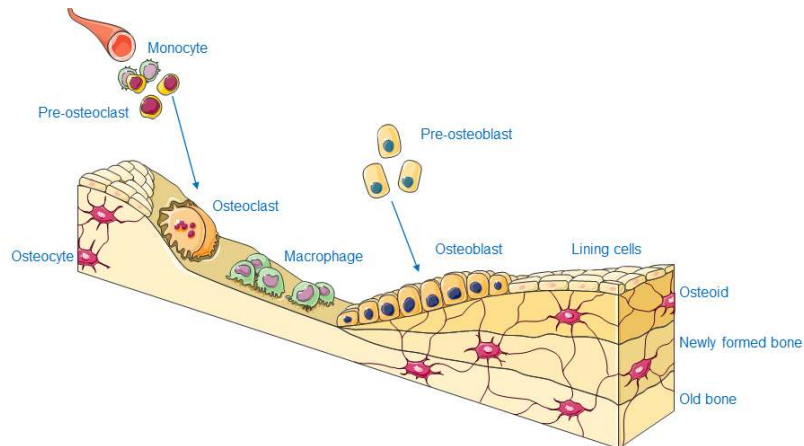


Figure 1.3.: Bone cells involved in the bone remodeling process. Osteoclasts are responsible for the resorption of bone tissue, and originate from the monocytic lineage. Osteoblasts are mainly involved in the formation of the osteoid, and they are part of the mesenchymal lineage. Osteocytes mediate both processes of bone formation and resorption by interacting with osteoblasts and osteoclasts through many processes reaching out within canaliculi. Adapted from Servier Medical Art.

Osteoblasts - Osteoblasts are mononuclear cells derived from the mesenchymal lineage. They are located on the surface of osteon seams and secrete a protein mixture known as osteoid, which then mineralizes to become mature bone tissue. Osteoid is mainly composed of type I collagen - 90% of the secreted mix -, and of non-collagenous SIBLING proteins - standing for small integrin-binding ligand, N-linked glycoprotein. Among these glycoproteins are fibronectin, vitronectin, osteopontin and osteocalcin, which allow bone mineralization after crystallization of hydroxyapatite *via* deposition of calcium and phosphate (Khurana et al., 2009).

Osteoblasts regulate differentiation and function of other bone cells like osteoclasts, through secretion of various molecules. Among them are notable cytokines such as RANK-L - receptor activator of nuclear factor κ -B ligand - and M-CSF - macrophage colony stimulating factor -, which can induce for *in vitro* osteoclastogenesis. Moreover, osteoblasts are actively involved in mineral homeostasis and bone metabolism through their response to two central hormones, namely parathyroid hormone and 1,25-dihydroxyvitamin D3.

Osteoclasts - Osteoclasts are multinucleated giant cells from the hematopoietic lineage. They are located on bone surfaces in what are called Howship's lacunae - or simply resorption pits. Their main function consists in degrading both organic and mineralized bone components. To do so, they actively secrete protons to locally decrease the pH and thus dissolve apatite crystals, and proteases to enable the breakdown of the protein scaffold (Coxon et al., 2008). Upon this bone matrix disassembly, minerals - calcium, phosphate, magnesium -, peptides from degraded proteins and signaling molecules are released in the cell microenvironment, and eventually reach the blood stream (Mulari et al., 2003; Yadav et al., 2011).

Osteoclast differentiation and function are monitored by osteoblasts and osteocytes through RANK-L expression, and also by immune cells through several others cytokines such as M-CSF, TNF- α and interleukins (Nakashima et al., 2011; O'Brien et al., 2013). In contrast, osteoclasts are involved in chemotactic migration processes of osteoblasts through PDGF expression (Sanchez-Fernandez et al., 2008).

Osteocytes - Osteocytes are mononucleated cells originated from osteoblasts that have embedded themselves in the newly formed bone matrix they secreted. They occupy lacunae, and display many processes reaching out within canaliculi, allowing them to communicate with other osteocytes *via* gap junctions as well as with other bone cells *via* secretion of signaling molecules (Tanaka-Kamioka et al., 1998; Khurana et al., 2009; Dallas et al., 2013). Indeed, they are known to be mechanosensory cells, able to translate loading stresses into facilitation of macromolecule diffusion, such as paracrine factors regulating bone remodeling (Santos et al., 2009; Paiva et al., 2017).

Osteocytes are involved in mediating osteoblast-induced bone formation through the expression of OSF-1 - osteoblast-specific factor 1 -, DMP1 - dentin matrix protein 1 - and sclerostin (Tezuka et al., 1990; O'Brien et al., 2013). They have also been shown to consist in the major source of RANK-L, a crucial cytokine for osteoclastogenesis and bone resorption (Xiong et al., 2011).

1.1.2. Bone remodeling process

Bone has the ability to remodel, by altering its size, shape and inner structure in order to meet the mechanical demands to which it is submitted (Buckwalter et al., 1995). Bone remodeling occur in discrete foci approximately 2-3 mm long and 200-300 μm wide (Gruber et al., 2008). These packets were termed "bone remodeling units" upon their first description by Frost in 1964 (Frost, 1965). They are also often found referred to as "basic multicellular units" in the recent literature, and are composed from the major bone cells accompanied by a blood supply and supportive connective tissue (Jilka, 2003; Sims et al., 2014).

Main stages of the remodeling cycle

The remodeling process allows for the replacement of "old" bone tissue presenting altered material properties, by newly formed bone matrix, *via* a resorption front. Thus, a given bone fraction is regenerated with a few year frequency, and the whole bone mass takes approximately 10 years to be entirely renewed (Couret, 2004).

The typical duration of a remodeling cycle spans approximately 4 months for an adult, with the bone formation phase being longer than the resorption phase. It can be initiated as a result of events such as microfracture, mechanical loading, or low calcium due to pregnancy or a deficient diet. Bone remodeling process can be divided in six main stages: activation, resorption, reversion, formation, mineralization and latency, even though the nomenclature for this process is not universal (Dempster et al., 2006; Kini et al., 2012).

Activation - The activation phase lasts approximately two to three days, during which osteocytes are activated through multiple environment stimuli such as local mechanical strains exceeding a certain value. They subsequently send out signals to promote both hematopoietic cell differentiation into osteoclasts, and mesenchymal cell differentiation into osteoblasts.

Resorption - The resorption phase spans from thirty to forty days. During this stage, osteoclasts adhere to the bone matrix in order to degrade its components through acidification and enzyme digestion. Each cell breaks down bone microstructure at an approximate speed of $40\mu m.day^{-1}$, for a duration of ten days and is eventually relayed by other osteoclasts.

Reversion - The reversion phase corresponds to the change in the active bone cells: osteoclasts are progressively replaced by osteoblasts over a period of approximately two days.

Formation - The formation phase spans approximately eighty days, during which osteoblasts mainly secrete collagenous and non-collagenous proteins, along with growth factors. The newly formed osteoid is created with a longitudinal speed of approximately $15\mu m.day^{-1}$ and a radial apposition speed of approximately $1\mu m.day^{-1}$.

Mineralization - The mineralization phase is the longest active one, as it spans months. Osteoblasts change their secretion from organic to mineral material, in order to promote the crystal growth of hydroxyapatite crystals within the collagen networks. A primary mineralization stage occurs for the first few days of this phase, during which more than half of the total mineralization of the new osteoid is achieved. Then, a secondary mineralization lasts approximately six months and is characterized by a decreasing rate of mineral apposition.

Latency - The last phase is an inactive one, during which the newly shaped bone microstructure is completely formed until the next remodeling cycle replaces it. Osteoblasts either transform into “bone lining cells”, which are quiescent cells present at sites where active bone formation is absent (Bartl et al., 2009), or into osteocytes. It can also be viewed as the first stage of the remodeling cycle, as seen in Figure 1.4.

Thus, the bone remodeling cycle results in the generation of a new osteon or bone lamella within pre-existing bone microstructure.

Factors influencing the bone remodeling process

The bone remodeling process depends on environmental factors to ensure that the specialized bone cells have access to the targeted remodeling site, they efficiently communicate and they are induced to normally function. This is achieved through the vascularization and innervation of the bone tissue, and also *via* numerous biochemical factors.

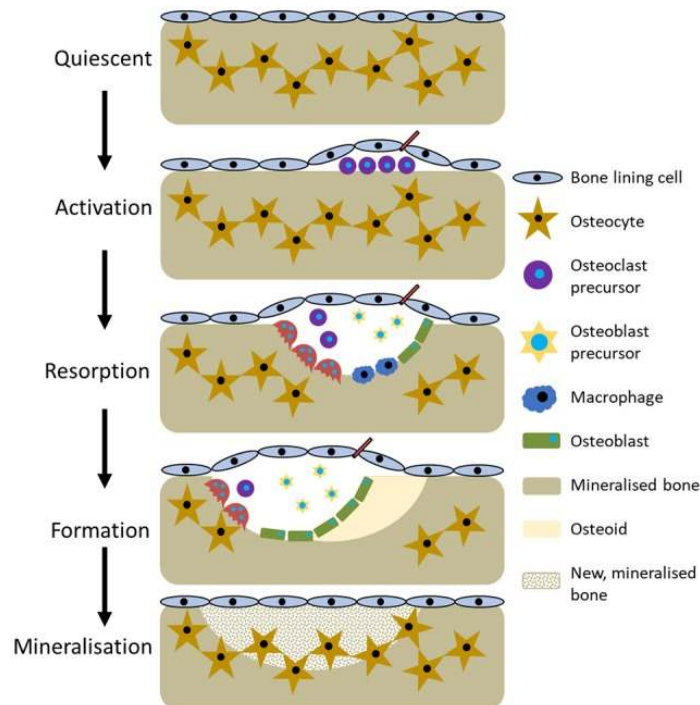


Figure 1.4.: The main stages of the bone remodeling process. Quiescent describes inactive bone prior to remodelling initiation. Then, as a result of events altering the bone tissue integrity, the activation phase begins. Resorption then begins, with osteoclasts degrading the bone and liberating growth factors. The formation phases begins with osteoid, a collagenous matrix, being deposited to fill the cavity. This is mineralised over the following 3-6 months by osteoblasts secreting matrix vesicles. Adapted from Owen et al., 2018.

Vascularization and innervation of bone - Vascularization of the bone tissue is ensured by a peripheral network of vessels located near the periosteum. As it has been stated earlier, blood vessels are allowed to enter bone *via* both Volkmann's and Haversian canal networks (Fig. 1.5). The major arterial supply to the diaphysis is from the nutrient artery. There is an abundant capillary bed throughout the bone tissue that drains outwards to the periosteal veins.

Along with the vessels, nervous fibers also run through inside these canals. Moreover, the nerve trunk is located inside the diaphysis, within the medullary cavity where it coexists with both bone marrow and feeding vessels (Wheater, 2006). Once osteoclast precursors have arrived at the remodelling site from the bloodstream or surrounding marrow, two factors are predominantly responsible for their maturation into osteoclasts: M-CSF and RANK-L.

Biochemical factors - In addition to the regulation of osteogenesis by genetic factors controlling the size and shape of bones and to mechanical cues inducing structural and material alterations, bone remodeling is governed by biochemical factors. Some of the major biomolecules involved in bone

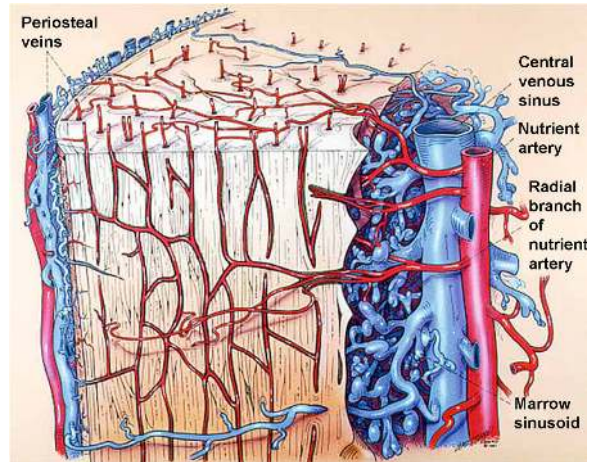


Figure 1.5.: The capillary network within cortical bone. The vascular connection between bone marrow, cortex, periosteum and attached muscle displays multiple pathways. The radial branches of the nutrient artery form a leash of arterioles that penetrate the endosteal surface to supply the bone capillary bed. Small arterioles from these radial branches supply the marrow sinusoids adjacent to the bone. The transcortical blood supply transits in the Volkmann canals and the longitudinal blood supply transits in Haversian systems or osteons. Adapted from Cowin et al., 2015.

homeostasis are listed as follows (Fig. 1.6):

- RANK, expressed on osteoclasts, and its ligand RANK-L, member of the tumour necrosis cytokine family that is predominantly produced by osteoblast-lineage cells; but also osteoprotegerin (OPG), which is a decoy receptor that prevents RANK activation through its binding to RANK-L. Therefore, the resorption process is directly dependent on the RANK-L:OPG ratio (Mizuno et al., 1998; Boyce et al., 2007);
- M-CSF that influences differentiation and survival of hematopoietic precursors. It is produced by osteoblasts and stromal cells, and binds on its specific receptor colony-stimulating factor-1 receptor (c-fms) (Hodge et al., 2007);
- osteopontin is part of the extracellular matrix glycoproteins which compose bone, it anchors osteoclasts to bone matrix during the remodeling process (Reinholt et al., 1990);
- cathepsin K, an osteoclastic cysteine protease, and matrix metalloproteinase-9 (MMP-9), an osteoclastic enzyme, both of which serve as catabolizing agents for the breaking down of collagen and gelatin (Sprangers et al., 2017);
- tartrate-resistant acid phosphatase (TRAP) is also an osteoclastic enzyme, of which activity strongly correlates with bone resorption, and consists in one the key features for osteoclastic cell identification (Hayman et al., 1996; Halleen et al., 2000);
- alkaline phosphatase is an enzyme secreted by osteoblasts that promotes the formation of hydroxyapatite crystals within the newly formed osteoid (Orimo, 2010);
- runt-related transcription factor 2 (RUNX2) is a key transcription factor associated with

- osteoblast differentiation, and has been described to regulate bone formation through its interaction with osterix (Nakashima et al., 2002; Komori, 2010);
- parathyroid hormone (PTH) can indirectly stimulate osteoclastogenesis by action on osteoblasts (Borba et al., 2010);
 - 1,25-dihydroxyvitamin D3 is the active form of vitamin D3, and has been shown to stimulate RANK-L expression in osteoblasts and osteocytes (Kitazawa et al., 2002; Shevde et al., 2002; You et al., 2008).
 - growth factors stimulate and activate osteoprogenitor cells, which will eventually differentiate into osteoblasts and osteocytes, and were proposed to be released during resorption and initiate local bone formation (Hauschka et al., 1986; Pfeilschifter et al., 1987; Mohan et al., 1991);
 - estrogens and steroid hormones have notably been shown to control the initiation of endochondral ossification processes, and to be important for promoting the differentiation of stem cells into osteoblasts (Gruber et al., 2008).

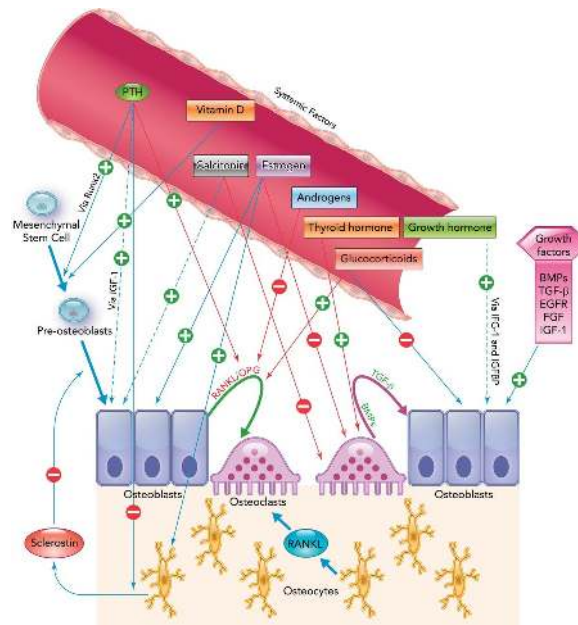


Figure 1.6.: Systemic and growth factor regulation of bone remodeling. Parathyroid hormone is involved in numerous signaling pathways, ranging from inducing differentiation of committed osteoblast precursors, stimulating the proliferation and differentiation of osteoprogenitors to mature osteoblasts via IGF-1, to inducing secretion of RANK-L and M-CSF from mature osteoblasts to promote osteoclastogenesis. Vitamin D3 stimulates osteoblastogenesis via differentiation of mesenchymal stem cells to osteoblasts. Calcitonin increases osteoblast proliferation and suppresses bone resorption by inhibiting the activity of osteoclasts. Estrogen inhibits bone resorption by directly inducing apoptosis of the bone-resorbing osteoclasts. Androgens can also indirectly inhibit osteoclast activity and bone resorption via effects on osteoblasts/osteocytes and the RANKL/RANK/OPG system. Besides systemic hormonal regulation, other growth factors, such as IGFs, TGF- β , FGFs, EGF, WNTs, and BMPs, also play a significant role in regulation of physiological bone remodeling. Adapted from Siddiqui et al., 2016.

Remodeling defects and bone diseases

Besides fractures and other dramatic physical defects, the previously cited environmental factors can also hamper bone integrity. Indeed, a slight divergence in the synergy between bone forming process and bone degrading process can induce either an increase of bone mass and density: osteopetrosis, or on the contrary a decrease in bone mass and density: osteopenia, and osteoporosis when the imbalance is substantially tilted towards bone loss.

While osteopetrosis is a hereditary genetic disorder that only rarely occurs in humans, osteoporosis is a prevalent disease mostly due to the decrease in steroid hormone expression with age. It affects humans with a ratio of one in every three women and one in every eight men worldwide (Bartl et al., 2004). It induces a greater risk of bone fractures which obviously impair the quality of life of the patients, but also pose an increased risk of mortality (Bartl et al., 2004). So far, most of the clinical treatment strategies have focused on hampering osteoclast-mediated bone resorption, so as to reduce the pathological decline in bone mass. Although, emerging treatments have rather elected to stimulate osteoblastic counter-activity of bone formation (Marie et al., 2011).

In the 1970s, growing evidence has been found of the possible regulation of bone cells by the immune system. Indeed, studies focusing on soluble factors secreted by leucocytes and myeloma cells, such as interleukin 1, have described their stimulating effect on osteoclastic activity (Horton et al., 1972; Mundy et al., 1974; Dewhirst et al., 1985). In addition to the subsequent findings of common signaling or cytokine regulation pathways, the fact that bone and immune systems share an immediate vicinity within bone microstructure has raised questions pertaining to a possible physiological cross-regulation. This exploration gave rise to a new scientific field, namely “osteimmunology” (Arron et al., 2000).

A large area of osteimmunology has focused on tackling the implication of autoimmune diseases in pathological bone remodeling. One example of such an implication is the case of rheumatoid arthritis, a systemic autoimmune disease, which is characterized by acute inflammation of the joints with severe articular bone and cartilage erosion (Schett et al., 2012) (Fig. 1.7). It is thought that at the preclinical stage, the interaction of aggravating environmental factors with genetic and epigenetic regulation would result in alterations of some self antigens (McInnes et al., 2011). The immune system would thus hypothetically decrease its tolerance to these altered antigens, inducing the release of autoantibodies in the bone marrow by lymphocytes. It has been demonstrated that one of these autoantibodies could promote osteoclastic differentiation, leading to an increased number of bone-resorbing cells and eventually to severe bone loss in joints (Harre et al., 2012).

Another example of the cross-talk between the immune system and bone cells is the observation of bone defects in the context of HIV infection (Cotter et al., 2014). Indeed, when HIV infection occurs, the balance between bone formation and resorption is impaired by an increase of osteoclast differentiation and activity (Gruber et al., 1995; Fakruddin et al., 2005) associated to apoptosis activation and biological activity inhibition of osteoblasts (Wang et al., 2002; Cotter et al., 2007; Gibellini et al., 2008) (Fig. 1.8). What is more, it has been recently demonstrated that HIV pathogen is able to directly elicit preferential bone resorption *via* its targeting of osteoclasts *in vivo* (Gohda

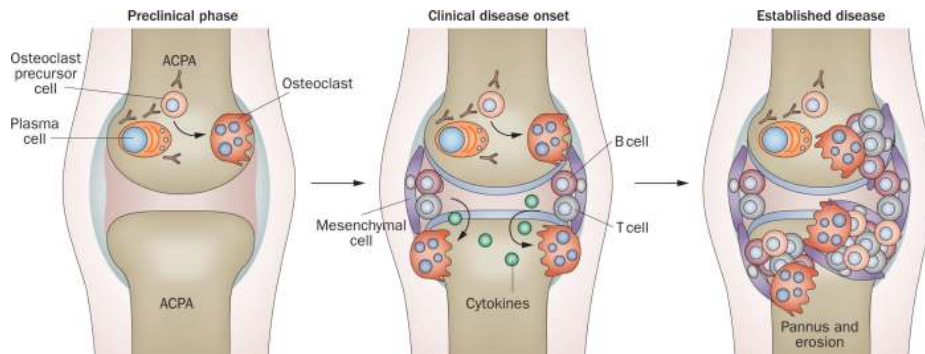


Figure 1.7.: Evolution of bone erosion in the course of rheumatoid arthritis. During the preclinical phase, anti-citrullinated protein antibodies are produced early on by plasma cells and can stimulate osteoclast differentiation and lead to initial bone loss. These early changes may initiate in the bone marrow adjacent to the joint. Synovitis at the onset of clinical disease leads to production of cytokines, which stimulate osteoclastogenesis by inducing expression of RANK-L, and synergize with RANK-L to enhance bone erosion. Established rheumatoid arthritis is characterized by the presence of large bone erosions filled with inflamed, synovially derived pannus tissue. Adapted from Schett et al., 2012.

et al., 2015; Raynaud-Messina et al., 2018) and their specific intracellular osteolytic structure.

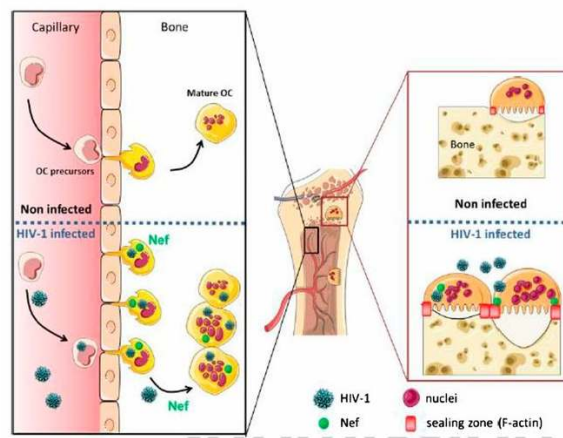


Figure 1.8.: Direct bone effect of HIV. HIV-1 directly infects circulating osteoclast precursors, enhancing their differentiation and migration to bones, and also alters the structure and function of the osteoclast sealing zone, the resorption apparatus of the bone. Adapted from Raynaud-Messina et al., 2018.

1.1.3. Bone resorption by osteoclasts

Mature osteoclasts have one main task as bone cells, which consists in bone resorbing and makes their specificity. As has been pointed out earlier, bone resorption is one of the main stages during the remodeling process, allowing for bone development and reshaping. Furthermore, most of the pathological bone conditions are due to an increase in osteoclastic activity. Hence, unraveling the intracellular mechanisms responsible for bone degradation has been of the utmost importance for the last decades. Bone resorption has been described as a multi-step process involving adherence to bone, cytoskeletal reorganization, membrane compartmentalization and vesicular trafficking.

Membrane compartmentalization and cytoskeleton rearrangement

Osteoclastic activity is notably defined by specific morphological alterations. Indeed, upon matrix recognition osteoclasts are switched to an active form, in which adhesion to the bone surface is followed by a rearrangement of their cytoskeleton. Osteoclast cytoskeleton is considered unique in its ability to polarize the cell resorptive machinery to the bone-cell interface, where it creates an isolated resorptive microenvironment consisting of an actin ring: the sealing zone, surrounding a specific membrane domain: the ruffled border (Teti et al., 1991). The sealing zone allows for the segregation of the resorptive microenvironment from the general extracellular medium (Teitelbaum, 2011), and will be discussed in further details in a specific section 1.3 of this chapter.

Osteoclast membrane display distinctive compartments: the basolateral membrane forms a functional secretory domain at its topmost location, and the apical domain is reorganized with multiple membrane convolutions and finger-like projections to form the so-called ruffled border (Vaananen et al., 2000; Mulari et al., 2003). These convolutions allow for an enhanced surface in contact with bone, even though the area defined by the sealing is restricted. Both domains display acute vesicular trafficking from the ruffled membrane to the opposite apical secretory domain during the degradation process.

Bone degradation - vesicle trafficking, acidification and proteolysis

Integrin-mediated transmission of extracellular signals induce the migration of proton pumps towards the ruffled membrane *via* their transport in acidifying vesicles. In the cell cytosol, lytic enzymes-containing vesicles are synthesized to be secreted into the resorption lacuna underneath the cell, *via* exocytosis (Fig. 1.9).

Osteoclasts acidify the extracellular confined environment by secreting protons, which are provided by the enzyme carbonic anhydrase, with the help of vacuolar electrogenic H^+ -transporting adenosine triphosphatase (v-ATPase) (Baron et al., 1985; Blair et al., 1989; Frattini et al., 2000). This proton evasion is counterbalanced by the chloride-carbonate exchange at the basolateral membrane, and the release of chloride ions through the CIC-7 channel at the ruffled border, in order to prevent an intracellular increase of pH value (Sly et al., 1985; Kornak et al., 2001). Hence, the resorption lacuna is filled with an hydrochloride-containing medium, which buffers its pH value at approximately 4.5.

This acidification allows for the break down of mineral apatite crystals, and subsequently providing access the matrix organic components such as type I collagen.

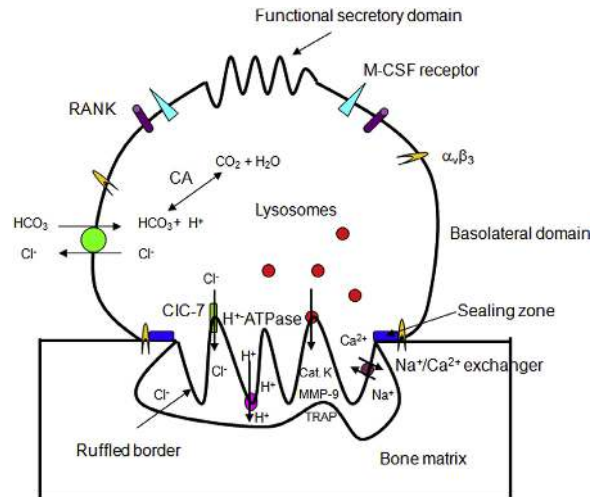


Figure 1.9.: Schematic view of a bone resorbing osteoclast. At the ruffled border, the extracellular vacuole is acidified by secreting protons thanks to transporting adenosine triphosphatase (v-ATPase). Collagen is degraded by proteases released by lysosomes such as cathepsin K, and metalloproteases such as MMP-9, including collagenase and gelatinase. Intracellular alkalization is prevented by expulsion of Cl^- through CIC-7 chloride channel and chloride-bicarbonate exchanges at the basolateral membrane. Adapted from Soysa et al., 2016.

The organic part of the bone matrix is digested by proteases such as cathepsin K, and metalloproteases including collagenase and gelatinase. The low pH zone provides the optimal conditions for cathepsin K to degrade the collagenous matrix (Drake et al., 1996). What is more, it has been shown to be associated with the lysosomal protein synaptotagmin VII (Syt VII) and lysosome-associated membrane protein-2 (LAMP2) within lysosomes. Thus, Syt VII regulates the secretion of cathepsin K in lysosomes. It has also been proposed to work along with SNARE proteins, which are known to be involved in the vesicular trafficking in exocytosis, in order to control the merging of lysosomes with the ruffled border by facilitating the apposition of both membranes (Zhao et al., 2008).

MMP-9 is the most expressed MMP by osteoclasts and is also capable of degrading demineralised collagen. However, in addition to this role it also appears to be involved in osteoclast recruitment through the conversion of the inactive form of $\text{TNF-}\alpha$ into the active cytokine, promoting osteoclast formation and survival (Paiva et al., 2017).

In addition, it has been demonstrated that the degraded matrix products are endocytosed at the ruffled border, subsequently submitted to further degradation within secondary lysosomes. Some are also transcytosed and transported to the basolateral secretory domain to be released into the cell environment (Bruzzaniti et al., 2006). This disposing of resorption products allows for the further excavation of bone tissue by osteoclasts, while maintaining their tight attachment to the matrix.

Autophagocytosis has also been shown to play a role in bone resorption, as facilitating ruffled border formation. Indeed, autophagy proteins Atg5, Atg7 and LC3 have recently been revealed to play a crucial role in the vectorial secretion of lysosomal constituents, including cathepsin K (DeSelm et al., 2011).

Resorption/migration cycles

The functional cycle of osteoclastic activity also relies on the alternation between a bone adhesion and resorption phase and a migration stage to bring the cell to new resorptive sites. Indeed, basic multicellular units dig and fill tunnels through cortical bone and in trabecular bone they create trenches on the surface (Fig. 1.10). The osteoclasts are at the front, forming the cutting cone, with osteoblasts behind forming the closing cone. The basic multicellular units can move in all three axes in cortical bone and in the two axes in trabecular bone as they lie on the surface of lamellae (Parfitt, 2002; Clarke, 2008).

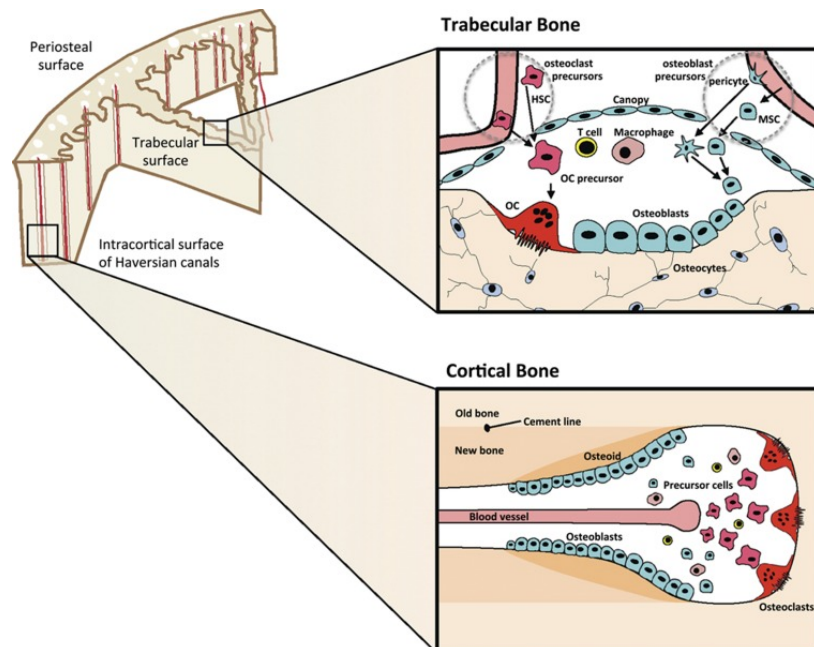


Figure 1.10.: Remodeling is initiated within basic multicellular units at points beneath the canopy of cells lining trabecular bone (upper panels) and within cortical bone Haversian canals (lower panels). Osteoclast and osteoblast precursors reach the basic multicellular units due to the proximity of blood vessels. Adapted from Sims et al., 2014.

As osteoclasts are part of the monocytic lineage, their migration during the bone remodeling process is thought to be driven by podosomes: punctate actin rich adhesion structures that have been found in the sealing zone (Linder et al., 2015), discussed in the next section of the chapter 1.2. Indeed, it was suggested that osteoclasts can assume a cyclic switch between a sealing zone-

associated state and a non-presenting sealing zone state, respectively alternating between resorptive activity and motility (Saltel et al., 2008; Novack et al., 2011). This hypothesis relies on two *in vitro* observations:

- the sealing zone structure appears quite stably maintained in a given location during the whole degradation process;
- the resorption traces observed after osteoclasts were plated on bone-mimicking matrices are shaped in individual pits, sometimes partially overlapping and displaying trail-like patterns.

Therefore, if this hypothesis proves to be true, it would mean that osteoclasts are able to undergo fast transitioning between two different axes of polarization: apico-basal polarization during resorption, antero-posterior polarization during migration.

However, recent studies have led to the emergence of another plausible mode to combine resorption and migration (Rumpler et al., 2013). Indeed, a distinction between osteoclasts preferentially forming individual pits and others displaying preferably continuous trenches has been proposed, based on the sex of the blood donors from which monocytes had been extracted (Merrild et al., 2015) (Fig. 1.11). Furthermore, time-lapse observation of degrading osteoclasts confirmed their capacity of temporally combining their resorptive and motile activities (Søe et al., 2017). This novel finding hence exhibits that a podosome superstructure such as the sealing zone endorses the dual function of adhesion and matrix remodeling.

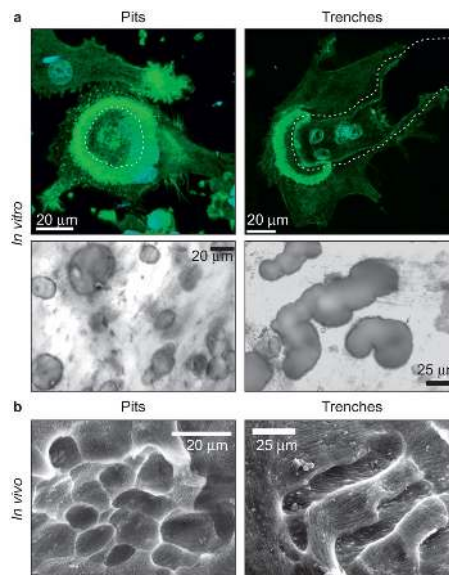


Figure 1.11.: Matching resorption patterns generated by OCs *in vitro* and *in vivo*. (a) Pits (left) and trenches (right) generated by OCs *in vitro* on bone slices, and corresponding actin configurations of these OCs as shown by confocal fluorescence imaging (green). (b) Pits (left) and trenches (right) generated by OCs *in vivo*. Trabecular bone surfaces from the iliac crest of adult sheep were observed through SEM. Adapted from Merrild et al., 2015.

1.2. Individual podosomes

Podosomes are dot-like, highly dynamic adhesion structures, which are found in various types of motile cells from myeloid origin, such as macrophages, dendritic cells or osteoclasts. They were first observed in monocytes and osteoclasts through fluorescence observation of actin distribution, as peculiar punctate aggregations (Zallone et al., 1983). They have been subsequently demonstrated to form either constitutively in monocytic cells such as monocytes, macrophages and immature dendritic cells (Linder et al., 2000b; Linder et al., 2000a; Burns et al., 2004; Linder, 2009), or in an induced manner in smooth muscle cells, endothelial cells or fibroblasts in response to soluble factors or oncogenes (David-Pfeuty et al., 1980; Moreau et al., 2003; Burgstaller et al., 2004; Burgstaller et al., 2005). In macrophages or dendritic cells, podosomes are mostly found randomly distributed in an individual manner throughout the ventral membrane, whereas they can also arrange into a superstructure called the sealing zone in osteoclasts. Their typical diameter ranges in the submicron scale, with a measured height of approximately $0.6 \mu\text{m}$ (Linder, 2009; Labernadie et al., 2010). They have been shown to be involved in the degradation of the extracellular matrix through a local proteolytic activity (Wiesner et al., 2010).

1.2.1. Podosome molecular composition and regulation

Even though their molecular composition is very similar to that of focal adhesions, owing to their sharing of a multitude of proteins included in the more than 300 members of the podosome proteome, podosome architecture greatly contrasts with focal adhesion organization (Cervero et al., 2012). Indeed, filamentous actin (F-actin) is assembled in a densely packed core facing the membrane. Surrounding the core, integrins form a ring in which are also found adaptor proteins linking them to actin filaments. A third functional subdomain has been recently located above the podosome core, namely the cap domain, and is currently under thorough scrutiny thanks to the acute advances in microscopy techniques. Each of these domains are characterized by a certain number of typical proteins, the presence and localization of which is closely related to various regulation pathways.

Podosome molecular composition

Individual podosomes have been geometrically characterized as displaying a core of approximately 200 nm in diameter, and a ring of adhesion proteins 200 nm wide and located at 350 nm from the core (Proag et al., 2015; Staszowska et al., 2017). Moreover, their spatial distribution shows no apparent lattice pattern, and within this randomly generated population each individual is separated from its closest neighbor of approximately $1.2 \mu\text{m}$, in human monocyte-derived macrophages (Proag et al., 2015). Each of the podosome subdomains is characterized with a specific arrangement of actin filaments: the core consists in a densely packed column of vertical filaments, which is connected to its adhesion ring *via* long radial filaments tilted relative to the membrane plane, and is covered at its topmost extremity by a cloak-like area (Fig. 1.12).

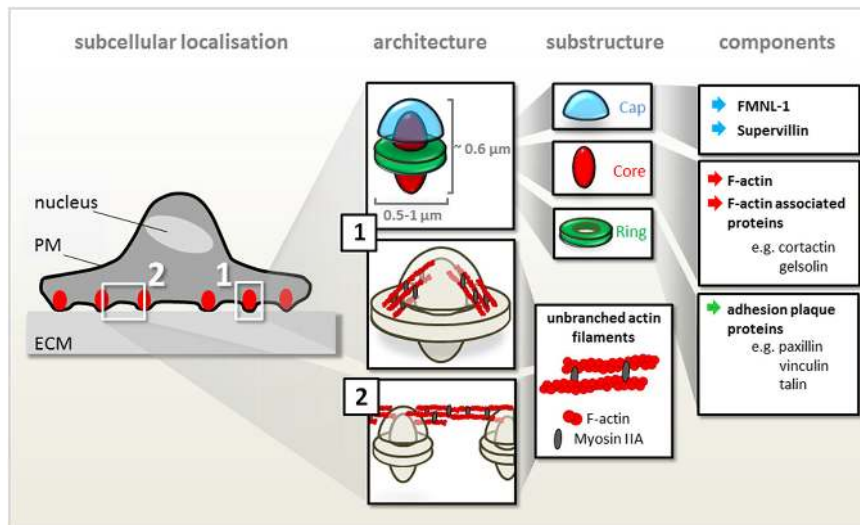


Figure 1.12.: Podosome architecture and composition. Podosomes are displayed as numerous dot-like structures at the substrate-contacting cell membrane, as in the case of a macrophage seeded on a 2D matrix (left). An architectural model is proposed of podosome substructures (cap, core and ring), as well as the arrangement of lateral unbranched acto-myosin filaments and acto-myosin cables connecting individual podosomes (center). Typical components of podosome cap, core and ring substructures are indicated (right). Adapted from Linder et al., 2015.

Podosome core domain - Both transmission and scanning electronic microscopy (TEM and SEM, respectively) techniques revealed the accumulation of actin filaments at podosome sites, and their close contact with the membrane below in the 80s (Hartwig et al., 1986; Gavazzi et al., 1989). Additionally, observation with electronic microscopy of cells with their dorsal membrane torn away by mechanical or chemical actions previous to image acquisition - this technique is subsequently referred to as unroofing (Heuser, 2000) - revealed precious ultrastructural insights: the preferential vertical orientation of F-actin at the core, the radial organization of filaments around each core, and the interaction of podosomes with other cytoskeleton polymers such as microtubules (Evans et al., 2003; Gawden-Bone et al., 2010). Advances in immunostaining techniques for TEM have allowed for the precise localization of podosome inner components in transverse two-dimensional (2D) sections: F-actin at the core distributed in a dome-like shape, but also other proteins such as gelsolin (Gawden-Bone et al., 2010).

It also contains actin-interacting proteins, such as α -actinin, gelsolin and cortactin (Fig. 1.13). Cortactin, *via* its interaction with F-actin and the Arp2/3 complex, is involved in the regulation and stabilization of the branched actin networks (Weed et al., 2001; Weaver et al., 2001; Weaver et al., 2002; Osiak et al., 2005). Its phosphorylation by the tyrosine kinase protein Src promotes actin filament assembly in podosome cores, and has been related to the invasiveness properties of tumor cells (Kaverina et al., 2003; Kirkbride et al., 2011). Additionally, as the Arp2/3 complex serves both as a nucleation site and a filament-branching anchorage point, its localization at the core substantiate

the hypothesis of a high interconnection degree of F-actin within the core (Linder et al., 2000a; Yamaguchi et al., 2005; Baldassarre et al., 2006). However, a more resolved technique of acquisition allowing in-depth exploration at the single filament scale, such as cryo-electron tomography, would greatly help in completely assessing the geometry of the actin network (Medalia et al., 2007).

FilaminA and α -actinin have also been observed in the core domain, in which they act as bundling proteins (Zhou et al., 2010; Kim et al., 2011). FilaminA has been shown to be involved in stabilizing podosomes in monocyte-derived macrophages (Guiet et al., 2012). Moreover, Tks5, which is an adaptor protein and a substrate for Src, has been located in podosome cores of human cancer cells, and appears to be required for both podosome formation and mesenchymal migration mode. Additionally, as it appeared to be overexpressed in human cancer cells and tumor tissues, and is involved in invasive processes (Seals et al., 2005).

Noticeably, some transmembrane proteins are also present at the core, such as CD44, which recognize hyaluronic acids, laminins and collagen (Chabadel et al., 2007). Indeed, it has been observed that activation of integrin sub-unit β 1 resulted in an increase in the degradation of the extracellular matrix by melanoma cells (Nakahara et al., 1998). Furthermore, this integrin appears as crucial for the integrity of podosomes, as its loss induced the dissolution of podosomes and its malfunction yielded a disorganization and disassembly of podosomes, being replaced by focal adhesions in Src-transformed fibroblasts (Destaing et al., 2010).

Podosome ring domain - Podosome adhesion ring is composed of both transmembrane proteins, and proteins involved in connecting the actin cytoskeleton to integrins or in transducing signals (Fig. 1.13). Integrin sub-unit β 2 has been localized in the adhesion ring of podosomes in macrophages and dendritic cells, and is considered to be the predominant representing member of the integrin family in individual podosomes in dendritic cells (Burns et al., 2004; Calle et al., 2004a; Gawden-Bone et al., 2014).

The most cited plaque proteins to characterize the adhesion ring are vinculin, talin and paxillin, and they are typically observed as a continuous annular area surrounding the F-actin core showing but little colocalization between the two (Linder et al., 2003). Talin binds directly to integrins, and connects them to the actin cytoskeleton *via* its own association with vinculin. What is more, paxillin is a protein known to be involved in mechanotransduction signaling pathways. However, in contrast to what is usually observed with traditional fluorescence microscopy techniques, super-resolution microscopy has been brought to light that the supposed “ring” domain is actually made of an accumulation of nanoscale restricted foci where adhesion proteins preferentially localize (Van den Dries et al., 2013b; Walde et al., 2014).

And indeed, super-resolution microscopy has largely benefited to the nowadays knowledge of the nanoscale organization of the ring domain. The study of Cox and coworkers on the dynamic of vinculin and talin, making use of the Bayesian analysis of blinking and bleaching method benefiting from a 50 nm resolution, not only proposed an uncharted view of the podosome organization, but also set the stage for the subsequent explorations (Cox et al., 2012). Shortly after, it was hence followed by the realization of the discontinuous organization of the ring domain, composed of islets

where talin and integrin $\alpha M\beta 2$ interact, thanks to the application of the direct stochastic optical reconstruction microscopy (dSTORM) technique (Van den Dries et al., 2013b; Van den Dries et al., 2013a).

Due to the conical shape of actin distribution when podosomes are observed with electronic microscopy techniques, it is thought that the radially emanating filaments could act as a link between the core and the ring domains (Proag et al., 2016). In addition, another set of actin filaments has been identified as running parallel to the ventral membrane and appeared to connect individual podosomes to some of its direct neighbors (Bhuwania et al., 2012; Labernadie et al., 2014). These observations have recently been shown to coincide with super-resolved fluorescence microscopy acquisitions. Indeed, dSTORM images have allowed the visualization of the single actin filaments emanating from the core and connecting two adhesion structures. What is more, vinculin has been preferentially located to single filaments of actin, close to the core and slightly tilted in a lateral direction (Van den Dries et al., 2013b). In contrast, myosin II has very recently been localized to the connecting filaments, while it appeared absent from the lateral set of F-actin, which further corroborates the hypothesis of different types of actin subsets forming the individual podosome structure (Van den Dries et al., 2019).

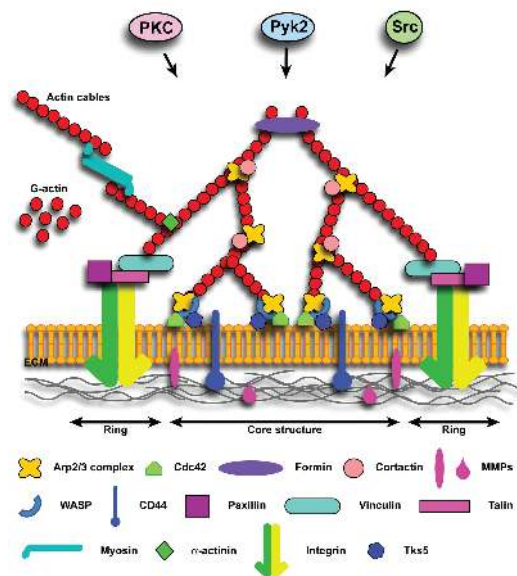


Figure 1.13.: Schematic showing a model for the organization of proteins in a single podosome. Podosome cores may contain both branched and bundled actin filaments. Actin associated proteins such as Arp2/3 complex and formins are found in the cores. Integrins span the plasma membrane in the podosome ring and are associated with focal adhesion proteins and scaffold proteins (*e.g.* vinculin, paxillin, and talin). Kinases such as src, PKC, and Pyk2 target focal adhesion proteins and some plasma membrane proteins to promote podosome formation and dynamics. Adapted from Schachtner et al., 2013.

Podosome cap domain - The third domain has only been proposed as an addition to the traditional “core-ring” model in the last few years. Indeed, its localization has been identified through the localization of new molecular components within the podosome structure. As its designation implies, the cap domain forms a cover over the core and extends to partly hover on the ring domain. This domain may serve as a regulator of podosome growth or podosome-associated contractility. Indeed, there is a prevalence of the acto-myosin regulators among the cap-localized proteins, as attested to by the presence of supervillin, lymphocyte-specific protein LSP1, and formins FMNL1 and INF2 (Mersich et al., 2010; Bhuwania et al., 2012; Panzer et al., 2016; Cervero et al., 2018). However, it appears that close scrutiny of the distribution of otherwise known components of the usual podosome domains with more resolved methods could lead to their relocation to the cap domain, as has been already the case for zyxin (Joosten et al., 2018). Indeed, some proteins had previously been described to span areas that now could be viewed as cap-compatible domains, such as caldesmon, gelsolin or fascin (Gu et al., 2007; Gawden-Bone et al., 2010; Van Audenhove et al., 2015). Due to the specific three-dimensional (3D) region occupied by the cap, it will thus be paramount in the following studies to make use of optical stacking in the vertical direction to assess whether a protein belongs to one of the described domains.

Regulation of podosome composition

Podosome core formation has been shown to involve the Cdc42-WASp-Arp2/3 signaling pathway, as well as depend on the activity of Src kinases (Linder et al., 1999; Linder et al., 2003) (Fig. 1.14).

Src kinases - Src kinase family is a family of non-receptor tyrosine kinases, which interact with many cellular membrane proteins, modifying these proteins by phosphorylation of tyrosine residues. Various kinases of the Src family have been identified as crucial moderators of the assembly and disassembly processes of podosomes. Indeed, Src kinase activity promotes actin nucleation in the podosome core, through its interaction with the Arp2/3 complex (Linder et al., 2000a; Destaing et al., 2008).

Hck is a Src family kinase specifically expressed in phagocytes, which has been shown to be involved in the phosphorylation of Wiskott-Aldrich syndrome protein WASp, an activator of the Arp2/3 complex. Although it had been initially studied for its implication in phagocytosis and lysosomal trafficking, it has also been identified in the context of the assembly of podosomes into rosettes (Guet et al., 2008; Cougoule et al., 2010; Van Goethem et al., 2011). Moreover, its expression is required for protease-dependent migration in 3D matrices *in vitro*, as well as for macrophage recruitment to inflammatory sites *in vivo*.

Rho GTPases - The members of the Rho GTPase family, and especially Rho, Cdc42 and Rac, have been shown to regulate many aspects of intracellular actin dynamics *via* the phosphorylation of multiple proteins. Together with Cdc42, WASp notably controls stimulus-induced actin cytoskeleton rearrangements that are involved in cell motility. Indeed, WASp has been identified as a key pro-

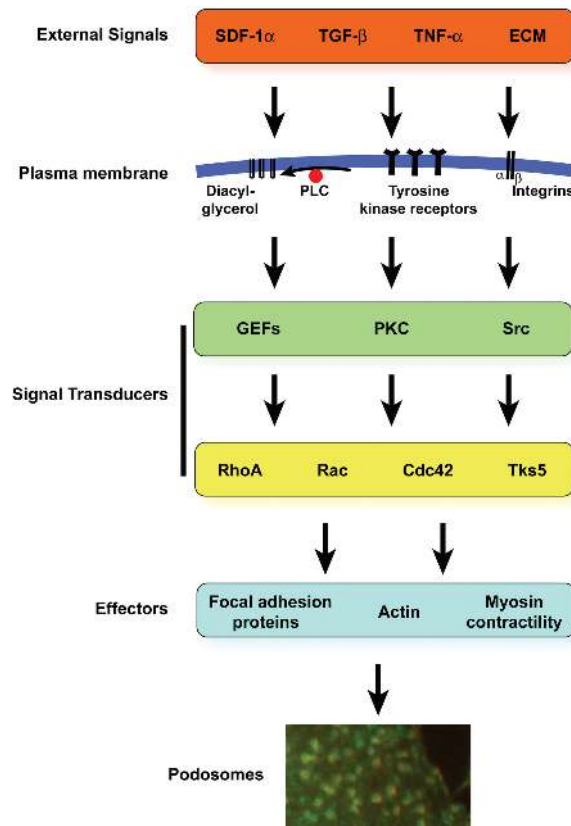


Figure 1.14.: Summary of the signaling hierarchy involved in the regulation of podosomes. External signals that can induce podosomes include SDF-1 α , TGF- β , TNF- α , and ECM. At the plasma membrane, signals to podosome formation include diacylglycerol, which results from hydrolysis of phosphatidylinositol-4,5-bisphosphate by phospholipase C (PLC), tyrosine kinase receptors and integrins. Signal transducers inside of the cell, such as GTP exchange factors, PKC, and src-family tyrosine kinases can trigger activation of secondary effectors, such as Rho-family small GTPases as well as activation of adapter signaling proteins to coordinate cytoskeletal reorganization. Downstream of these molecular cascades are focal adhesion proteins, actin cytoskeletal proteins and myosin driven contractility, which all contribute to podosome formation and dynamics. Adapted from Schachtner et al., 2013.

tein in podosome formation and cell polarization processes. When it is absent from dendritic cells or macrophages, they shown the inability to assemble podosomes, as well as to polarize and migrate efficiently (Linder et al., 2000a; Jones et al., 2002; Calle et al., 2004a; Bouma et al., 2009). Furthermore, WASp phosphorylation regulates actin filament stability in macrophages, and is required in the processes of podosome formation on vitronectin coating and its degradation. This observation points to the possible role of WASp in an integrin-mediated signaling pathway, especially since integrin clustering has been demonstrated to induce WASp phosphorylation. WASp interaction with Arp2/3

could also be involved in chemotactic processes, as its cyclic phosphorylation-dephosphorylation yields alterations in F-actin stability and the dynamic activation of Arp2/3 promoting actin filament nucleation (Dovas et al., 2009).

1.2.2. Podosomes as dynamic, matrix-probing structures

Podosomes have been shown in numerous studies to be highly dynamic structures, with an average lifespan ranging from a few minutes to a dozen minutes. Furthermore, these actin-related oscillations have been demonstrated to be closely related to their activity as mechanosensitive subunits.

Podosome actin-related dynamics

The highly dynamic features of podosomes can be observed on different scales: considering the whole population, down to focusing on one podosome inner dynamics. The average lifespan of one individual podosome ranges from 2 to 20 minutes (Linder, 2007; Proag et al., 2015).

Podosome assembly - The podosome formation process can be described in four main situations (Albiges-Rizo et al., 2009) (Fig. 1.15).

- The initial step consists in the binding of integrins to their extracellular matrix ligand and their grouping together. The process of integrin clustering has been described to require some crucial factors, such as: integrins switching to their activated conformation, integrins interacting with their immobilized ligand, integrins interacting with talin, and the presence of polyphosphoinositides, especially of phosphatidylinositol-4,5-triphosphate (PI(4,5)P₂) (Cluzel et al., 2005).
- Then, Src is recruited to the adhesion sites, and its activity yields the phosphorylation of various integrin-interacting proteins and regulating proteins, such as WASp, focal adhesion tyrosine kinase FAK and Rho-GTPase regulators, which in turn actin nucleators. Hence, Arp2/3 recruitment along with WASp and cortactin activation are enhanced by the continuous process of actin nucleation.
- Filaments grow and are further crosslinked *via* the Src-WASp-Arp2/3-cortactin signaling pathway. Formins also accelerates actin nucleation and elongation by interacting with barbed ends (fast-growing ends) of actin filaments (Mersich et al., 2010; Panzer et al., 2016).
- The interconnecting network of radial filaments establishes between the podosome cores, and spans the inner surface of the ventral membrane.

Podosome dynamics - Podosomes have been shown to have the capacity to interact with each other, notably through their fusion. Indeed, as one individual is not spatially restricted to one location during its lifetime and moves in a random walk manner, two podosomes sometimes get nearer until they happen to fuse together to yield one new actin core (Proag et al., 2016). What is more, the inverse phenomenon has also been observed: one core giving birth to two daughter podosomes through fission (Proag et al., 2016). Fission events have been observed either at the

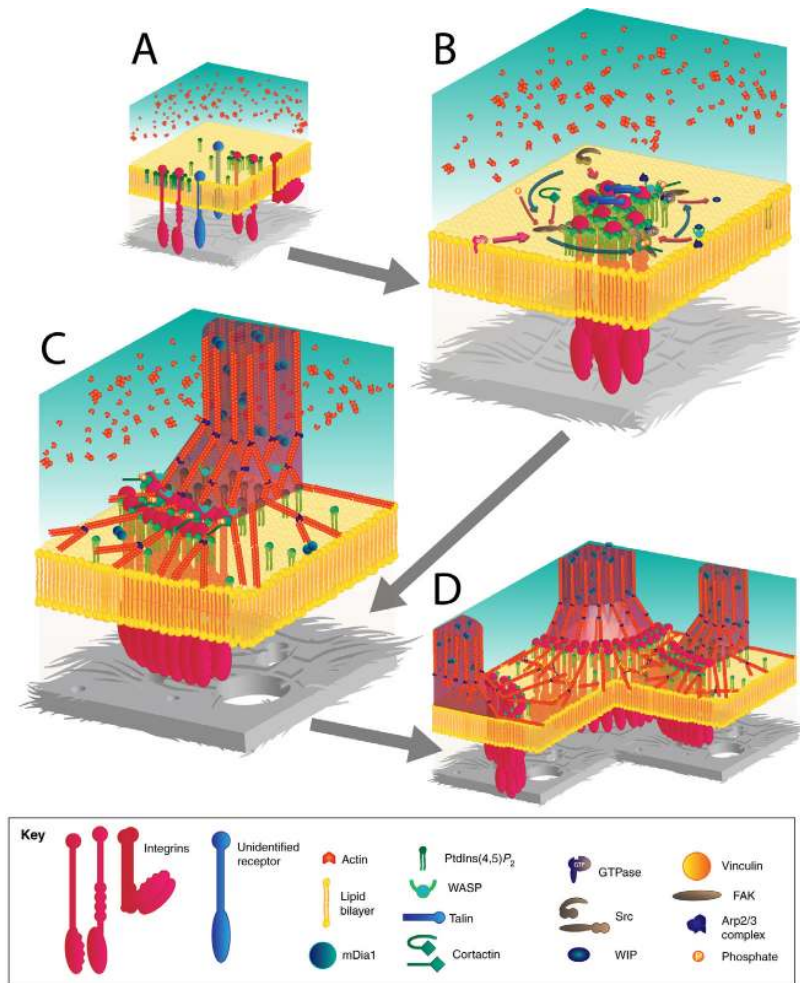


Figure 1.15.: Schematic view of signaling pathways that lead to actin organization at podosomes. (A) Integrins or other receptors bind to components of the ECM (grey), leading to clustering of receptors into PI(4,5)P₂-enriched areas of plasma membrane. (B) Recruitment of Src to adhesion sites leads to phosphorylation of several proteins involved in the podosome architecture and regulators of small GTPases. Actin nucleation depends on the activation of the Arp2/3 complex at the membrane through the synergistic action of cortactin and WASP-family proteins. (C) Elongation of actin filaments into columnar structures from the branched actin network thanks to the action of DRF/mDia1. (D) Podosomes are mechanically connected through a network of radial actin filaments that lie parallel to the substratum. Adapted from Albiges-Rizo et al., 2009.

migration front of moving cells, or simply at the periphery of cells in a resting phase (Evans et al., 2003; Kopp et al., 2006). This mechanism allows for the swift *de novo* formation of multiple new adhesion sites. While some of the newly formed podosomes tend to disassemble in less than a minute, especially when they are located near the cell periphery, more mature podosomes are mostly found

in the central area of ventral membranes, displaying more stable properties and a lifespan reaching up to 20 minutes.

Individual podosomes observed with time-lapse microscopy techniques reveal an oscillatory behavior of their actin-associated signal, with a typical period of approximately 30 s (Van den Dries et al., 2013a; Labernadie et al., 2014; Proag et al., 2015; Proag et al., 2016). These variations of actin intensity point to a highly dynamic actin polymerization process inside the podosomes core, and have been put in relation with the earlier proposed actin treadmilling at the core (Gawden-Bone et al., 2010; Luxenburg et al., 2012). Interestingly, such an oscillatory behavior has also been observed in the temporal analyses of proteins located in the ring domain, such as zyxin and paxillin (Van den Dries et al., 2013a; Proag et al., 2016).

Moreover, when considering a pair of podosomes, it has been shown that their fluctuations tended to be more synchronous with a decreasing distance between the two cores. This synchrony coefficient peaked for a distance value under approximately $2 \mu\text{m}$, which corresponds to the average distance range between two neighboring cores (Proag et al., 2015) (Fig. 1.16). This interesting result points out to the possible role of mechanical springs for radiating actin filaments connecting two cores, as has been observed with electronic microscopy.

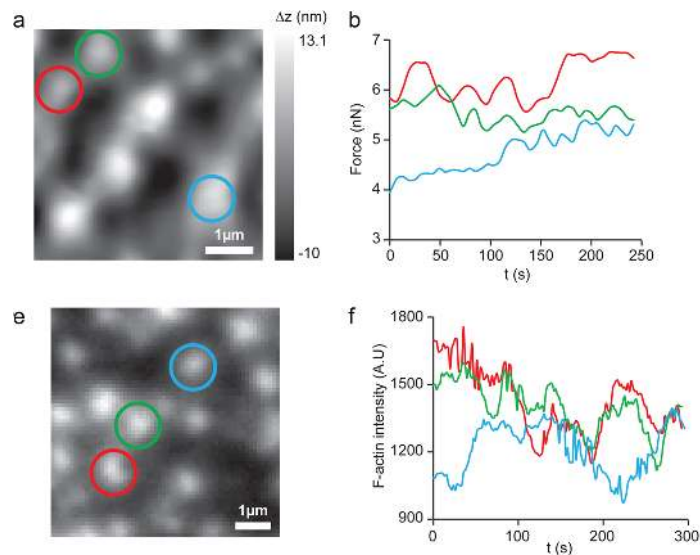


Figure 1.16.: Force and actin synchrony between close neighbors. (a,b) Time-lapse protrusion force microscopy experiments revealed oscillatory podosome-induced deformations. The synchrony coefficient is highest for red *versus* green and no significant synchrony was reported for red/blue and for green/blue. (e,f) Time-lapse TIRF imaging of podosome F-actin cores within a live mCherry-Lifeactin-expressing macrophage. The synchrony coefficient is highest for red *versus* green and no significant synchrony was reported for red/blue and for green/blue. Adapted from Proag et al., 2015.

Myosin II - Non-muscle myosin II is an actin crosslinker that controls contractility of actin filaments. In the specific context of podosomes, myosin II has been localized surrounding the core domain (Van Helden et al., 2008; Gawden-Bone et al., 2010; Linder et al., 2011; Bhuwania et al., 2012). It has also been recently detected in close association with the lateral filaments surrounding the core, and along the interconnecting filaments thanks to super-resolved techniques (Labernadie et al., 2014; Meddens et al., 2016; Van den Dries et al., 2019). Myosin IIA appears as the prevailing motor protein within podosomes, and its activity is regulated *via* the RhoA-ROCK-myosin II signaling pathway (Linder et al., 2005; Gimona et al., 2008; Dovas et al., 2011). However, while many studies have been carried out to decipher its role in podosome dynamics, they seem to have yielded contradictory results depending on the cell model used for the investigation. Indeed, in smooth muscle cells and neuroblastoma cells podosome formation appeared to be concomitant with myosin activity inhibition (Burgstaller et al., 2004; Clark et al., 2006). In contrast, both in macrophages and fibroblasts, myosin activation seemed required to induce both formation and stability of podosomes (Kopp et al., 2006; Collin et al., 2006). To explain this discrepancy, the following hypothesis has been proposed: a basal level of activated myosin II would be necessary to initiate podosome formation, and abrupt stimuli-dependent variations in this expression could increase the activated myosin level and yield the disassembly of podosomes. And indeed, treating dendritic cells with a low dose of blebbistatin, which inhibits ATPase activity of myosins, reduces podosome loss while leaving their actin-related dynamics untouched (Van Helden et al., 2008). But with a higher dose of blebbistatin, podosome disassembly is promoted and their formation is prevented.

Microtubules - Microtubules have been identified as playing a crucial role in the podosome dynamics. Indeed, each podosome is associated with at least one microtubule reaching out to the cell periphery, and a few podosomes have also been visualized along one same microtubule (Evans et al., 2003; Kopp et al., 2006). This proximity has been associated with a stabilizing action of microtubules over podosomes, and interfering with microtubule dynamics, with paclitaxel or taxol, results in increasing podosome lifespan without preventing their actin renewal process. Additionally, microtubule vicinity with podosomes has been shown to mediate both fusion and fission processes of the latter, and *de novo* formation seems to follow a contacting event by microtubule plus-end (Evans et al., 2003; Zhu et al., 2016). To be noted, the K40 acetylation process of α -tubulin is dependent on the enzyme MEC-17, and overexpressing the latter has been found to result in decreasing the number of podosomes while not interfering with their dynamics (Bhuwania et al., 2014). It would also seem that actin flow could in turn affect microtubule reorganization, as CLASP-associated microtubules tend to bend backwards at the cell periphery due to retrograde actin flow (Zhu et al., 2016).

Besides, microtubule plus-ends have also been identified as interacting with the molecular motor myosin IIA, which would promote podosome dynamics through the mediation of kinesin KIF1C and would allow for efficiently targeting podosomes, acting as a physical link between tubulin and actin (Kopp et al., 2006). Thanks to immunofluorescence, KIF1C has been majorly localized at the cell periphery, where podosomes are the most dynamic and co-exist within short range of microtubule plus-ends, but increasing microtubule acetylation seems to cause a relocalization of the kinesin

towards the cell interior (Bhuwania et al., 2014). Other kinesins such as KIF5B, KIF3A/KIF3B (Wiesner et al., 2010) and KIF9 (Cornfine et al., 2011) have also been researched in the context of matrix degradation by podosomes. KIF5B and KIF3A/KIF3B have been hypothesized to be involved in the delivery of MT1-MMP-containing vesicles to podosome sites, where MT1-MMP is needed for the shedding of matrix receptors such as CD44 or syndecan-1 and eventually to promote the degradation of a wide set of substrates (Wiesner et al., 2010). KIF9 C-terminus has been identified as interacting with Golgi proteins reggie-1/flotillin-2, a signaling mediator between intracellular vesicles and the cell periphery, and this coupling seems to be involved in the regulation of podosome *de novo* formation, and required for the matrix-degrading ability of these structures (Cornfine et al., 2011).

Recently, another protagonist may have been identified to act as a link between microtubule tips and integrin-based adhesions *via* binding with talin: KANK proteins. Indeed, KANK1 has been localized at the adhesion ring of podosomes in THP1 macrophages, and knocking down this protein resulted in the same effect on podosomes as disrupting microtubules with nocodazole, namely the total disappearance of podosomes (Rafiq et al., 2019). Moreover, KANK knockdown or treatment with nocodazole appeared to induce an increase of RhoA-GTP levels, apparently due to the release of GEF-H1 associated with microtubules. It would thus seem that maintenance of podosomes is controlled by linking of microtubules to these adhesions via KANK1, and such linking regulates the Rho/ROCK signalling axis and hence the myosin IIA filament assembly in a GEF-H1-dependent manner (Fig. 1.17).

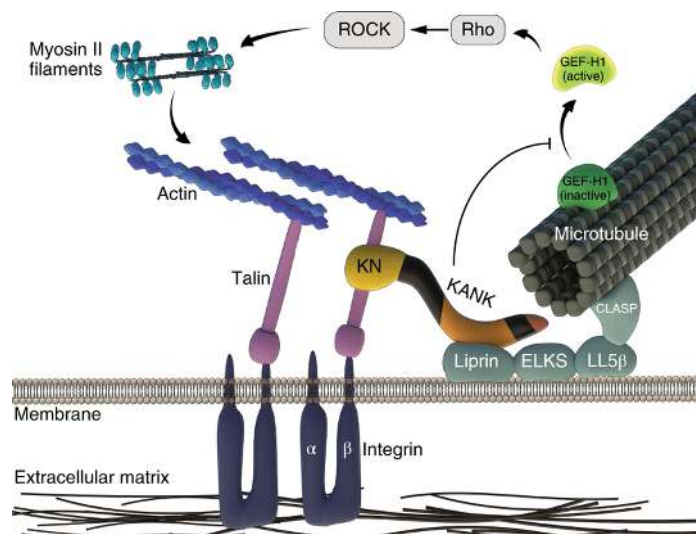


Figure 1.17.: Microtubules are coupled to integrin-containing adhesions via links formed by KANK family proteins between talin and the cortical microtubule docking complex. KANK binds talin via the KN domain and liprin via the coiled-coil domain. The microtubule docking complex captures the microtubule plus-end through interaction with CLASP proteins. GEF-H1 is associated with microtubules. Adapted from Rafiq et al., 2019.

Podosomes are mechanosensitive cell subunits

In addition to sensing matrix composition by engagement of specific transmembrane matrix ligands, podosomes also gather information about the physical properties of the substrate, such as rigidity and geometry. It has also been well documented that the acto-myosin complex is a key effector in generating dynamic tensions across the cell cytoskeleton, allowing for a coherence between cytoskeleton rearrangements and cell movements, as well as transmitting forces from the cell to its surrounding matrix (Cai et al., 2009). While signaling pathways involved in myosin activation, and myosin interacting partners in the cytoskeleton are becoming clearer, the mechanisms for perception and transmission of forces are subjects to numerous investigations and *in silico* modellings.

Podosomes probe the matrix properties - Acto-myosin contractility properties seems to be central in perceiving substrate mechanical signals by cells. A study has shown that podosome rosette formation is largely promoted when the substrate is stiffer, and the superstructure dynamics and stability depends on acto-myosin contractility (Collin et al., 2006). In the same study, it was also determined that the shape factor of the rosettes did not vary with the substrate mechanical properties. However, at the single podosome scale, their lifespan and inter-podosome distance are altered in relation with the matrix stiffness, namely the lifespan increases and the distance decreases with stiffer materials.

Podosome as individual adhesion structures have also shown signs of mechanosensitivity. Indeed, when macrophages are plated on various substrates with Young's modulus values ranging from 1 to 100 kPa, it has been observed that both the podosome density decreased and their vinculin arrangement was altered (Labernadie et al., 2014). Furthermore, they have been identified as mechanotransduction devices, notably thanks to the elucidation of internal cycles of varying stiffness controlled by actin polymerization and myosin II contractility (Collin et al., 2008; Labernadie et al., 2010). The subsequent findings that growth of the actin core drives the recruitment of tension sensitive ring components zyxin and vinculin have further attested to this function (Van den Dries et al., 2013a).

It is to be noted that podosome formation could also be induced in response to environmental stress *in vitro*, by mimicking ischemic conditions. In such a context when the tissue oxygen supply is low, cardiomyocytes have been discovered to rearrange their cytoskeleton in such a way that they displayed podosomes. This modification is associated with an acute collagen production and could consist in a cell-induced defense mechanism to locally reduce the contractile loads exerted on them by the surrounding pathological matrix (Zhao et al., 1987; VanWinkle et al., 1995).

Podosomes are also able to probe the matrix geometry. They have been exhibited as topography sensors by plating cells on 3D micropatterned substrates and observing the preferential localization of podosomes to the edges of the motifs (Van den Dries et al., 2012). Interestingly, podosomes formed in the vicinity of the topographical changes appeared as more stable, while the overall distribution of podosomes in the cell does not seem to vary in number, due to the presence of the motifs. This points to an upstream action of topography over the process of podosome formation. The link between

substrate topography and podosome formation has no yet been completely deciphered, though.

Thus, collectively as well as individually, podosomes have been revealed as adhesion structures sensitive to matrix stiffness and geometry (Fig. 1.18).

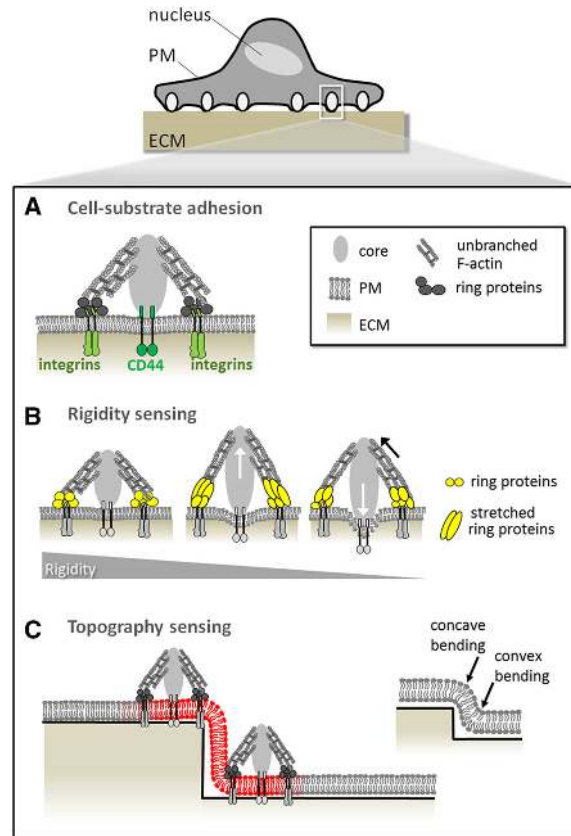


Figure 1.18.: Established functions of podosomes in ECM sensing. Cell-substrate adhesion: Adhesion to substratum is established by podosomelocalized transmembrane proteins such as integrins (light green) and CD44 (dark green). Rigidity sensing: Podosomes exert forces on the plasma membrane by growth of the actin-rich core structure (white arrows), counterbalanced by lateral cables tension (black arrow). Topography sensing: Podosomes are formed especially at topographical discontinuities in the substrate. Adapted from Linder et al., 2015.

Podosomes apply forces to the matrix - While varying the mechanical properties of the substrate, podosome rosettes have been highlighted as force-exerting structures. Indeed, on matrices characterized by Young's modulus values ranging from 2 to 6.5 kPa, the traction forces induced by the rosettes proportionally ranged from 200 to 600 Pa (Collin et al., 2008). Upon observation of single podosomes with internal reflection microscopy methods, it has been revealed that they consist in punctate sites of close proximity between the substrate and the above-lying cell

membrane (Evans et al., 2003; Linder et al., 2005; Van den Dries et al., 2013a). Moreover, membrane protrusions associated with F-actin rich structures and reaching inside gelatin-filled pores have been characterized in dendritic cells plated on polycarbonate filters (Gawden-Bone et al., 2010). These structures appeared less similar to podosomes and more resembling invadopodia, usually found in cancer cells associated with a highly invasive behavior (Bowden et al., 1999; Enderling et al., 2008; Lizárraga et al., 2009).

With the development of a smart way of assessing the podosome-induced deformations on their substrate thanks to atomic force microscopy (AFM) probing, single podosomes have effectively been identified as able to exert vertical forces (Labernadie et al., 2014). Indeed, protrusion force microscopy (PFM) allowed for the quantification of the bulge heights that have been detected with AFM below podosomes, and for the computation of the vertical forces required to yield such deformations: estimated values spanning a few tens of nanoNewtons (Labernadie et al., 2014; Proag et al., 2015). These analyses have resulted in a draft of the internal mechanical processes: the podosome core is a site where actin polymerization process generates a protruding force, while the adhesion ring is thought to consist in an upward pulling area, so as to confine the bulging of the thin Formvar film to the projected area of the core. Subsequent super-resolved and three-dimensional imaging of podosomes revealed the stretched conformation of talin within the adhesion rings of macrophage podosomes, and specifically its elongation appeared increased for the molecules positioned nearest to the core (Bouissou et al., 2017) (Fig 1.19). This observation, paired with the fact that talin expression knock-down drastically reduced the protrusion forces, further validated the presence of a necessary balance between protrusion at the core and traction at the ring, which was first hypothesized by Gawden-Bone and colleagues (Gawden-Bone et al., 2010).

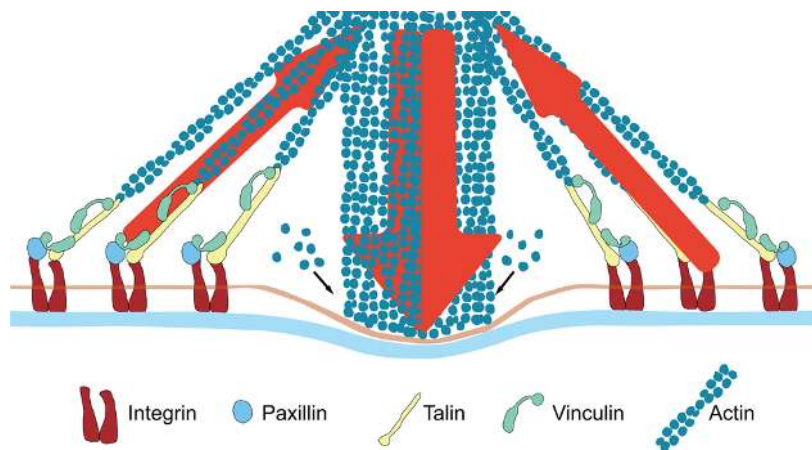


Figure 1.19.: Model of ring protein organization and podosome force generation. At the core of the podosome, F-actin polymerizes against the substrate; it is surrounded by a spatially structured ring-shaped integrin-based adhesion complex. Talin assumes an open conformation under traction probably mediated by lateral actin filaments, all the more stretched as it nears the core. Adapted from Bouissou et al., 2017.

Podosomes can form superstructures - Podosomes have also been shown to assemble into various superstructures, depending on the cell type and the activation state of the cell, that are described as follows (Fig. 1.20):

- Podosome rosettes consist in densely packed individual podosomes, forming an annular shape. They are either a transient organization which can be observed in macrophages, displaying a high versatility in size and shape (Poincloux et al., 2006); or can be stably assembled in some endothelial cells with a typical diameter ranging from 5 to 20 μm (Osiak et al., 2005). In macrophages, they have further been associated with an activated state of the cells, in the presence of a cytokine such as M-CSF or when plated on a specific matrix protein coating such as fibronectin or gelatin (Yamaguchi et al., 2006; Cougoule et al., 2010). Podosome rosettes can also be observed in osteoclast, as a temporary structure leading to a final stable podosome assembly (Saltel et al., 2008).
- Podosome clusters are defined as groupings of variable number of individual podosomes in a restricted area of the cell ventral membrane. They have been observed in multiple podosome-forming cell types such as macrophages or osteoclasts (Poincloux et al., 2006).
- Podosome belts and sealing zones consist in superstructures that have been shown to be specific to osteoclasts. Podosome belts have been characterized to be observed on glass or non-physiological substrates, while the sealing zone only assembles on bone-related materials.

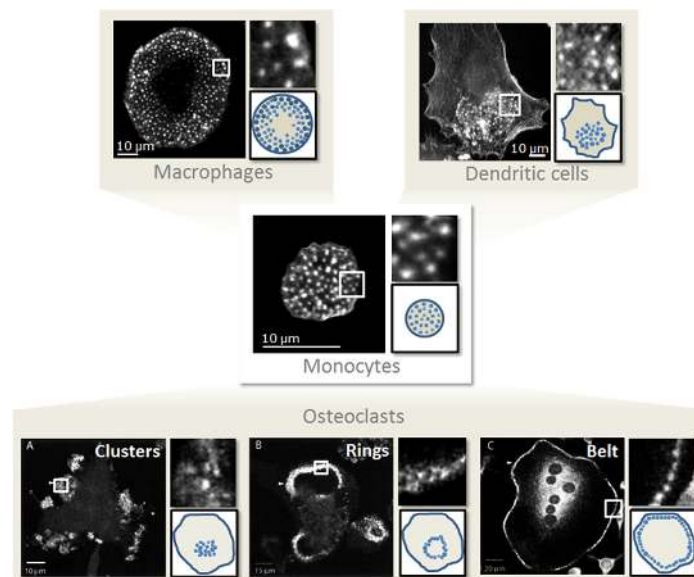


Figure 1.20.: Podosomes in monocytic cells display various global organizations. Middle panel: blood-derived monocytes exhibit a homogeneous distribution of individual podosomes; upper panel: monocyte derived macrophages and immature dendritic cells displaying spatially arranged individual podosomes; lower panel: osteoclasts showing various podosomes arrangements, including clusters, rings and belts. Adapted from Linder et al., 2015.

1.3. The sealing zone - towards a molecular representation

Osteoclasts are giant multinucleated cells from the monocytic lineage that spontaneously develop specific cell-adhesion devices called podosomes. An individual podosome is a complex network of filamentous actin unit structure that collectively self-organizes in osteoclasts into a superstructure called the sealing zone. Major matrix degradation on bone-mimicking substrates seems to proceed under the bone resorption area, namely the ruffled-border, which is an enclosed extra-cellular compartment tightly sealed off by this sealing zone. The capacity of the osteoclast to resorb bone is distinctive. Deciphering the key components of this structure has been investigated for the past decades, but insights into their generation mechanisms emanated from more recent studies. These new findings include the role of integrins - particularly $\alpha v \beta 3$ - in cytoskeletal organization and the signaling pathways they activate, as well as better comprehension of the multiscale dynamic events occurring in the process of osteoclastic activity.

1.3.1. Architecture of the osteoclast actin cytoskeleton

The sealing zone marks the periphery of the ruffled border, and is characterized by its dense F-actin structure. F-actin is present not only in the actin ring but also at the ruffled border, which has been recently parted into distinctive functional domains . Indeed, scanning electron microscopy (SEM) combined with confocal imaging revealed that the distributions of v-ATPases, which pump protons across the plasma membrane, and F-actin were very similar, with frequent co-localization in the area circumscribed by the peripheral ring, in addition to the presence of v-ATPase in the ruffled border. The distribution of cathepsin K, an acid cysteine proteinase, was essentially the inverse of that of actin and v-ATPase, as it was seen in areas within the actin ring where actin and v-ATPase were absent, associated in the SEM images with smooth, orifice-bearing membrane. And finally, ClC-7, a channel through which chloride ions are released, was immunolocalized as a sharp band immediately juxtaposed to the inner side of F-actin rings and immediately outside the v-ATPase (Szewczyk et al., 2013). Its distribution as a distinct band is thought to prevent the lateral diffusion of protons, which would cause mineral dissolution and subsequently result in release of $\alpha v \beta 3$ ligands and termination of resorption.

Considering the sealing zone, its exact structure and dynamics have been elusive, owing to the lack of techniques simultaneously enabling high-resolution imaging and physiologically relevant conditions for observation. Although, in the last decade, intensive *in vitro* studies have provided crucial insights into the structure of its actin arrangement, and the multiple molecular components involved in the complex 3D scaffold.

Spatial arrangement of actin filaments in the sealing zone

The sealing zone was originally identified as the structure formed by chondroclasts adhering on mineralized cartilage and the activity of which is the resorption of its mineralized components, before being observed in avian osteoclasts *via* epifluorescence and transmission electron microscopy (TEM)

(Schenk et al., 1967; Marchisio et al., 1984; Zambonin-Zallone et al., 1988). Upon TEM observation, the sealing zone was first denominated as a “clear zone”, due to its electron-dense material and apparent lack of cytoplasmic organelles (Zambonin-Zallone et al., 1988; Kanehisa et al., 1991; Teti et al., 1991). Shortly after this finding, podosomes were identified in the F-actin band surrounding the ruffled border and were proposed to coincide with clear zone structure confining the resorption lacuna (Kanehisa et al., 1990; Teti et al., 1991). From this moment on, subsequent studies have striven to decipher the specific spatial arrangement of actin filaments in the sealing zone.

Podosomes in the sealing zone ? - Kanehisa and coworkers were the first to propose podosomes as playing an essential part in the resorption apparatus of osteoclasts . Indeed, they not only observed F-actin bands in bone-resorbing rabbit osteoclasts on the endocranial surface of growing calvariae *in vivo*, they also identified podosomes as subdomains of this actin-rich ring thanks to phase-contrast microscopy (Kanehisa et al., 1990). However, contemporary studies argued differently. Indeed, the combined facts that the vitronectin receptor was not detected at the sealing zone, and that the association of actin and vinculin seen in podosomes was clearly different in the sealing zone area led to another hypothesis (Lakkakorpi et al., 1991b; Lakkakorpi et al., 1991a; Lakkakorpi et al., 1993). As vinculin was apparently lacking from the most central area of the sealing zone, it indicated that some organization other than a high density of podosomes mediated the attachment of resorbing osteoclasts to bone surface, and it was proposed that sealing zone was rather a high condensation site for F-actin resulting from the fusion of numerous podosomes (Lakkakorpi et al., 1996) (Fig. 1.21).

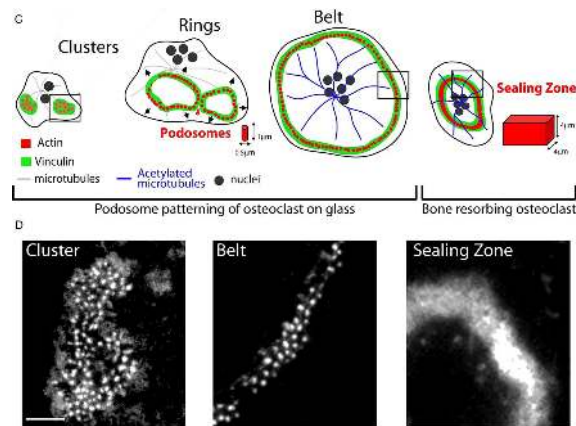


Figure 1.21.: Schematics of the different actin structures observed along osteoclast differentiation and activation. (C) At the beginning of the differentiation, podosomes are organized in clusters (C, D), which evolve into dynamics rings. These rings are stabilized at the cell periphery to form a podosome belt through the action of acetylated microtubules (C, D). When osteoclasts are adherent on surfaces containing apatite crystals, they form a sealing zone necessary for bone resorption (C, D). Adapted from Jurdic et al., 2006.

Both assumptions coexisted in different subsequent studies, certainly due to the poor resolution of confocal microscopy on non-optically transparent substrates mimicking bone matrix, and the association of the adhesion structures observed on glass with the functional superstructure imaged on bone (Horton et al., 1995; Lakkakorpi et al., 1999; Chellaiah et al., 2000a; Ochoa et al., 2000; Akisaka et al., 2001; Krits et al., 2002; Jurdic et al., 2006). Indeed, the variability in staining pattern between osteoclasts plated on glass coverslips and bone slices *in vitro* was proposed to reflect the organization and reorganization of the osteoclast cytoskeleton accompanied by the cellular activity during the bone resorption cycle, and eventually gave rise to two distinct denominations: the actin belt on glass and the sealing zone on bone-related materials (Akisaka et al., 2001; Jurdic et al., 2006). The pioneering study of Luxenburg and coworkers definitely unveiled the presence of single actin cores both in actin belts on glass and in sealing zones on apatite, the main mineral component of the bone matrix, similar in their actin arrangement to what they observed with single podosomes in the same cells (Luxenburg et al., 2007). They characterized the sealing zone as a 3 to 6 μm wide band displaying podosomal units, interspaced with an average distance of approximately 250 nm (Fig. 1.22).

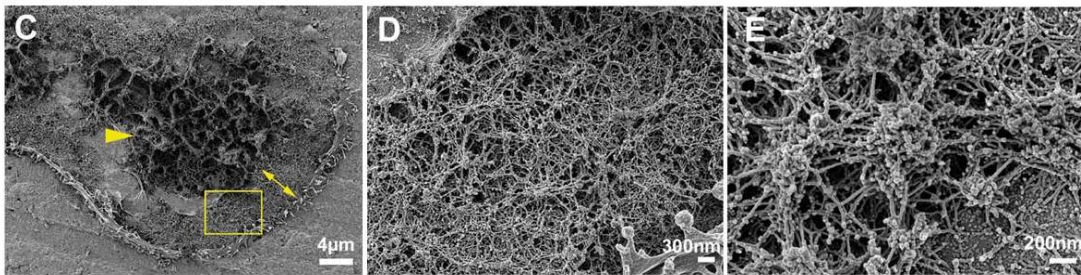


Figure 1.22.: Observation of osteoclast ventral membrane on bone with scanning electron microscopy. (C) Overview of the ventral membrane of a cell plated on bone. The central area (arrow head) presumably corresponds to the ruffled border. The sealing zone (double arrow) is thicker than on glass. (D, E) Higher magnification views (from yellow box in (C)) of the podosomes forming the sealing zone. Adapted from Luxenburg et al., 2007.

A complex 3D actin network - Luxenburg and coworkers' seminal study also provided the first insights into the 3D arrangement of actin filaments within the sealing structure (Fig. 1.22). They developed a specific ventral membrane preparation, inspired by the classic unroofing procedures, allowing for the direct visualization of cell inner components while preserving the integrity of the ventral membrane and its associated cytoskeleton. The detected podosomal units appeared connected by numerous inter-pillar filaments running parallel to the substrate, and radial filaments were observed around each densely bundled pillar, namely the actin cores. Additionally, the use of correlative imaging revealed that intense actin fluorescence was associated with both the actin cores and the radial actin cables, pointing to the presence of an "actin cloud" domain where the plaque protein paxillin and actin fibers both localize (Luxenburg et al., 2007).

Subsequent studies further characterized the spatial arrangement of actin cores within the sealing zone *via* SEM observation of unroofed cells, and proposed the identification of different structural subdomains: the core vertical bundles, the radial filaments composing the cloud, and interconnecting filaments above the ventral membrane. The actin cores within the sealing zone were approximately 100 to 300 *nm* in diameter, 800 *nm* high, and the average core-to-core distance spanned from 250 to 450 *nm* (Luxenburg et al., 2007; Geblinger et al., 2009; Anderegg et al., 2011; Akisaka et al., 2016; Akisaka et al., 2019). In addition, it recently appeared that actin cores displayed two different phenotypes within sealing zones: a small symmetrical form characterized by its high circularity, and another population displaying more irregular and unsymmetrical shapes (Akisaka et al., 2019). Accordingly with the previous phase-contrast microscopy observations, the cores are in close contact with the underlying matrix, displaying a gap of only a few tens of nanometers (Akisaka et al., 2008; Akisaka et al., 2015).

High-resolution electron microscopy imaging has further allowed the characterization of the actin filament distribution within the sealing zone structure thanks to the generation of 3D anaglyphs. It revealed differences in filament lengths and organization between the different subdomains: shorter actin filaments were specific of the meshwork within the core, and relatively long actin filaments indicated the surrounding cloud portion when terminating on the ventral membrane, or connected neighboring actin cores when assembled into horizontal cables (Akisaka et al., 2008; Anderegg et al., 2011; Akisaka et al., 2016). Furthermore, decorating actin filaments with myosin S-1 subunit helped figuring how filaments were oriented. The polarity of actin filaments was not uniform, however different predominant orientations were identified in the core and cloud subdomains (Fig. 1.23):

- in the core, the actin filaments oriented with their barbed ends toward the podosome core with their pointed end facing outward in the core domain;
- in the cloud, the radial filaments and the interconnecting cables among the podosomes contained more filaments with the barbed ends away from the podosome core (Akisaka et al., 2008; Akisaka et al., 2015).

Differences in the density of the filament network also seemed to be dependent on their axial localization within the structure. Indeed, the top filament layer contained a coarser arrangement of long filaments, while in the deeper layer a densely arranged filament network was seen on the surface of the ventral membrane (Akisaka et al., 2015). Variations in the branching were hence also observed, with core-related shorter filaments that appeared less branched than the radiating long filaments. Indeed, radiating long actin filaments appeared to be branched in the network or cross-linked at various angles or anastomosing, and some of them also were identified to terminate directly on the ventral membrane, through their interaction with membrane-associated particles (Akisaka et al., 2016; Akisaka et al., 2019). What is more, analyzing the branching of filaments has most recently brought to light the presence of the cap domain over actin cores within the sealing zone (Akisaka et al., 2019).

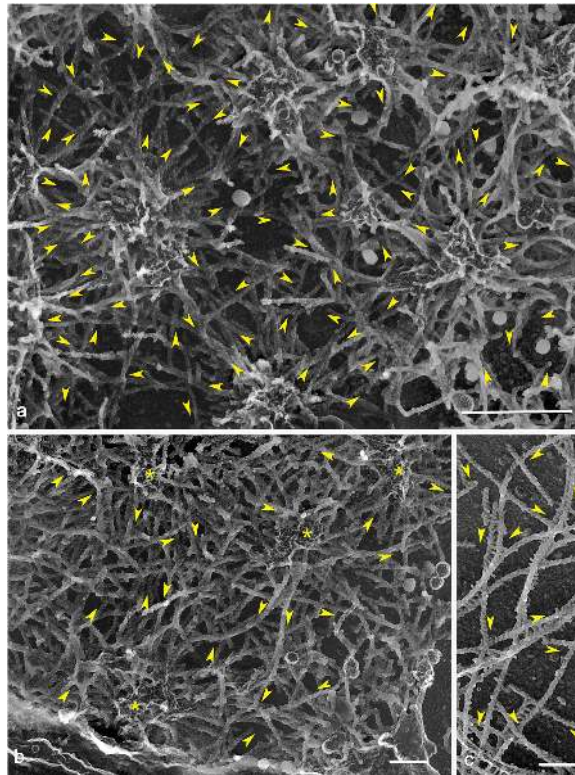


Figure 1.23.: Replica images of podosomes decorated with myosin S1 in osteoclasts. Replica images of podosomes decorated with myosin S1. S1-decorated actin filament displays a helical rope-like appearance. An arrowhead on the replica image indicates the direction of the pointed end of a filament. (a) actin filament orientation in clustered podosomes. (b) A narrow zone of dense filament network associated with actin sealing zone. A distinct arrowhead pattern on helical rope-like F-actin appearance can be seen in the top filament layer. F-actin appears to be organized with a mixture of polarities at the cell edge. Several rudimentary podosomes can be distinguishable (asterisks). (c) Several decorated F-actin splayed off from the dense actin network. Individual filament shows a distinct arrowhead pattern on rope-like actin filament appearance. Filaments are oriented primarily with pointed end toward the ventral membrane. Scale bars (a-b) $1 \mu\text{m}$, (c) $0.1 \mu\text{m}$. Adapted from Akisaka et al., 2015.

Distribution of integrins and transmembrane proteins

Forming one class of the various cell adhesion receptors, integrins are heterodimeric adhesion receptors that mediate cell-matrix and cell-cell interactions (Hynes, 1992). Integrin-mediated adhesion and subsequent signaling consists in a major regulating factor in the bone resorption of osteoclasts (Duong et al., 2000). Three conformations, each associated with a specific activation state, have been described for integrins: the bent-closed conformation with low affinity for extracellular ligands, the extended-closed conformation with an intermediate affinity for ligands, and the extended-open conformation with a high affinity for ligands at the binding site (see Fig. 1.24). Moreover, when

integrins are bound to a ligand, they have been observed to cluster together, subsequently leading to the formation of adhesion sites through interaction with cytoskeletal complexes and actin filaments. Each subunit of integrins, namely the α and β chains, come in a variety of molecular composition, such that in human cells 18 different α subunits and 8 β subunits have been identified in 24 heterodimers. Each $\alpha\beta$ combination does not have a particular ligand, but rather they show versatile affinity for a few extracellular matrix proteins (see Fig. 1.25).

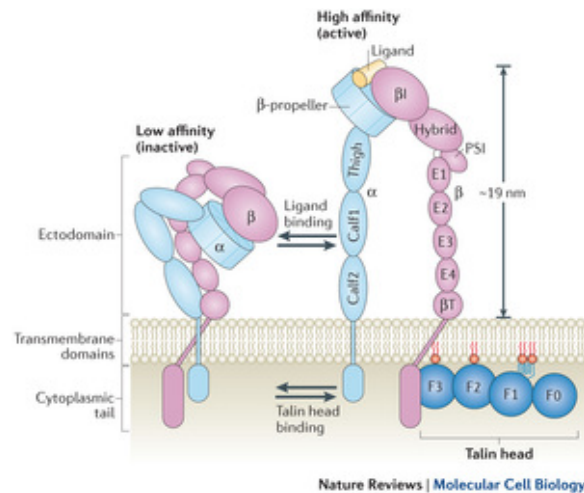


Figure 1.24.: Schematics displaying integrin structure and activation. The subunits have large ectodomains that are constructed from various modular units, including calf and thigh domains. Each α - and β - subunit has a single trans-membrane helix and, usually, a short unstructured cytoplasmic tail. Integrins exist in equilibrium between a bent, low-affinity state and an upright, high-affinity state. They can be activated by the binding of extracellular ligands to integrin ectodomains (known as ‘outside-in’ activation) and by the binding of the talin head (an atypical FERM domain with F0, F1, F2 and F3 domains) to β -integrin tails and acidic membrane phospholipids (known as ‘inside-out’ activation). On the left, the bent and inactive conformation of an integrin is held in place by transmembrane interactions between the α - and β - subunits. On the right, conformational activation results in an elongation of both α - and β - subunit, reaching a total height of approximately 19 nm. Adapted from Calderwood et al., 2013.

Integrin $\alpha v \beta 3$ - In osteoclasts, the vitronectin receptor $\alpha v \beta 3$, is highly expressed compared to other cell types (Horton, 1996; Horton, 1997). Rat osteoclasts adhere in an $\alpha v \beta 3$ -dependent manner to extracellular matrix protein containing the tri-peptide sequence Arg-Gly-Asp (RGD), including vitronectin, fibronectin, osteopontin and bone sialoprotein (Helfrich et al., 1992; Flores et al., 1992; Flores et al., 1996). Furthermore, its crucial role in the osteoclastic function was first brought to light when a monoclonal antibody was found to inhibit bone resorption *in vitro*, and the antigen was subsequently determined to be the $\alpha v \beta 3$ integrin (Chambers et al., 1986; Davies et al., 1989; Clover et al., 1992). Indeed, subsequent studies showed the ability for RGD-containing peptides, disintegrins or blocking antibodies against $\alpha v \beta 3$ to inhibit the resorption efficiency of osteoclasts *in*

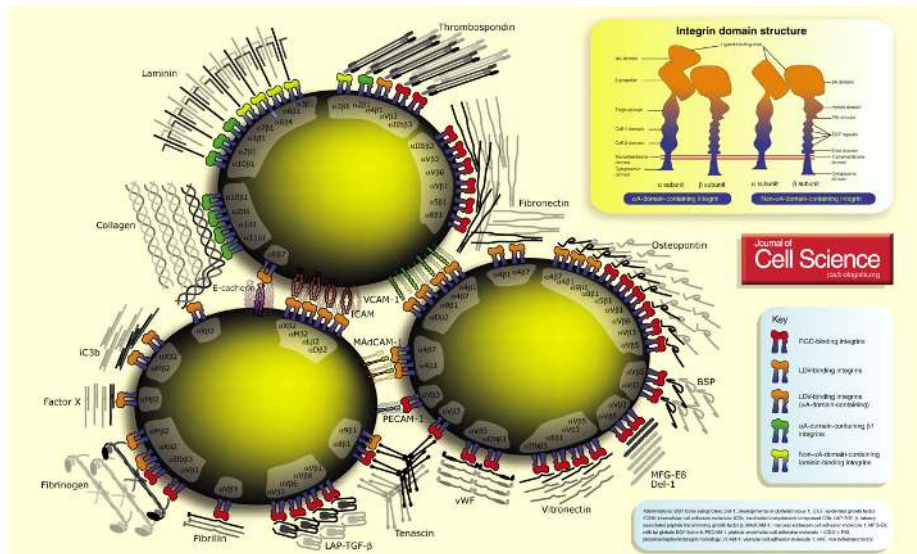


Figure 1.25.: Schematic view showing the major integrin-ligand combinations, using hypothetical cell surfaces. Despite their wide variety, it is possible to cluster integrin-ligand combinations into four main classes, reflecting the structural basis of the molecular interaction. All five αV integrins, two $\beta 1$ integrins ($\alpha 5$, $\alpha 8$) and $\alpha IIb\beta 3$ share the ability to recognise ligands containing an RGD tripeptide active site. $\alpha 4\beta 1$, $\alpha 4\beta 7$, $\alpha 9\beta 1$, the four members of the $\beta 2$ subfamily and $\alpha E\beta 7$ recognise related sequences in their ligands. $\alpha 4\beta 1$, $\alpha 4\beta 7$ and $\alpha 9\beta 1$ bind to an acidic motif, termed ‘LDV’, that is functionally related to RGD. Four α subunits containing an αA -domain ($\alpha 1$, $\alpha 2$, $\alpha 10$ and $\alpha 11$) combine with $\beta 1$ and form a distinct laminin/collagen-binding subfamily. Three $\beta 1$ integrins ($\alpha 3$, $\alpha 6$ and $\alpha 7$), plus $\alpha 6\beta 4$, are highly selective laminin receptors. Adapted from Humphries et al., 2006.

vitro (Sato et al., 1990; Horton et al., 1991; King et al., 1994; Van der Pluijm et al., 1994). *In vivo* studies in thyroparathyroidectomized or ovariectomized rodents confirmed the blocking ability of integrin ligands regarding the bone resorption activity (Crippes et al., 1996; Engleman et al., 1997; Yamamoto et al., 1998).

Considering the localization of integrin $\alpha v\beta 3$, observations have led to seemingly antagonist distributions. Indeed, some studies have located the vitronectin receptor in the area of the sealing zone of resorbing osteoclasts, and in individual podosomes of cells plated on glass, showing colocalization of $\alpha v\beta 3$ with vinculin, paxillin and talin (Teti et al., 1989; Zallone et al., 1989; Reinholt et al., 1990; Hulthenby et al., 1993; Nakamura et al., 1996; Neff et al., 1996; Pfaff et al., 2001). In contrast, other studies also observed an enrichment of $\alpha v\beta 3$ in the basolateral membranes, intracellular vesicles and the ruffled border of osteoclasts, thanks to confocal and electron microscopy examination (Lakkakorpi et al., 1991b; Lakkakorpi et al., 1993; Masarachia et al., 1995; Nakamura et al., 1999; Lakkakorpi et al., 2001). More recently, a study focused on localizing $\alpha v\beta 3$ in human osteoclasts depending on its conformation state (Faccio et al., 2002). Their results reconciled the apparently contradictory former observations, as they localized the ‘activated’ form to be present mainly at the

edge of the ruffled border, whereas the 'basal' conformation is also present in the sealing zone, where it colocalizes with the actin ring (Fig. 1.26). It was then further acknowledged that integrin $\alpha v \beta 3$ was present at the sealing zone, where it is excluded from the F-actin core domain (Chabadel et al., 2007; Ma et al., 2010). It is hence thought that low-affinity $\alpha v \beta 3$ is preferentially localized to the actin cloud, and redistributes to newly formed membrane protrusions upon activation.

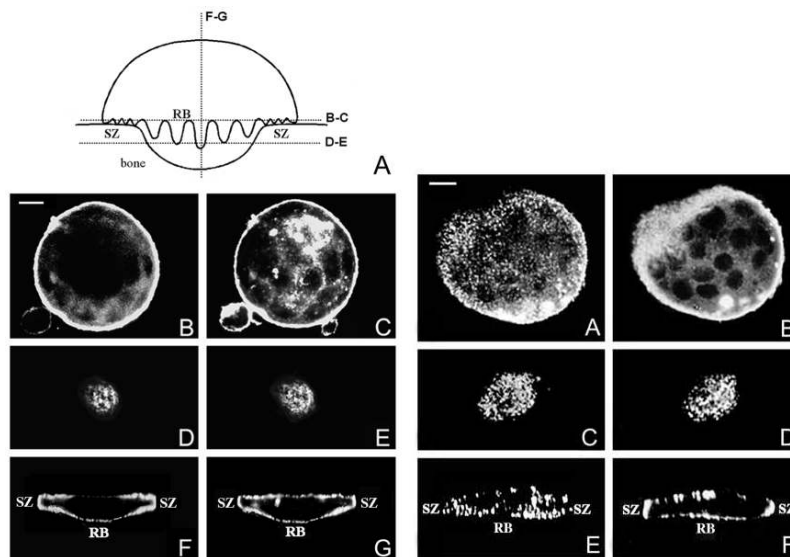


Figure 1.26.: Localization of total (left panel) and "activated" (right panel) $\alpha v \beta 3$ in resorbing osteoclasts. Left panel: A resorbing OC is schematically represented in A, and microscopic images show the three different axial sections indicated in A. (B-C) At the level of the sealing zone, where $\alpha v \beta 3$ (B) appears as a circular line at the cell periphery that perfectly colocalizes with the actin ring (C); (D-E) in the ruffled border $\alpha v \beta 3$ and actin show a punctuate distribution; (F-G) an optical yz-plane confirms the distribution of the integrin and of actin in the sealing zone and in the ruffled border. Right panel: At the level of the sealing zone, the "activated" $\alpha v \beta 3$ (A) only partially colocalizes with the actin ring (B) and displays a discrete pattern. In the ruffled border area the "activated" $\alpha v \beta 3$ (C) is very abundant, with a punctuate distribution similar to that of the actin microfilaments of D. In the optical yz-plane, note the presence of actin in the sealing zone (F) as a line at the edge of the cell that only partially colocalizes with the "activated" integrin, whereas they are both present in the ruffle border. Scale bars 5 μm . Adapted from Faccio et al., 2002.

Other integrins in osteoclasts - Expression of other integrins has also been described in mammalian osteoclasts: the collagen/laminin receptor $\alpha 2 \beta 1$ and the vitronectin/fibronectin receptor $\alpha v \beta 1$ (Horton et al., 1989; Clover et al., 1992; Nesbitt et al., 1993). It was reported that rat osteoclasts adhere to native collagen type I using $\alpha 2 \beta 1$, in an RGD-dependent manner (Helfrich et al., 1996). Interestingly, osteoclastic bone resorption is partially inhibited by the presence of antibodies targeting $\alpha 2$ and $\beta 1$ subunits. What is more, immature osteoclasts precursors were shown to express $\beta 2$ and $\beta 5$ subunits (Takahashi et al., 1994; Teitelbaum et al., 1997; Duong et al.,

1998). Whereas the absence of αv combined with either $\beta 1$ or $\beta 2$ abolished the formation of the sealing zone, silencing single or both β subunits still resulted in the normal assembly of the actin superstructure (Schmidt et al., 2011). Furthermore, silencing only αv subunit yielded a slightly stronger decrease in resorption activity compared with single $\beta 3$ subunit silencing, which points to the importance of another αv subunit containing integrin besides $\alpha v\beta 3$, plausibly $\alpha v\beta 1$.

It has been proposed that recognition of bone sialoprotein involves $\alpha v\beta 1$ in addition to $\alpha v\beta 3$ (Horton et al., 1995). Affinity precipitation experiments revealed significant binding of PYK2 and paxillin to the full-length $\beta 1$ tail and differing binding requirements for $\beta 1$ and $\beta 3$ tails (Pfaff et al., 2001). However a study reported that $\beta 1$ subunit seemed absent from mouse osteoclast sealing zones (Chabadel et al., 2007), it has been later localized with αv around actin cores (Schmidt et al., 2011).

Transmembrane protein CD44 - CD44 is a cell-surface, single-pass transmembrane proteoglycan expressed in most cell types, and a receptor for hyaluronic acid, osteopontin, collagen and laminin (Goodison et al., 1999; Ponta et al., 2003). It has been described for its capacity to mediate osteoclast migration through its interaction with osteopontin, as blocking antibodies to CD44 blocked osteopontin stimulation of motility in avian osteoclasts (Chellaiah et al., 2003a). It is also involved in the regulation of bone resorption through its expression level at the cell surface under the regulation of osteopontin and Rho kinase phosphorylation (Chellaiah et al., 2003c; Chellaiah et al., 2003b). In addition, silencing either CD44 or $\beta 3$ in mice resulted in only a mild osteopetrotic phenotype, which points to the importance of a possible cooperativity between both transmembrane protein, especially as they share osteopontin as a ligand. CD44 surface expression was also described to depend on actin polymerization process. Indeed, decrease in the surface expression of CD44 after treatment with either cytochalasin D or alendronate resulted in the decrease in CD44-associated MMP-9 activity in osteoclasts (Samanna et al., 2007).

Upon observation with confocal microscopy, it was asserted that CD44 is present at the osteoclast membrane in the sealing zone, and is localized beneath the actin cores, and appeared as a key organizing factor for F-actin in the sealing zone, due to its complete disappearance along with the cores in WIP-deficient mouse osteoclasts or in the presence of blocking antibodies targeting CD44 (Chabadel et al., 2007) (Fig. 1.27).

Between the anchor and the web - a multitude of proteins

In order to assemble in such a complex 3D network as it has been described, F-actin interacts with a multitude of proteins within the sealing zone. Some are involved in binding actin filaments to the cell membrane *via* interaction with integrins, some take part in the polymerization process, and some establish the specific spatial arrangement of filaments among them. However, as more than 300 proteins have been identified in the podosome-associated proteasome and the literature focusing on deciphering sealing zone specific components cannot be considered as extensive, the following paragraphs are by no means exhaustive. They rather aim at giving a basic overview of the localization for a variety of proteins and of actin-related interactions that may occur within the

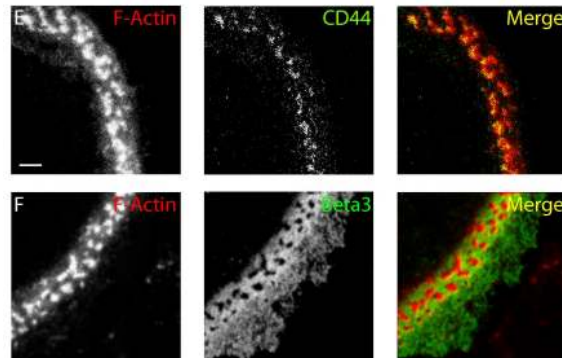


Figure 1.27.: OC podosome belt is composed of two F-actin domains specifically associated with CD44 and the $\beta 3$ integrin subunit. (E and F) Differentiated wild-type osteoclasts were observed after actin staining by phalloidin and immunolabeling for CD44 and the $\beta 3$ integrin subunit. CD44 receptor (E) colocalized with actin dots, whereas the $\beta 3$ integrin subunit (F) was specific to the actin cloud. Adapted from Chabadel et al., 2007.

sealing zone (Fig. 1.28).

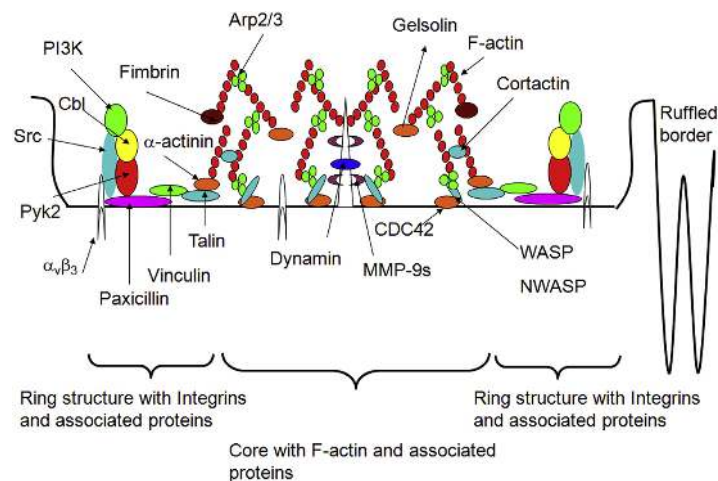


Figure 1.28.: Schematic view of the sealing zone components at the podosome scale, in a bone resorbing osteoclast. The podosomal core consists of F-actin colocalized with actin-associated proteins like α -actinin, fimbrin, cortactin, gelsolin and the actin regulatory proteins such as WASp-family proteins and Arp2/3. The core is surrounded by a ring structure of integrins and integrin-associated proteins paxillin, talin and vinculin. The core and ring are probably linked by bridging molecules such as α -actinin. Integrin-mediated complex is formed to contain c-src, Pyk-2 or Cbl. Podosomes also contain matrix metalloproteases (MMP-9s), and might be thought to display an invagination at the core where dynamin is localized. Adapted from Soysa et al., 2016.

Anchoring and signal transducing proteins

Talin: Talin links the cytoplasmic domains of integrin β subunits to actin filaments. Its binding to β -integrin cytoplasmic domains triggers a conformational change in the integrin extracellular domain that increases its affinity for ECM proteins. Talin has first been identified in osteoclast podosomes on glass, and at the sealing zone, thirty years ago (Zambonin-Zallone et al., 1989; Lakkakorpi et al., 1990). It has profusely been cited as a crucial protein associated with the double circle domain surrounding the actin ring, subsequently renamed the actin cloud (Lakkakorpi et al., 1993; Lakkakorpi et al., 1996; Pfaff et al., 2001; Chabadel et al., 2007). Although it has not been cited as profusely as its binding partners vinculin and β 3-subunits, their colocalization further suggested that talin and the latter connection provides a linkage between matrix proteins and cytoplasmic components and, thereby, with the actin cytoskeleton.

Tensin: Tensin is a cytoplasmic phosphoprotein that binds to actin filaments and contains a phosphotyrosine-binding domain, which interacts with the cytoplasmic tails of β integrin. Like talin, it was located at the cloud domain in the sealing zone (Pfaff et al., 2001). Furthermore, its 3D localization with 3D-structured illumination microscopy (SIM) revealed a similar axial localization as vinculin, and a preferential interaction with Dock5, an exchange factor for the small GTPase Rac (Touaitahuata et al., 2016).

Paxillin: Paxillin is a signal transduction adaptor protein, also involved in actin-membrane attachment at sites of cell adhesion to the extracellular matrix. Paxillin distribution was reported for the first time *via* its colocalization with PYK2 and p130Cas in the sealing zone of murine osteoclasts, and then further assimilated with the vinculin double circle (Lakkakorpi et al., 1999; Lakkakorpi et al., 2001; Luxenburg et al., 2006a; Gil-Henn et al., 2007). What is more, paxillin and PYK2 were observed to accumulate close to the extracellular substrate-oriented plasma membrane, along with phosphoprotein zyxin (Pfaff et al., 2001). Due to this localization and its binding ability towards both Src kinases and scaffolding proteins vinculin and talin, it has thus been asserted to take part in the signaling mechanisms elicited by the interaction between integrin $\alpha v \beta 3$ (Jurdic et al., 2006; Chellaiah, 2006). Indeed, its localization was also investigated using correlative microscopy, revealing paxillin association with podosome radial actin fibers, reaching up to but not co-localizing with the central bundle. And further electronic observation of paxillin labelled with colloidal gold particles confirmed its association with actin fibers in close proximity with the ventral membrane (Luxenburg et al., 2007).

Vinculin: Vinculin is an actin-binding protein involved in cell-matrix adhesion and cell-cell adhesion, which is notably known for its direct interaction with talin. It is one of the first protein to be associated with the podosome structures in osteoclasts, although not directly with the sealing zone as cells were observed on glass (Marchisio et al., 1984). However, it was already proposed that the vinculin rings surrounding each core were apparently formed by discrete subunits. Shortly after,

it was colocalized with $\beta 3$ -integrin and talin in avian osteoclasts, and around F-actin cores in human osteoclasts (Zamboni-Zallone et al., 1989; Teti et al., 1989). It has been then observed multiple times in osteoclasts plated on bone, or bone matrix-mimicking substrates, and is infallibly excluded from the dense F-actin area and appears to delineate the resorption lacunae in the inner side of the sealing zone (Lakkakorpi et al., 1990; Lakkakorpi et al., 1993; Babb et al., 1997; Duong et al., 1998; Pfaff et al., 2001). It resulted in the description of the sealing zone as a bipartite annular structure, displaying a dense and broad ring of F-actin flanked by a “double circle” of vinculin (Lakkakorpi et al., 1993). Hence, it was subsequently identified as a key protein associated with the actin cloud of the sealing zone (Jurdic et al., 2006; Saltel et al., 2008; Ory et al., 2008).

Moreover, the first z-scanning confocal studies revealed its axial localization closer to the ventral membrane than F-actin, and that it spanned a few microns in height (Lakkakorpi et al., 1993). A recent study confirmed its low axial colocalization thanks to 3D- SIM, in addition to narrowing its range to only approximately 1 μm (Touaitahuata et al., 2016). These results are in agreement with the general assumption that vinculin is preferentially located at the ends of the actin filaments (Van den Dries et al., 2013b; Bouissou et al., 2017).

Actin polymerization regulating proteins

Gelsolin, adseverin and tropomyosin: Gelsolin is the most potent actin filament severing protein, targeting the barbed ends of actin filaments and preventing monomer exchange. It has been proposed as the substrate responsible for podosome disassembly in response to calcium and pH changes in osteoclasts (Teti et al., 1991). It was colocalized with F-actin in a more diffuse pattern within the sealing zone, and in the cytoplasmic area where G-actin was also localized (Chellaiah et al., 2000b; Akisaka et al., 2001). This organization would seem to be suited for promoting rapid regulation of actin assembly and disassembly, and this regulation of cytoskeletal reorganization could result from gelsolin association with PI 3-kinase, with which it colocalizes (Chellaiah et al., 2000a; Chellaiah, 2006). Moreover, osteopontin binding with integrin $\alpha v \beta 3$ was shown to stimulate tyrosine phosphorylation of phosphoinositide (PI)3-kinase associated with gelsolin, necessary for the organization of functional sealing zone (Biswas et al., 2004).

In contrast, deletion of adseverin, a Ca^{2+} -dependent actin filament-severing protein, was shown to have but little effect on bone metabolism, while certainly preventing the normal organization of actin filaments and the sealing zone (Cao et al., 2017). However its role in mediating osteoclastogenesis has been researched, its possible localization within the sealing zone has not been investigated yet (Jiang et al., 2015; Song et al., 2015).

Tropomyosins are a large family of proteins, which stabilize the actin cytoskeleton by binding along filaments and preventing the action of severing proteins. Murine osteoclasts have been reported to express various tropomyosin (Tm) isoforms: Tm-2, Tm-3, Tm-5a, and Tm-5b from the α gene; 5NM-1 from the γ gene, and Tm-4 from the δ gene (McMichael et al., 2006). Interestingly, these different isoforms do not localize at the same subcellular domains. Indeed, Tm-2, Tm-3 and 5NM-1 were rarely associated with the sealing zone, except within its top half section and with no apparent

enrichment. In contrast, Tm-4 and Tm-5a/5b associated predominantly with osteoclast attachment structures. Indeed, Tm-4 was preferentially found at the F-actin cores, whereas Tm-5a and Tm-5b appeared to strongly interact with the cloud domain. However, all three isoforms clearly associated with the top half of the actin ring forming a dense cap (McMichael et al., 2006). Furthermore, Tm-4 was proposed to play a consistent role in stabilizing actin filaments within the sealing zone, likely by regulating access of other proteins that may play roles in actin turnover, as its suppression or overexpression induces an impairment in bone resorption and cell motility (McMichael et al., 2008).

Cofilin and profilin: Cofilin is a key protein responsible for actin filament disassembly. It binds to actin filaments and enhances the rate of dissociation of actin monomers from the minus end. Furthermore, cofilin activity is held in balance by the opposing action of kinases that inactivate it and phosphatases that activate it. It was localized in its active form at the junction between the cloud and the core domains, while its inactive phosphorylated form was restricted to the cloud domain (Blangy et al., 2012; Zalli et al., 2016). Indeed, the phosphatase SSH1 was colocalized with inactive cofilin in the cloud domain, which hints at its possible contribution to the activation of cofilin, induced by RANK-L signaling (Blangy et al., 2012). In addition, acetylated cofilin was found to interact with cortactin at the core domain and this interaction was determined to be critically important for the formation of podosome belts in osteoclasts (Zalli et al., 2016).

In contrast, profilin can reverse the effect of cofilin and stimulate the incorporation of actin monomers into filaments, by stimulating the exchange of bound ADP for ATP. Interestingly, it was however found that osteoclast stimulation with osteopontin had no effect on phosphoinositides associated with profilin, and hence on its enhancing of actin filament formation (Chellaiah et al., 1996b). However, it was proposed that v-ATPases in osteoclasts require a profilin-like domain to interact with actin-filaments, hinting at a possible role in the endocytic or exocytic processes associated with osteoclastic resorption (Holliday et al., 2005).

Cortactin, the Arp2/3 complex and WASp: Cortactin has been shown to activate the Arp2/3 complex and to promote formation of filament branching from pre-existing filaments. The latter is accomplished by the ability of cortactin to bind simultaneously F-actin, Arp3, and another Arp2/3 activating protein, neural-Wiscott Aldrich Syndrome protein N-WASp. Cortactin was located at the core domain within the sealing zone, where it is thought to interact with various other proteins such as dynamin2, the Arp2/3 complex, WASp and N-WASp (Ochoa et al., 2000; Pfaff et al., 2001; Hurst et al., 2004; Tehrani et al., 2006; Chabadel et al., 2007; Ma et al., 2010). Moreover, z-scanning observations showed that it preferentially localized towards the membrane near the substrate, along with WASp and Arp3 (Pfaff et al., 2001; Hurst et al., 2004). Cortactin was also proposed to be involved in the rapid actin turnover in podosomes through its interaction with EB1 and microtubules, cortactin deletion resulting in disorganized actin structures and impaired bone resorption in osteoclasts (Duplan et al., 2014). Indeed, it seems that an alternate and dynamic process of acetylation/phosphorylation of cortactin is required for podosome belt formation, possibly in relation with cofilin (Duplan et al., 2014; Zalli et al., 2016).

Actin-related proteins 2 and 3 form a massive complex composed of seven highly conserved subunits. The Arp2/3 complex is a central actin nucleator that binds to the side of existing filaments to promote new filament growth as a branch, with an approximate 70° orientation. It appears as a key protein to promote actin arrangement into sealing zone, as Arp2 deletion or its activator cortactin *via* siRNA completely suppressed actin rings in murine osteoclasts (Hurst et al., 2004; Tehrani et al., 2006). Most recently, the Arp2/3 complex was localized thanks to electron microscopy, which interestingly revealed that it spanned the entire volume of the sealing zone actin network, and that its localization was not restricted to the sites of actin filament branching and crossing (Akisaka et al., 2019).

WASp functions as a scaffolding protein for the Arp2/3 complex, and both localize at the core domain in osteoclasts (Chellaiah, 2005; Jurdic et al., 2006). Arp3 association with WASp seems to be in competition with gelsolin, and whereas its interaction with Arp2 was stimulated in the presence of osteopontin (Biswas et al., 2004; Chellaiah, 2005). In addition, WASp appears to simultaneously interact with membrane phospholipid phosphatidylinositol (4,5)-bisphosphate (PIP2), which in turn facilitates its binding to Rho GTPase Cdc42, and the formation of this molecular complex is crucial for the organization of actin rings (Calle et al., 2004b; Chellaiah, 2005). CD44 might also be involved in a major signaling pathway inducing sealing zone formation and bone resorption in osteoclasts, in which its activation can compensate for the deletion of WASp interactin protein (WIP) (Chabadel et al., 2007).

Actin filament arranging proteins

Fimbrins: Fimbrins are actin bundling proteins, binding to F-actin as a monomer and holding two parallel filaments less than 20 *nm* apart. Fimbrin was first located at the core domain in osteoclasts (Marchisio et al., 1984; Babb et al., 1997; Ma et al., 2010). Fimbrin isotype analysis revealed that T-fimbrin and L-fimbrin shared similar distributions strongly correlating with that of F-actin, whereas I-fimbrin was absent from avian osteoclasts (Babb et al., 1997). This information, combined with the knowledge that fimbrin isoforms exhibit specificity in their binding to actin isoforms hints at the possible diversity of actin isoform within F-actin cores. Moreover, biochemical evidence suggests that F-actin properties may vary according to the mix of isoforms in the filament, and the resulting filaments have polymerization and depolymerization rates that vary according to the mix ratio (Bergeron et al., 2010). More specifically, L-fimbrin binds solely to β -actin and in its serine phosphorylated state is found associated with actin bundles. Interestingly, its expression in both phosphorylated and dephosphorylated forms seems to decrease progressively as the resorption stages are advancing (Ma et al., 2010). Indeed, it was hence proposed as a potential regulator of the early phase of sealing zone formation upon TNF- α regulation of the phosphorylation of two serine residues (Chellaiah et al., 2018).

Filamin: Filamin is a large actin-binding protein, which interacts with filaments as a dimer. Its actin-binding domains and dimerization domains are at opposite ends of each subunit, so the

filamin dimer is a flexible V-shaped molecule with actin-binding domains at the ends of each arm. As a result, filamin forms cross-links between orthogonal actin filaments, creating a loose three-dimensional meshwork. It was reported to display a similar distribution as talin in the sealing zone, where they compete for the same integrin β subunit binding site (Marzia et al., 2006; Steenblock et al., 2014). Interestingly, either proteins are thought to be involved in a Src-dependent protein complex crucial for sealing zone formation (Steenblock et al., 2014). Furthermore, filamin binding LIM protein 1 - or migfilin - has been identified as a key regulator of bone homeostasis: migfilin-deficient mice display an osteopenic phenotype, possibly resulting from a decrease of osteoblast precursors and dramatic increase in osteoclastogenesis (Xiao et al., 2012).

α -Actinin: α -Actinin also bundles actin filaments, but as a dimer, and is generally associated with acto-myosin contractility. It presents binding sites for direct interaction with integrin β subunits, similar to talin, and could thus also be involved in the anchorage of actin cytoskeleton to the membrane proteins. Indeed, this duplicity is also reflected in its localization both at the core and the cloud domains in actin ring structures (Marchisio et al., 1984; Babb et al., 1997; Pfaff et al., 2001; McMichael et al., 2008). Interestingly, similar to profilin, osteopontin stimulation of integrin clustering had no effect on PIP2 association with α -actinin, although PIP2 is known for its regulation of actin-binding activity (Chellaiah et al., 1996b). However, no other signaling pathway has yet been explored to decipher α -actinin regulation in osteoclasts.

Myosins: Myosin superfamily members are the only known actin-based motor proteins, and different isoforms have been identified in various specific activities. Myosin II powers muscle contraction and cytokinesis, whereas myosins I and V are involved in cytoskeleton-membrane interactions such as the transport of membrane vesicles. Murine osteoclasts have been reported to express both myosin heavy chain isoforms IIA and IIB, but only myosin IIA is enriched in sealing zones, particularly within the cloud domain (Krits et al., 2002; Chabadel et al., 2007; Saltel et al., 2008). There, it was also proposed to be involved in the possible contractile function of the cloud domain (Saltel et al., 2008).

Other myosins were reported in osteoclasts:

- myosin X, acting as a physical link between microtubules and the forming sealing zone and completely absent from mature structures (McMichael et al., 2010a);
- and myosin IXB, acting as a critical regulator of podosome patterning and osteoclast function, possibly *via* its involvement in spatial organization of signaling proteins such as Src kinase (McMichael et al., 2014).

1.3.2. Regulation of the sealing zone

As previously stated, bone resorption is an active process requiring massive cytoskeletal rearrangements, which is reflected by the abundance of proteins involved in actin polymerization within the sealing zone. To allow efficient bone degradation, a tight regulation of the activity of these proteins

is regulated through signaling events. In particular, the binding to RGD-containing ECM of integrin $\alpha_v\beta_3$, the major integrin receptor in osteoclasts, induces its clustering and signal transducing *via* signaling phosphoproteins, such as Rho family members and protein kinases of the Src family (Faccio et al., 2002) (Fig. 1.29).

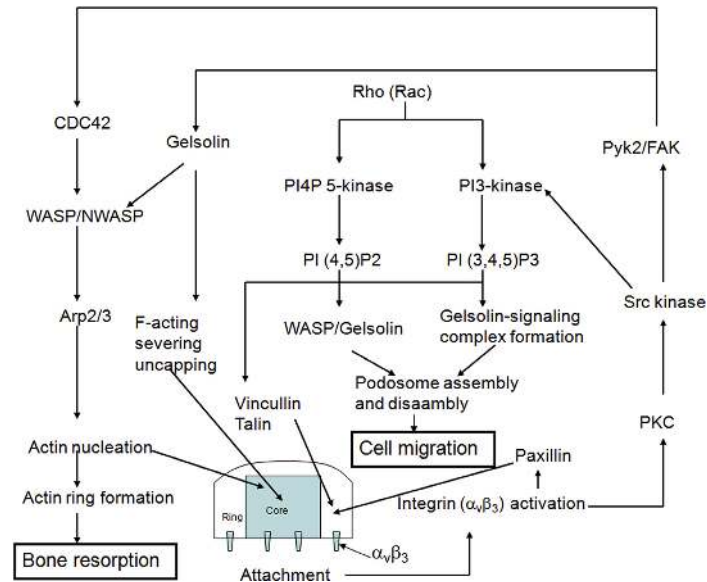


Figure 1.29.: Signaling pathways involved in the regulation of the sealing zone components. Osteoclast attachment causes integrin activation and binding of Src with PYK2 and PI3K. Activation of PI3K causes the activation of PI (4,5)P2 and PI(3,4,5)P3 to activate gelsolin to cause F-actin severing and uncapping in the core. CDC42-GTP causes the activation of WASp and N-WASp which in turn stimulates the actin nucleation and polymerization function of the Arp2/3 complex. Adapted from Soysa et al., 2016.

The activity of small Rho GTPases

Rho GTPases promote F-actin and adhesion structure rearrangements and appear to be the probable signaling intermediates between microtubules and F-actin (Burrige et al., 2004). Moreover, activation of the major Rho family members: RhoA, Rac1 or Cdc42, induces the formation of specific F-actin and adhesion structures (Raftopoulou et al., 2004). Various Rho GTPases are expressed in osteoclasts and they play important functions in many aspects of osteoclast biology, from differentiation and fusion of osteoclast precursors to osteoclast migration and bone resorption activity (Brazier et al., 2006; Chellaiah, 2006; Ory et al., 2008). Indeed, Rho GTPase activity is required for maintaining and modulating sealing zone organization in osteoclasts *via* interaction with various actin-binding proteins.

RhoA - First evidence of the importance of Rho GTPase activity was reported upon the observation of the effect of C3 exoenzyme on osteoclast function and actin organization (Zhang et al., 1995). ADP-ribosyltransferase C3 (C3 exoenzyme) selectively and specifically ADP-ribosylates Rho proteins RhoA, RhoB and RhoC. Inactivation of Rho proteins was associated with inhibition of tyrosine phosphorylation and activation of PI3-kinase, disruption of sealing zone and impairment in bone resorption (Zhang et al., 1995). Specifically, RhoA inhibition was reported to result in the formation of podosome belts, instead of functional sealing zones in osteoclasts plated on bone, or in osteoclasts lacking PYK2 (Saltel et al., 2004; Gil-Henn et al., 2007). To confirm this observation, podosome belt formation coincided with low levels of RhoA activation in osteoclasts plated on glass (Destaing et al., 2005). Yet, RhoA activation appears not to be sufficient to induce sealing zone formation. Rather, it could be involved in the stabilization of actin structures *via* its interaction with microtubules (Destaing et al., 2005; McMichael et al., 2014). Importantly, PI3-kinase, which produces PIP2 and regulates many sealing zone components, such as profilin, gelsolin and α -actinin, has also been shown to interact with $\alpha v \beta 3$ and to increase its activity in a RhoA-dependent manner (Lakkakorpi et al., 1997; Chellaiah et al., 2000a).

Cdc42 - While transduction of activated Cdc42 in osteoclasts first showed little effect in sealing zones, it was later reported to increase PIP2 interaction with WASp, a major effector of Cdc42 (Chellaiah et al., 2000a; Chellaiah, 2005). Binding of PIP2 to WASp increases the effectiveness of Cdc42 binding to WASp, this cooperation being necessary for actin ring formation (Chellaiah, 2005). This observation hints at the requirement of both Rho- and Cdc42-mediated events for WASp activation, interaction of Arp2/3 with WASp, and cortical actin polymerization. Similar to RhoA, Cdc42 may also be involved in the stabilization of the sealing zone by microtubules *via* interaction with WASp, although this association has only been reported in macrophages (Linder et al., 2000b).

Rac - Rac1 and Rac2 are both expressed in osteoclasts, and were first reported to display distinct roles in osteoclast precursor chemotaxis and differentiation *in vivo* (Wang et al., 2008). Indeed, Rac1 was proposed as the predominant isoform because of its regulatory role in M-CSF-mediated chemotaxis and actin assembly of pre-osteoclasts. However, a subsequent study refuted this hypothesis, showing that Rac1 and Rac2 were not involved in osteoclastogenesis, but rather showed overlapping roles by localizing Arp3 within the sealing zone during its formation (Croke et al., 2011). What is more, Rac double deletion resulted in the absence of sealing zones and bone resorption defects (Croke et al., 2011).

Rho GTPases GEFs and GAPs - The activity cycle of Rho GTPases is regulated on one hand by guanine nucleotide exchange factors (GEFs), which activate the GTPases by catalyzing the release of GDP and allowing the binding of GTP (Gadea et al., 2014; Fort et al., 2017). On the other hand GTPase-activating proteins (GAPs) inactivate the GTPases by stimulating their GTP hydrolysis activity (Tcherkezian et al., 2007). Various Rho GTPase GEFs and GAPs are expressed in osteoclasts (Brazier et al., 2006). Considering RhoA, myosin IXB was reported to

modulate osteoclastic resorption while not apparently disrupting sealing zones upon its suppression (McMichael et al., 2014). Indeed, myosin IXB acts as a GAP for RhoA, and increase in RhoA activity appeared to have an influence on the stability of the microtubule network.

Considering Cdc42, FGD6 was reported to act as a GEF, and to coordinate cell polarity and membrane recycling through its Src-dependent interaction with different actin-based protein networks, such as talin or filamin A (Steenblock et al., 2014). Considering Rac, one of its GEF Dock5 was reported to be required for sealing zone formation, within which it localizes in the cloud domain and interacts with scaffold protein Tensin 3 (Vives et al., 2015; Touaitahuata et al., 2016; Blangy, 2017). Another Rac-GEF is Vav3, of which deficiency has been identified as an osteopetrotic factor in mice (Faccio et al., 2005).

Phosphorylation activity of the Src family kinases

Phosphorylation at tyrosine residues controls a wide range of properties in proteins such as enzyme activity, subcellular localization, and interaction between molecules.

Src - A new area was opened in osteoclast research when it was first observed that the targeted disruption of c-Src in mice induced osteopetrosis, and that the kinase was highly expressed in osteoclasts (Soriano et al., 1991; Horne et al., 1992). Initial localization studies preferentially located the kinase in membrane associated domains, such as vesicles or the ruffled border (Horne et al., 1992; Tanaka et al., 1992). Proto-oncogene product c-Cbl is tyrosine-phosphorylated in a Src-dependent manner in vesicular structures, which is required for bone resorption, yet was later localized within the sealing zone (Tanaka et al., 1996; Szymkiewicz et al., 2004). In addition, several cytoskeleton-associated proteins, such as vinculin, talin, paxillin, cortactin, and focal adhesion tyrosine kinase (FAK), are known substrates for Src kinase, and have been identified as components of the sealing zone, which hints at a possibly similar localization for Src. It has been reported that upon attachment to bone, tyrosine phosphorylation increased to higher levels than PI3-kinase and RhoA, without apparently direct binding of Src with $\beta 3$ integrin (Chellaiah et al., 1996a; Lakkakorpi et al., 1997). Indeed, Src was notably identified to associate with gelsolin, which in turn stimulates cytoskeletal reorganization through PI3-kinase signaling (Chellaiah et al., 1998; Chellaiah et al., 2000b). Furthermore, Src-deficient mice were reported to display defective sealing zone organization on bone (Lakkakorpi et al., 2001).

The tyrosine kinase Src preferentially localizes to the actin cloud domain, where it is notably required for the organization of this domain (Sahu et al., 2007; Saltel et al., 2008; Heckel et al., 2009). Indeed, Src-deficient osteoclasts displaying peculiar actin structures, in which podosomes seemed to exhibit only the core domain (Destaing et al., 2008). What is more, it appeared that both Src localization and enzymatic activity were essential for optimal sealing zone assembly (McMichael et al., 2010b). In contrast to the observations of previous studies, Src has been reported to bind to the cytoplasmic tail of $\beta 3$ integrin, and to anchor PYK2 along (Zou et al., 2007; Destaing et al., 2008). Yet, it has also been reported to interact with proteins located in the core domains, such as

dynamamin and cortactin, known as a major Src substrate (Ochoa et al., 2000; Bruzzaniti et al., 2005; Tehrani et al., 2006; Bruzzaniti et al., 2009; Ma et al., 2010; Duplan et al., 2014).

Src kinase activity has also been linked to the activation of another tyrosine kinase Syk, involved in facilitating Rac GTPase activation *via* its GEF Vav3 (Faccio et al., 2005).

PYK2 - Proline-rich tyrosine kinase 2 (PYK2) is a cytoplasmic kinase related to the focal adhesion kinase (FAK), is calcium-calmodulin sensitive, and can bind protein tyrosine kinase Src and paxillin (Dikic et al., 1996; Hiregowdara et al., 1997). PYK2 expression is abundant in osteoclasts *in vitro* and *in vivo*, where it has been reported to form a molecular complex with Src and integrin $\beta 3$ subunit (Duong et al., 1998). Osteoclast adhesion to osteopontin or vitronectin induced the translocation of PYK2 into the cytoskeletal fraction, and it was observed to colocalize with vinculin, paxillin and p130Cas in sealing zones (Duong et al., 1998; Lakkakorpi et al., 1999; Lakkakorpi et al., 2001; Pfaff et al., 2001). Its association with p130Cas, a major tyrosine-phosphorylated protein, indicates that it may serve as a docking protein for multiple Src homology (SH)2 and SH3 domain-containing molecules, such as PI3-kinase, in a Src-independent manner (Lakkakorpi et al., 1999; Heckel et al., 2009). PYK2 has thus been suggested to participate in the transfer of signals from the cell surface to the cytoskeleton, due to its significant binding to both integrin $\beta 1$ and $\beta 3$ tails, independently of paxillin (Pfaff et al., 2001). This signaling pathway is required for efficient bone resorption and sealing zone formation in osteoclasts (Jurdic et al., 2006; Gil-Henn et al., 2007). Interestingly, PYK2-null mice not only displayed an osteopetrotic phenotype associated with a loss of actin superstructures, their osteoclasts exhibited enhanced Rho GTPase activity and decreased levels of microtubule acetylation (Gil-Henn et al., 2007). In addition, PYK2 interaction with large GTPase dynamamin in the cloud domain has been reported to decrease its phosphorylation and association with Src, independently of integrin $\alpha v\beta 3$ activation (Bruzzaniti et al., 2009).

Interaction with microtubules

Microtubules can contact focal adhesions, thereby inducing their destabilization (Kaverina et al., 1999; Krylyshkina et al., 2003). In osteoclasts, microtubules have also been reported in close relation with the sealing zone. Indeed, they display a radial organization from the nuclei to the peripheral actin ring, and are enriched in a concentric manner in its upper portion (Zallone et al., 1983; Lakkakorpi et al., 1991a; Lakkakorpi et al., 1996; Babb et al., 1997; Okumura et al., 2006). Observation of electron micrographs of sheared-open osteoclasts exhibited several podosomes distributed along the length of a single microtubule, or single podosomes targeted by single microtubules (Akisaka et al., 2008). In addition, a dense network of microtubules reaches deep down into the resorption pit, strongly suggesting an active role for microtubules in the membrane traffic to the ruffled border (Lakkakorpi et al., 1991a). Interestingly, microtubule depolymerization *via* treatment with nocodazole induced the loss of actin superstructures, individual podosomes rather exhibiting random pattern throughout the cytoplasm (Babb et al., 1997; Okumura et al., 2006). This observation hints at a possible role for the interaction between actin- and microtubule-based cytoskeletal components

in the promotion of sealing zone and bone resorption (Fig. 1.30).

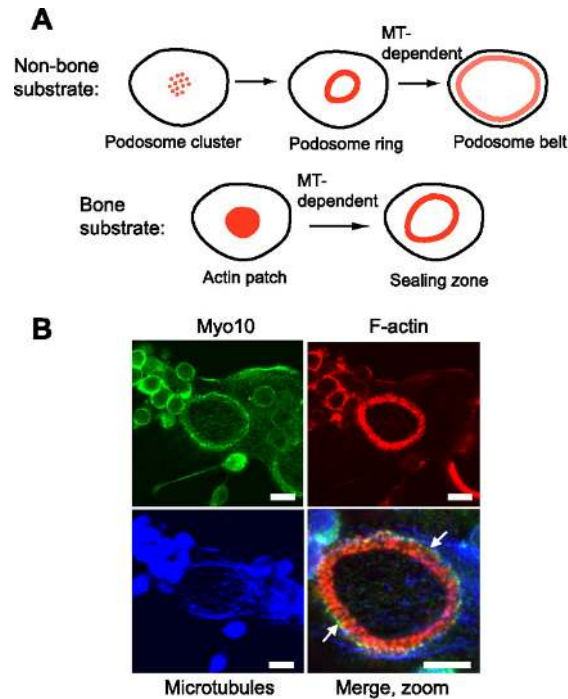


Figure 1.30.: Myosin X is positioned between microtubules and actin of forming podosome belts and sealing zone. A, schematic of podosome belt and sealing zone formation in cultured osteoclasts. B, a marrow-derived osteoclast on glass with an immature podosome ring was labeled for Myosin X (green), F-actin (red), and microtubules (blue). Myosin X localizes between F-actin and microtubules, as shown in the merged image. Scale bars 10 μm . Adapted from McMichael et al., 2010a.

Indeed, disrupting microtubules in osteoclasts on bone with colchicine induced a decrease in the amount of PI3-kinase translocated in cytoskeletal fraction (Lakkakorpi et al., 1997). And conversely, inhibition of PI3-kinase enzymatic activity with wortmannin or protein kinase B caused rounding of the cells, suggesting dramatic disassembly of the microtubule network, and bone resorption defects (Lakkakorpi et al., 1997; Matsumoto et al., 2013). Subsequently, acetylation of microtubules has been proposed to be under control of Rho GTPase activity. Indeed, C3 exoenzyme treatment drastically delayed podosome belt disassembly, *via* increase of the acetylated microtubule level (Destaing et al., 2005; Gil-Henn et al., 2007). This interaction between RhoA and microtubule has been described to involve histone acetylase HDAC6, which is recruited and activated by formin mDia2 (Destaing et al., 2005). What is more, it has been reported that RhoA activity was enhanced in PYK2-null osteoclasts, but its inhibition was able to reinduce the formation of a belt-like structure at the cell periphery (Gil-Henn et al., 2007). In contrast, myosin X has been proposed to act as a physical link between actin and microtubule at the sealing zone, yet its suppression did not apparently alter

RhoA nor Rac GTPase activity (McMichael et al., 2010a).

Microtubule acetylation has further proved to be crucial for actin organization in osteoclasts and bone resorption. Calpain-6, a nonproteolytic member of the glucocorticoid family, complexes with tubulin in the vicinity of the sealing zone, and its absence inhibits microtubule acetylation and stability in the osteoclast (Hong et al., 2011). In addition, microtubule acetylation might also be involved in the activation cycles of cofilin and cortactin. Cofilin interacts with microtubule plus end proteins to target microtubule to podosomes, where it interacts with EB1 and cortactin under the control of HDAC6. Indeed, acetylation and phosphorylation of cofilin are mutually exclusive, acetylation of cofilin favoring interaction with cortactin in its activated form, whereas its phosphorylation prevents this association (Blangy et al., 2012; Zalli et al., 2016).

In a reciprocal manner, F-actin depolymerization by cytochalasin D affected microtubule networks, resulting in the loss of its circumferential organization, and osteoclast function (Okumura et al., 2006). Interestingly, treatment with calcitonin achieved total disruption of sealing zones, without affecting microtubule network, but probably associated with the impairment of v-ATPase distribution in a microtubule-independent manner (Okumura et al., 2006).

1.3.3. Scale-dependent dynamics of the sealing zone

Cell migration requires spatial and temporal regulation of filamentous actin (F-actin) dynamics. This regulation is achieved by distinct actin-associated proteins, which mediate polymerization, depolymerization, severing, contraction, bundling or engagement to the membrane. In the case of osteoclasts, cells need to migrate toward their next resorption site, establish the sealing zone and ruffled border domains and maintain them throughout the whole degradation process, then disassemble the entire membrane apparatus to start all over again. To achieve the specific arrangement of filamentous actin into the sealing zone, where multiple actin-related proteins and potential effector proteins coexist, dynamic processes occur at various scales in osteoclasts.

At the cell scale: adhesion and migration

Substrate adhesion - In order to seal the acidic environment of the resorption lacuna, osteoclasts make close contact with the underlying material. In fact, osteoclast adhesion to their substrate has been reported to be very tight, exhibit only a few tens of nanometers gap (Lakkakorpi et al., 1996; Akisaka et al., 2008; Akisaka et al., 2015). This acute proximity on a restricted area of the cell results in local membrane curvature, as seen with interference microscopy (Marchisio et al., 1984; Kanehisa et al., 1990; Nakamura et al., 1999; Calle et al., 2004b; Tehrani et al., 2006; Chabadel et al., 2007). These protruding characteristics hint at a possible involvement of a force generation process within the sealing zone. Therefore, adhesion force and energy have recently been measured by probing osteoclasts with tipless bone-coated AFM cantilevers. These experiments showed that adhesion force was stronger towards bone material compared to bovine serum albumine (BSA) coating: 100 nN against 30 nN, respectively. In addition, adhesion energy increased with longer periods

of probe contact, spanning 30 s to 300 s (Deguchi et al., 2016). However, it is uncertain whether this timing was sufficient for the establishment of osteoclast specific adhesion structures.

As pointed, the degree of osteoclast adhesion appears to be substrate-dependent. Osteoclasts plated on glass coated with either osteopontin or bone sialoprotein show a characteristically irregular and extended morphology, whereas when adhering to vitronectin they show a much more regular and spread morphology (Horton et al., 1995). It suggests a possible role for integrin “outside-in” signaling in regulating the internal cell tension *via* cytoskeletal rearrangement. Indeed, it was notably reported that Src, PYK2 and p130Cas were tyrosine-phosphorylated in a time-dependent manner upon attachment to vitronectin, or that adhesion kinetics were impaired in Src-deficient osteoclasts (Lakkakorpi et al., 1999; Lakkakorpi et al., 2001; Pfaff et al., 2001). Furthermore, calcitonin was able to induce the detachment of osteoclasts, seemingly *via* decreasing PYK2 phosphorylation and increasing its interaction with Src (Shyu et al., 2007).

Substrate topography sensing - In addition to chemically-induced integrin signaling, osteoclasts have also been proposed to modulate their adhesion according to substrate topography sensing. Indeed, first observation that increasing the degree of apatite crystallinity coincided with an increase in cells exhibiting sealing zone (Saltel et al., 2004). Another study related membrane structure differences depending on the roughness of the substrate by comparing glass, calcite and bone slices. On glass osteoclasts exhibited a flat membrane domain within sealing zone-like structure, while on bone the typical ruffled border with finger-like structures delimited by membrane folds was observed and on calcite sparse deep extrusions apparently replaced the ruffled border and membrane was following the local topography (Geblinger et al., 2009). Further exploration of the influence of roughness revealed that rougher surface promoted the formation of few large and stable sealing zones, whereas osteoclasts on smooth surfaces preferentially formed multiple small instable actin rings, independently of the presence of extracellular matrix proteins (Geblinger et al., 2010) (Fig. 1.31). The same reports that sealing zone stability increases substantially with increasing roughness also proved true on aluminum gradients and bone (Geblinger et al., 2011; Shemesh et al., 2015; Shemesh et al., 2017).

It appeared that sensing of the substrate roughness occurs not at the scale of individual podosomes, but of a number of podosomes linked together in the sealing zone. Indeed, extracellular microtopographic obstacles affected sealing zone formation and local turnover, its progression in the region encountering a topographic barrier being stalled relative to its surroundings until flanking regions have advanced beyond the barrier (Geblinger et al., 2011). Interestingly, osteoclasts plated on crystal cleavage-induced steps displayed extensive nucleation of new, short-lived rings along the imperfection (Geblinger et al., 2010). Indeed, abrupt local changes in the axial direction have been identified to direct the formation of sealing zones. They were rarely observed in proximity to osteocyte lacunae, saw markings, or surface cracks, while bumps appeared to not only preferentially promote their formation around bulges size, but are also to stabilize them (Shemesh et al., 2015).

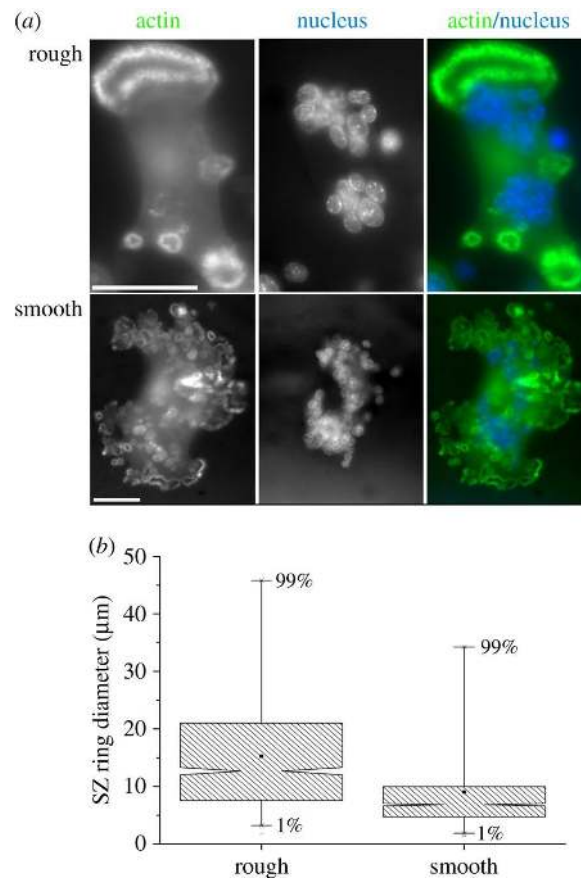


Figure 1.31.: Osteoclasts adhering to different bone topographies differ in the size of their sealing zone rings. (a) Representative fluorescence images of RAW 264.7 cells plated on rough and smooth bone surfaces and stained for actin (left panels), nuclei (middle panels) and actin and nuclei overlaid (right panels). Scale bars $50 \mu m$. (b) Box chart of the sealing zone ring size populations on each of the surfaces. Adapted from Shemesh et al., 2017.

Migration - Initial observations of osteoclasts plated on bone and the associated resorption trails led to hypothesize that bone degradation and cell motility could be temporally correlated. Osteoclasts were seen to cover only part of the resorption lacunae, and the convex part of crescent shaped bands of podosomes was outlining the advancing edge of the lacunae (Kanehisa et al., 1990). In fact, numerous biochemical treatments were simultaneously reported as altering the sealing zone and motile properties of osteoclasts. Integrin clustering stimulation *via* binding to osteopontin has hence been associated with increased migrated distances, specific directionality and higher rates of motility in phagokinesis or transwell migration assays (Chellaiah et al., 2000b; Chellaiah et al., 2000a; Faccio et al., 2002; Chellaiah et al., 2003c; Samanna et al., 2007). In addition, signaling proteins associated with cytoskeletal remodeling and matrix metalloproteinases have also been proposed to modulate osteoclast migration (Chellaiah et al., 2000a; Goto et al., 2002; Bruzzaniti et al., 2005; Samanna

et al., 2007; Georgess et al., 2014). Moreover, migration towards bone fragments has been reported to be quite a long process, spanning a few hours (Ma et al., 2010).

Accordingly, cyclic podosome ring expansion has been described to drive osteoclast migration periodically every two hours (Hu et al., 2011b) (Fig. 1.32). The formation and expansion of podosome rings inside the osteoclast accompany its elongation in one given direction, until the cell length reaches a maximum. At this time point, as osteoclasts mostly displayed at least two actin rings, the widest actin structure disappears from one side, and the cell retracts toward the remaining structure on the opposite side, which becomes the leading edge. This results in a “jump” of the cell in the corresponding direction approximately 10 minutes after the cell length has reached a maximum. Subsequently, the cell elongates in an almost perpendicular direction due to the growth of two new rings from the remaining structure at the leading edge. Interestingly, observation of this dynamic process on a soft substrate allowing for the visualization of its deformations revealed that podosome rings are subjected to an internal tension that tends to increase their perimeter, extend the ring toward the periphery and subsequently stretch the cellular membrane (Hu et al., 2011b).

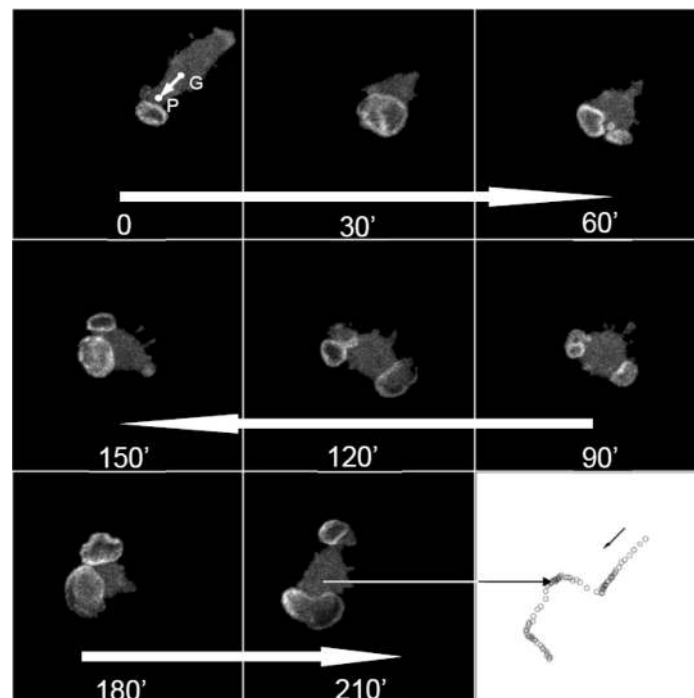


Figure 1.32.: Podosome ring expansion and osteoclast migration are correlated. The dynamics of an osteoclast expressing GFP-actin moving on the surface of a polyacrylamide gel. Adapted from Hu et al., 2011b.

Yet, a more recent study also used substrates with varying stiffness and not functionalized with extracellular matrix proteins. Its findings most surprisingly revealed that such substrates did not support podosome formation in osteoclasts, even though osteoclasts migrated efficiently (Touaitahu-

ata et al., 2013). What is more, identification of two types of resorption traces suggested specific relations between migration and degradation in physiological conditions: some osteoclasts specifically break down sparse locations on the bone by alternating stationary resorption and migration phases, and some osteoclasts can combine both function simultaneously (Rumpler et al., 2013; Merrild et al., 2015; S e et al., 2017).

Transmigration - Osteoclasts have been reported to migrate through cell layers found in the bone microenvironment, stromal, endothelial cells or adipocytes, but not through epithelial cells (Saltel et al., 2006; Saltel et al., 2008). This feat suggested that osteoclast transmigration is more a transcellular process than intracellular diapadesis. Interestingly, molecular components exclusively associated with the core domain were not required (Saltel et al., 2008). Instead, proposed transmigration regulating factors consisted in Src, seemingly acting downstream of orphan nuclear estrogen receptor-related receptor α and upstream of phosphorylated paxillin, and matrix metalloproteinases (Saltel et al., 2006; Badowski et al., 2008; Bonnelye et al., 2010).

Mesoscale patterning and dynamics of the sealing zone

Patterning of podosomes in osteoclasts - Given that resorption pits have been observed in sparse distributions on substrates degraded by osteoclasts, numerous studies have striven to document the possible cytoskeletal rearrangements leading to the establishment of the sealing zone. Therefore, five main podosome patterns in osteoclasts have been identified: individual podosomes, podosome clusters, small podosome rings, and either podosome belts on glass or sealing zone on bone (Zambonin-Zallone et al., 1988; Lakkakorpi et al., 1991a; Calle et al., 2004b). These podosomes arrangements have been sequentially identified in osteoclasts throughout differentiation or upon substrate adhesion (Zambonin-Zallone et al., 1988; Destaing et al., 2003; Calle et al., 2004b; Shyu et al., 2007; Akisaka et al., 2008; Badowski et al., 2008; Ory et al., 2008). Hence, it has been proposed that they were actually temporally related (Fig. 1.33):

- individual podosomes aggregate to a few restricted membrane regions to assemble clusters;
- within clusters, central podosomes tend to translocate centrifugally and disassemble more rapidly than peripheral ones, which gives rise to small podosomes rosettes;
- podosome rings expand radially by incorporation of podosomes towards its periphery, until contact between two rings leads to their fusion into a larger, still-expanding ring;
- peripheral podosome belt is described to contour the cell membrane domain which is in contact with the substrate, and sealing zones delimitate the resorption lacuna.

Electron microscopy observations further supported this proposed patterning cycle by highlighting increased interconnectivity, proximity and complexity of the actin filament arrangement with each stage (Luxenburg et al., 2007; Akisaka et al., 2015; Akisaka et al., 2019). In addition, patterning stages are associated with specific actin dynamics. Individual podosomes and clusters exhibit highly dynamic actin turnover, small rosettes tend to be more transient structures, and podosome belts display stationary behavior (Destaing et al., 2003; Luxenburg et al., 2006b; Akisaka et al., 2008;

Geblinger et al., 2009). Interestingly, formation of podosome clusters and rings is microtubule independent, whereas the podosome belt depends on stabilized acetylated microtubules (Saltel et al., 2008).

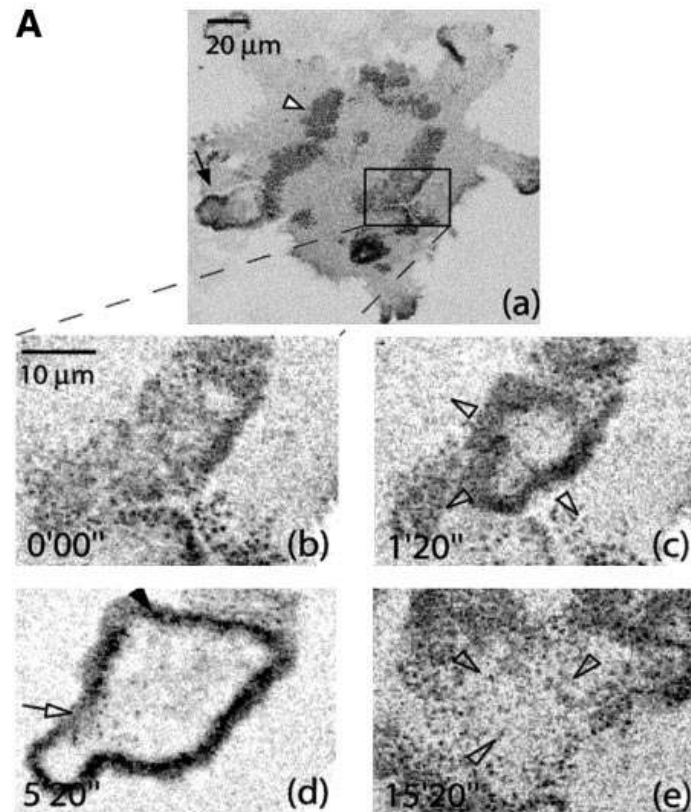


Figure 1.33.: Expanding podosome rings are formed inside podosome clusters and grow larger as differentiation progresses. Actin-GFP RAW osteoclasts at early stage of ring formation (a) overview of the cell with a mix of rings (black arrow) and clusters (white arrowhead). Inside a cluster (b), a ring formed and expanded (c). No podosome formation was observed inside the area delimited by the ring. (d) The ring eventually stopped and collapsed back to a cluster. Adapted from Destaing et al., 2003.

However, some of these studies were carried out with glass substrates, on which osteoclasts form podosome belts instead of sealing zones. In fact, these structures exhibit several differences, restraining from hasty homologies, notably the chemical and physical cues initiating their assembly and the apico-basal polarization. Therefore, time-lapse observations of osteoclasts on apatite-coated slides revealed successive cycles of sealing zone formation associated with resorption interrupted by intermediate periods without clearly recognizable actin structures (Saltel et al., 2004). Sealing zones would not apparently evolve from successive fusion stages of podosomes, but rather expand centrifugally from small induction centers (Ma et al., 2010). These initiator actin patches have notably been

observed to be surrounded by myosin X and v-ATPase (McMichael et al., 2010a; Deguchi et al., 2016).

Dynamics of the sealing zone - Upon adhesion to bone-mimicking substrates, osteoclasts develop a limited number of large actin rings, delineating an area corresponding roughly to half of the cell projected area (Geblinger et al., 2010). The life span of the sealing zone during a resorption cycle spanned from slightly more than two hours to over six hours (Saltel et al., 2004; Geblinger et al., 2010; Geblinger et al., 2011). Interestingly, it was reported that sealing zones display different overall dynamic behaviors in a substrate-dependent manner, even on resorbable materials. On calcite, small rings were apparently merging in a continuous manner to form fewer large rings stable for several hours, whereas on bone several small rings were stable for hours with little spatial variations (Geblinger et al., 2009). This might be explained by discrepancies in the roughness of the material surface (Shemesh et al., 2017). Fusion events have been further characterized as rapid processes, during which the apparent merger of neighboring actin rings was followed by a gap in the actin bundle around the middle of the overlap region (Geblinger et al., 2010). As the gap widens, the sealing zone grows towards the cell periphery. In addition, fusion events are independent of variations in overall sealing zone geometry, but strictly dependent on the continuity of matrix adhesion (Andregg et al., 2011). Interestingly, trench-forming osteoclasts have been visualized as exhibiting a crescent-formed sealing zone throughout the entire resorption process, while analyses in sealing zone-like structures had reported that local curvature influenced on local stability (Søe et al., 2017; Batsir et al., 2017). Indeed, convex contours located near the leading edge are mostly stable, whereas concave regions are unstable, associated with fast displacement or complete disassembly of the podosome belt.

Microscale actin turnover within a single core

Analysis of the dynamics of individual dots using phase-contrast microscopy showed that the phase-dark dots at the cell periphery were highly dynamic, changing in size, their life span varied between 2 and 12 minutes (Kanehisa et al., 1990). Subsequent fluorescence recovery after photobleaching (FRAP) experiments brought into light the cause for these oscillations: recovery was not due to the assembly of new podosomes, but rather to a high turnover of actin in the podosomes themselves, characterized by a characteristic dynamical time of 30 seconds, both at the core and cloud domains (Destaing et al., 2003; Saltel et al., 2004; Luxenburg et al., 2012). In fact, during the life span of podosomes, more than twice the amount of actin that composes a podosome at a given time is incorporated and removed from it. Interestingly, small GTPase RhoE has been identified to facilitate fast actin turnover in podosomes, without affecting the expression levels of essential podosome components (Georgess et al., 2014).

Fluorescence microscopy-based studies have also explored the spatiotemporal arrangement of podosomes in osteoclasts. Luxenburg and coworkers suggested that individual podosome formation involves an early local accumulation of paxillin, subsequent nucleation and stabilization of actin by cortactin and its bundling by α -actinin, followed by a major increase of β 3 integrin levels (Luxenburg

et al., 2012). Interestingly, the same type of experiments in osteoclast-like BHK RSV-transformed cells rather showed that newly assembled invadopodia contained exclusively core proteins. Mature invadopodia were constituted by core proteins and surrounding proteins, and older invadopodia were devoid of any core (Badowski et al., 2008).

Hu et al. proposed an elegant, although elementary, *in silico* modeling of the molecular regulation for internal actin dynamics by gelsolin (Hu et al., 2011a) (Fig.1.34). In this model, filaments are not branched, and supposed to grow from a nucleation site located at the cell membrane, by addition of monomers, in a restricted area corresponding to the functional perimeter of gelsolin. Solving the diffusion equations resulted in pointing out that the characteristics of the podosome in the steady-state are not sensitive to the local concentration of gelsolin, when considering only its filament severing activity. This modeling could also be adapted to further explore the dependency of the actin polymerization frequency on the local concentration at the core, and the interaction between neighboring cores through the diffusion fields in the cloud domain. This analysis, combined with state-of-art observation of the sealing zone components might be crucial for a better comprehension of its multiscale dynamics.

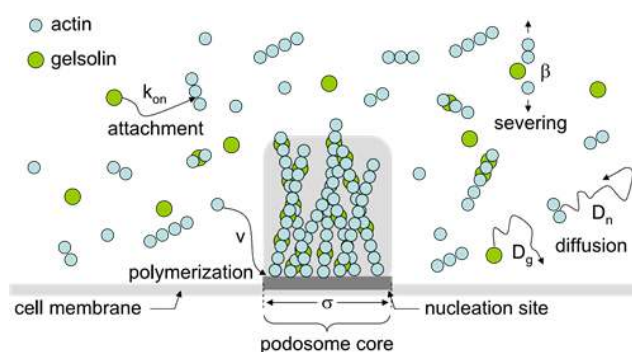


Figure 1.34.: Schematic view of the dynamic regulation of actin filament length by the severing activity of gelsolin. Adapted from Hu et al., 2011a.

1.4. Conclusions and perspectives

Through this extensive review of the published literature focusing on deciphering sealing zone molecular components and dynamics, a more detailed and comprehensive model of the specific architecture regulation can be envisioned, and has yet to be completed thanks to ever-challenging studies.

As has been stated earlier, some proteins have extensively been cited to be associated with specific domains within the sealing zone, while not having effectively been localized in osteoclasts. This is mainly due to the assumption of high similarity between individual podosomes and the osteoclast specific adhesion and functional actin superstructure. However, it is highly possible that reality may prove to be more complex than what is commonly assumed.

What is more, with the recent identification of the cap domain in individual podosomes and the

technological advances in high-resolution microscopy compatible with observations on bone substrates, it would be of the utmost interest to explore *de novo* the specific localization of well-known proteins within the sealing zone. Fluorescence-based techniques such as stimulated emission depletion (STED) or structured illumination microscopy (SIM) could already provide crucial insights as to the submicron scale distribution of various proteins, both in 2D and 3D (Deguchi et al., 2016; Touaitahuata et al., 2016). Better still, this information could be coupled with ultrastructural localization through the use of correlative microscopy, hence substantially allowing for the thorough understanding of the specific arrangement of actin filaments composing the sealing zone (Akisaka et al., 2019). More challenging but not less exciting, developing sample preparation processes compatible with observation of the sealing zone *via* cryo-electron tomography would provide unique insights into the branching patterns of filaments within the cores, which is otherwise inaccessible with other acquisition methods.

In addition, internal dynamics of the sealing zone has been but poorly researched, and the proposed model for the temporal organization and modifications of the sealing are vastly theoretical. Indeed, few studies have explored actin time-dependent variations at the single core scale, and none in the specific context of the sealing zone in resorbing osteoclasts. And yet, considering the various signaling pathways previously identified as regulating actin polymerization processes, it is highly conceivable that actin turnover would be paramount for both the establishment and the integrity of this structure. Therefore, in-depth characterization of actin-related dynamic events within the sealing zone requires both spatial and temporal high-resolution microscopy techniques. It would be expected to allow for further deciphering the apparently close relation between neighboring cores and, through the use of inhibitors, for identifying the various roles of signaling pathways at different stages of the resorption cycle. Another major question to be tackled with this type of exploration would consist in the identification of the main phases of sealing zone formation and disassembly on bone, as no consensus has been reached and antagonist results hint at different hypotheses, without having provided sufficient data to establish their veracity.

Eventually, the sealing zone as a potential probing and sensing structure, similar to what has been observed with individual podosomes, is still an elusive concept. Interestingly, expansion of the actin ring has been associated with the generation of in-plane forces (Hu et al., 2011b). But the sealing zone is also expected to be mainly a site of generation of forces protruding against the bone matrix, in order to efficiently confine the resorption acidic environment. Therefore, attempting at characterizing the sealing zone mechanical properties would require tools to evaluate forces in 3D, and at the scale of single subunits. However, such a technique has not yet been made available.

In contrast, the sealing zone sensitivity to micro- and nanotopographies has effectively been reported (Geblinger et al., 2011; Shemesh et al., 2015; Shemesh et al., 2017). But since these observations were carried out on non-transparent substrates, they did not allow for the precise characterization of the mechanisms involved in topography sensing. Hence, renewing this exploration on fabricated substrates, mimicking the physiological range of bone topography and allowing for high-resolution microscopy, would proved crucial insights into osteoclast responses to extracellular matrix physical cues.

Chapter 2.

Nanoscale architecture and dynamics of the sealing zone

This chapter presents the main results obtained through the systematic characterization of the sealing zone in human osteoclasts with super-resolution microscopy techniques. It consists in a quasi-final version of an article to be submitted by the end of 2019.

Contents

2.1. Abstract	68
2.2. Introduction	68
2.3. Results	70
2.3.1. Nanoscale organization of actin cores in the sealing zones formed by human osteoclasts	70
2.3.2. Local synchrony of sealing zone actin cores	72
2.3.3. Sealing zone podosome cores are organised into islets surrounded by adhesion complexes	73
2.3.4. Three-dimensional nanoscale organization of the podosome belt	77
2.4. Discussion	80
2.5. Materials and methods	83
2.5.1. Differentiation and culture of primary monocyte-derived osteoclasts	83
2.5.2. Cleaning of precision glass coverslips	84
2.5.3. Primary antibodies	84
2.5.4. Immunofluorescence	84
2.5.5. Scanning Electron Microscopy imaging	84
2.5.6. Analysis of SEM images	85
2.5.7. RIM 2D super-resolution imaging	85
2.5.8. Analysis of RIM images of fixed samples	86
2.5.9. Analysis of RIM live acquisitions	87
2.5.10. DONALD 3D super-resolution imaging	88
2.5.11. Analysis of DONALD 3D super-resolution images	89
2.5.12. Statistical analysis	89

2.1. Abstract

The osteoclast is a cell type of the hematopoietic lineage dedicated to the resorption of mineralized bone matrix. To achieve this degradation process, osteoclasts form a superstructure called the sealing zone, which creates a close contact with bone. Hence, it confines the release of protons and proteinases to facilitate the dissolution of the mineral components and the digestion of organic components. Electron microscopy has shown that the sealing zone is composed of actin cores nested in a dense actin network that has so far prevented their observation by fluorescence microscopy. How cores are organized and coordinated to allow efficient bone degradation is therefore still unknown. In this work, we combine cutting-edge super-resolution microscopy methods with scanning electron microscopy to reveal the architecture and dynamics of the sealing zone formed by human osteoclasts degrading bone. We show that random illumination microscopy allows the identification and live imaging of densely packed actin cores within the sealing zone. A cross-correlation analysis of the fluctuations of the sealing zone actin cores indicates that they are not coordinated at the whole structure level but that they are synchronized locally. Further analysis of the organization of adhesion components and actin crosslinkers shows that the sealing zone is composed of groups of α -actinin1 linked podosomal cores encircled by adhesion complexes. Thus, the confinement of the bone degradation machinery is not achieved through the global coordination of all subunits composing the sealing zone, but at the level of dynamic, functional islets of podosome cores.

Key words

Human osteoclasts - Sealing zone - Podosomes - Bone remodeling - Super-resolution microscopy

2.2. Introduction

Osteoclasts are giant multinucleated cells of the hematopoietic lineage, specialized in the degradation of bone matrix. To do so, they pump protons into the resorption lacuna with vacuolar H^+ -ATPase (v-ATPase), thus lowering the local pH and facilitating the solubilization of apatite, the main bone mineral component. This acidic environment is also prone to enhance the digestion of bone organic matrix by the acid cysteine proteinase, cathepsin K, secreted by osteoclasts (Teitelbaum, 2007; Soysa et al., 2016). The efficiency of this process relies on the ability of the cell to create an enclosed resorption compartment, *via* the formation of a unique cytoskeletal structure, the sealing zone (Jurdic et al., 2006).

First described as subcellular entity made of electron dense material and apparently deprived of any organelle, thus resulting in first denomination as the “clear zone”, the sealing zone was then revealed to consist in a dense accumulation of actin filaments forming a circular shape surrounding the resorption lacuna (Zambonin-Zallone et al., 1988; Kanehisa et al., 1990; Teti et al., 1991).

Examination with scanning electron microscopy (SEM) of cells removed of their basal membrane brought to light the peculiar arrangement of actin filaments within this structure, and particularly unveiled the existence of a dense network of podosomes composing this structure (Luxenburg et al., 2007; Akisaka et al., 2015; Akisaka et al., 2019). Accordingly, podosome typical components, such as vinculin, paxillin, talin or cortactin, are localized in the sealing zone (Lakkakorpi et al., 1993; Lakkakorpi et al., 2001; Pfaff et al., 2001; Hurst et al., 2004; Gil-Henn et al., 2007; Chabadel et al., 2007; Saltel et al., 2008; Ory et al., 2008; Ma et al., 2010). In a distinct way compared to single podosomes, vinculin, paxillin and talin were reported to form a “double circle” flanking the sealing zone on either side, while cortactin mainly colocalized with actin (Lakkakorpi et al., 1993; Lakkakorpi et al., 1996; Lakkakorpi et al., 1999; Pfaff et al., 2001; Tehrani et al., 2006). Noteworthy, most of the sealing zone studies were carried out based on observations of osteoclasts on glass substrates instead of bone, due to the lack of optical transparency and high autofluorescence of the mineralized matrix. Yet, it has been suggested that actin structures on bone and on glass differ, mainly in their total width, and the interconnectivity and density of cores within (Luxenburg et al., 2007). Therefore, only structures formed on bone or bone-mimicking materials are called sealing zone, structures on glass being denominated as “sealing zone like” or podosome belts (Saltel et al., 2004; Jurdic et al., 2006).

As a result, only poor knowledge has been collected about the architecture and dynamics of the sealing zone. In particular, how podosome are organized and coordinated to allow efficient bone degradation is therefore still unknown. Hence, it appears paramount to develop higher-resolution microscopy techniques compatible with observation on bone substrates. This could yield valuable information concerning the spatial distribution of major actin-binding proteins within the sealing zone, otherwise only arduously accessible *via* electron microscopy and correlative microscopy (Luxenburg et al., 2007; Geblinger et al., 2009; Akisaka et al., 2015; Akisaka et al., 2016; Akisaka et al., 2019). What is more, observation of the sealing zone internal dynamics would provide substantial hints to decipher how the sealing ability of such a structure is attainable *in vitro*. This exploration would require both a spatial and temporal high-resolution microscopy technique.

In this work, we use cutting-edge super-resolution microscopy methods to reveal the architecture and dynamics of the sealing zone formed by human osteoclasts degrading bone. First, comparison between scanning electron microscopy (SEM) and random illumination microscopy (RIM) acquisitions of sheared-open human osteoclasts confirmed the presence of single actin cores composing the sealing zone. RIM technique also proved to be efficient in deciphering this nanoscale organization in living samples. Hence, cross-correlation analysis of the fluctuation of the sealing zone actin cores could show that podosome cores are synchronized locally. Further analysis of the organization of adhesion components and actin crosslinkers revealed that the sealing zone is composed of groups of α -actinin1 linked podosome cores encircled by adhesion complexes. Therefore, the confinement of the bone degradation machinery is not achieved through the global coordination of all podosomes composing the sealing zone, but at the level of dynamic functional islets of podosome cores.

2.3. Results

2.3.1. Nanoscale organization of actin cores in the sealing zones formed by human osteoclasts

We first investigated the organization of podosomes within the sealing zones of human osteoclasts.

Human osteoclasts derived from blood monocytes were differentiated for 10 days before being plated on bovine bone slices. After 3 days, osteoclasts efficiently degraded bone, as shown by scanning electron microscopy (SEM) observations (Fig. 2.1A). SEM acquisitions of unroofed cells confirmed that the sealing zones formed by human osteoclasts are composed of individual F-actin rich podosome cores (Fig. 2.1B-B'), similarly to what was shown in osteoclasts induced from RAW 264.7 cells or harvested from rabbit long bones (Luxenburg et al., 2007; Akisaka et al., 2019). These podosome cores were nested in a dense network of actin filaments, and appeared connected to their neighbors by filaments running parallel to the substrate (Fig. 2.1B", arrowheads). The morphometric characteristics of the network were assessed by encircling each core and estimating their radius from the selected area. Analysis of 457 cores in 9 different cells yielded an average radius of 114 ± 155 nm (median \pm standard deviation, Fig. 2.1D). Furthermore, applying Delaunay's tessellation to each dataset allowed for the characterization of the average inter-core distances within the same cell. Direct neighbor pairs were 705 ± 886 nm apart (Fig. 2.1E), and first neighbors were 443 ± 617 nm apart (Fig. 2.1F).

F-actin distribution in human osteoclasts unroofed on bone was then observed by a new super-resolution method called random illumination microscopy (RIM). RIM consists in illuminating a sample with a series of random speckles and processing the stack of images using signal processing and statistical tools, to gather a lateral and axial resolution of 100 and 300 nm, respectively. This method benefits from similar resolution as with traditional structured illumination microscopy (SIM), while not requiring any initial calibration step. In addition, its super-resolution capability allows for characterization of events within thick samples, until 30 μ m in unknown optical medium (Mangeat et al., in preparation). Actin staining showed a dense though discontinuous pattern within the sealing zone (Fig. 2.1C,C'", Fig. 2.2). Signal analysis localized local intensity maxima, the geometric features of which were assessed by extracting both the coordinates of the local maxima, and the signal intensity values along 8 directions, evenly distributed from the center. Signal variations were quantified along these eight 1 μ m long segments, and the half-width of the peak in each direction was computed after spatial derivation. The peak radii were computed by averaging the 8 values, and in total 2781 local maxima, divided into 16 cells from 2 donors, were analyzed. The radius distribution yielded an average value of 97 ± 60 nm (Fig. 2.1D). Delaunay's tessellation was applied to the peak coordinates to characterize their spatial arrangement. Direct neighbors were in a 694 ± 867 nm distance range (Fig. 2.1E), with first neighbors being 399 ± 194 nm apart (Fig. 2.1F).

As the distribution of radii and neighbor distances were similar with SEM and RIM, we concluded that RIM efficiently allows for the observation of single actin cores within the sealing zones of human osteoclasts.

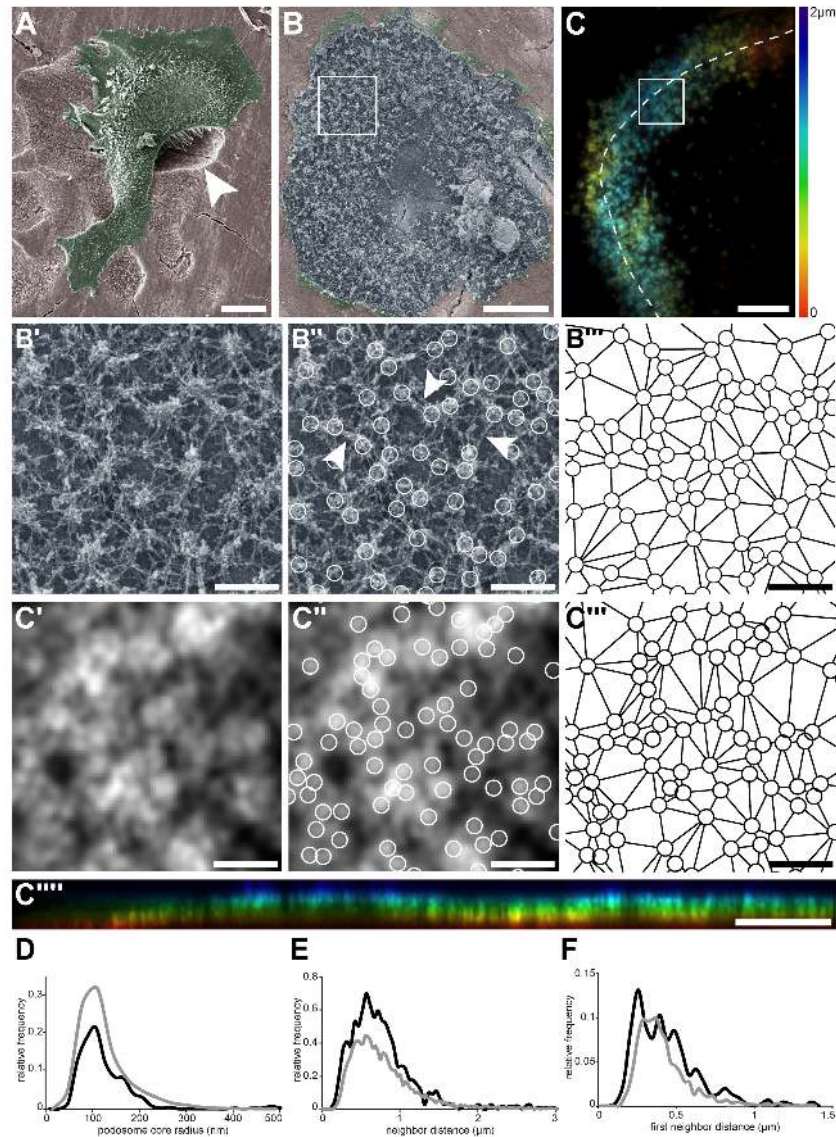


Figure 2.1.: Nanoscale organization of actin cores in the sealing zones formed by human osteoclasts. (A) Pseudo-colored scanning electron micrograph of a human monocyte-derived osteoclast degrading bone. (B) Scanning electron microscopy image of an unroofed osteoclast. (B') Enlarged view of (B). (B'') Localization of actin cores (circles). Arrowheads point to lateral actin filaments linking actin cores together. (B''') Delaunay triangulation from the cores in (B''). (C) RIM image of a sealing zone stained for F-actin. Color codes for height using a rainbow scale. (C') Enlarged view of (C). (C'') Localization of actin cores (circles). (C''') Delaunay triangulation from the cores in (C''). (C''') Orthogonal projection along the line marked in (C). (D) Histogram of the core radii, as measured by SEM (black) and RIM (grey) (457 cores). (E) Histogram of the average distances to direct neighbors measured as Delaunay edges, as measured by SEM (black) and RIM (grey) (2781 cores). (F) Histogram of the average distances to first neighbors, as measured by SEM (black) and RIM (grey) (457 cores for SEM and 2781 cores for RIM). Scale bars: 20 μm (A), 5 μm (B, C, C'''), 1 μm (B', B'', B''', C', C'').

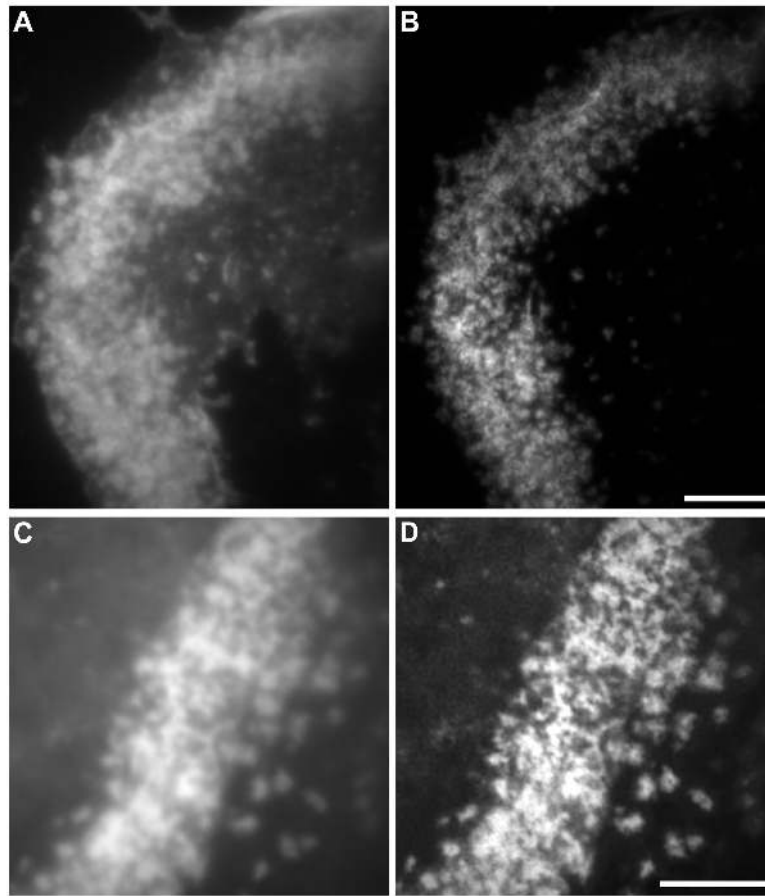


Figure 2.2.: Comparison between epi-fluorescence and RIM super-resolution microscopy. (A) Widefield image of the sealing zone already shown in Fig. 2.1C. (B) RIM image of the sealing zone shown in Fig. 2.1C. (C) Widefield image of the sealing zone already shown in Fig. 2.3B. (D) RIM image of the sealing zone shown in Fig. 2.3B.

2.3.2. Local synchrony of sealing zone actin cores

We then used RIM to image living human osteoclasts degrading bone to address the dynamics of podosome cores within the sealing zone.

Human osteoclasts transduced with GFP-tagged LifeAct lentiviruses and actively degrading bone slices were observed by wide field fluorescence microscopy over 30 min. Subsequent deconvolution of the images and color-coding for time using a rainbow scale revealed that podosome cores appeared stable over at least 30 min (Fig. 2.3A-A”). Furthermore, analysis of kymographs delineating inner parts of seemingly static regions of sealing zones revealed actin intensity oscillations during the entire duration of the acquisitions.

To further characterize this dynamic process, small regions of the sealing zone were observed at a higher spatial and temporal resolution with RIM. Similar to actin staining in fixed cells, single

actin cores within the sealing zone were observable (Fig. 2.3B), and appeared spatially stable over the entire duration of the acquisition. Actin dynamics could be measured and appeared to correlate between podosome neighbors (Fig. 2.3B'). To quantify to what extent podosome actin content varied concomitantly between neighbors, 2840 cores distributed in 10 different cells were localized, and their associated actin intensity signal was extracted for further analysis. Preferential frequencies in the signal-corresponding Fourier spectra were identified for each core, then pooled together. The analysis of their statistic distribution revealed two large peaks, centered around the frequency values 0.01 Hz and 0.15 Hz, corresponding to actin oscillations of 100 s and 7 s periodicity, respectively. The distance between every possible core pair was estimated and their respective signals were compared using Pearson cross-correlation analysis. A high Pearson coefficient corresponded to acute temporal synchrony for the analyzed pair of actin signals. Highest Pearson coefficient values were obtained for cores within a 700 nm radius distance, where they were greater than 0.37 (corresponding to half of the maximum value). They slowly decreased to approximately 0.10 at greater distances (Fig. 2.3C). This result hinted at the existence of a spatial synchrony between neighbors within the sealing zone, comparable to similar observations for podosomes in human macrophages (Proag et al., 2015).

In order to obtain a graphical representation of podosome synchrony, differential films were assembled by subtracting 2 sequential time points, therefore representing local actin intensity gradients. Orange stands for a positive gradient, *i.e.* local polymerization, and blue represents a negative gradient, *i.e.* local depolymerization. Strikingly, polymerization and depolymerization regions appeared as clusters with slowly varying areas, containing a few actin cores (Fig. 2.3D-D'''). Actin polymerization and depolymerization processes thus appeared to be synchronous within restricted groups of core clusters.

2.3.3. Sealing zone podosome cores are organised into islets surrounded by adhesion complexes

Although no partitioning of podosome cores was evident solely on the basis of the actin staining, we then reasoned that, since groups of podosome cores display local synchrony, the sealing zone could show a specific organization of these cores. Spatial distributions of key structural components of the sealing zone, namely cortactin, α -actinin1, filamin A and vinculin, were thus explored by RIM, and we developed a quantitative image workflow to analyze the localization of these proteins with respect to the actin cores.

Protein localizations were evaluated along 1.5 μm long and 100 nm wide lines, in longitudinal and transverse directions relative to the local sealing zone orientation. Then, normalizing the actin core width allowed for the localization of the target proteins with respect to the core domain. Cortactin was localized within the core domain, as had been previously reported, and displayed a wider distribution compared to the average core diameter (Fig. 2.4A,A',A'',E). α -actinin1 mostly colocalized with actin at the close periphery of the core, and appeared less present in the most central part of the core (Fig. 2.4B,B',B'',E). Filamin A was preferentially localized to the cloud domain, with little staining in between cores in the inner part of the sealing zone (Fig. 2.4C,C',C'',E). Vinculin

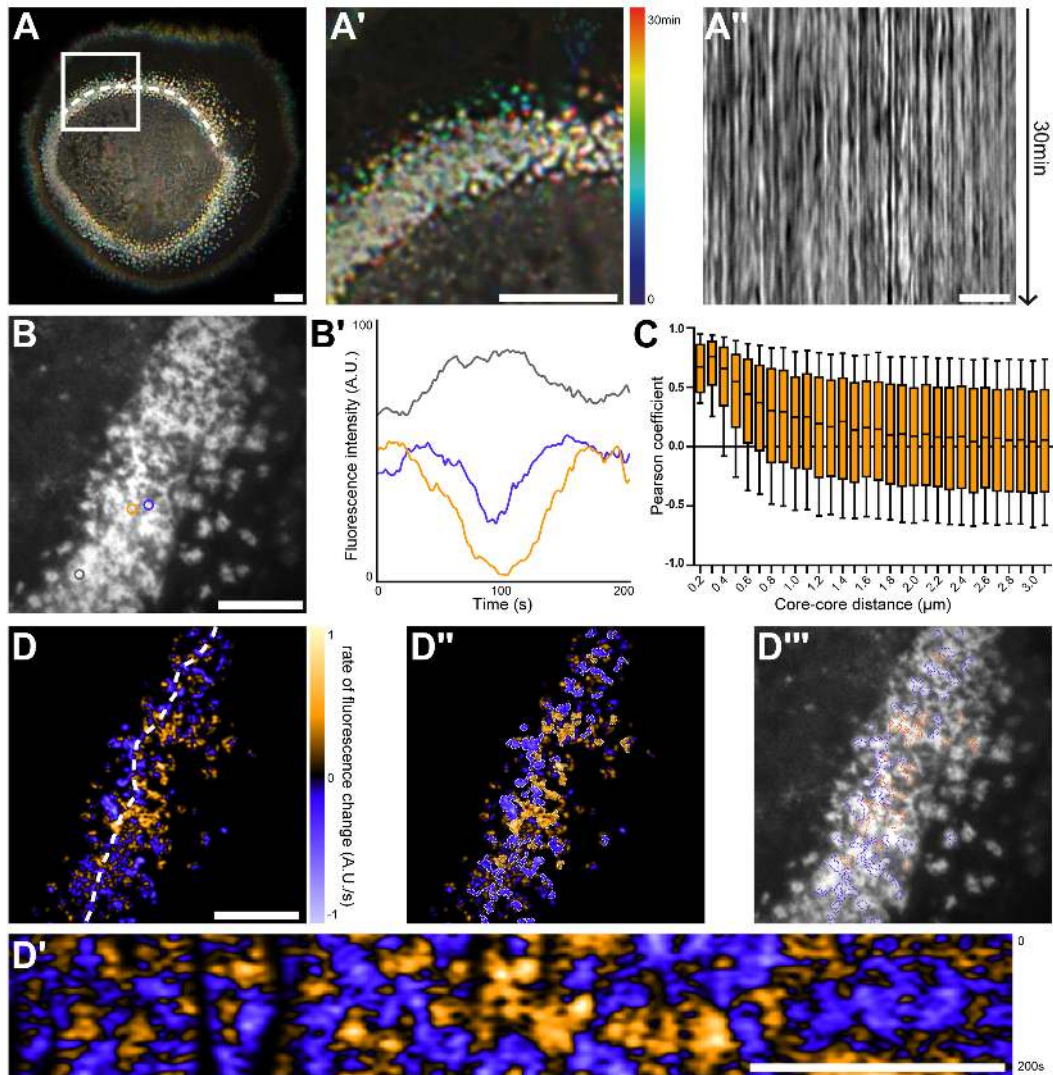


Figure 2.3.: Nanoscale analysis of the dynamics of the sealing zone with RIM technique. (A) Temporal projection of deconvolution images of a sealing zone over 30 min, color-coded for time using a rainbow scale so that the structures that remain at the same spot tend to appear whiter whereas short-lived or mobile podosomes remain colored. (A') Enlarged view of (A). (A'') Kymograph along the line marked in (A). (B) RIM image of a sealing zone stained for F-actin with Lifeact-GFP. (B') Measurements of Lifeact-GFP of podosome cores marked in (B). (C) Pearson coefficients of actin intensity fluctuations of podosome pairs as a function of distance between pairs (2839 cores). (D) Image of the rate of fluorescence change corresponding to the cell shown in (B). (D') Kymograph along the line marked in (D). (D'') Segmentation of the growing and decreasing clusters of actin cores. (D''') Superimposition of the RIM image with the segmented regions of coordinated actin clusters shown in (D''). Scale bars: 10 μm (A), 5 μm (A'-D').

was also localized to the cloud domain, but it was also found surrounding single actin cores (Fig. 2.4D,D',D",E). These observations greatly contrasted with the “double circle” distribution described in earlier works (Lakkakorpi et al., 1993; Lakkakorpi et al., 1996).

In addition, two other colocalization methods were applied to the different proteins to quantify their proximity with actin cores. An object-based method was applied to the segmented images for both actin and co-stained protein, based on the evaluation of Ripley’s K function at various distances from segmented actin cores. Until approximately 200 nm from the core, only α -actinin1- and cortactin-associated curves display a rapid increase of coupling efficiency. Cortactin exhibits higher coupling efficiency values compared to α -actinin1, which is in good agreement with the observation of α -actinin staining surrounding actin cores rather than clear colocalization as with cortactin. From 300 nm from the core and further, filamin A and vinculin curves start increasing towards higher coupling efficiency values. However, filamin A appears to be more prone to interact with actin than vinculin (Fig. 2.4F).

Moreover, taking advantage of the accurate reconstruction of intensity densities of RIM, an intensity-based method allowed for the quantification of the correlation coefficient between actin fluorescence signal and the co-stained protein signal. Pearson coefficient quantifies pixel coincidence, and computes a correlation score of the intensity values in dual-channel images. Actin signal was used as the reference signal for each protein, and a high Pearson score expresses a highest probability of spatial correlation between the two stainings. According to the previous results, cortactin and α -actinin scored the highest values, with Pearson coefficients of 0.93 ± 0.01 and 0.87 ± 0.03 , respectively. Filamin A and vinculin displayed wide distribution of Pearson’s coefficient values, with lesser average values of 0.82 ± 0.1 and 0.68 ± 0.08 , respectively. (Fig. 2.4G).

These statistical analyses confirmed and added to the previous observations of the in-plane distributions for the different target proteins. Cortactin was clearly colocalized with actin cores, displaying a larger range of localization than F-actin. Vinculin and filamin A appeared to be mostly excluded from the core domain, and localized to the cloud domain, which was not restricted to two bands flanking the actin cores. Moreover, vinculin and filamin A appeared to encircle actin core clusters, and might thus be involved in the dynamic segmentation of the sealing zone subunits. α -actinin1 localized nearer to the core than the latter cited proteins, even though it appeared to be less present in the most central part of the core domain compared to cortactin. It has recently been proposed to be part of ring and cap domains, in individual podosomes, hence situated both around podosome cores and at the topmost part of cores (Van den Dries et al., 2019). To address the 3D organization of osteoclast podosomes, a 3D super-resolution method called DONALD was used.

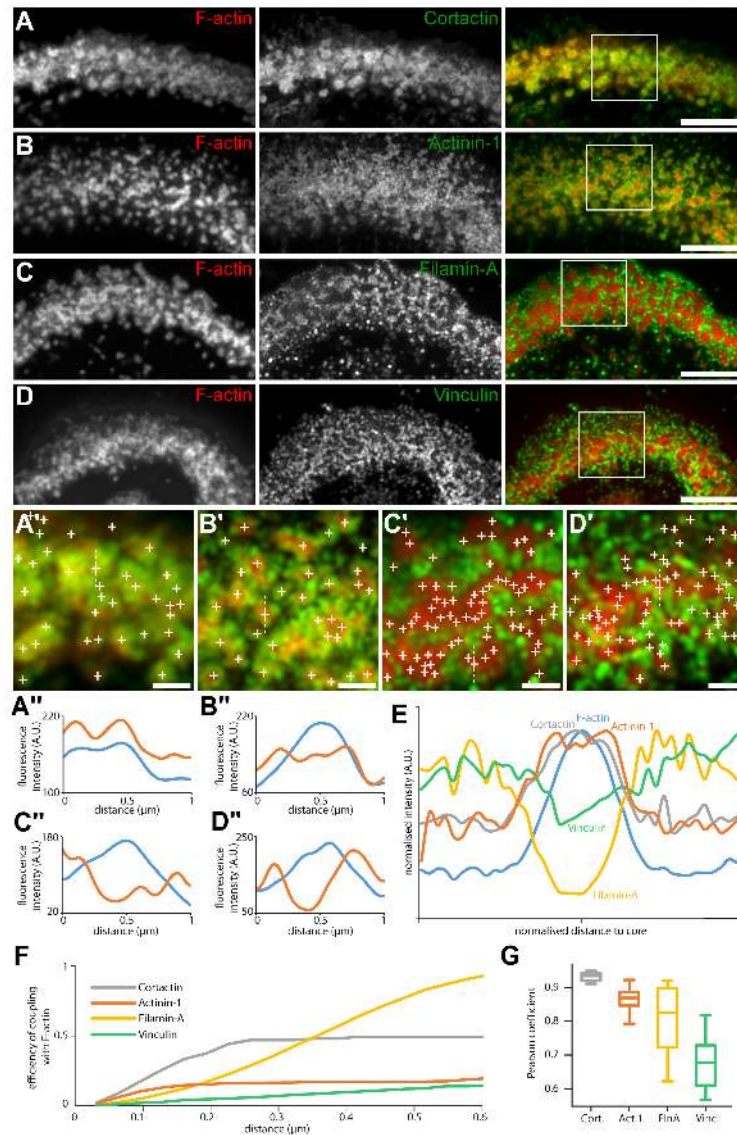


Figure 2.4.: Localization in the sealing zone of cortactin, α -actinin 1, filamin A and vinculin with RIM technique. (A) Representative immunofluorescence images of sealing zones co-stained for F-actin (red) and cortactin (green). (A') Enlarged view of (A). (A'') Intensity profiles along the dotted lines marked in (A'). (B) Representative immunofluorescence images of sealing zones co-stained for F-actin (red) and α -actinin1 (green). (B') Enlarged view of (B). (B'') Intensity profiles along the dotted lines marked in (B'). (C) Representative immunofluorescence images of sealing zones co-stained for F-actin (red) and filamin A (green). (C') Enlarged view of (C). (C'') Intensity profiles along the dotted lines marked in (C'). (D) Representative immunofluorescence images of sealing zones co-stained for F-actin (red) and vinculin (green). (D') Enlarged view of (D). (D'') Intensity profiles along the dotted lines marked in (D'). (E) Normalized intensity profiles of F-actin, cortactin, α -actinin1, filamin A and vinculin (medians of 1080, 239, 265, 277, and 299 cores for each staining, respectively). (F) Efficiency of coupling with F-actin of cortactin, α -actinin1, filamin A and vinculin. The curves result from a colocalization method based on the evaluation of Ripley's K function. (G) Pearson coefficient expressing the spatial correlation of cortactin-, α -actinin1-, filamin A- and vinculin-associated signal intensity with actin signal intensity, respectively. Scale bars: $5 \mu\text{m}$ (A, B, C, D), $1 \mu\text{m}$ (A', B', C', D').

2.3.4. Three-dimensional nanoscale organization of the podosome belt

DONALD is a single molecule localization method combining direct stochastic optical reconstruction microscopy for the in-plane detection of proteins, and SAF analysis to gain access to the absolute axial position of fluorophores relative to the glass coverslip. This nanoscopy technique thus benefits from approximately 15 *nm* localization precision in the three dimensions (3D) (Bourg et al., 2015). Samples were observed with this 3D super-resolution technique combining and the actin-associated fluorescence was acquired in wide field microscopy conditions. The target proteins for this analysis were the same as previously imaged with RIM technique, and in addition stainings of paxillin and the C-terminal of talin (talin-C), the elevation of which was correlated with podosome protrusion forces, were also performed.

Image analysis consisted in localizing the various target proteins with respect to the actin cores composing the podosome belts. Around each core, a vicinity area was determined by a rectangle, 10 μm in length and 500 *nm* in width, the major axis of which either followed the local orientation of the belt, or was perpendicular to it. This yielded in-plane and axial distributions for each protein, as well as preferential axial variations depending on the distance to the actin cores (Fig. 2.5).

F-actin and cortactin displayed similar in-plane distributions, characterized by an accumulation of proteins in the first 250 *nm* surrounding the cores. F-actin mean height appeared to decrease drastically with an increasing distance from the cores, especially towards the center of the cell, where its mean height was only 49 *nm* (Fig. 2.6B"). In contrast, cortactin did not display this trend, but kept at a rather constant height of approximately 164 *nm* (Fig. 2.6D"). α -actinin1 was preferentially localized in the vicinity of the actin cores, up to 500 *nm* in distance. Similarly to cortactin, its height stayed approximately constant throughout the distance profile, at approximately 126 *nm* (Fig. 2.6F").

Vinculin, paxillin, talin and filamin A were mostly absent from the regions of dense actin staining, similar to what had been observed for on bone slices for vinculin and filamin-A. Vinculin and paxillin displayed rather similar in-plane distributions, with peaks on the external side of the podosome belt at 350 *nm* and 510 *nm*, and on the internal side at 570 *nm* and 510 *nm*, respectively (measurements not shown). In contrast, talin and filamin A displayed large ranges of preferential localization, with first peaks situated at 630 *nm* for both proteins on the external side, and at 610 *nm* and 710 *nm* towards the inner part of the cell, respectively. Talin-C and vinculin heights declined by nearly 20 *nm* towards the inner part of the cell (Fig. 2.5E, F). This variation in height hinted at a possible increasing tension of talin towards the actin cores, resembling the recent findings in human macrophage podosomes (Bouissou et al., 2017). In contrast, paxillin and filamin A, which average heights were 45 *nm* and 139 *nm*, respectively, exhibited almost no change in height when away from the belt center (Fig. 2.6H", J").

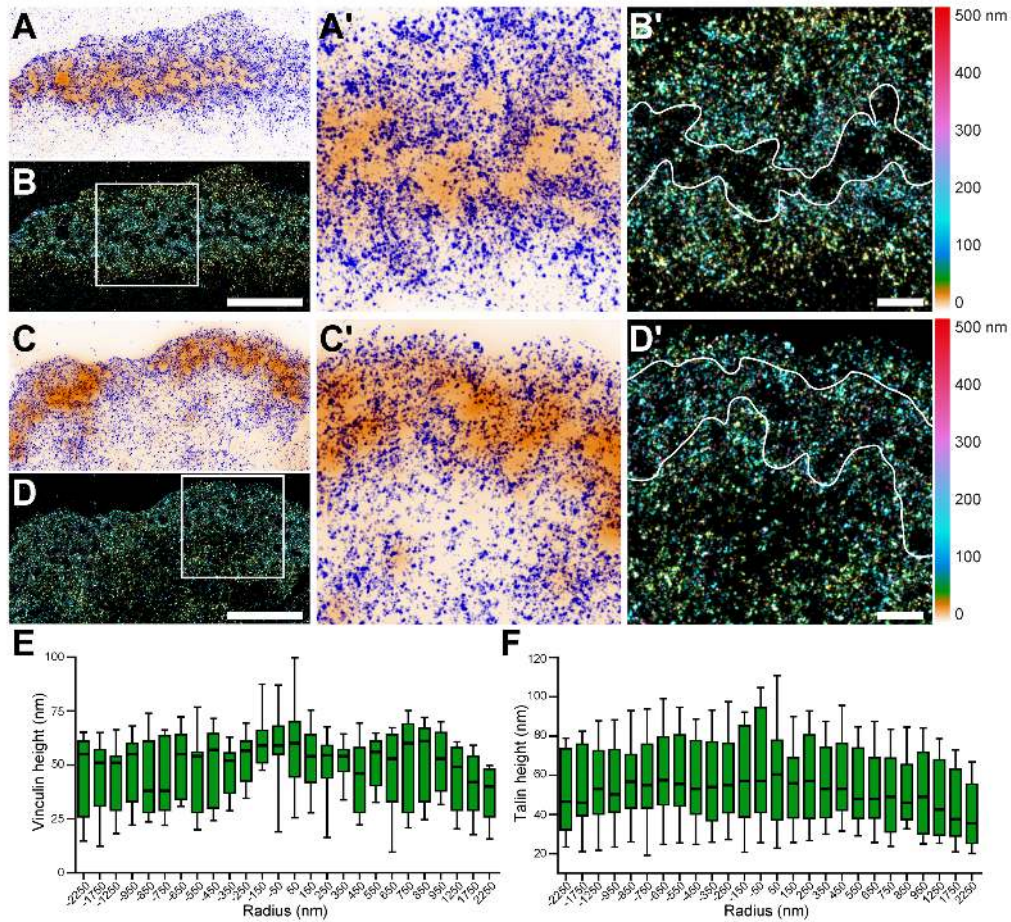


Figure 2.5.: 3D nanoscopy of vinculin and talin-C in the podosome belt of human osteoclasts. (A) Representative dSTORM images of vinculin (purple) merged with the corresponding epifluorescence images of the F-actin cores (ochre). (A') Enlarged view of (A). (B) DONALD images corresponding to (A) where the height is represented in false color (scale shown in (B')). (B') Enlarged view of (B). (C) Representative dSTORM images of talin-C (purple) merged with the corresponding epifluorescence images of the F-actin cores (ochre). (C') Enlarged view of (C). (D) DONALD images corresponding to (A) where the height is represented in false color (scale shown in (D')). (D') Enlarged view of (D). (E-F) Height profiles of the vinculin (E) and talin-C (F) with respect to the distance to the center of the sealing zone. Scale bars: $5 \mu\text{m}$ (B, D), $1 \mu\text{m}$ (B', D').

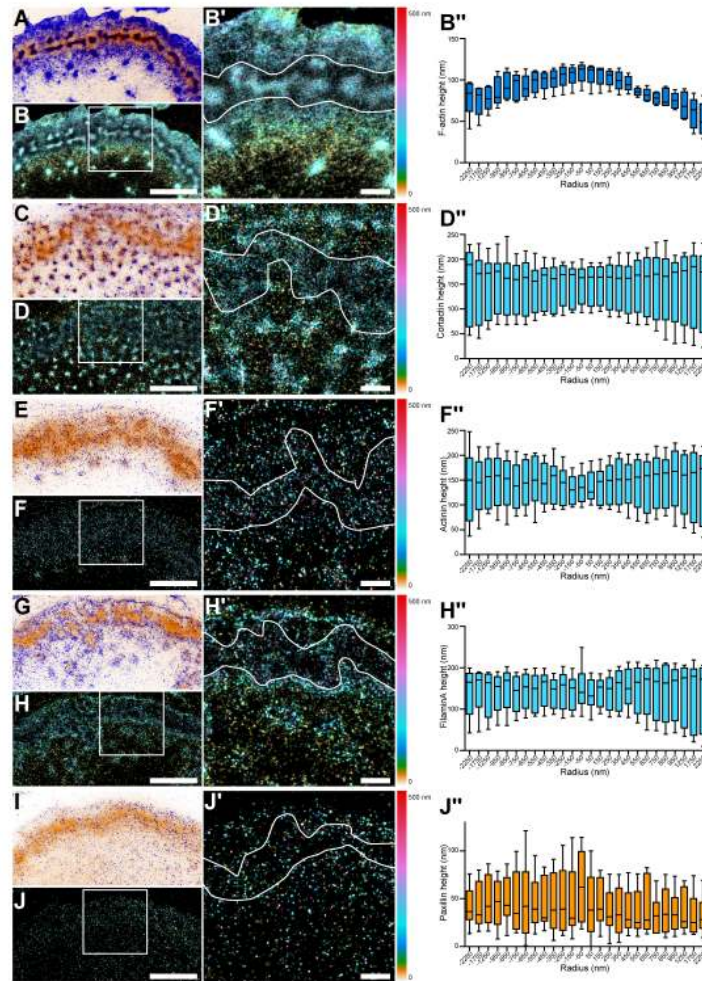


Figure 2.6.: 3D nanoscopy of F-actin, cortactin, α -actinin1, filamin A and paxillin in the podosome belt of human osteoclasts. (A) Representative dSTORM images of F-actin (purple) merged with the corresponding epifluorescence images of the F-actin cores (ochre). (B) DONALD images corresponding to (A) where the height is represented in false color (scale shown in (B')). (B') Enlarged view of (B). (B'') Height profiles of F-actin with respect to the distance to the center of the sealing zone. (C) Representative dSTORM images of cortactin (purple) merged with the corresponding epifluorescence images of the F-actin cores (ochre). (D) DONALD images corresponding to (A) where the height is represented in false color (scale shown in (D')). (D') Enlarged view of (D). (D'') Height profiles of cortactin with respect to the distance to the center of the sealing zone. (E) Representative dSTORM images of α -actinin1 (purple) merged with the corresponding epifluorescence images of the F-actin cores (ochre). (F) DONALD images corresponding to (A) where the height is represented in false color (scale shown in (F')). (F') Enlarged view of (F). (F'') Height profiles of α -actinin1 with respect to the distance to the center of the sealing zone. (G) Representative dSTORM images of filamin A (purple) merged with the corresponding epifluorescence images of the F-actin cores (ochre). (H) DONALD images corresponding to (A) where the height is represented in false color (scale shown in (H)). (H') Enlarged view of (H). (H'') Height profiles of filamin A with respect to the distance to the center of the sealing zone. (I) Representative dSTORM images of paxillin (purple) merged with the corresponding epifluorescence images of the F-actin cores (ochre). (J) DONALD images corresponding to (A) where the height is represented in false color (scale shown in (J')). (J') Enlarged view of (J). (J'') Height profiles of paxillin with respect to the distance to the center of the sealing zone. Scale bars: $5 \mu\text{m}$ (B, D, F, H, J), $1 \mu\text{m}$ (B', D', F', H', J').

2.4. Discussion

The different results presented in this study allow for a more precise and detailed insight into the inner organization of the sealing zone. We showed that actin cores were present within the sealing zone of human osteoclasts, and their morphometric analysis both with SEM and RIM revealed that the small subunits were within the submicron range from their direct neighbors. With time-lapse imaging, we characterized the long-term spatial stability of actin cores during active resorption of bone. Moreover, short-term signal correlation analysis yielded a synchronous behavior for cores within nearly a micron range. Synchronous neighbors were apparently grouped within clusters of various sizes, which seemed to correspond to islets surrounded by adhesion complexes formed by vinculin and filamin A. Eventually, the 3D localization of major actin crosslinkers hinted at the possible existence of tension within the actin cloud of the sealing zone. Overall these results allow for a new model of the internal architecture and dynamics of the sealing zone (Fig. 2.7, Fig. A.4 and Fig. A.5).

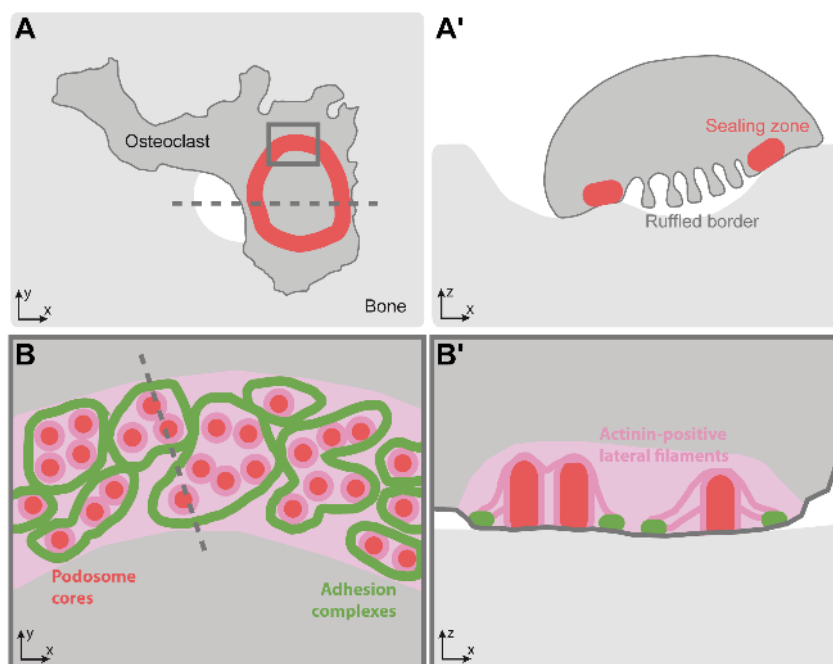


Figure 2.7.: Model of the organization of the sealing zone into islets. (A-A') Osteoclast form an actin rich superstructure called the sealing zone to confine bone degradation. (B-B') Zooming inside the sealing zone reveals the organization into islets of coordinated podosome cores. (A'-B') Representation of orthogonal out-of-plane cross-sections along the dashed line for the (A-B) schematics, respectively.

SEM observations of unroofed human osteoclasts revealed similar actin filament organization within the sealing zone as previous ultrastructural studies on RAW 264.7 cells or rabbit osteoclasts.

Single actin cores were clearly identified, surrounded by radial filaments oriented toward the ventral membrane, and interconnected *via* actin cables roughly parallel to the membrane (Luxenburg et al., 2007; Akisaka et al., 2016; Akisaka et al., 2019). The geometric characteristics of this complex network were assessed to yield the mean core size, and the inter-core distance distribution. It was found that actin cores were approximately 200 nm in diameter, which coincides with the results from previous studies (Luxenburg et al., 2007; Anderegg et al., 2011; Akisaka et al., 2019). However, the mean inter-core distances were larger than that proposed in previous studies: 210 ± 50 nm on bone and 442 ± 126 nm on vitronectin (Luxenburg et al., 2007; Anderegg et al., 2011). Indeed, Delaunay’s tessellation results led to a mean distance between neighbors of 705 nm, and decreased to 443 nm when considering only the first neighbor. This discrepancy might be due to the difference in cell models, as previous results were extracted from observations in RAW 264.7 macrophage cell line, induced to differentiate into osteoclasts, and not in primary osteoclasts.

This study proposed for the first time to visualize the submicron sealing zone organization with a super-resolved microscopy technique compatible with imaging cells on bone. The RIM technique has been characterized in various complex and dynamic biological contexts, such as mitosis, 3D cell migration and cell differentiation in thick tissues. This approach takes advantage of random punctate excitation patterns to gain access to object information otherwise inaccessible with widefield microscopy. A dedicated reconstruction scheme has been developed accordingly, which allows for a higher rendering of the dynamic range of the fluorescence density. Hence, processed images are less prone to reconstruction artefacts, and display a spatial resolution of approximately 100 nm. Furthermore, compared to STED, it requires much lesser laser power to achieve the same range of resolution, which further makes it a powerful tool to acquire time-lapse movies over long periods of time. With this novel technique, single actin cores within the sealing zone of human osteoclasts were localized for the first time *via* fluorescence staining. This allowed for their geometric characterization following the same algorithm as for SEM observations. This comparison between the two imaging methods resulted in similar data: 194 nm for the mean diameter of cores, 694 nm and 399 nm as inter-core distances considering all neighbors or only the first neighbor, respectively. This successful comparison confirmed the efficiency of the RIM technique as a tool to decipher the nanoscale organization of the sealing zone.

As RIM also benefits from low toxicity and high temporal resolution, it was applied to image actin dynamics within the sealing zone of resorbing human osteoclasts on bone. Preliminary deconvoluted movies had revealed the apparent spatial stability of actin cores for long time periods. Hence, the local oscillations associated with actin remodeling within the cores were characterized for the first time. Actin signal processing yielded a time periodicity for these oscillations of approximately 100 seconds. Furthermore, cross-correlation analysis between signals associated with two cores in the same cell brought to light the existence of a, partial, spatial synchrony between neighbors up to an approximate 2 μ m distance scale. This distance coincides with the mean neighbor-to-neighbor distance computed based on SEM and RIM observations. Therefore, this interesting finding might hint at a functional role for the interconnecting actin cables, as has been previously suggested from similar observations in human macrophage podosomes (Labernadie et al., 2014; Proag et al., 2015).

It would thus be most interesting to explore the effects of drugs interfering with actin polymerization on both the periodicity and the spatial synchrony properties of the sealing zone. To investigate the role of the interconnected actin cables, actin core dynamics could be characterized after inhibition of myosin II activity with blebbistatin. Indeed, its inhibition in human macrophages induced a decrease in protrusion forces associated with actin oscillatory behavior in individual podosomes (Labernadie et al., 2014).

As the deconvoluted videos showed, actin cores acted as stable actin remodeling foci for nearly 30 minutes. This observation hinted at the preservation of a stable core network throughout the resorption process. Consequently, time-lapse acquisitions with the RIM technique over long periods of time might help in assessing whether the spatial synchrony is a transient event or if it is maintained for several minutes. What is more, evaluation of the actin flux within the sealing zone revealed that clusters of a few cores seemed to share the same actin polymerization/depolymerization rates within well-delimited areas. Simultaneous visualization of the localization of an adhesion plaque protein would greatly help in understanding the internal organization of the sealing zone. Notably, paxillin has been shown to display an oscillatory behavior in the ring domain surrounding human macrophage podosomes, and its variations correlated with actin intensity oscillations (Proag et al., 2016).

The in-plane localization of vinculin, paxillin, talin, cortactin, filamin A and α -actinin1 was assessed thanks to RIM technique in sealing zones of unroofed human osteoclasts plated on bone slices. In contrast to previous observations, vinculin, paxillin, talin and filamin A were not distributed in a double band domain flanking either side of the sealing zone (Lakkakorpi et al., 1993; Babb et al., 1997; Pfaff et al., 2001; Lakkakorpi et al., 2001; Gil-Henn et al., 2007). The high-resolution imaging rather revealed that the four proteins were present within the superstructure, where they appeared to encircle clusters composed of a few actin cores. In contrast, α -actinin1 was mostly located in a small ring around single actin cores, which might explain its ambiguous localization in previous studies (Babb et al., 1997; Pfaff et al., 2001; McMichael et al., 2008). According to anterior observation, cortactin greatly colocalized with actin cores in the sealing zone (Ochoa et al., 2000; Pfaff et al., 2001; Tehrani et al., 2006; Chabadel et al., 2007; Ma et al., 2010). Interestingly, cortactin distribution was seemingly found wider than the typical core diameter. This could be explained *via* its close association with the Arp2/3 complex, which has recently been located along filaments in the vicinity of actin cores by high-resolution SEM imaging (Akisaka et al., 2019). To further the presently reported results, it would be most beneficial to combine high-resolution RIM observations with SEM acquisitions to be able to precisely place proteins relative to the three different actin filament populations. This would consist in an efficient approach to decipher the 3D localization of proteins in the sealing zone.

Precisely, the 3D distribution of the same proteins was carried out in the podosome belts of human osteoclasts on glass. Acquisitions were performed with the DONALD imaging technique, which combines dSTORM and SAF analysis for the efficient 3D detection of single fluorophores with a precision of 15 nm (Bourg et al., 2015). This 3D nanoscopy technique has recently been applied in the context of human macrophage podosomes. It allowed for the identification of a close relationship between paxillin, vinculin and talin, and its requirement for efficient protrusion force

generation (Bouissou et al., 2017). Likewise, vinculin, paxillin and talin-C were localized in the close vicinity of the ventral membrane of osteoclasts. Moreover, vinculin and talin-C also appeared to rise when situated closer to the actin cores. This interesting finding could be the first insight into the identification of possible tension within the podosome belt. In contrast, cortactin, filamin A and α -actinin1 were located preferentially to the topmost part of the podosome belt. For cortactin, this result is contradictory to what had been previously observed with confocal z-scanning in previous studies (Pfaff et al., 2001; Hurst et al., 2004). Moreover, α -actinin1 has recently been proposed as one of the component of the cap domain in podosomes (Van den Dries et al., 2019). Hence, it could also be the case in the context of podosome belts. To try and ascertain this hypothesis, valuable information could be extracted from applying the novel version of the DONALD module. This improved version combines SAF analysis and point-spread function engineering to allow for precise axial localization over a greater depth range in samples (Cabriel et al., 2019).

This study consists in the first extensive and quantitative study of the nanoscale organization and dynamics of the sealing zone in human osteoclasts. It provided the geometric characterization of the actin core network within this functional superstructure. It also allowed identification of dynamic processes related to actin cores during active bone resorption. Eventually, it proposed precise localization of six major actin-binding proteins associated with the sealing zone: vinculin, paxillin, talin, cortactin, filamin A and α -actinin1. Their colocalization with actin was studied in the context of the sealing zone, while their 3D distribution was quantified in podosome belts. Furthermore, it aimed at paving the way for future studies to decipher both the ultrastructural and dynamic properties of osteoclasts.

2.5. Materials and methods

2.5.1. Differentiation and culture of primary monocyte-derived osteoclasts

Human monocytes were isolated from blood of healthy donors as previously described (Van Goethem et al., 2010). Cells were re-suspended in cold PBS supplemented with 2 mM EDTA, 0.5% heat-inactivated foetal calf serum (FCS) at pH 7.4 and magnetically sorted with using magnetic microbeads coated with antibodies directed against CD14 (Miltenyi Biotec). Monocytes were then seeded on plastic at 2×10^6 cells/well in six-well plates in RPMI 1640 (Invitrogen) without FCS. After 2 h at 37°C in humidified 5% CO₂ atmosphere, the medium was replaced by RPMI containing 10% FCS, 100 ng/mL of macrophage colony-stimulating factor (M-CSF, Peprotech) and 60 ng/mL of human receptor activator of NF- κ B-ligand (RANK-L, Miltenyi Biotec). The medium was then changed every third day by RPMI containing 10% FCS, 100 ng/mL of RANK-L and 25 ng/mL of M-CSF. For experiments, cells were harvested at day 10 using Accutase solution (Sigma-Aldrich) and centrifugation (1100 rpm, 10 min), and were then plated either on clean 1.5H precision glass coverslips (Marienfeld 0117640) or on bovine bone slices (Immuno Diagnostic Systems DT-1BON1000-96). Cells were left to adhere in cytokine-supplemented medium for 3 days before fixation.

2.5.2. Cleaning of precision glass coverslips

Before letting cells adhere on them, 1.5H precision glass coverslips (Marienfeld) were cleaned as follows: they were placed on staining racks (Thermo Scientific 12627706) and immersed in a RBS 35 solution (Carl Roth 9238, 1/500 diluted in milliQ water) heated up to 80°C while stirred with a magnetic bar. After 15 min, coverslips were rinsed three times with milliQ water and patted dry. They were put in a dry oven set at 175°C for 120 min to sterilize. These clean coverslips were used within two weeks after RBS treatment.

2.5.3. Primary antibodies

The following antibodies were used: goat anti-talin C-20 (Santa Cruz sc-7534, IF 1/50), mouse anti-vinculin clone hvin-1 (Sigma-Aldrich V9131, IF 1/50), mouse anti-paxillin (BD Biosciences 61005, IF 1/50), mouse anti-cortactin clone 4F11 (p80/85) (Sigma-Aldrich 05-180, IF 1/50), mouse anti-filamin A clone PM6/317 (Sigma-Aldrich MAB1678, IF 1/50), and mouse anti- α -actinin1 clone BM-75.2 (Sigma-Aldrich A5044, IF 1/50).

2.5.4. Immunofluorescence

Osteoclasts plated on glass coverslips and bone slices for 3 days were fixed for 10 min in a 3.7% (wt/vol) paraformaldehyde (Sigma Aldrich 158127) solution containing 0.25% glutaraldehyde (Electron Microscopy Sciences 16220) in Phosphate Buffer Saline (PBS) (Fisher Scientific) at room temperature. When indicated, before fixation, cells were mechanically unroofed at 37°C using distilled water containing cOmpleteTM protease inhibitors (Roche) and 10 μ g/mL phalloidin (Sigma-Aldrich P2141) at 37°C: cells were left still in this solution for 10 s, then a flow was created by flushing a dozen times so that cell dorsal membranes were ripped off. After fixation, quenching of free aldehyde groups was performed by treatment with PBS/50 mM ammonium chloride and PBS/1 mg/mL sodium borohydride. Non-unroofed cells were permeabilized for 10 min with PBS/0.3% Triton and all cells were blocked with PBS/1% BSA for 30 min. Samples were incubated with the primary antibodies for 90 min and then during 60 min with fluorescent dye conjugated-phalloidin and secondary antibodies for F-actin and proteins, respectively.

2.5.5. Scanning Electron Microscopy imaging

Osteoclasts plated on bone slices for 3 days were unroofed as described above and fixed for 10 min in a 0.2M sodium cacodylate buffer (pH 7.4) containing 2% paraformaldehyde (Electron Microscopy Sciences 15710) and 2.5% glutaraldehyde (Electron Microscopy Sciences 16220), then washed with distilled water. The samples were then prepared for observation following the protocol: they were dehydrated through a graded series (25–100%) of ethanol, transferred in acetone and subjected to critical point drying with CO₂ in a Leica EM CPD300, then sputter-coated with 3 nm platinum with a Leica EM MED020 evaporator, and were examined and photographed with an FEI Quanta FEG250.

2.5.6. Analysis of SEM images

Actin cores were manually encircled using ImageJ oval selection tool, then the area and its center coordinates of these selected regions were extracted. A dedicated Python script was written to extract statistical information. The inter-core distances were computed using Delaunay tessellation on each image, using SciPy spatial algorithm “Delaunay” in order to create the interconnection matrix, then the distance between each pair of connected vertices was computed and stored in a matrix. In order to avoid plausible errors, the edges of the Delaunay tessellated space were excluded of the distance computations. To identify them, the SciPy spatial algorithm “ConvexHull” was applied to the coordinates, and whenever two points were identified as pertaining to the convex envelope, the distance between them was not computed. Finally, for each vertex the minimum distance to all neighbors was kept for the nearest neighbor analysis.

2.5.7. RIM 2D super-resolution imaging

For live imaging, osteoclasts were transduced with GFP-tagged LifeAct lentivirus 3 days before being harvested and plated on bovine bone slices, and were observed the day after being plated on bone slices. Bone slices were placed on a FluoroDish (WPI FD35-100) with cells facing down and immersed with RPMI without phenol red, supplemented with 10% FCS (Thermo Fisher 32404-014). During observations, samples were maintained at 37°C in humidified 5% CO₂ atmosphere. Images were acquired every 12 ms for a total of 211 seconds (streams) using an inverted microscope (TEi Nikon). A fiber laser combiner with 4 fast diode lasers (Oxxius) with respective wavelengths 405 nm (LBX-405-180-CSB,) 454 nm (LBX-445-100-CSB), 488 nm (LBX-488-200-CSB), and 561 nm (LMX-561L-200-COL) are used to excite fluorophores. A corrected fiber collimator (RGBV Fiber Collimators 60FC Sukhamburg) is used to produce collimated TEM₀₀ 2.2 mm diameter output beam for all wavelengths. The polarization beam is rotated with an angle of 5 degrees before hitting a X4 Beam Expander beam (GBE04-A) and produces 8.8 mm beam TEM₀₀ beam. A fast spatial light phase binary modulator (QXGA fourth dimensions) is conjugated to the image plane to make speckle random illumination. The objective lens used in experiments is a 100x magnification with 1.49 numerical aperture (CFI SR APO 100XH ON 1.49 DT 0;12 NIKON). A band pass filter was used for Green Fluorescence Protein (GFP) emission (Semrock FF01-514/30-25). A motorized high speed wheel filter is used to sequentially turn the two band pass filters in 30 ms after each 200 speckle frames. A piezoelectric Z stage (Z INZERT PIEZOCONCEPT) is used for fast z stack acquisition. For triggering, the camera sCMOS is used as master, and a rolling shutter output is used to trigger binary phase sequence to the SLM. The SLM output triggers the laser when binary phase mask is stable. A script from micromanager software was written to select the number of speckles used, the temporal resolution for each frame, the depth of z stack, the step of each z stack and the number of colors used for the acquisition. For stream recording, speckle frames were acquired continuously over the whole duration of the movie. Widefield time-lapse acquisitions were also carried out with the same microscope, but using a 60x objective (CFI PLAN APO LBDA 60XH 1.4/0.13 NIKON). Images were captured every 2 seconds, and were restored with Huygens Software (classical

maximum likelihood estimation with 30 iterations and theoretical PSF).

For imaging of fixed samples, osteoclasts were unroofed and fixed as described above and stained for vinculin, cortactin, filamin A, or α -actinin1 with the corresponding primary antibody and an Alexa Fluor 488-coupled secondary antibody (Cell Signaling Technology 4408, 1/500) or an Alexa Fluor 546-coupled secondary antibody (Molecular Probes A11056, 1/500). Actin cores were labelled with Texas Red-phalloidin (Molecular Probes T7471, 1/200) or Alexa Fluor 488-phalloidin (Molecular Probes A12379, 1/200) respectively. Bone slices were placed in a FluoroDish, upside down on a droplet of Vectashield mounting medium (Vector Laboratories H-1000). Samples were excited with 488 *nm* and 561 *nm* laser diodes with the same setup as for time-lapse imaging. 200 speckle images for each channel were acquired sequentially to yield z stacks of various depths.

2.5.8. Analysis of RIM images of fixed samples

Reconstruction of raw images was carried out as described in Mangeat et al., in preparation. Briefly, the method is based on decreasing the computational cost of the inversion method described in Idier et al., 2017. This new method uses a variance matching process, instead of the marginal minimization methods based on the full covariance matrix of the data (Mangeat et al., in preparation). The only input for the super-resolution reconstruction process is the knowledge of spatial statistics of speckle patterns limited by the OTF of the imaging system (Fourier transform of the PSF). Contrary to SIM, the exact knowledge of the illumination function is not necessary, and the protocol of the reconstruction is therefore drastically reduced. The inversion code is implemented on Matlab. The input are the excitation and collection PSF, generated with Gibson and Lanny 3D optical model implemented in the plugin PSF generator (Kirshner et al., 2013). The PSF dimension is equal to the final size reconstruction with a pixel size equal to 32.25 *nm* for 100x magnification. The position of the fluorophores is defined from the cover slide in each sample. The number of iterations during the variance matching process is defined by the user, mainly depending on the signal to noise ratio of the raw data.

Drift correction was performed on z-stacks with ImageJ plugin Linear Stack Alignment with SIFT. To create images on which to perform further analyses, 3 to 5 z slices per acquisition stack were selected on their sharpness, depending on the quality of the original signal, and summed with ImageJ Z Project tool.

In order to characterize the actin network, actin cores were detected as local maxima using ImageJ Find Maxima tool with the threshold set as half of background intensity. The coordinates of these maxima were weighted considering all pixel intensity in a 200 *nm* radius, and exported in a text file. These points were positioned both on RIM reconstructed image and on its spatial derivative version created thanks to ImageJ Find Edges tool. From these locations, 8 radius profile were traced with length 1000 *nm* and width 100 *nm* on both images, and intensity values along this line were extracted and stored in a text file. A dedicated Python script was then written to extract statistical data. Core radii were computed by detecting the first intensity maximum along the Find Edges profile. Inter-core distances were computed thanks to weighted coordinates following the same Delaunay

algorithm already described in the SEM analysis section (see Fig. A.1).

For the analysis of two-color acquisitions, actin cores were detected following the same procedure as described for the analysis of the actin network. Then, both signals were extracted along $1.5 \mu m$ long and $100 nm$ wide lines drawn so that each core coordinates were placed at the middle of the line, and its orientation either followed the local curvature of the sealing zone, or was transverse. This process was repeated on the reconstructed actin image, the actin image after spatial derivation with ImageJ Find Edges tool and the protein image. All data were extracted and stored in a text file to be read by a dedicated Python script. This script computed the median core size for all data thanks to Find Edges signals, in order to establish a normalized profile length. Then, both actin- and protein-associated signals were interpolated along this new axis to yield comparable intensity profiles. Median profiles were eventually computed (see Fig. A.2).

Colocalization studies were carried out with two different methods, either intensity- or object-based. The first method is a pixel-based method, where a correlation coefficient, here Pearson coefficient, is computed by comparing the two channel-associated spatial signal. The expression of the Pearson coefficient is $R = \frac{\bar{I}_1\bar{I}_2 - \bar{I}_1\bar{I}_2}{\sigma(I_1)\sigma(I_2)}$ where the bar stands for the mean and $\sigma(I_{1/2})$ is the standard deviation of pixel intensities for each channel. Conceptually, Pearson coefficient measures the part of the measured variations in one channel that can be explained by variations in the other channel, and it ranges between -1 and 1. The extreme values -1 and 1 indicate respectively perfect anti-correlation and correlation, whereas $R = 0$ means that channels are not correlated. It is a very popular method if the estimation of the fluorescence intensity after restauration is rigorous. Furthermore, Pearson cross-correlation does not require any decision rule.

For the statistical object-based method, the objects were first segmented with a wavelet adaptive threshold and were then represented as points through coordinates of their mass center in the delimited region of interest (Olivo-Marin, 2002). The test statistic chosen to analyze the relations between the spatial distributions of the two populations was Ripley's K function. The evaluation of Ripley's K function values for various distance parameter values allowed for computing the coupling efficiency between the two channel-associated populations. The coupling efficiency combines the probability that a (green) object located at position x is coupled with a (red) object located at y and the number of coupled objects in each population. Its mathematical formalism is defined in the work of Lagache and coworkers (Lagache et al., 2018).

2.5.9. Analysis of RIM live acquisitions

Reconstruction of raw images was carried out as described previously. To combine robust statistical estimation of object and temporal resolution, an interleaved reconstruction method has been made as previously proposed for SIM (Ma et al., 2018). 800 speckles were grouped to reconstruct one time slice, and the time step between two images corresponds to 200 speckles. Drift correction was performed on stacks with ImageJ plugin Linear Stack Alignment with SIFT, with the same parameters as for fixed samples. Actin intensity levels were normalized throughout the stack by using ImageJ Bleach Correction tool, with the correction method set to histogram matching.

To detect the single actin cores, all the time slices were summed with ImageJ Z project tool and the coordinates were extracted according to the same procedure as for fixed samples. The dynamic characteristics of actin were assessed by extracting the time-dependent signals in a circular selection or radius 100 *nm* around each core, and storing them in a text file. A dedicated Python script was developed to compute the distance between all core pairs in the same cell from, the Fourier spectrum associated with each signal and the Pearson cross-correlation between two signals in the same cell. Natural frequencies were identified as the frequencies associated with Fourier coefficients greater than a threshold value proportional to the median value for Fourier coefficients over the spectrum. Pearson coefficients were eventually sorted according to the distance between the core pair coordinates.

2.5.10. DONALD 3D super-resolution imaging

Osteoclasts plated on glass coverslips of accurate thickness ($0.170 \text{ mm} \pm 0.005 \text{ mm}$, Marienfeld 0117640) were unroofed and fixed as described above. Vinculin, paxillin, talin, cortactin, filamin A or α -actinin1 were stained with the corresponding primary antibody and an Alexa Fluor 647-coupled secondary antibody (Molecular Probes A21237, 1/1000) for dSTORM and podosome cores were labelled with Alexa Fluor 488-phalloidin (Molecular Probes A12379, 1/500) for epifluorescence. dSTORM imaging of F-actin was performed on samples stained in situ by diluting Alexa Fluor 647-coupled phalloidin (Molecular Probes, A22287, 1/100) directly in the microscopy buffer (Smart-kit buffer, Abbelight, France). All dSTORM experiments were performed with the Smart-kit buffer (Abbelight, France).

3D super-localization images were acquired using an inverted IX83 microscope (Olympus) combined with SAFe module (Abbelight, France), and a TIRF module (Abbelight, France). Samples were excited with 405 *nm* (200mW, ERROL Laser), 488 *nm* (150 mW, ERROL Laser), and 640 *nm* (400mW, ERROL Laser) lasers in a HILO illumination (Highly Inclined and Laminated Optical sheet), and controlled *via* NEO Software (Abbelight, France). GFP / Alexa 532 / mCherry / Alexa 647 fluorescence filters (Semrock, LF-405/488/532/635-B-OFF) were used, and the objective was a 100x/1.49 N.A oil immersion objective (Olympus). All images were acquired using a sCMOS ORCA FLASH4.0 v3 (100 fps, cable camera link, Hamamatsu) camera, split on two regions of 300x300 pixels area and positioned on the focal plane of the SAFe module (2.7x magnification, optical pixel size of 108 *nm*). The two imaging paths are calibrated in terms of transmission efficiency to define a permanent correction factor that compensates the imperfect beam splitter. Images were collected once the density of fluorescent dye was sufficient (typically, under 1 molecule. μm^{-2}). About 5000 frames were recorded to compute one image of protein, and 500000 frames were acquired to obtain one image of actin. For all recorded images, the integration time was set to 50 ms and the EMCCD gain to 150. Laser power was adapted depending on the fluorophore density.

2.5.11. Analysis of DONALD 3D super-resolution images

The super-localization of molecules and drift correction were performed on raw images via NEO Software (Abbelight, France) to achieve a final pixel size of 15 *nm*. Images were grouped in batches accounting for 5% of the total frames, and were submitted to drift correction by comparison batch per batch and according to a sliding window. Eventually, z correction was performed thanks to a dedicated Python script, to account for the calibration value of the SAFe module.

The spatial organization of proteins within the sealing zone like was characterized following an adapted version of the algorithm described previously (Bouissou et al., 2017). Briefly, actin cores in-plane coordinates (x_{core}, y_{core}) were determined from actin epifluorescence images from the 488 *nm* channel after Gaussian-filtering. The angle between the podosome belt portion and the horizontal was measured by the user. Then, centered on each core, a rectangle bounding box of length 10 μm and width 200 *nm* was drawn and the 3D coordinates (x_i, y_i, z_i) of the molecules inside this box were converted to a local r-z space (r_i, z_i). This operation was repeated twice for each core: once along the structure direction, and once in the transversal direction. This analysis was performed for all cores of a given cell.

To further the analysis of the spatial organization of molecules within the podosome belt, a dedicated Python script was written to extract statistical information. Each cross-section direction for each cell was treated independently, except for distributions along r-axis and along z-axis for which all molecules detected for all cells were considered. Points were sorted in classes of varying lengths, depending on their distance to the corresponding actin core and whether they were located towards the exterior or the internal part of the cell. For each r-class, median height of the distribution was estimated cell by cell. Also, the symmetry between internal and external distribution of proteins in terms of quantity was assessed by comparing the total amount of molecules on the exterior side to the total amount of points on the interior side, normalized by the total amount of points detected for each cell considered (see Fig. A.3).

2.5.12. Statistical analysis

All box-and-whisker plots show the median, lower and upper quartiles (box) and the 10th and 90th percentiles (whiskers).

Chapter 3.

Developing new substrates for the characterization of podosome mechanical properties and topography sensing with super-resolution microscopy

This chapter describes the methodologies developed in order to design substrates for the characterization of podosome mechanical properties and topography-sensing with super-resolution microscopy. The first section is assembled from the preliminary exploration for designing new substrates to research cell mechanics at the nanoscale, carried out in parallel with the work presented in the previous chapter. The second section has been adapted from the report written by Lucie Albert, an intern supervised during this PhD work, who has focused on designing culture coverslips to assess the topography sensing properties of human macrophage podosomes.

Contents

3.1. Introduction	92
3.1.1. Mechanical sensing of ECM	92
3.1.2. Probing ECM geometric characteristics	94
3.1.3. ECM proteins interactions with associated integrins	94
3.2. Towards the development of a 3D super-resolved traction force microscopy setup	96
3.2.1. Characterization of cell adhesion forces	96
3.2.2. Towards a super-resolved 3D TFM setup	109
3.2.3. Trying to meet the requirements specification point by point	118
3.2.4. Possible improvement strategies	142

3.3. Designing nanoscale 2.5D glass substrates for assessing of macrophage topography sensing	147
3.3.1. Characterization of cell topography sensing	147
3.3.2. Generation of wet-etched glass coverslips to study topography sensing	156
3.3.3. Main results	162
3.3.4. Discussion	169
3.4. Discussion	172

3.1. Introduction

Given the diversity of tissues found in the human body, it is clear that cell-matrix interactions display complex and versatile physical and chemical factors. In particular, the extracellular matrix (ECM) provides numerous specific local cell environments and is involved in multiple functions at the cell and tissue scales (Rozario et al., 2010). It provides:

- a substrate for cell adhesion, affecting physico-chemical cues for fundamental cell processes such as migration, survival, differentiation or morphogenesis;
- a mechanical support facilitating tissue cohesion and barriers between tissue compartments;
- a spatial control of diverse cell functions through confinement of growth factors or other secreted molecules, notably during inflammatory events.

Cell interactions with their environment regulate an extensive number of cellular processes. Within these interplays, cell adhesion mechanisms provide a paramount platform for the perception of ECM physical and chemical parameters (Fig. 3.1).

3.1.1. Mechanical sensing of ECM

The stiffness of the ECM plays an instrumental role in regulating cell proliferation, signaling and differentiation. It has been reported that substrates of different Young's moduli can regulate the differentiation of murine bone marrow-derived endothelial progenitor cells toward a specific endothelial cell phenotype. Specifically, very stiff substrates (10:1 PDMS, Young's modulus value of approximately 2 MPa) upregulated an arterial phenotype, while softer substrates (40:1 PDMS, Young's modulus value of approximately 5 kPa) encouraged a venous phenotype (Xue et al., 2017). Different endothelial subtypes plated on fibronectin or collagen-coated polyacrylamide gels have been shown to proliferate more when placed on a stiffer substrate, and their migration trends were specific to endothelial subtype (Wood et al., 2011).

A pioneering set of experiments conducted on fibroblasts grown on protein-laminated polyacrylamide gels showed that the spreading area, traction force, speed of migration and size and dynamics of focal adhesions are regulated by the mechanical rigidity of the cell substrates (Pelham et al., 1997; Pelham Jr et al., 1998; Pelham Jr et al., 1999). Similar alterations in adhesion size and density according to substrate stiffness have been reported in human macrophages. What is more, delocalization of vinculin from podosomes was observed when the substrate stiffness decreased (Labernadie et al., 2014).

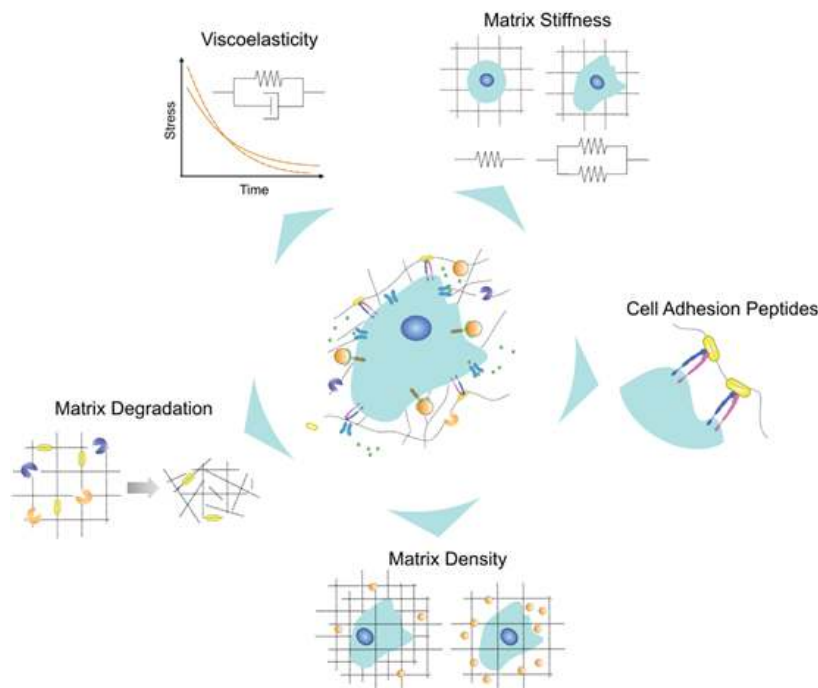


Figure 3.1.: Cell responses to physical cues that are transduced through the mechanical properties, the architecture of fibrous structural proteins and receptor-binding peptides contained within the native ECM. Adapted from Crosby et al., 2019

Recently, it has become evident that studying only the effect of the elastic modulus does not capture the complex mechanical signaling that may be imparted by biomaterials (Zhao, 2014; Goetzke et al., 2018). As cells migrate through a biological matrix, they attach to the ECM *via* various adhesion structures and exert forces on the ECM components. Yet, the apparent matrix stiffness rapidly fluctuates during the remodeling process of the surrounding ECM as these exerted forces are dissipated. This temporal dependence of matrix mechanical properties demonstrates viscoelastic behavior. The impact of matrix viscoelasticity on encapsulated cells is relatively unexplored and has been limited to the study of human mesenchymal stromal cells or murine myoblasts, for now. Furthermore, distinguishing the effect of matrix viscoelasticity from the sole effect of matrix elastic properties on cell behavior is a significant challenge. On the one hand, many synthetic engineered matrices are crosslinked with covalent bonds, which creates materials with nearly pure elastic behavior. On the other hand, if the synthetic materials display viscoelastic properties, they are invariably coupled to the bulk elastic modulus of the material. In contrast, most common ECM-derived proteins currently used in tissue engineering already demonstrate optimized viscoelastic properties (Nam et al., 2016).

3.1.2. Probing ECM geometric characteristics

ECM-mimicking biomaterials primarily consist of an aggregation of fibrous, bioactive polymers. Generally, increasing the polymer concentration or density will enhance the structural integrity of the material. The synthetic fibrils can be assembled in various polymerization states with different crosslinking ratios, eventually yielding a wide range of 3D-microenvironments with specific geometric characteristics. However, these modifications of the 3D cell environment affect cell migration. Indeed, it has been reported that human macrophages use either the amoeboid migration mode in fibrillar collagen I or the mesenchymal migration mode in Matrigel and gelled collagen I, whereas HT1080 tumor cells only perform mesenchymal migration (Van Goethem et al., 2010). Furthermore, macrophages infiltrating matrices of similar composition but with variable elastic modulus adapt their migration mode primarily to the matrix architecture.

When synthetic matrices become denser, their pore size subsequently decreases. However, smaller pore sizes lengthen the diffusion time and limit the penetration depth of growth factors. Experimental and computational studies have further illuminated the details of this mechanism. For example, an application of the Stokes–Einstein and Wilke–Chang relations to a fibrin model of sprouting angiogenesis confirmed that the diffusive transport of pro-angiogenic factors is limited in high ECM density hydrogels (Ghajar et al., 2008; Shamloo et al., 2010; Shamloo et al., 2016).

It is also hypothesized that the existence of an optimal matrix density is closely linked to the alignment of the matrix fibers *i.e.* the anisotropy parameters of the fibrillary organization. As matrix density increases, the fibers are less likely to be randomly arranged *i.e.* shifting towards an isotropic arrangement. The hypothesis that local anisotropic disturbance impacts local branching has been explored in a computational model of sprouting angiogenesis. Upon increase of the matrix density, the bulk fibers became homogeneous and thereby deprived the cells of crucial physical branching cues (Bauer et al., 2009). Hence local topography sensing is essential in stimulating cell functions.

3.1.3. ECM proteins interactions with associated integrins

The ECM is composed of two main classes of macromolecules: proteoglycans (PGs) and fibrous proteins (Järveläinen et al., 2009; Schaefer et al., 2010). The main fibrous ECM proteins are collagens, elastins, fibronectins and laminins (Alberts et al., 2007). Collagen is the most abundant fibrous protein within the interstitial ECM and constitutes up to 30% of the total protein mass of a multicellular animal. Collagens, which constitute the main structural element of the ECM, provide tensile strength, regulate cell adhesion, support chemotaxis and migration, and direct tissue development (Rozario et al., 2010). In addition, it associates with elastin, another major ECM fiber. Elastin fibers provide recoil to tissues that undergo repeated stretch (Wise et al., 2009). A third fibrous protein, fibronectin (FN) is intimately involved in directing the organization of the interstitial ECM and, additionally, has a crucial role in mediating cell attachment and function. Fibronectin can be stretched several times over its resting length by cellular traction forces. Such force-dependent unfolding of fibronectin exposes cryptic integrin-binding sites within the molecule that result in changes

in cellular behavior (Smith et al., 2007).

Integrins are membrane-bound heterodimers that serve as the critical bridge between the ECM and the cytoplasm (Humphries, 2000; Hynes, 2002; Hynes, 2009). As such, integrins are vital for cell-to-matrix and cell-to-cell adhesion. A characteristic feature of most integrin receptors is their ability to bind a wide variety of ligands, which constitute microenvironment major components. Moreover, many ECM and cell surface adhesion proteins bind to multiple integrin receptors. The geometrical organization and concentration of Arg-Gly-Asp peptide (RGD) - a three amino-acid chain derived from fibronectins and laminins - are critical in regulating endothelial cell morphogenesis. Intermediate concentrations of RGD promoted tubulogenesis, while higher concentrations of the peptide inhibited endothelial vascular assembly (Moon et al., 2008). Linear RGDs (targeting $\beta 3$ integrins) immobilized in polyethylene glycol (PEG) hydrogels led to increased EC focal adhesion formation when compared to cyclic RGDs (targeting both $\beta 1$ and $\beta 3$ integrins) (Wacker et al., 2008).

Given the complexity of the extracellular matrix at the physical, architectural and structural levels, recent experimental strategies have focused on trying to decouple the various ECM characteristics in order to identify their specific effects. In this chapter, two independent exploratory projects will be presented, revolving around the common aim at better understanding how cells probe and react to specific physical features of their environment. The first project focuses on the experimental exploration of the possible development of a three-dimensional super-resolved traction force microscopy technique. The second study presents the early results in the designing of 2.5D glass substrates displaying nanoscale crenellations.

3.2. Towards the development of a 3D super-resolved traction force microscopy setup

The following section details the development of a new traction force microscopy (TFM) setup, allowing for the evaluation of three-dimensional nanoscale cellular forces. This technique is based on the absolute localization of single molecules embedded on the surface of a compliant hydrogel, on which cells are free to adhere. Upon adhesion, depending on the cell type being examined, cell traction structures such as focal adhesion or protruding structures like podosomes are formed at the cell basal membrane. The proposed system would thus enable to determine with an unprecedented precision the amplitude and the application point of both tangential and perpendicular forces applied by such adhesion structures.

3.2.1. Characterization of cell adhesion forces

The development of novel techniques to address cell mechanics either at a cell global scale or at a cell local scale allowed a better comprehension of mechanosensing processes. These approaches highlighted the fundamental role of dynamic intracellular stresses in the environment probing mechanisms. In order to characterize the cell tension and force parameters, various techniques have been designed and are now integral to the exploration of mechanosensing-related mechanisms. They are briefly introduced in the following section, with a specific focus on traction force microscopy (TFM), as it has been mainly explored in the subsequently described experiments.

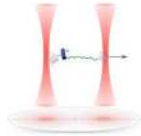
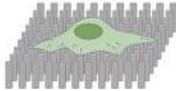
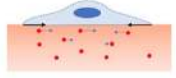
Force quantification techniques can be described and segregated according to numerous criteria. Here, to simplify the analysis, they will be categorized as either "active" or "passive" methods (Fig. 3.2).

Passive methods

Passive methods rely on deformable materials as cell substrates, the strain tensor quantification of which yields force values associated with cell adhesion or migration events.

Traction force microscopy - Traction force microscopy (TFM) is a technique that is based on observing fiducial markers embedded in a hydrogel, and characterizing their displacements. Real-time measurement of the strains associated with the marker movements allows the estimation of the cell forces inducing substrate deformations. The force value assessment is achieved through solving an inverse problem, for which input data gathers both the hydrogel material properties and the marker displacement maps. Among other findings, the repartition of traction forces in a moving cell has been highlighted thanks to this technique, with a specific coupling of traction forces with F-actin dynamics at the migrating front of the cell and at its uropodium. Additionally, it has been shown that acto-myosin complex contraction is more prominent in generating traction forces than actin treadmill process in the context of cell motility (Fournier et al., 2010). Light has also been shed on the direct correlation between focal adhesion size and acto-myosin-mediated traction force values,

Chapter 3. Developing new substrates for the characterization of podosome mechanical properties and topography sensing with super-resolution microscopy

Mode	Technique	Sketch	Typ. force range	Strengths/limitations	References
ACTIVE	AFM	 <p>Adapted from: Liu et al. (2012)</p>	5 pN ÷ 10 nN	<ul style="list-style-type: none"> ✓ Wide force range –well established technique × Direct contact with the specimen otherwise tip must be labeled 	Lam et al., 2011
	TWEEZING OPTICAL	 <p>Adapted from: Hâti et al. (2015)</p>	0.1 ÷ 100 pN	<ul style="list-style-type: none"> ✓ High sensitivity ✓ Wide force range × Heating issues 	Guck et al., 2001; Galbraith et al., 2002; Wang et al., 2005
	MAGNETIC	 <p>Adapted from Poh et al. (2009)</p>	0.01 ÷ 100 pN	<ul style="list-style-type: none"> ✓ High sensitivity ✓ Wide force range × Custom equipment – little standardization 	Wang et al., 1993; Ziemann et al., 1994; Hu et al., 2004
	ACOUSTIC	 <p>Adapted from: Topal et al. (2018)</p>	0.1 ÷ 30 nN	<ul style="list-style-type: none"> ✓ Highly cytocompatible × Fewer force and stress application modalities 	Ding et al., 2013; Guo et al., 2015; Li et al., 2015
PASSIVE	MICRO-ENGINEERED PLATFORMS		10^{-12} ÷ 10^{-8} N	<ul style="list-style-type: none"> ✓ Different designs translate into extremely wide force range ✓ Stability, scalability of manufacturing process ✓ Sophisticated microfabrication procedures/facilities 	Yang and Sait, 2005; Polacheck and Chen, 2016
	TRACTION FORCE MICROSCOPY		2 ÷ 120 nN	<ul style="list-style-type: none"> ✓ Widespread (needs standard lab equipment) ✓ Easily coupled with microscopy equipment (i.e., fluorescence/confocal) ✓ 2D/3D measurements × Computationally demanding × Non-linear behavior of ECM-mimicking hydrogels 	Polacheck and Chen, 2016

For each technique, the force range and a brief description of the main strengths and limitations are reported.

Figure 3.2.: Summary of the most relevant techniques for cell mechanical characterization, and their main technical characteristics. Adapted from Basoli et al., 2018

and that this relation is restricted to the early formation phase of focal contacts (Stricker et al., 2011). In the case of mature focal adhesions, these structures have been shown to generate stresses on their substrate ranging from 200 to 600 Pa, and optimizing force measurement has yielded stress values of approximately 2 to 4 kPa (Stricker et al., 2010). These values are consistent with previous work findings of 5.5 kPa on elastic substrates (Balaban et al., 2001). Podosome rosettes have also been studied with a TFM approach, pointing to a correlation between stress values - ranging from 200 to

600 Pa, similar to focal adhesions - and the substrate material stiffness - ranging from 2 to 6.5 kPa. In this case, substrate deformation is caused by podosome ring centrifugal expansion, and mediated by acto-myosin complex contraction, too (Collin et al., 2008; Hu et al., 2011b).

Deformation of substrate motifs - Techniques to assess the deformation of substrate topography rely on shaping the surface of a deformable material on which cells are seeded. The quantification of the motif strains allows for measuring adhesion-associated stresses and intra-cellular force values at the nanoNewton scale (Tan et al., 2003; Du Roure et al., 2005; Schoen et al., 2010; Le Digabel et al., 2010; Deguchi et al., 2011; Rape et al., 2011). These techniques make use of two main categories of substrate surface shaping: macro-motifs and micro-pillars.

Macro-motifs have been used in combination with TFM method in order to explore the effect of microtubule depolymerization on cell traction forces (Rape et al., 2011). This work has pointed out two signaling pathways involved in microtubule depolymerization - myosin II dependent/FAK independent and myosin II independent/FAK dependent -, which in turn increased cell stress from 0,6 to 2 kPa without changing focal adhesion size. Another use of macro-motifs has complemented the work of Thery and colleagues on cytoskeleton stress repartition *via* micro-contact printing of ECM-protein (Théry et al., 2009). Indeed, using flexible motifs of the same size as ECM-protein motifs allowed for tension analyses and confirmed the preferential localization of focal adhesions in areas of increased intra-cellular tension (Deguchi et al., 2011).

Micro-pillars display the advantage of isolating cell-generated strains more easily than in a TFM experiment, in which the inter-bead distance limits the resolution. Knowing the geometric and mechanical parameters of the shaped posts, it is possible to compute the stress that generated the observed deflection. This approach has allowed for quantification and comparison of traction forces generated by motile or confluent epithelial cells, ranging from approximately 50 pN to 150 nN (Li et al., 2010). This type of setup has also been used to discriminate two force-dependent processes associated with two adhesion structure classes, and coexisting within the same cell. Indeed, it was observed that focal adhesions of size greater than $1 \mu m^2$ apply forces proportional to their size, while adhesions displaying areas lesser than this threshold can generate forces of the same value order as bigger structures (Tan et al., 2003). A subsequent work has reached similar conclusions that two classes of force-supporting adhesions exhibited distinct force-size relationships (Stricker et al., 2011).

Another use of this setup has consisted in generating a sparse distribution of micro-pillars to study real-time deflection of the posts, and thus following the dynamics of cell generated stresses. For instance, the accumulated stress involved in the growing process of multicellular tumor spheroids was assessed *via* placing spheroids at the center of a circle of PDMS pillars and recording their deflections at various stages of growth (Aoun et al., 2014). Pillars can also be made use of in a sparse distribution to quantify and characterize the cell forces in a context of migration through 3D constricting environments (Desvignes et al., 2018).

Active methods

The techniques categorized as active allow for evaluating several physical cell parameters either locally or globally. These methods are based on dynamically probing cells while recording their response.

Optical and magnetic tweezers - Optical or magnetic tweezer and trap experiments assess the force values required in order to induce the oscillation of beads under magnetic or laser influence. Beads can either be localized inside cells or interact on their surface (Conroy, 2008), which leads to quantification of: chemical force interactions between functionalized beads and the associated ligands; local rheology within the cell; cytoskeleton-generated stresses (Puig-De-Morales et al., 2001; Litvinov et al., 2002; Jiang et al., 2003; Balland et al., 2005; Wei et al., 2008; Veigel et al., 2011). Optical and magnetic tweezers are particularly powerful to perform *in silico* dynamic quantification of molecular force interactions (Rio et al., 2009) and of cytoskeleton-associated stresses (Kaya et al., 2010), as they display very high measuring accuracy (Neuman et al., 2008):

- optical tweezers - spatial resolution ranging from 0.1 to 2 *nm* - force domain ranging from 0.1 to 100 pN;
- magnetic tweezers - spatial resolution ranging from 5 to 10 *nm* - force domain ranging from 0.001 to 100 nN.

Additional characterization with optical tweezers and molecular biology techniques by Galbraith and coworkers identified the integrin-cytoskeleton adhesion protein talin as a sensor of force exerted at integrin-ECM binding sites, recruiting vinculin for subsequent focal adhesion growth, and strengthening of integrin-ECM interactions (Galbraith et al., 2002). Furthermore, and testifying of the acute sensitivity of these approaches, it has been shown that force values as low as 2 to 12 pN induce talin extension, thus respectively releasing one to six vinculin interaction sites (Rio et al., 2009).

However, optical trap experiments have proven more complex, particularly in the case of endocytosed ferromagnetic beads. Indeed, cytoplasmic volume hinders bead movement detection and dramatically decreases the spatial resolution, while in a context of hardly controllable interactions of the beads with intracellular components (Conroy, 2008). Due to this, beads have preferentially been placed on the surface of cells to assess local or global membrane rheology (Bausch et al., 2001; Galbraith et al., 2002; Balland et al., 2005), as well as filopodium-generated forces (Kress et al., 2007; Moore et al., 2009).

Micropipette aspiration - Micropipette aspiration measures the mechanical properties of single cells by the observation of cell deformation upon controlled pressure suction. Dynamic measurement of the membrane geometry being drawn in at a given pressure allows for estimation of cell visco-elastic properties and cortical surface tension with a stress precision of approximately 0.1 to 0.2 Pa (Hochmuth, 2000; Colbert et al., 2010; Fu et al., 2011). Numerous pioneering studies using micropipette aspiration were conducted using lipid bilayer vesicles (Bo et al., 1989; Evans et al., 1990; Olbrich et al., 2000; Longo et al., 2007). These cell-sized lipid vesicles can be prepared by

rehydrating dried synthetic or natural lipids in aqueous buffer, and are devoid of any intracellular organelles or cytoskeleton components. When performing this type of experiment on whole cells, the model basically assumes a homogeneous elastic membrane holding a drop of homogeneous Newtonian liquid inside. Under micropipette aspiration and weak osmotic pressure difference, the cell deforms with a constant volume. The use of micropipette aspiration under different mechanical models has enabled new knowledge in understanding the bulk mechanical behaviors during different biological processes (Evans et al., 1989; Jones et al., 1999; Ricca et al., 2013). Using this method, it has been reported that breast cancer cells become more deformable upon successive extension and relaxation events due to the reorganization and alignment of cytoskeletal network (Mak et al., 2013). Micropipette aspiration has also been used to decipher dynamic processes such as acto-myosin cortex growth modulating behavior of membrane protrusions and generating oscillations at a typical timescale of approximately 10 to 15 seconds (Brugués et al., 2010).

Uniaxial rheology - Uniaxial rheology makes use of micro-plates of various mechanical properties, in between which cells adhere. Movement of the plates along a unidirectional trajectory generates global dynamic stresses that can be either tension or shear stresses, and allows for recording of the cell response to the stress. Applicable forces span a large range from 10 nN to 10 μ N, inducing the possibility to estimate visco-elastic properties of whole cells (Desprat et al., 2005; Fernández et al., 2006; Pullarkat et al., 2007; Mitrossilis et al., 2010). It has been shown that under oscillating load, fibroblasts go from a linear visco-elastic regime to a non-linear elastic behavior coupled with an increase of their stiffness (Fernández et al., 2006). This phenomenon has also been described *in silico* with reconstituted F-actin networks in the presence of crosslinking protein filamin A (Gardel et al., 2006a; Gardel et al., 2006b).

Laser ablation - Laser ablation enables the characterization of tension in cytoskeleton fibrillary components, within living cells. Focusing a pulsating laser beam on these structures induces their local breakdown on a region of approximately $0.5 \mu\text{m}^2$, without damaging the rest of the cell. The subsequent behaviors - such as retraction or depolymerization - are then recorded to infer the previous tension state of microtubules or stress fibers (Botvinick et al., 2004; Kumar et al., 2006; Colombelli et al., 2007; Tanner et al., 2010). This type of approach has notably been used to confirm *in cellulo* the visco-elastic behavior of actin stress fibers, acting as tensed cables *via* acto-myosin complex activity (Kumar et al., 2006). Furthermore, it has been reported that actin stress fibers are connected to the plasma membrane, where they can initiate adhesion structure formation under intracellular tension local variations (Colombelli et al., 2009). Upon sectioning of stress fibers, zyxin and vinculin are rapidly recruited to the damage site and induce nascent adhesion formation where local tension is higher.

Atomic force microscopy - Atomic force microscopy (AFM) was first introduced in 1986 by the work of Binnig and co-workers (Binnig et al., 1986), and is based on scanning tunneling microscopy (STM) also developed by Binnig (Binnig et al., 1982). Contrary to STM, AFM allows

for nanoscale characterization of non-conductive materials, and has promptly been adapted for applications in liquid environment and thus biological applications (Marti et al., 1987). A flexible micron-sized cantilever is equipped with a tip which serves at the same time as an imaging device and a stress sensor, and the 3D displacement amplitudes of which are detected laser beam reflection on its extremity. Biological samples can either be imaged in contact mode - with a constant force being applied to the sample -, or in tapping mode - with given cantilever oscillation frequency and amplitude. Contact mode has been widely used in the context of imaging living cells (Braet et al., 1998; Zanger, 1998; Le Grimellec et al., 1998; Plodinec et al., 2010; Hecht et al., 2011), observing single DNA molecules (Samori et al., 1993) or proteins (Müller et al., 2002). Thanks to dynamic topographical information acquisitions, it has been possible to observe cell morphological responses to chemical stimuli (Schneider et al., 2000; Rotsch et al., 2000; Oberleithner et al., 2007; Martens et al., 2008), or to study the behavior of membrane protrusions or sub-cellular structures over time (Schoenenberger et al., 1994; Szabó et al., 2002; Friedrichs et al., 2007). It has also been applied to fixed cells to extract qualitative information on global cell topography or on microstructure repartition, and thus allowed for drug effect comparison among other explorations (Riethmüller et al., 2007; Docheva et al., 2008; Deng et al., 2009).

Tapping mode was introduced in order to reduce the risks of damaging fragile samples and the bias in topography measurements induced by material compression under the load of the tip (Schoenenberger et al., 1994; Radmacher et al., 1996; You et al., 2000). Indeed, tapping mode imaging displays lower friction and adhesion of the tip on the sample, which is paramount when imaging fragile or non-adherent samples such as macromolecules grafted on DNA or proteins (Möller et al., 1999; Moreno-Herrero et al., 2003; Hamon et al., 2010; Kodera et al., 2010; Lyubchenko, 2011). However, tapping mode in liquid environment yields poorer resolution than contact mode imaging due to lesser definition of oscillation peaks in liquids (Dreier et al., 1994).

Focus on TFM

Developing new tools to study cell-exerted forces has represented a great leap forward in terms of understanding mechanosensitivity and mechanotransduction mechanisms (Roca-Cusachs et al., 2017). In 1980, Harris proposed using silicon thin films to identify forces applied by cells during migration (Harris et al., 1980). The observation of wrinkling on the hanging films confirmed the ability of fibroblasts to exert traction forces on their substrate in order to propel their migration.

If this approach did not allow for computing the force amplitudes, it paved the way for the development of novel force evaluation techniques, including traction force microscopy (TFM), which has since been profusely applied to study forces generated at focal adhesion sites (Dembo et al., 1996; Dembo et al., 1999). Traction force microscopy is one of the most successful and broadly-used force probing technologies, chosen for the simplicity of its implementation, flexibility to mimic cellular conditions, and well-established analysis pipeline.

TFM main concepts - TFM is based on accessing the strain tensor component values for an elastic material, typically a polyacrylamide (PAA) hydrogel, on which cells have been plated (Fig. 3.3). Indeed, as cells apply forces on their substrate, these induce quantifiable stress given that:

- the substrate is compliant enough,
- its material properties are well-known, especially its mechanical properties,
- the gel deformations are observable.

Substrate strains can be assessed by comparing fiducial marker localizations, which are embedded inside or on the surface, at two different mechanically relevant time points: in a stressed conformation - i.e. with a cell applying tension; and in a relaxed conformation - i.e. without any adherent cell. This specification thus induces to acquire two images of the device: one image is taken with a cell adhering to the substrate; the other one must be taken either after having removed adherent cells - *e.g.* with a detergent solution or trypsin -, or before cell-seeding if the initial positions of the fiducial markers are well-characterized - *e.g.* if they have been organized in a crystal lattice (Bergert et al., 2016). Once the deformation cartography is obtained, its information can be converted in a traction map with an algorithm dedicated to solve the inverse problem (Butler et al., 2002; Del Alamo et al., 2007; Trepap et al., 2009).

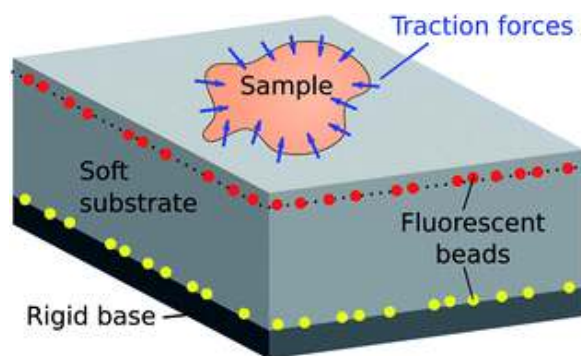


Figure 3.3.: Schematic diagram of a TFM substrate. A soft substrate (light grey) is bonded to a rigid base (dark grey). Fluorescent beads (yellow, red) are sometimes embedded at the substrate base, and near its surface. A continuous stress distribution is applied by a contractile sample, causing the displacements of fluorescent beads. Adapted from Style et al., 2014

TFM workflow The typical protocol for most elementary TFM experiments has been extensively documented (Cretu et al., 2010; Aratyn-Schaus et al., 2010), and is briefly described as follows:

- surface treatment of one set of glass coverslips including hydrophilicity boost, silanization of glass and addition of active aldehyde groups - namely the activated coverslips;
- preparation of working solutions containing the final desired concentrations of acrylamide/bis-acrylamide, depending on the desired gel mechanical properties;
- integration of fiducial markers directly inside the acrylamide solution, or through spin-coating them on another set of clean glass coverslips;

- initiation of the gel polymerization with a radical source and a catalyst, pipetting of a given volume of acrylamide solution onto the activated coverslip and sandwiching the gel with a clean or fluorescent bead-coated coverslip;
- after complete polymerization of the hydrogel at room temperature, separation of the sandwich to only keep the activated coverslip on which PAA has been covalently bound;
- PAA surface grafting of an amine-reactive crosslinker for subsequent coating of any ECM protein;
- placing PAA-coated samples in sterile-compatible conditions prior to cell seeding;
- loading of the samples in the imaging chamber for microscopic observation of either the fluorescent displacement markers, the cell adhesion structure characteristics, or both;
- detachment of the cells *via* addition of a detergent or highly concentrated solution of adhesion protein cleaving agent;
- imaging of the fiducial markers at the exact same localization as before cell detachment;
- comparison of the two fluorescent bead acquisitions to extract the associated displacement field;
- solving of the inverse problem with the PAA gel Young's modulus value and the inferred displacement field as input data, yielding a force mapping of the hydrogel surface.

Analysis of TFM data - Extraction of the displacement field is preferentially carried out through cross-correlation based particle tracking velocimetry (PTV) and particle image velocimetry (PIV) methods to track the fiducial marker movements. PTV tracks the individual displacements of all the beads on the region of interest (Legant et al., 2010), while PIV estimates the displacements from piecewise local correlations performed on image blocks of varying sizes (Tolic-Nørrelykke et al., 2002). Hence, PIV automatically assumes the local deformations to be approximated by simple rigid translations.

Then, traction stresses are computed from the measured displacements by solving a boundary-value problem (Style et al., 2014). Assuming the substrate is a linear-elastic solid, stresses $\sigma(x)$ are related to displacements $u(x)$ by the tensorial version of Hooke's law: $\sigma = \frac{E}{1-\nu}(\frac{1}{2}(\nabla u + \nabla u^T) + \frac{\nu \nabla \cdot u}{1-2\nu} I)$ where I is the identity tensor, and ν is Poisson's ratio. As mechanical equilibrium requires that $\nabla \cdot \sigma = 0$, this yields from the previous equation: $(1 - 2\nu)\nabla^2 u + \nabla(\nabla \cdot u) = 0$. The substrate is rigidly attached to a stiff base at $z = 0$, and has a free surface at $z = h$. Traction stresses at the surface can be computed if the displacement field is known on a horizontal plane located at or just below the surface - at $z = z_0 = < h$. Stress features with a length scale lesser than $h - z_0$ cannot be accurately resolved, so the finest spatial resolution is achieved when the displacement field is assessed at the free surface. This is the elected hypothesis for the following, which yields system boundary conditions defined as: $u(z = h) = u^*(x, y)$ and $u(z = 0) = 0$, with $u^*(x, y)$ being the PTV or PIV inferred displacement field. The mechanical equilibrium equation can be solved by applying Fourier transform in x and y (Dembo et al., 1999). This results in an ordinary differential equation in z for the Fourier transform $\hat{u}(k_x, k_y, z)$ of u , with k_x and k_y being the x - and y -wavenumbers, respectively. Evaluating the result at the substrate surface gives that the Fourier transform of the

traction stresses $\hat{\sigma}$ is linearly related to \hat{u} : $\hat{\sigma}_{iz}(k_x, k_y, z = h) = Q_{ij}(k_x, k_y, h)\hat{u}_j(k_x, k_y, z = h)$ with summation over repeated indices.

Thus the basic procedure for computing surface traction stresses from the surface displacement is as follows:

- compute the in-plane Fourier transform of the displacements;
- for each wavenumber pair, compute the associated matrix $Q_{ij}(k_x, k_y, h)$;
- apply Q to the displacement data for each wavenumber in order to evaluate the Fourier transform of the traction stress;
- eventually compute the traction stress field *via* inverse Fourier transformation.

As summarized in Fig. 3.4, the two main analysis steps, namely the displacement field determination and the computation of traction forces, are subjected to factors potentially influencing the final results (Zündel et al., 2017). Identification of these factors, and exploration of their potential impact has led to various improvements of both the TFM experimental setup and its associated data analysis.

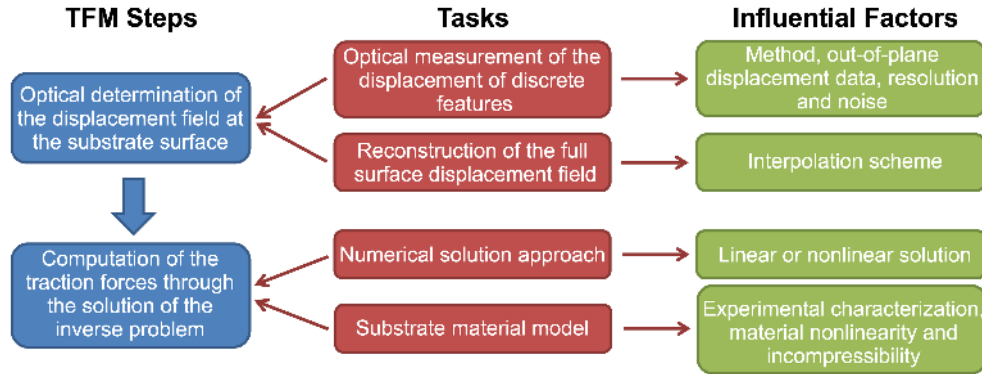


Figure 3.4.: Main steps in TFM analyses and associated influential factors. Adapted from Zündel et al., 2017

Improving TFM experimental aspects

Recent developments have been pushing the performance limits of the traditional TFM technique. Some works have focused on improving in-plane traction resolution, while others have implemented the determination of axial strain components.

Improvements on microscopy - Technical improving of the traditional microscopy techniques allowed for their introduction in the TFM workflow. Indeed, instead of classic confocal microscopes, more advanced microscope setups have recently been used to acquire the load-free and stressed images, such as spinning disk confocal scanner microscopy (Del Álamo et al., 2013; Plotnikov et al., 2014), total internal reflection microscopy (Han et al., 2015), stimulated emission depletion (STED) microscopy (Colin-York et al., 2016; Colin-York et al., 2017) (Fig. 3.5), and structured illumination microscopy (SIM) (Colin-York et al., 2019). The spatial resolution of TFM is determined by the

spatial sampling of the displacement field (Sabass et al., 2008), which is limited by both the density of fiducial markers and the optical resolution of the microscope. By improving the optical resolution of the microscopy, it has hence been proposed to increase the density of the fluorescent beads, in order to gain a finer evaluation of the displacement field. Indeed, the work of Colin-York and coworkers showed that increasing the 40 nm fluorescent bead density up to $15 \mu\text{m}^{-2}$ drastically improved the recovery of the traction field, thanks to lesser sparse displacement field information (Colin-York et al., 2016; Colin-York et al., 2017). Another strategy to increase the fiducial marker density consists in embedding two different color fluorescent beads (Sabass et al., 2008; Plotnikov et al., 2012; Plotnikov et al., 2014).

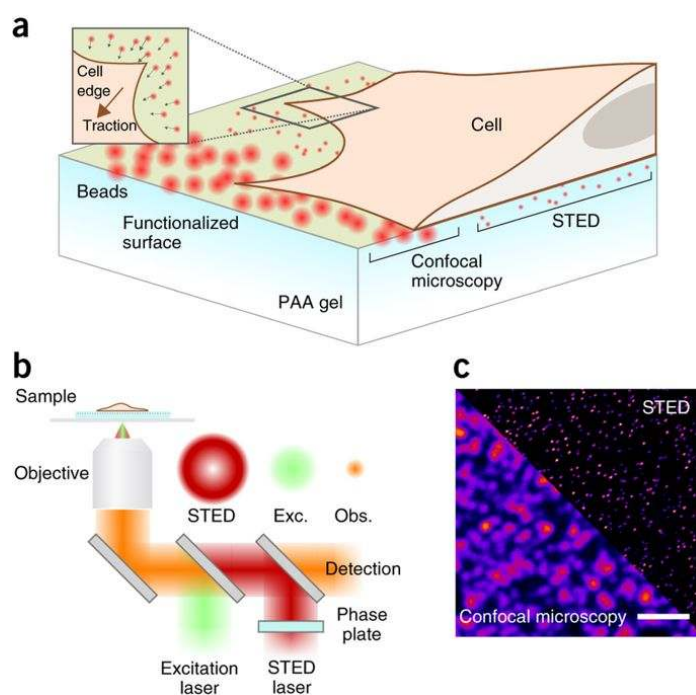


Figure 3.5.: Outline of STED-TFM. (a) Schematic representation of a typical STED-TFM setup. Traction forces applied by the cell to the top surface of the gel result in lateral displacement of the beads within the gel. (b) Schematic showing the beam path of a STED microscope. (c) Side-by-side comparison of the resolution enhancement offered by STED microscopy as compared to with confocal microscopy. Adapted from Colin-York et al., 2017

An original alternative to the previous limited approach has been proposed by the work of Bergert and colleagues, in which they suggested a specific arrangement of the fiducial so that no reference configuration image was required (Bergert et al., 2016) (Fig. 3.6). Indeed, through the use of electrohydrodynamic nanodrop printing, a crystalline lattice of Quantum Dots nanodiscs were deposited on the surface of a polydimethylsiloxane (PDMS) gel. This lattice was finely characterized and provided a geometrically controlled meshing of the surface of the substrate, allowing for a precision of

approximately 30 nm. While this setup also allowed for the detection of out of plane loads due to the highly confined localization of Quantum Dots, it also displayed higher sparsity in the displacement field evaluation due to the value of spacing between nanodiscs just over 1 μm .

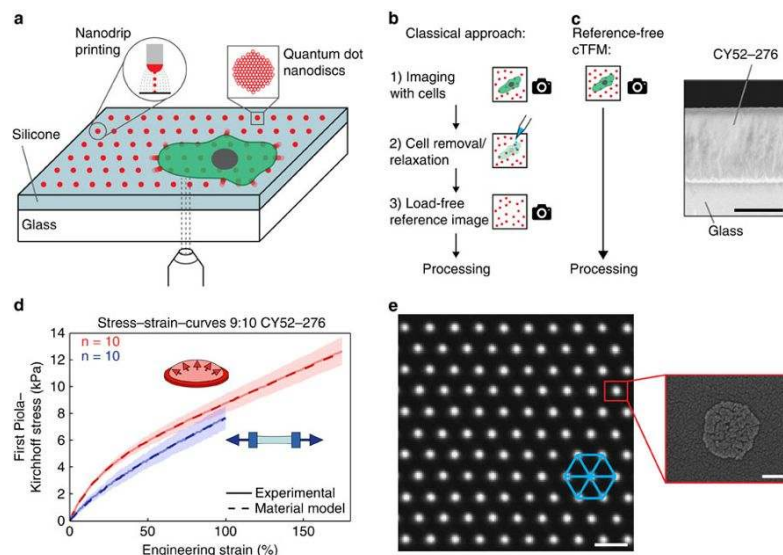


Figure 3.6.: (a) Schematic of the confocal reference-free TFM setup and involved techniques. (b) Workflow of the classical continuum approach versus the one-step confocal reference-free TFM process. (c) Scanning electron microscopy image of cross-section of elastic silicone layer on glass coverslip. Scale bar 20 μm . (d) Results of tensile (uniaxial) and inflation (equibiaxial) testing of CY52-276 silicone.(e) Representative example of quantum dots nanodisc printing on elastic silicone substrates. Scale bar 2 μm . Adapted from Bergert et al., 2016

Improvements on force detection - Another aspect of TFM which has recently been explored towards improvement, lies in the detection of axial forces applied on a 2D substrate. Indeed, the realization that cells could generate out-of-plane traction stresses even when they adhere on flat surfaces (Hur et al., 2009) has prompted an increased demand for the characterization of the error that the widely used 2D TFM methods might have incurred by neglecting these stresses. In the work of Hur and colleagues, 3D evaluation of forces relied on 3D single particle tracking of the fiducial markers to infer a 3D assessment of the displacement field.

A computation of the 3D cell traction forces using Fourier transform has been proposed by the work of del Alamo (Del Álamo et al., 2013) (Fig. 3.7). In this experimental setup, the PAA gel was bi-layered so that a first fluorescent bead-free film was deposited before the addition of the top layer, in which fluorescent beads were embedded. Sub-pixel resolution was attained by tri-quadratic polynomial interpolation of the image correlation function. This method notably allowed for the characterization of 3D forces exerted by leukocytes and vascular endothelial cells, showing their role in dynamically facilitating diapedesis (Yeh et al., 2018); or for deciphering the roles of axial

actomyosin contractility and cortical tension mechanisms in the context of *Dictyostelium* amoeboid migration (Alvarez-Gonzalez et al., 2015).

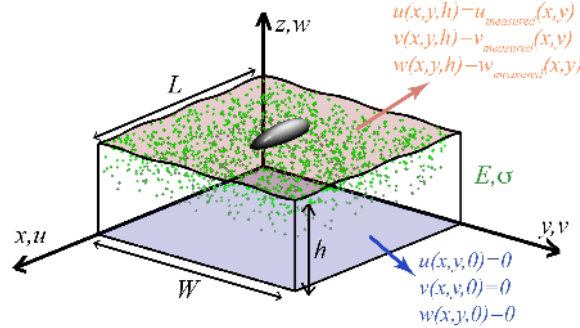


Figure 3.7.: Configuration of the 3D TFM mathematical problem. The input data are the measured three-dimensional deformation caused by the cell on the free surface of the substratum ($z = h$, red), and it is assumed that the deformation of the substratum is zero at the bottom surface in contact with the glass coverslip ($z = 0$, blue). Adapted from Del Álamo et al., 2013

Another approach to visualizing 3D displacements induced by traction and normal forces consists in inferring the displacement field from fluorescent beads dispersed in the whole volume of the PAA gel. Franck and coworkers notably developed a method for measuring large deformations in optically transparent soft materials (Franck et al., 2007; Maskarinec et al., 2009; Franck et al., 2011; Toyjanova et al., 2014a). The technique utilizes a digital volume correlation (DVC) algorithm to track motions of subvolumes within 3-D images obtained using fluorescence confocal microscopy. In order to extend the strain measurement capability to the large deformation regime ($>5\%$), a stretch-correlation algorithm was developed and implemented into the Fast Fourier Transform (FFT)-based DVC algorithm. What is more, it yielded some of the first experimental evidence that cells were indeed capable of exerting large material deformations (Toyjanova et al., 2014a; López-Fagundo et al., 2014). This finding highlighted the requirement of the formulation of a new theoretical TFM framework to accurately calculate the traction forces. In the work of Legant, a volume dispersion of the fluorescent markers was also implemented for the exploration of out-of-plane tractions (Legant et al., 2013). However, in this study, each of the fluorescent bead centroids were identified using a 3D Gaussian maximum likelihood estimator. This methodology revealed the exertion of rotational moments at the site of focal adhesions in migrating fibroblasts.

Improving TFM data reconstruction

Historically, the first approach to compute traction force from the measured displacement field consisted in an inversion of the reduced equilibrium equation in real space (Dembo et al., 1999). However, despite its being quite flexible, constructing the required matrices and inverting them is computationally demanding (Sabass et al., 2008; Herant et al., 2010).

Identification of force application area - Considerable simplification can be achieved if the position and the extension of the adhesive sites are known. Traction reconstruction with point forces avoids numerical integration by assuming the force in the generalized Hooke's law equation is confined to small regions. However, it raises the question whether all adhesion structures exert forces on their substrate. Han and coworkers showed in their work that only approximately half of nascent adhesions in epithelial cells did spatially coincide with local force maxima (Han et al., 2015). To do so, they implemented a method of sparsity regularization to the solution of the inverse problem, suppressing noise without underestimating traction magnitude.

Force reconstruction algorithms - With Fourier transform traction cytometry (FTTC), the mechanical equilibrium equation is solved in Fourier space, where the convolution integral becomes a simple matrix multiplication (Butler et al., 2002). This method is efficient and reliable, and has thus found wide popularity (Sabass et al., 2008; Plotnikov et al., 2014; Kulkarni et al., 2018), to the point where it has been implemented in a routine ImageJ plugin (Martiel et al., 2015). Indeed, FTTC benefits from a very fast computation time and that no additional information apart from the measured displacement field is required. However, the resolution of the final traction field depends strongly on the local resolution of substrate deformations according to the Saint-Venant's principle. Therefore, it is paramount to record the fluorescent marker displacements close to the force-generating processes -*i.e.* under the cell body - to resolve the details of the traction pattern. What is more, according to Nyquist criterion, the spatial resolution is mainly determined by the bead density, being resolved in the image processing phases, which is why nanobeads are preferred over microbeads. Alternatively, the differential equations can be solved with a finite element method (FEM) (Yang et al., 2006). FEM displays the advantage that almost unspecified geometries and nonlinear gel responses can be explored. However, the need to discretize the whole bulk inside the gel makes FEM computationally demanding. FEM approaches are especially suited for 3D systems (Legant et al., 2010; Munoz, 2016). Additionally, it has been shown that TFM can be completely based on such a discretized approach, for example in order to take into account finite substrate thickness (Yang et al., 2006). Here, the agreement between measured and simulated displacements has been optimized using a FEM-formulation. A mathematically elegant way to reconstruct traction with FEM has been introduced by Ambrosi and coworkers (Ambrosi, 2006; Ambrosi et al., 2009). The basic idea relies on considering the traction reconstruction as a partial differential equation constraint optimization problem.

Displacement field extraction - Upstream of the traction reconstruction, other works have also strived to improve the accuracy of TFM through displacement field extraction from imaging of the fiducial markers. As has been previously said, while PIV is the most commonly used method to quantify the substrate deformations, some other works have implemented other displacement reconstruction methods. Among these: single and multiple particle tracking (Bloom et al., 2008; Bar-Kochba et al., 2015), hybrid combination of particle tracking and correlation tracking (Style et al., 2014), digital volume correlation (Franck et al., 2007; Maskarinec et al., 2009; Franck et al.,

2011), or a recently introduced free form deformation-based image registration algorithm (Jorge-Penas et al., 2015). What is more, polyacrylamide gels have been proved to display nonlinear elastic behaviors, contrary to which is mostly assumed in TFM traction reconstructions. Even though their Poisson’s ratio was quantified and yielded values well according with the incompressibility hypothesis (Takigawa et al., 1996; Boudou et al., 2006a; Boudou et al., 2006b; Legant et al., 2013), it was also pointed out that gels exhibited nonlinear elastic behavior (Boudou et al., 2009). Additionally, their viscoelastic behavior has been but poorly characterized (Weiss et al., 1977; Heemskerk et al., 1984; Kumar et al., 2010; Abidine et al., 2015). However, works on implementing these kinds of non-basic mechanical behaviors in TFM force recovery strategies have been conducted recently. Palacio and coworkers proposed numerical estimation of cell forces by solving a minimization problem that combines multiple non-linear FEM solutions, yielding a higher accuracy in traction prediction (Palacio et al., 2013). Another case of non-linearity was tackled in the specific context of hyperelastic substrates, also *via* minimization problem resolution (Dong et al., 2017). Eventually, viscoelasticity was also explored from its experimental characterization methodology to its mathematical implementation in the 3D TFM framework (Toyjanova et al., 2014b).

In the specific context of podosomes, or podosome superstructures such as the sealing zone, the main component of the exerted forces is the axial one. However, recent TFM techniques are not suited for the precise evaluation of axial forces applied on submicron areas. To overcome this drawback, previous works in the lab led to the development of a technique specifically designed for the quantification of forces applied by podosomes. This method is based on observing the deformations of a thin Formvar film *via* atomic force microscopy, and was named protrusion force microscopy (Labernadie et al., 2014; Bouissou et al., 2018). Indeed, when macrophages formed podosomes on this hanging film, bulges below the sites of podosome formation were measured, and related to the required force for their generation based on the mechanical properties of Formvar. This original technique also allowed for the dynamic characterization of podosomes Proag et al., 2015. However, it still lacks access to two major information: the in-plane components of forces, and the possible coupling with fluorescence imaging to follow the localization of target proteins. However, these information are available with typical TFM setup, but not the precise estimation of axial force components. Hence, it was explored whether attempting to include this information was feasible by developing a new super-resolved 3D TFM setup.

3.2.2. Towards a super-resolved 3D TFM setup

Given the previously stated pros and cons of the numerous TFM systems that have been developed, we have set out to find out whether we could design and deliver an “all-inclusive” super-resolved 3D-TFM setup. We have thought of the various aspects of a TFM experiment walkthrough, and how we ought to adapt them in a context of super-resolution 3D microscopy. We have sorted them in four different categories, and listed for each one the requirement specifications implied by the corresponding technologies and processes. These considerations are detailed in the following paragraphs.

Choosing a microscopy technique

As has been emphasized in the first chapter, the current lack of deformation resolution lies in the mismatch between well-resolved in-plane displacement information and poor axial deformation information in order to characterize forces that are growingly thought to be applied at an angle relative to the substrate surface. In order to address this issue, an obvious solution is to seek an observation technique that would benefit from an excellent resolution in the three space dimensions. An overview of the available super-resolution microscopy techniques is summarized in Fig. 3.8 and the comparison of their technical characteristics is described in Fig. 3.9.

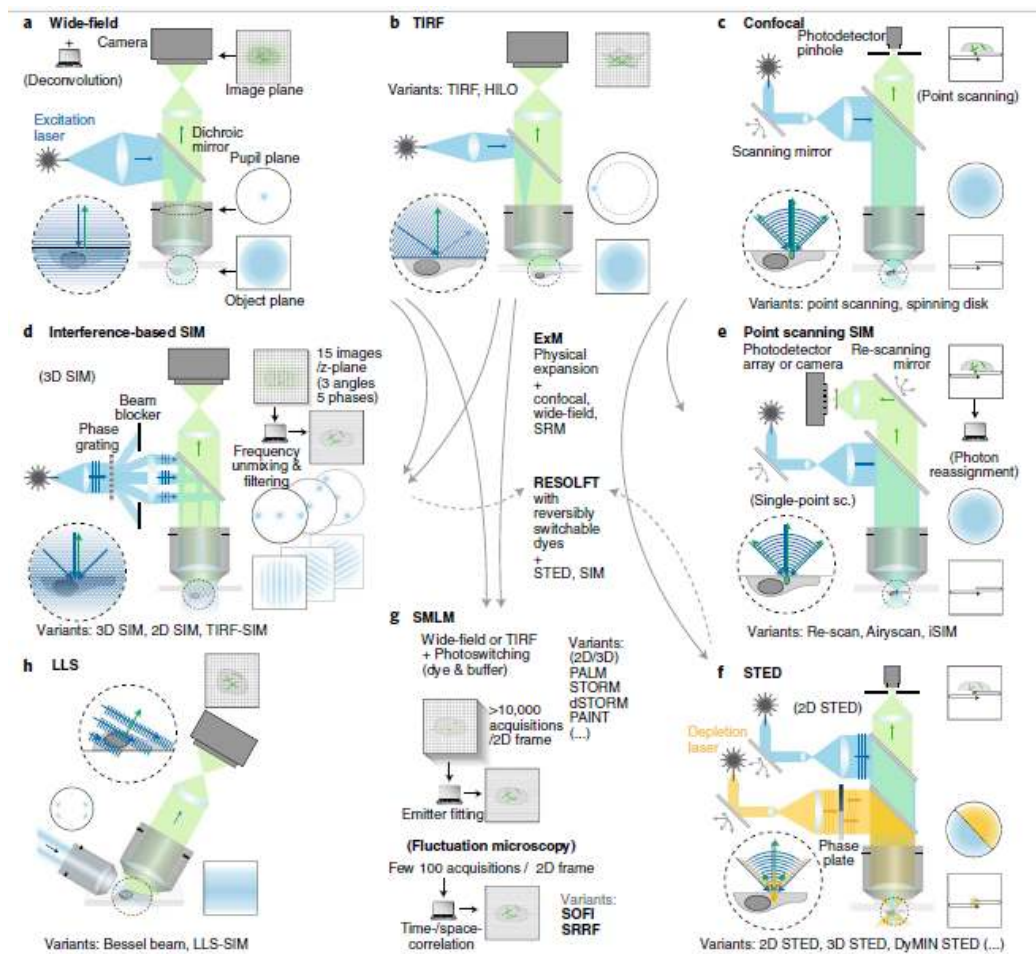


Figure 3.8.: Basic principles of super-resolution microscopy. Simplified light-paths of common conventional (a–c) and super-resolution microscopy techniques (d–h). For better comparison, all techniques are displayed in an upright configuration, though inverted configurations are more common, particularly for TIRF, SIM and SMLM systems. Adapted from Schermelleh et al., 2019

Considering in-plane resolution, two major types of super-resolved microscopy techniques rival

with typical x-y localization precision under 100 *nm*: single molecule localization microscopy and controlled illumination-based microscopy. PAINT, PALM and STORM techniques fit in the first category, while SIM and STED fit in the second one. The technical specificities for each of these super-resolved techniques will be discussed in this paragraph.

Controlled illumination-based microscopy

Stimulated emission depletion microscopy - Stimulated emission depletion (STED) microscopy was developed by the work of Hell and Wichmann in 1994 (Hell et al., 1994). It consists in exploiting the non-linear response of fluorophores and selectively deactivating fluorescence. STED interrupts the relaxing process of dye electrons before the photon is released, forcing it to relax into a higher vibration state and thus red-shifting the photon eventually released, allowing it to be discarded by signal filtering. This alternative emission occurs when an incident photon strikes the stimulated fluorophore. Lateral resolution using STED can go down to approximately 50 *nm*.

Structured illumination microscopy - Structured illumination microscopy (SIM) works by using a patterned illumination, usually stripes, to excite the sample (Guerra, 1995). The stripe position and orientation is changed a number of times, and the emitted fluorescence signal is recorded for each one of those positions. The interaction between the excitation and the sample produces Moiré patterns as a result of interference between the fine-striped excitation striped pattern and the sub-diffraction details in the sample emission. These Moiré patterns contain high frequency spatial information that would not be decipherable through diffraction-limited imaging. Following processing with a specialized algorithm, this information can be extracted from the raw data of the multiple images, to produce a reconstructed final image that has a lateral resolution approximately twice that of diffraction-limited instruments, i.e. close to 100-130 *nm*. SIM techniques shortcomings lie in the length of processing time necessary to achieve high-resolution images, and its sensitivity to errors in grating position, system calibration, refractive index mismatch and/or poor sample quality.

Single molecule localization microscopy techniques - PALM - photoactivated localization microscopy - and STORM - stochastic optical reconstruction microscopy - techniques rely on the same fundamental concept: activating the fluorescence then switching it off in individual molecules that are far apart so that their halos do not overlap, coupled with multiple time point acquisitions to result in a crisper image. While PALM technique exploits the spontaneously occurring phenomenon of photobleaching, STORM relies on the reversible switching between a fluorescent on-state and a dark off-state of a dye. Another single molecule localization microscopy technique relies on the transient binding and unbinding of fluorophores to achieve similar emission dynamics: point accumulation for imaging in nanoscale topography, or PAINT.

PALM - PALM was introduced in 2006 by the work of Betzig and Hess (Betzig et al., 2006; Hess et al., 2006), and was awarded with the 2014 Nobel Prize for Chemistry. In a typical PALM

experiment, fluorophores are stochastically activated by laser power, emit for a short period of time before bleaching and multiple time points are acquired until the optimal number of fluorophores have emitted. The same process for center of mass precise reconstruction for each fluorescence signal is applied to each time point data, and a complete super-resolution microscopy image is compiled. Three commonly used types of dyes can be applied to PALM technique: photoactivatable fluorophores (PA-GFP/mCherry -> UV activation); photoconvertible fluorophores (mEOS proteins -> UV activation) and photoswitchable fluorophores (chemical dyes, also used for STORM applications). Another application for PALM technique is single particle tracking.

STORM - STORM was introduced in 2006 by the work of Rust (Rust et al., 2006). Two variants of STORM have been developed: the first is based on the interaction of a pair of activator-reporter dyes, and direct STORM in which fluorophores are converted to the off state using specific excitation parameters in combination with a specialized oxygen-scavenging imaging buffer (Bates et al., 2007; Huang et al., 2008; Van de Linde et al., 2011). The “activator” dye induces a switching and the “reporter” dye emits the signal which is detected by the camera. While this STORM system allows multicolor applications and requires less substantial laser power in order to achieve the energy jump from on-state to off-state, it implies dual labelling of the same target molecule and relies on the proximity of the two dyes and is not commonly used. Nowadays, dSTORM is most preferentially used in microscopy experiments, compared to the first STORM version. Ideal fluorophores for STORM technique should be bright, have a high rate of photoswitching and be minimally prone to photobleaching in observation conditions.

PAINT - PAINT stands for point accumulation for imaging in nanoscale topography, and was first introduced in the 2000s by the work of Sharonov and coworkers (Sharonov et al., 2006). The general principle of this technique lies in the use of fluorescent dyes that transiently bind and quickly dissociate from their targets, resulting in a “blinking” signal. This blinking can be captured over a consequent amount of time points, with each time point acquisition presenting a sparse pattern of switched-on pixels. This sparsity is then tapped in order to finely recover every center of fluorescence peaks with a precision of 25 nm. This process is applied on each time point acquisition, and eventually the whole sample image is reconstructed.

In their simplest implementations, these methods typically improve lateral resolution by one order of magnitude, however their axial resolution is still limited by diffraction. Specific techniques must be developed to tackle this strong anisotropy resolution, which compromises 3D imaging.

Confocal microscopy - When it comes to axial localization, a massive breakthrough in the late 50s has consisted in the introduction of confocal microscopy. Its principle was patented by Minsky in 1957 (Marvin, 1961) and consists in using point illumination materialize by a spot close to the diffraction limit in size, coupled with a pinhole in an optically conjugate plane in front of the microscope’s photodetector or camera in order to eliminate out-of-focus signal. As illumination is focused on only one point at a time, retrieving an entire image of the region of interest requires

scanning over a rectangular raster at a prescribed scan speed. Variation of this scan speed influences signal-to-noise ratio as well as photobleaching. Acquisition of successive 2D slices make up a z-stack, which can be processed to yield a 3D reconstruction of the sample by optical sectioning. The achievable thickness of the focal plane is mostly defined by the wavelength of the used light source over the numerical aperture of the objective lens, but it also depends on the optical properties of the sample. Also, as the pinhole blocks off a major part of the signal emitted by the sample fluorescence, the increased axial resolution is at the cost of decreased signal intensity. Thus, long exposures are required, at the risk of great photobleaching. To counterbalance this drawback, use of more sensitive detectors - photomultiplier tube or avalanche photodiode - or of a series of moving pinholes on a disc - enabling them to hover over a specific area for a longer time, the so-called spinning disk technique - have been proposed as improvements for instance.

Total internal reflection fluorescence - The idea of using total internal reflection to illuminate cells contacting the surface of glass was first described by E.J. Ambrose in 1956 (Ambrose, 1956). This idea was then extended by Daniel Axelrod in the early 1980s as TIRFM (Axelrod, 1981). A TIRFM uses an evanescent wave to selectively illuminate and excite fluorophores in a restricted region of the specimen immediately adjacent to the glass-water interface. The evanescent wave is generated only when the incident light is totally internally reflected at the glass-water interface. The evanescent electromagnetic field decays exponentially from the interface, and thus penetrates to a depth of only approximately 100 *nm* into the sample medium. Thus the TIRFM enables a selective visualization of surface regions such as the basal plasma membrane (which are about 7.5 *nm* thick) of cells. By comparison, this optical section thickness is approximately one-tenth that produced by confocal fluorescence microscopy techniques. However, this technique does not allow for sample-sectioning in its entire depth.

Engineering point spread function - A technical way of axially localizing fluorescent light sources consists in deforming their point spread function (PSF) through the use of unconventional optics on the emission optical path. This idea was brought up by the work of Izeddin and colleagues (Izeddin et al., 2012), in which a 52-actuator deformable mirror was used to both correct aberrations and induce two-dimensional astigmatism in the point-spread-function. Depending on its z position with respect to the image plane, the point source will be imaged on the detector as a more or less defocused spot. Unfortunately, analysis of this defocused signal cannot precisely determine the source position along the z-axis due to:

- the symmetry of the PSF deformation above and below the focal plane;
- the small change in the PSF shape for molecules within the focal depth of the objective (typically 0.5 μm).

Thanks to this imbalance, on each z-stack slice one can relatively place one source above or beneath the other and quantify the height difference relatively to the PSF aspect (Pavani et al., 2009; Badieirostami et al., 2010). Single- (Huang et al., 2008) and double- (Xu et al., 2012) cylindrical-lens methods have achieved axial-localization precisions 60 and 20 *nm*, respectively. The former is very

stable and straightforward to implement, whereas the higher precision of the latter comes at the cost of increased complexity.

Interferometric microscopy - Interferometric microscopy has also been proposed to further push the boundaries of axial resolution, *via* combination with photoactivated localization microscopy (iPALM) (Shtengel et al., 2009). Quantitative high-precision positional measurements are commonly made with phase-based interferometry, where coherent light waves from two optical paths (a reference path and a measured path) are combined to create a signal that modulates on the length scale of an optical wavelength (Hariharan, 2003). Interferometry is widely applied to position objects to 10^{-10} -meter accuracy, measure optical surfaces, and even scout for gravity waves with 10^{-18} -meter sensitivity. Interferometric microscopes when combined with phase-shifting techniques can form subnanometer-height images and are routinely used in industry to qualify semiconductor processing or hard disk drive head profiles (Linnik, 1933; Delaunay, 1953; Bhushan et al., 1985). A novel optical system was configured based on a combination of insights. First, single fluorescent molecules are intrinsic quantum sources. Thus, wave-particle duality allows a single fluorescent photon to form its own coherent reference beam. An emitted photon can simultaneously travel two distinct optical paths, which are subsequently recombined so that the photon interferes with itself. The position of the emitter directly determines the difference in the path lengths, hence the relative phase between the two beams. Second, the optical system can be configured so that interference can take place over a wide range of lateral source positions to form interference images on an area array detector, such as a CCD for rapid parallel acquisition. Finally and most importantly, simultaneous multiphase detection must be implemented for each photon, which represents the requirement of highly elaborate computational resources.

However, all these strategies provide only the relative axial positions of the fluorophores with respect to an arbitrary focal plane. Hence, 3D optical nanoscopy is in need of a method that combines high nanometer axial precision, simplicity of implementation and absolute axial positioning.

Combining 2D and axial super-resolution - Using a microscopy system which couples single molecule localization with supercritical angle fluorescence detection has been proposed, namely the direct optical nanoscopy with axially localized detection (DONALD) setup (Bourg et al., 2015). The specificity of DONALD setup lies in its novel use of the nearfield component of fluorescent emitted signal. Indeed, when considering a fluorescent source localized in the close proximity of the observation medium-glass coverslip interface, the evanescent component propagates within glass with a refraction angle superior to the critical angle: this is referred to as supercritical angle fluorescence (SAF). This SAF component intensity decreases exponentially when the fluorescent source is farther away from the optical interface, and thus leads to determining the absolute axial localization of the fluorophore relative to the glass coverslip surface. This axial localization benefits from a 20 nm precision within the first 200 nm from the coverslip, and decreases down to approximately 100 nm when being 600 nm high within the sample (Bourg et al., 2015).

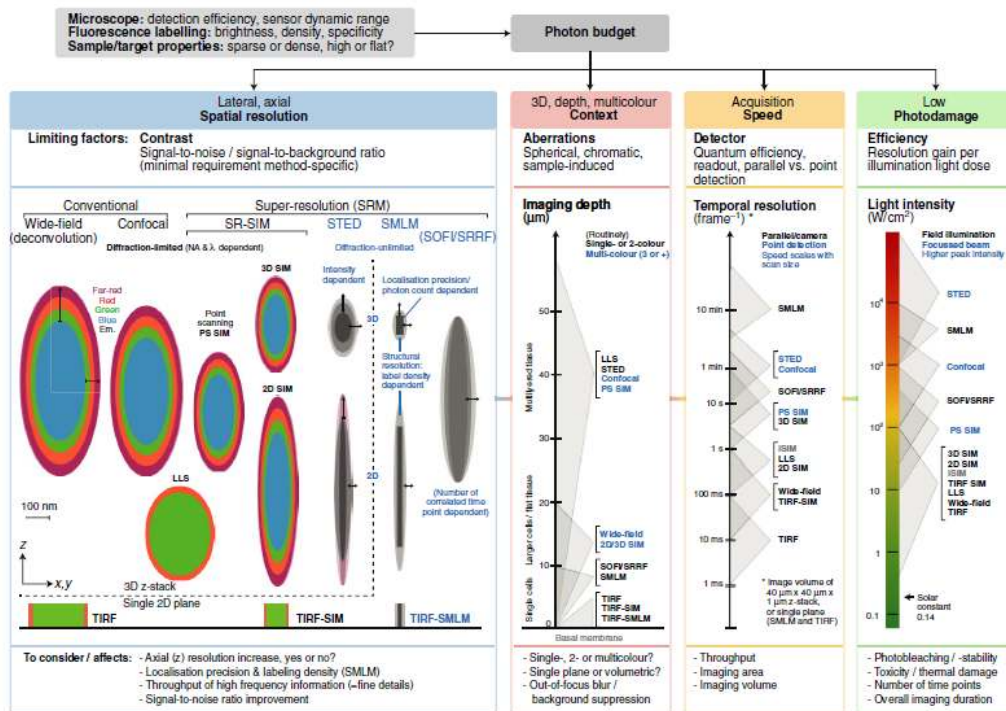


Figure 3.9.: Inherent trade-offs in super-resolution microscopy. Diagram illustrating the main properties of commercially available super-resolution and conventional microscopy techniques. Adapted from Schermelleh et al., 2019

Choosing a deformable material

Polyacrylamide has been used for many years as a compliant substrate for attachment of ECM (Wang et al., 1998). It is optically clear, colorless and has a similar refractive index to that of water. It is considered as linearly elastic and can be easily and reproducibly prepared to exhibit a wide range of well-defined compliances. Finally, polyacrylamide is biochemically inert, allowing cells to specifically engage only the ECM that is covalently coupled to its surface. Indeed, as polyacrylamide is uncharged and does not react with proteins, cells will not adhere directly to poly-acrylamide surfaces. Even though, unpolymerized acrylamide is highly toxic to many cell types, sufficiently long wash times once the polyacrylamide gel has been formed and overnight incubations in large volumes of buffer are optimal to minimize this cytotoxic effect. What is more, it has been shown that cells will ‘feel’ and respond to a stiffer substrate beneath a softer one if the soft substrate is sufficiently thin (Buxboim et al., 2010). Which means in our specific case that using great Young’s modulus PAA values will not be necessary to induce formation of adhesion structures.

Hence, choosing polyacrylamide for the hydrogel coating of glass coverslips appeared as an obvious decision.

Choosing a deformation marker

The Alexa Fluor family of fluorescent dyes is a series of dyes commercially available and frequently used as cell and tissue labels in fluorescence microscopy. They were intended to improve upon the properties of previously developed biological fluorescent dye families and solve some of the issues that they possessed. Structurally, the Alexa Fluor dyes are generated through the sulfonation and additional modification of certain well known dye families. In particular, the dye families of coumarin, rhodamine, xanthene (of which the industry-standard fluorescein is a member), and cyanine dyes were used. Sulfonation makes the Alexa Fluor dyes negatively charged and more hydrophilic than their precursors, while additional modification was used to improve the performance in photo-bleaching and pH dependent fluorescent intensity. The Alexa Fluor 647 specific ability to rapidly switch in energy states in the presence of oxygen-deprived observation buffers has made it suitable for single molecule localization microscopy techniques.

However, in the specific context of this study, it is required that fluorescent markers emit with a blinking pattern in a water-based observation buffer such as PBS. An early test was carried out on unroofed macrophages stained for actin with Alexa Fluor 488-tagged phalloidin and observed in PBS. It yielded satisfactory results concerning the Alexa Fluor-based fluorophores ability to blink in water-based medium. Indeed, the apparent blinking dynamics were comparable for Alexa Fluor 488 in PBS and Alexa Fluor 647 in STORM imaging buffer.

Choosing a cell-adhering coating

A characteristic feature of most integrin receptors is their ability to bind a wide variety of ligands. Moreover, many extracellular matrix and cell surface adhesion proteins bind to multiple integrin receptors (Humphries, 1990; Plow et al., 2000; Van der Flier et al., 2001; Humphries et al., 2006). The main fibrous ECM proteins are collagens, elastins, fibronectins and laminins (Alberts et al., 2007). However, each tissue is notably characterized by its specific variety and respective proportions of proteins from these four ECM fiber families. To promote integrin-mediated cell anchorage and signaling, the short peptide Arg-Gly-Asp (RGD), derived from laminin, fibronectin and vitronectin, has been widely incorporated into protease-sensitive, synthetic hydrogels. For example, RGD conjugated to heparin-PEG hydrogels promoted the formation of a well-organized cytoskeleton in HUVECs and increased their viability upon encapsulation (Oliviero et al., 2012).

All five α_v integrins, two β_1 integrins (α_5 , α_8) and $\alpha_{IIb}\beta_3$ share the ability to recognise ligands containing an RGD tripeptide active site. Crystal structures of $\alpha_v\beta_3$ and $\alpha_{IIb}\beta_3$ complexed with RGD ligands have revealed an identical atomic basis for this interaction (Xiong et al., 2002; Xiao et al., 2004). RGD binds at an interface between the α and β subunits, the R residue fitting into a cleft in a β -propeller module in the α subunit, and the D coordinating a cation bound in a von Willebrand factor A-domain in the β subunit. The RGD-binding integrins are among the most promiscuous in the family, with β_3 integrins in particular binding to a large number of extracellular matrix and soluble vascular ligands. Although many ligands are shared by this subset of integrins, the rank order of ligand affinity varies, presumably reflecting the preciseness of the fit of the ligand

RGD conformation with the specific α - β active site pockets. Due to this versatility and its small size compared to the total-length matrix proteins, RGD peptide was chosen to coat polyacrylamide gels.

Listing the requirement specifications

Development of cell force evaluation methods has allowed better comprehension of the processes by which cell adhesion structures probe extracellular environment rigidity, and thus enabled to start investigating the mechanotransduction signaling pathways involved in the process. However, current TFM techniques lack acute three-dimensional resolution in order to assess forces exerted by protrusive submicron adhesion structures such as podosomes. Indeed, as mean podosomal diameter is approximately 500 nm (Proag et al., 2016), quantifying associated forces requires being able to assess substrate deformations at the same scale, *i.e.* benefiting from a 3D resolution lesser than 100 nm. To this day, only protrusion force microscopy (PFM) has succeeded in this task (Labernadie et al., 2014; Proag et al., 2015; Proag et al., 2016; Bouissou et al., 2017). However and unlike with TFM, in-plane strain components are not accessible through PFM. Nor is the simultaneous imaging of the deformation-inducing structures, even though it constitutes a prerequisite in studying forces applied by complex adhesion structures such as sealing zones (Jurdic et al., 2006).

The specific objective of this project is thus to design a TFM setup that would allow for mapping cell forces at 3D nanoscale, in order to access to both in-plane and axial forces applied by submicron adhesion structures such as podosomes, sealing zones or nascent focal adhesions.

Developing such a technique, which counts no existing equivalent, is thought to represent a matter of utmost interest to the mechanobiology community, aiming at deciphering the relations between adhesion structure architecture and signaling processes.

1. In order to design a TFM approach allowing for mapping of 3D nanoscale cell forces, an imaging method sharing the same resolution is required to assess the substrate topography in its deformed and relaxed conformations.
2. In order to comply with the super-resolved microscopy detection and live cell observation requirements, the deformable material on which to seed cells has to be biocompatible, optically transparent and have an optical index close to that of water (1.33).
3. Furthermore, as it was stated earlier, optimal axial localization precision is met within the close vicinity of the coverslip. This specificity dictates that the PAA gel coating should ideally be no more than 200 nm thick.
4. The material strains induced by cell adhesion structures should have component values superior to the precision limits in all space directions, in order to be discernable from uncertainties of measurements. As a first approach, expected strain values were evaluated with finite element method simulations in the case of an adhesion structure applying nanoNewton forces on a thin coating of PAA bound to a glass coverslip. In the case of a single podosome protruding on the substrate, its geometric and mechanic features were extracted from PFM and SIM results (Proag et al., 2015). Early results point to axial displacements just below the load

surface application ranging in a few tens of nanometers, which further supports the need for 3D nanoscopy. In the future, FEM simulations could help assess how the cell-probed material stiffness varies with the gel coating thickness and PAA Young's modulus value. The resulting information would also be crucial in order to extract force values from displacement amplitudes quantified *via* nanoscopy, as well as to estimate their variation relative to substrate properties.

5. Finally, fluorescent fiducial markers embedded on the hydrogel have to be compatible with the single molecule localization microscopy technique.

3.2.3. Trying to meet the requirements specification point by point

Localization precision in x, y, z directions

Direct optical nanoscopy with axially localized detection (DONALD) is based on the principle that a fluorophore can be modeled as a dipolar emitter radiating in the far field. This dipole also emits a non-propagative near field wave component that depends on the surrounding refractive index n_m . In the presence of an interface with a medium with a greater refractive index n_g - such as in the case with glass compared to water-based observation medium-, the transmitted light follows Snell-Descartes law of refraction (Fig. 3.10). The refracted light is emitted within a cone that is limited by the critical angle $\theta_c = \arcsin(\frac{n_m}{n_g})$. This component is referred to as under-critical angle fluorescence (UAF).

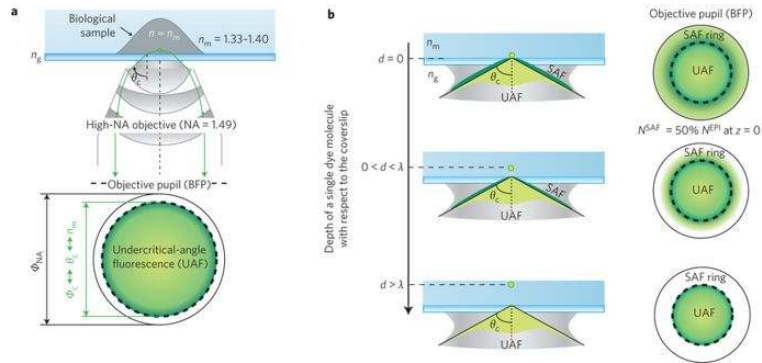


Figure 3.10.: Far and near field emission components. The far-field emission component UAF has an angular distribution determined by the law of refraction and limited by the critical angle θ_c (left). A portion of the near field component SAF of a dye molecule located in the near-field region is collected by the objective beyond θ_c (right). Adapted from Bourg et al., 2015

In the specific configuration when the fluorophore-interface distance d is smaller than the emission fluorescence wavelength $\lambda_e m$, then additional SAF emission is observed (Ruckstuhl et al., 2000). The evanescent near field component in the homogeneous medium surrounding the fluorophores becomes propagative beyond the critical angle θ_c inside the medium of higher refractive index. SAF emission can be detected for fluorophores in the observation medium located in this emission wavelength-

limited vicinity of the coverslip. The SAF intensity potentially represents up to half of all fluorescence emitted into the coverslip when the fluorophore is in direct contact with the interface ($d = 0$) (Fort et al., 2007). Absolute axial localization is obtained through the discrimination between UAF and SAF signal components. This is achieved with DONALD setup *via* extracting NSAF indirectly, by measuring NEPI and NUAF on two simultaneously acquired PSFs. Both these PSFs can thus be used to compute the lateral 2D super-localization with a good signal-to-noise ratio. Indeed, whereas the number of UAF photons N_{UAF} remains nearly constant as a function of the interface-fluorophore distance d , the number of SAF photons N_{SAF} decreases approximately exponentially (Ruckstuhl et al., 2003). Meaning that the simultaneous measurement of N_{SAF} and N_{UAF} and the computation of the fluorophore SAF ratio $\rho_{SAF} = \frac{N_{SAF}}{N_{UAF}}$ for each detected fluorophore allows for determining the absolute axial position of the fluorophore, d .

DONALD module uses a beamsplitter to split the fluorescence emission into two imaging paths (Fig. 3.11). The first EPI path is directly imaged on half of the EMCCD detector and is used to compute N_{EPI} for a given PSF. On the second path, the SAF ring is blocked out in the image plane of the objective back focal plane in order to generate a corresponding UAF-only PSF on the other half of the EMCCD detector. N_{UAF} is computed from this image.

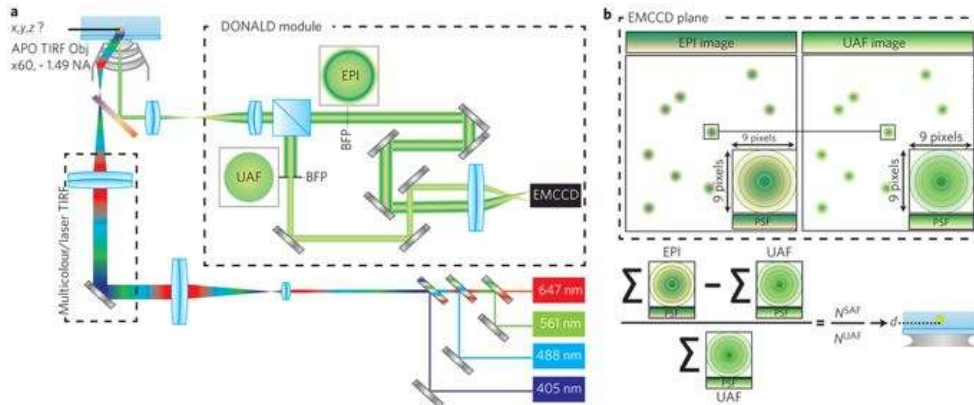


Figure 3.11.: Direct optical nanoscopy with axially localized detection setup and data analysis. A laser TIRF stage is connected to the input of a conventional wide field microscope. TIRF excitation light passes through a 4 color filter-set and an apochromatic TIRF objective of high numerical aperture. The fluorescence emission of dye molecules is collected by the objective and reflected to the DONALD module which splits the fluorescence into two parts: the EPI part is directly imaged on one half of the camera, and the UAF part is recorded on the other half (left). First, in the UAF and EPI portions of the frame, each PSF is super-localized in 2D and the number of UAF and EPI photons are computed *via* signal integration. Then, SAF ratio is computed and converted into the absolute dye depth d . (right) Adapted from Bourg et al., 2015

When a fluorophore is imaged on both paths, it is first super-localized in 2D using a wavelet segmentation algorithm (Izeddin et al., 2012). Then, N_{EPI} and N_{UAF} are quantified *via* numerical integration within a PSF region of 9×9 pixels. $\rho_{SAF}(d)$ is then computed to determine the depth d of the fluorophore. The precision of axial localization depends on both observation medium and glass

coverslip optical indices and the signal-to-noise ratio (SNR) which is defined as $SNR = \frac{I_{EPI_{max}}}{\sqrt{2\pi I_{EPI_{max}}}}$, where $I_{EPI_{max}}$ is the maximum intensity of the EPI PSF (Izeddin et al., 2012). The dependence of SAF ratio, and thus of axial localization precision, on SNR value is represented in Figure 3.11. Within this configuration, DONALD achieves an iso-3D nanometer resolution, yielding the absolute axial position of the fluorophores with a precision of approximately 15 nm (Bourg et al., 2015).

Suitability of PAA properties with experimental setup

As stated previously, PAA has been widely used in the context of TFM experiments, and as such its binding to glass protocol is well-documented. The main stages presented in the following paragraph have been adapted from previous works (Tse et al., 2010; Aratyn-Schaus et al., 2010; Colin-York et al., 2017) (Fig. 3.12).

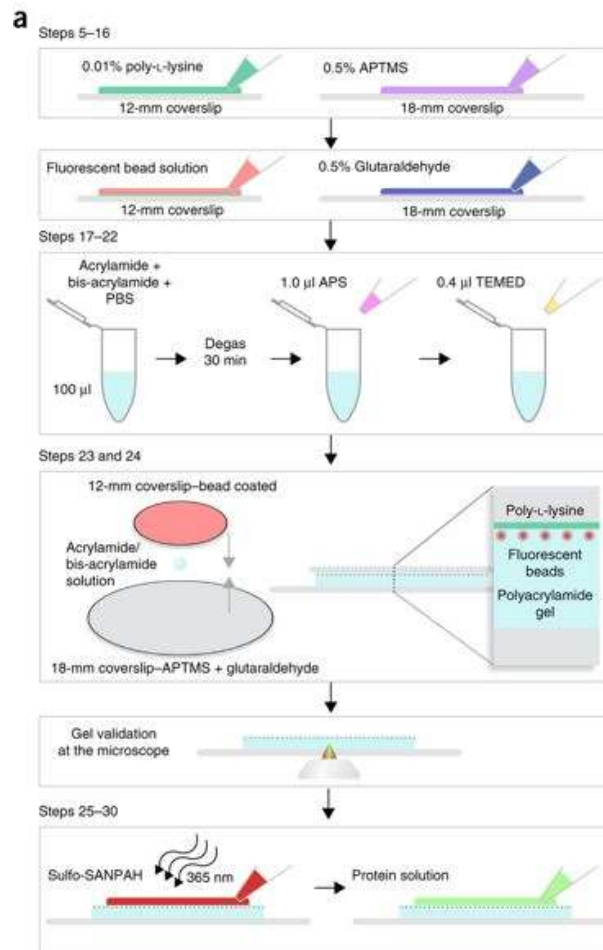


Figure 3.12.: Main steps for the preparation of polyacrylamide-coated coverslips for a traction force microscopy experiment. Adapted from Colin-York et al., 2017

First is a cleaning step of glass coverslips, in order to rid their surface of all impurities and to boost its hydrophilicity. For our study, the coverslips which were to be coated with PAA were chosen for their adequacy with super-resolution imaging technique DONALD. Marienfeld high-precision borosilicate glass coverslips with the thickness no. 1.5H ($170 \pm 5 \mu\text{m}$) and 25 mm diameter were chosen. The cleaning was carried out using RBS diluted to 2% in deionized water, the solution was heated up to approximately 80°C under magnetic stirring and coverslips were immersed for 10 minutes. An additional set of typical culture 30 mm diameter coverslips were cleaned alongside with the high-precision ones, for later use in the protocol. All coverslips were then rinsed in deionized water three times, then once in 70% ethanol.

Next is a surface chemistry modification of the high-precision glass coverslips. Coverslips were first incubated with (3-aminopropyl)trimethoxysilane (APTMS) diluted to 10 % in deionized water for 10 minutes. They were rinsed three times in deionized water under agitation. They were then incubated with glutaraldehyde diluted to 0.5 % in deionized water for 45 minutes at room temperature and under a light shielding atmosphere. Lastly, coverslips were rinsed once in deionized water and left to dry under a chemical hood. This coverslip silanization step is necessary to ensure a good attachment between the PAA gel and the underlying glass substrate. The APTMS treatment grafts a $\text{Si}(\text{CH}_2)_3\text{NH}_2$ chain onto the previously hydrated glass surface. Then, the primary amine group reacts with one of both glutaraldehyde aldehyde groups, which leaves an activated glass surface able to react with PAA presenting amine groups. The 30 mm diameter coverslips were not submitted to this silanization step.

PAA gel is prepared from 40% acrylamide and 2% N,N'-methylenebis(acrylamide) (bis-acrylamide) stock solutions, diluted and mixed in deionized water according to the desired properties of the gel. In this work, only two working solutions were used, in order to give PAA hydrogels with Young's modulus value of 10 kPa and 40 kPa. The respective acrylamide/bis-acrylamide ratios corresponding to these respective material properties were extracted from Tse and Engler recapitulative table in (Tse et al., 2010). In order to initiate and maintain the radical polymerization process, ammonium persulfate (APS) 10% solution and tetramethylethylenediamine (TEMED) were added to the solution with a specific care not to induce bubbles. After careful homogenization of the solution, a given volume was pipetted and deposited on the surface of an untreated coverslip. The solution droplet was then sandwiched between the activated high-precision coverslip and the other non-reactive cover glass, and left to polymerize for approximately 10 minutes under a chemical hood. When the unused remnant PAA solution appeared fully polymerized, the sandwiches were placed in deionized water for an additional 10 minutes in order to rehydrate the gel and facilitate the subsequent sandwich separation. The untreated 30 mm diameter coverslip was removed from the top of the gel by carefully sliding a scalpel blade along the in-between space, and gently lifting the cover glass until full detachment. Lastly, PAA-coated high-precision coverslips were left to further hydrate in deionized water before characterization.

PAA optical index was elementarily measured in a refractometer by allowing PAA solution to polymerize inside the observation chamber. Indices for two PAA solutions leading to 10 kPa and 40 kPa gels were evaluated, along with deionized water as control solution. This simple experiment

yielded that both PAA gel displayed the same optical index - approximately 1.35 - independently of their Young's modulus value. What is more, this optical index value is close enough to that of water - namely approximately 1.33 - to allow for use of PAA with DONALD setup for single molecule localization microscopy.

In order to estimate possible thickness inhomogeneities due to local roughness, PAA surface topography was assessed thanks to AFM measurements. A thick coating of PAA was bound to glass slides as previously described, with two different Young's moduli associated coatings. Coating top surface was imaged with a Bruker JPK NanoWizard III AFM stage mounted on a Zeiss Axiovert 200 inverted microscope, and equipped with a Veeco MLCT-AUHW tip mounted on a silicon nitride cantilever, immersed in deionized water. During imaging the tip velocity was set to approximately 100, 10 or $1 \mu\text{m}\cdot\text{s}^{-1}$ depending on the probed area, and the line rate ranged from 0.5 to 1 Hz, according to the signal quality. For each sample, three images were acquired of respective dimensions $100*100$, $10*10$ and $1*1 \mu\text{m}^2$. Acquisitions were post-processed using JPK Data Processing software. Third degree polynomial fits were subtracted from each scan line independently and using limited data range [0%,70%], as well as error pixel values were replaced with the median of neighboring pixels in order to improve the images for statistical analysis. For each image, root mean squared roughness was assessed on four squares representing approximately a third of the total acquired surface. Results are shown in Figure 3.13. For both PAA coatings, independently of their material properties, roughness appeared to decrease with the probed area. Values were approximately two orders of magnitude lesser than the desired coating surface, confirming that measured thicknesses were widely distributed due to defects in global planarity of the polymerized gel surface. Furthermore, these results demonstrated that root mean squared roughness was increased for the 40 kPa gel, compared to the 10 kPa. This hinted at an increase of roughness depending on the acrylamide/bis-acrylamide ratio, and is consistent with Stellwagen's study of pore sizes according to acrylamide/bis-acrylamide ratio (Stellwagen, 1998).

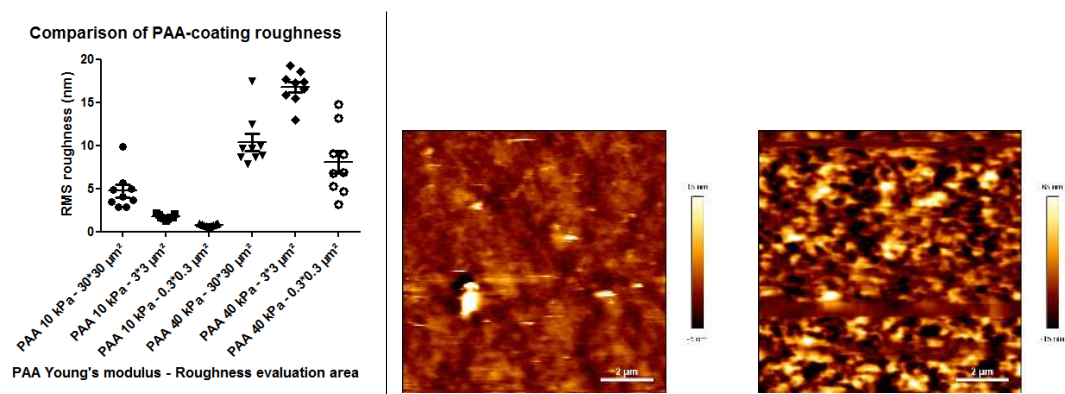


Figure 3.13.: Comparison of two polyacrylamide coating roughness with AFM (left), and the corresponding acquisitions for $10*10 \mu\text{m}^2$ areas for Young's modulus value of 10 kPa (center) and 40 kPa (right). For the statistics corresponding to each dataset, see Table 3.1.

Table 3.1.: Roughness (nm) analysis of polyacrylamide gels with Young’s modulus value of 10 kPa or 40 kPa.

	Mean	Median	Std Deviation
PAA 10 kPa - 30*30 μm^2	4.721	4.108	2.172
PAA 10 kPa - 3*3 μm^2	1.723	1.503	0.284
PAA 10 kPa - 0.3*0.3 μm^2	0.784	0.746	0.149
PAA 40 kPa - 30*30 μm^2	10.36	9.632	2.977
PAA 40 kPa - 3*3 μm^2	16.77	17.28	1.876
PAA 40 kPa - 0.3*0.3 μm^2	8.073	6.881	3.858

Forming a thin layer of PAA bound to glass coverslip

PAA-coated sample heights were extensively characterized through the use of a mechanical profilometer in a clean room facility. PAA coating was scratched in order to reveal the glass surface underneath previous to height measurements. The height difference between the glass and the top of the coating was assessed on a few localizations along both sides of the scratch border. The scan parameters were set to an applied force of 1 mg on a scan length of approximately 400 μm , with a scan speed of 5 $\mu m.s^{-1}$ and a sampling rate of 50 Hz. The height difference values were assessed far from the border area. The hydration level of the hydrogel was tuned so that excess water did not hinder profilometer measurements, and at the same time as the characterized gel was ascertained not to be dry.

Sandwich coating technique - The first approach to decrease the thickness of the PAA coating was rather simple as it consisted in decreasing the volume of deposited solution before polymerization. The PAA solution volumes pipetted onto coverslips ranged from 15 μL to 1 μL , and the corresponding coating thicknesses were evaluated with a mechanical profilometer, as described above. The results are gathered in the graph presented in Figure 3.14. Briefly, as both 15 and 10 μL droplets yielded a PAA coating approximately 2 μm thick, drastic decrease of the volume to 2 and 1 μL resulted in thicknesses ranging from 800 to approximately 150 nm . However, for each deposited volume, the thickness distribution spanned a large range between samples, but also when considering a single coating. This feat highlighted the presence of surface inhomogeneities over the whole samples, probably due to a major lack of planarity.

The PAA solution volume was further decreased to 0.5 μL and assessed both with the mechanical profilometer and with DONALD setup. To do so, after the final rehydration step of the gel, submicron-sized fluorescent beads were pipetted onto the PAA coating surface and left to settle in the presence of poly-L-lysine. The beads were then observed using DONALD, and axially localized following the same protocol as for SAF calibration routine (Bourg et al., 2015). The same samples were scratched and assessed for PAA gel thickness with the mechanical profilometer. The results are displayed in Figure 3.15, and show that both measurement techniques yield the same tickness

Polyacrylamide height measurements for manual spreading

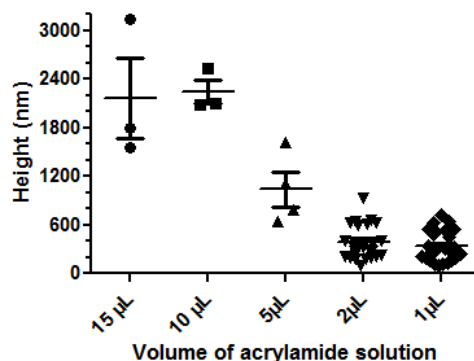


Figure 3.14.: Polyacrylamide thickness measurements by profilometry, corresponding to the deposition of a decreasing solution volume.

range. What is more, with this drastically reduced volume, PAA coatings approximately 200 nm thick were apparently achievable, yet prone to poor reproducibility.

Comparison between profilometre and DONALD polyacrylamide height measurements

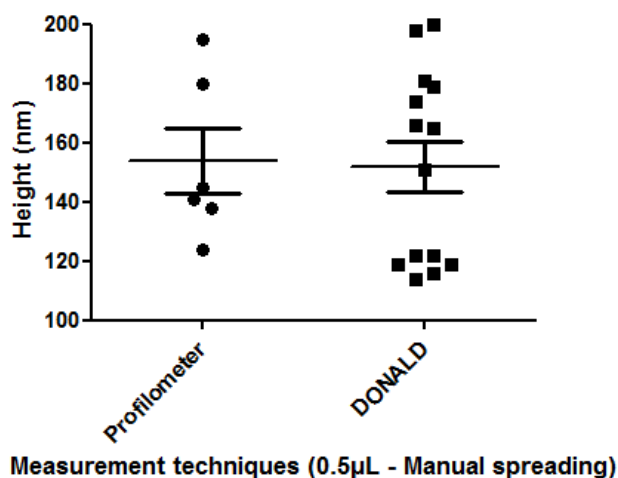


Figure 3.15.: Polyacrylamide thickness measurements performed by either profilometry or with DONALD setup, corresponding to the deposition of a 0.5 μL solution volume.

PAA coating with a nano-imprint machine - Given the obvious lack of reproducibility in assigning a restrained range of coating thickness to a given PAA solution volume, improvements

in homogeneously spreading the gel were explored. The adopted approach consisted in axially constraining the sandwich during the polymerization process. To do so, samples were placed in a nano-imprint NANONEX machine upon the initiation of vinyl addition polymerization. The general concept of nano-imprinting is based on applying pressure on membranes, in between which the sample is placed and submitted to an equally distributed constraint. This homogeneous pressure ensures the pattern transfer from the mold to the sample being shaped. Here, the coverslip standing in place of the mold is the untreated coverslip, which is supposed to transfer its flat surface onto the polymerizing PAA. The nano-imprint process main stages are as follows: first pressure is decreased between the membranes by pumping, then a pre-imprint pressure is progressively applied to the system before the main imprint phase is started, with an applied pressure value greater than the pre-imprint one, finally the whole system is ventilated in order to reach back atmospheric conditions. Thermic treatment of the samples can be implemented as both pre-imprint and imprint phase temperatures can be set and monitored, as well as UV-treatment can be performed with a given exposition dose during the imprint stage.

The first experiments solely explored the influence of the imprint phase pressure on the homogeneity of the measured coating thicknesses. To do so, 4 imprint conditions were tested: pre-imprint pressure was set to either 120 PSI or 50 PSI; imprint pressure values were assigned to either 400, 200, 100 or 50 PSI; and imprint phase duration was fixed for 5 minutes. A droplet of 2 μL of PAA solution was pipetted onto the untreated coverslip, covered with an activated high-precision coverslip and placed in between the membranes. The polymerized gel was then allowed to rehydrate in deionized water before and after sandwich separation, following the same protocol as described earlier. Surprisingly, increasing the pressure during the imprint phase did not induce decrease of coating thickness. Furthermore, no specific pressure combination seemed to yield a tightened distribution of measured thicknesses. The results are presented in Figure 3.16.

Given the previous results, another approach was to modify other peripheral imprint parameters. The various tested conditions were:

- PAA solution was forced to spread on a wider area by sliding the two coverslips relatively to each other,
- two silicon wafers were placed additionally to the membranes in order to provide samples with a firmer and flatter base,
- pumping time was set to last 1 minute in order to increase the vacuum between the membranes prior to the imprinting process,
- temperature was arbitrarily increased to 60°C during the main imprint phase.

As before, samples were allowed to rehydrate before thickness measurements were carried out. The results are summarized in Figure 3.17. The only imprint condition which gave highly reproducible results was the condition in which pumping was performed prior to increasing the applied pressure on the membranes. However, the resulting mean thickness was still greater than the desired range of 200 to 300 *nm*.

In order to decrease the thickness of the coating, further experiments were carried out in which either the deposited PAA solution volume was decreased to 0.5 μL , or the pumping time was increased

Polyacrylamide height measurements for $V = 2\mu\text{L}$

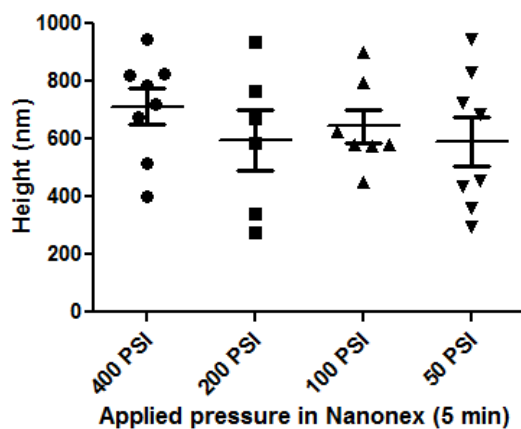


Figure 3.16.: Polyacrylamide thickness measurements by profilometry, depending on the applied pressure with NANONEX machine, corresponding to the deposition of a $2\mu\text{L}$ solution volume.

Polyacrylamide height measurements

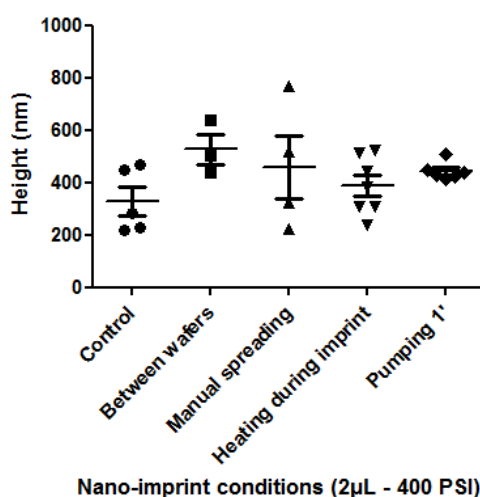


Figure 3.17.: Polyacrylamide thickness measurements by profilometry, depending on the nano-imprint conditions with NANONEX machine, corresponding to the deposition of a $2\mu\text{L}$ solution volume. For the statistics corresponding to each dataset, see Table 3.2.

from 1 to 2 minutes. However, no coating thickness measurements could be recorded in these cases as the gel strangely appeared too hard to scratch on some samples, as if it had crystallized. From this observation, the 2 minute pumping condition was discarded as it was hypothesized that the sudden plummeting of the pressure between the membranes might alter the PAA solution properties

Table 3.2.: Thickness (nm) analysis of polyacrylamide gels shaped with NANONEX machine, with varying process conditions.

	Mean	Median	Std Deviation
Control	329.4	282	121.4
Between wafers	527	503	101.2
Manual spreading	457.3	419.5	240.9
Heating during imprint	388.6	383	108.8
Pumping 1 min	442.7	433	35.21

and interfere with its polymerization process. Instead, experiments were again carried out combining pumping prior to imprint and mild heating during the imprint phase.

For this set of experiments, PAA coating thicknesses were solely assessed with DONALD imaging, as described in the previous paragraph. The tested deposited volumes were $1 \mu L$ and $2 \mu L$, and the thickness measurement results are displayed in Figure 3.18. Surprisingly so, once again the various imprint conditions yielded approximately the same mean coating thickness. However, in this particular case, the desired coating thickness was obtained. What is more, the condition in which $1 \mu L$ of PAA solution was placed between coverslips to polymerize with the following imprint parameters:

- pumping for 1 minute,
- pre-imprint pressure of 120 PSI, at room temperature,
- imprint pressure of 400 PSI, at $50^\circ C$, for 5 minutes,
- venting at $55^\circ C$,

appeared as the optimal protocol to obtain highly reproducible $200 nm$ thick PAA coatings.

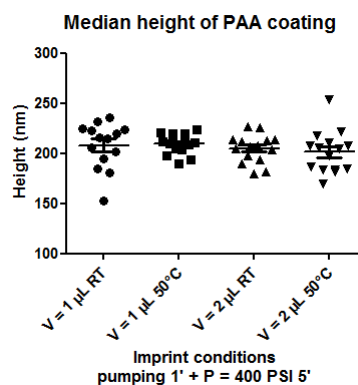


Figure 3.18.: Polyacrylamide thickness measurements by profilometry, depending on the thermal nano-imprint conditions with NANONEX machine, and the deposition of a decreasing solution volume. For the statistics corresponding to each dataset, see Table 3.3.

Table 3.3.: Thickness (nm) analysis of polyacrylamide gels shaped with NANONEX machine, with varying process temperature and solution volume.

	Mean	Median	Std Deviation
$V = 1\mu L$ RT	208.1	215.5	23
$V = 1\mu L$ 50°C	209.5	211	9.98
$V = 2\mu L$ RT	204.9	207	14.05
$V = 2\mu L$ 50°C	201.5	205	20.93

Blinking ability of fluorescent markers in PBS

As the objective of PAA coating thickness was seemingly achieved, the embedding of displacement markers was next explored.

Testing FluoroNanogold - Here, instead of usual submicron fluorescent beads, gold nanoparticles covalently coupled with approximately 2-3 Alexa Fluor (AF) molecules were made use of. Alexa Fluor 488 and 647 FluoroNanogold reagents consist of affinity-purified Fab' fragments conjugated to both Alexa Fluor (AF) 488 or 647 dye and the 1.4 nm Nanogold particle (Fig. 3.19) (Liu et al., 2002). Both AF488 and AF647 fluorophores were tested, as AF647 is typically used in single molecule localization microscopy routines and early first-hand explorations revealed that phalloidin AF488-staining of cells observed in PBS displayed a blinking emission pattern, possibly suitable for single molecule detection. First observation tests were carried out by simply letting Fluoronanogold particles settle on clean glass coverslips, and observing them with DONALD setup in PBS. Qualitative analysis of the acquisitions revealed that while AF488-coupled Fluoronanogold probes seemed to blink, AF647-coupled Fluoronanogold probes showed more photobleaching events than real on-and-off switch cycles. Hence, AF488-coupled Fluoronanogold probes were further used in this study.

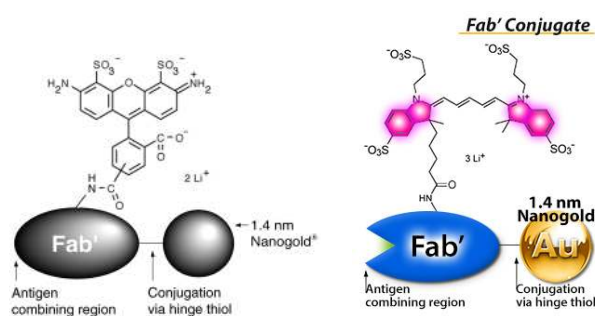


Figure 3.19.: Schematic representation of Alexa Fluor 488-coupled Fluoronanogold particle (left), and Alexa Fluor 647-coupled Fluoronanogold particle (right). Adapted from the commercial website www.nanoprobes.com.

A first approach consisted in mimicking typical TFM protocols, in which the fluorescent beads used as markers are spin-coated onto the inactivated coverslip prior to forming the PAA sandwich. This allows the fluorescent beads to be adsorbed into the topmost part of the gel when it is polymerizing. Fluoronanogold coupled with Alexa Fluor 488 were diluted at either 1/1000 or 1/500 in poly-L-lysine, and spin-coated at speed 400 rpm and acceleration 200 rpm.s⁻¹. They were then used in PAA sandwiches as was described earlier. Some coverslips were kept as they were after spin-coating, in order to compare the ratio of transferred fluorescent particles during polymerization (Fig. 3.20). However, observation of the different coverslips showed that few particles really did blink when embedded in the gel, and that continuous background noise hindered fluorophore optimal detection.

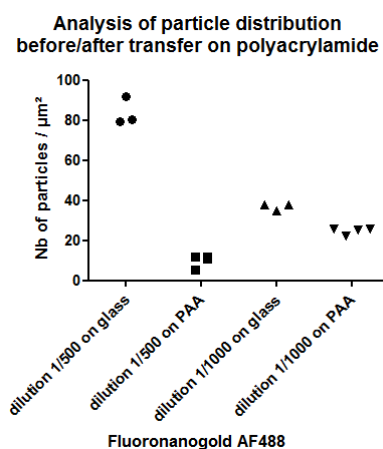


Figure 3.20.: Analysis of particle distribution before and after transfer on polyacrylamide gels, for two dilutions of AF488-coupled Fluoronanogold particles.

Testing Alexa Fluor fluorophores - Possible use of other Alexa Fluor coupled probes was then investigated. Fluoronanogold probes were compared to AF-coupled secondary antibodies and AF488-coupled cadaverine, which were directly grafted on the glass coverslips after air plasma treatment of their surface for 5 minutes, with 50 W power and 0.5 mbar pressure. Another approach consisted in covalently binding the fluorescent markers directly onto the surface of the PAA coating. This approach presented the main advantages of theoretically increasing the marker surface density as it would directly depend on the availability of free binding groups, and of limiting the potential direct interaction of cells with markers that would not have been well embedded in the gel, thus decreasing the probability of overestimating or misplacing the resolved deformations. To do so, sulfosuccinimidyl 6-(4'-azido-2'-nitrophenylamino)hexanoate (sulfo-SANPAH) provided a well-suited adaptor to create a covalent link between PAA surface and potential fluorescent markers. Indeed, sulfo-SANPAH is a hetero-bifunctional cross-linker, that contains two amine-reactive groups:

- a N-hydroxysuccinimide (NHS) ester group which reacts efficiently with primary amino groups (-NH₂) in pH 7-9 buffers to form stable amide bonds;

- a photoactivatable nitrophenyl azide group, which notably forms subsequent ring expansion to react with a nucleophile (*e.g.*, primary amines) upon activation by UV light exposition at 320-350 nm.

After the last rehydration phase described in the previous paragraphs, PAA coatings were rinsed once in a HEPES 0.1 mol.L⁻¹ solution buffered at pH=8.5. They were then incubated with sulfo-SANPAH diluted in HEPES and exposed to 365 nm UV light with a power of 120 W, during 10 minutes. The gels were then rinsed three times in the same basic HEPES solution, and submitted to another UV-exposition cycle in the presence of sulfo-SANPAH. The samples were finally rinsed three times with HEPES, and once with deionized water.

All samples were incubated with their respective fluorescent marker solution overnight to ensure a high attachment ratio, and were subsequently imaged with DONALD setup in PBS. Two exposure times were tested: 50 ms and 200 ms, in order to possibly counterbalance slow blinking dynamics, while keeping a similar total acquisition duration. The acquisitions were then quantitatively contrasted based on their median photon number counts emitted during the whole imaging timespan (Fig. 3.21). For all fluorescent markers, an increase in median photon number is obtained with a longer exposure time, as expected. The best results were obtained with AF488-coupled cadaverine grafted on PAA *via* sulfo-SANPAH crosslinking.

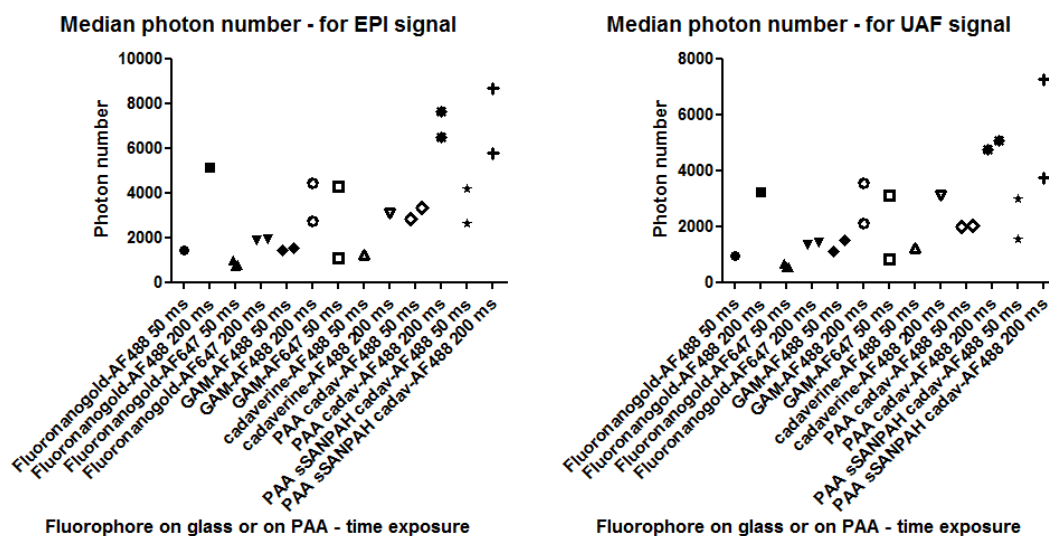


Figure 3.21.: Median photon number corresponding to EPI signal (left), and UAF signal (right), depending on the exposure time of polyacrylamide gels coated with various fluorescent markers.

This mode of integrating fluorescent probes was further explored by varying exposure times from 25 ms to 200 ms, while still keeping a similar total acquisition duration. Acquisition results were again quantified for median EPI and UAF photon numbers (Fig. 3.22). While seemingly optimal mean inter-fluorophore distance was achieved with the highest temporal rate, the emitted photon

numbers for both EPI and UAF signals represented less than half of what had been detected with lesser temporal acquisition rate. This was also coupled with greater background noise, meaning minimal SNR values and thus poor detection efficiency. Hence, and as the three other exposure conditions appeared to yield similar results, the 50 ms time exposure was elected as the best-suited exposure time. Indeed, it allowed for a good SNR value, with an inter-fluorophore distance just above the lateral localization precision and a satisfactory acquisition rate for observing dynamic events.

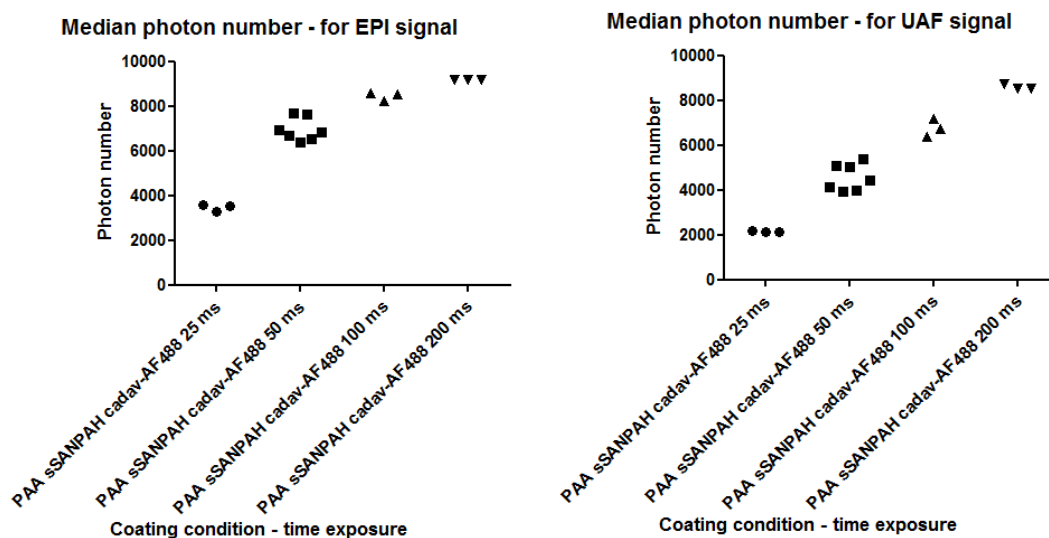


Figure 3.22.: Median photon number corresponding to EPI signal (left), and UAF signal (right), depending on the time exposure of polyacrylamide gels coated with AF488-coupled cadaverine.

Testing optimal observation conditions

Having found an apparently suitable way to graft fluorescent markers on top of the PAA coating, it was next explored which observation conditions were optimal with the DONALD microscopy setup. To do so, the sample preparation followed the same coverslip cleaning and activating steps, as well as:

- 10 kPa PAA coating of the high-precision coverslip with the usual sandwich technique, pipetting only a $0.5 \mu\text{L}$ volume of solution and spreading it by sliding the coverslips before letting it polymerize;
- surface activation of PAA through grafting of sulfo-SANPAH under UV light to make it reactive to primary amine groups;
- coating of the PAA surface with the fluorescent marker and/or with an ECM protein.

For this set of experiments, it is noticeable that the PAA coating of the coverslips was once again performed manually and not using NANONEX nano-imprint machine, in order to simplify the time-

consuming protocol. What is more, as for this phase of the study PAA coatings were destined for cell culture, all stages of the protocol were performed under a sterile hood, all solutions were sterile filtered with $0.2 \mu\text{m}$ membrane filters and deionized water was replaced with sterile distilled water.

Optimal ECM coating and fluorophore embedding for cell adhesion - In order to confirm the previous choice of ECM protein to use for coating the PAA gels, tests were carried out on 3T3 fibroblasts. PAA gels were prepared until the sulfo-SANPAH activation step as described previously, then were incubated with various combinations of solutions:

- AF488-coupled cadaverine (1/1000) and Arg-Gly-Asp peptide (RGD, $10 \mu\text{g.mL}^{-1}$) mixed together in sterile distilled water;
- AF488-coupled cadaverine (1/1000) and fibronectin ($10 \mu\text{g.mL}^{-1}$) mixed together in sterile distilled water;
- AF488-coupled cadaverine (1/1000) only, then RGD ($10 \mu\text{g.mL}^{-1}$);
- AF488-coupled cadaverine (1/1000) only, then fibronectin ($10 \mu\text{g.mL}^{-1}$);
- AF488-coupled cadaverine (1/1000) only, as a negative control.

The first incubation time was set to overnight in a light-blocking case under a sterile, then for the additional coatings the incubation time was set to 3 hours in the same conditions. PAA gels were rinsed once in sterile distilled water before being placed in contact with the additional ECM protein coating solution.

After all coatings were done, PAA gels were rinsed once with sterile distilled water, once with warm serum-supplemented culture medium (DMEM), and were eventually left to soak in culture medium in an incubator (37°C , 5% CO_2 , humidity controlled) for at least 3 hours. Cells were prepared for seeding on the gels, aiming at approximately 5000 cells per PAA gel and left to adhere in serum-deprived medium for 15 minutes, then serum-supplemented medium was added to the culture wells.

Overall, 3T3 fibroblasts were left to adhere on the coated PAA gels for 2 hours before fixation with a paraformaldehyde and sucrose in PBS solution. They were then stained with TexasRed-coupled phalloidin and observed with a wide field fluorescence microscope (LEITZ DMRB, Leica) equipped with an oil immersion 63x objective. At least a dozen cell images were blindly acquired for each condition, except for the negative control coverslip on which very few cells were adherent. Acquisitions were analyzed with ImageJ Threshold and Analyze Particles tools in order to evaluate cell area and cell circularity for each condition. The results for one experiment are presented in Figure 3.23. As expected, only coating PAA with AF488-coupled cadaverine yielded low spreading areas along with rounded cells, indicating that this condition was not optimal for TFM-oriented cell observation. When comparing RGD with fibronectin coating directly mixed with AF488-coupled cadaverine, not one ECM protein seemed to surpass the other. However, when comparing RGD and fibronectin coating subsequent to AF488-coupled cadaverine, fibronectin appeared to faintly improve spreading of elongated cells, as is expected of fibroblastic phenotypes. Notwithstanding this slight difference, it appeared that any of the ECM protein and fluorescent marker coating condition would be adapted to TFM-oriented observations. For the following experiments, RGD was then solely used

for ECM protein coating.

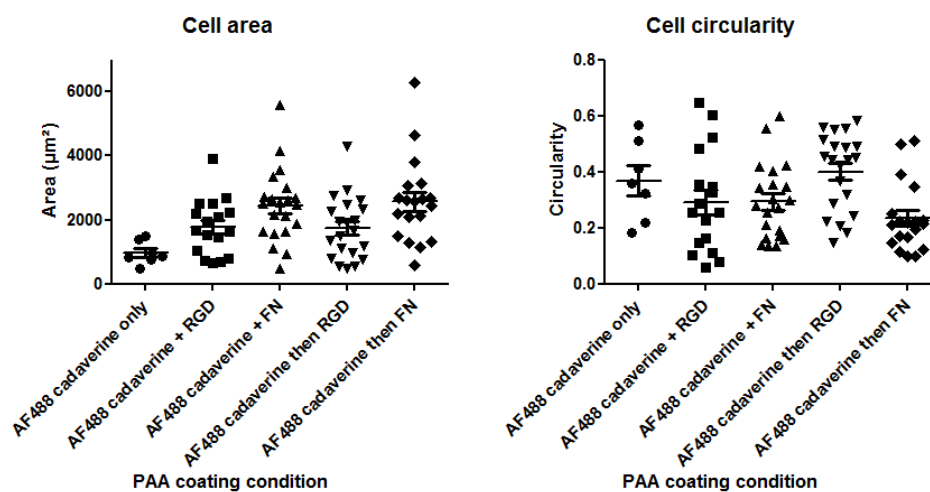


Figure 3.23.: Measurements of 3T3 fibroblast cell area (left), and cell circularity (right), depending on the coating conditions of polyacrylamide gels coated with AF488-coupled cadaverine and ECM protein. For the statistics corresponding to each dataset, see Table 3.4 for cell area, and Table 3.5 for cell circularity

Optimal ECM coating and fluorophore embedding for observation - On the other hand, another set of PAA gels were coated with AF488-coupled cadaverine and RGD as described for cell seeding, but were directly observed with DONALD microscopy setup in various conditions. AF488-coupled cadaverine was tested with two dilutions: 1/500 and 1/1000 with or without being coated alongside RGD, samples were observed in PBS or in FluoroBrite medium, and were imaged either at room temperature or in a 37°C temperature controlled environment. FluoroBrite medium was chosen for this set of tests as it features a background fluorescence that is comparable to PBS and 90% lower than that emitted by standard phenol red-free DMEM, while being completely suitable

Table 3.4.: Area (μm^2) analysis for 3T3 fibroblasts plated on polyacrylamide gels, depending on the gel coating conditions.

	Mean	Median	Std Deviation
AF488 cadaverine only	964.8	871	355
AF488 cadaverine + RGD	1775	1669	878
AF488 cadaverine + FN	2445	2509	1138
AF488 cadaverine then RGD	1733	1683	971
AF488 cadaverine then FN	2572	2568	1318

Table 3.5.: Circularity analysis for 3T3 fibroblasts plated on polyacrylamide gels, depending on the gel coating conditions.

	Mean	Median	Std Deviation
AF488 cadaverine only	0.368	0.359	0.142
AF488 cadaverine + RGD	0.292	0.255	0.182
AF488 cadaverine + FN	0.293	0.277	0.134
AF488 cadaverine then RGD	0.401	0.444	0.137
AF488 cadaverine then FN	0.233	0.214	0.121

for cell culture. It is also advertised for its providing enhancement of fluorescence signal during live-cell imaging.

The same samples were then observed twice at room temperature with either PBS or FluoroBrite medium, then twice again at $37^{\circ}C$ with either PBS or FluoroBrite. Acquisition parameters were set as follows, and were kept unchanged for all samples in a series of observations:

- exposure time was 50 ms;
- ROI size was 300*300 px;
- laser power was 50% of its maximum dose;
- TIRF depth ranged from 120 to 130 *nm* depending on experimentation series;
- 2000 images were acquired on three different zones on each samples.

Acquisitions were then post-processed using NEMO Software for super-localization and drift-correction steps, and molecule coordinates were further filtered to suppress cases of multiple axial detection of the same fluorescent marker. Resulting images were treated with ImageJ Analyze Particles tool. From these analyses, parameters were extracted in order to assess for optimal observation conditions, and are listed thereafter:

- median EPI and UAF photon number to characterize the emission efficiency of fluorescent markers;
- surface density of fluorescent markers, and mean inter-molecule distance to estimate the in-plane attainable displacement resolution.

The results for each of these parameters are presented in graphs shown in Figure 3.24 for RT experiments, and in Figure 3.25 for $37^{\circ}C$ experiments. The values from two independent sample sets were pooled to obtain these graphs. Examination of the various results yielded two optimal observation conditions:

- for room temperature observation, coating the PAA gels with AF488-coupled cadaverine diluted at 1/500 and mixed with RGD, and imaging them in PBS lead to greater values of EPI and UAF photon numbers, as well as a high density of fluorescent marker coupled with a mean inter-particle distance of approximately 50 *nm*;
- for $37^{\circ}C$ observation, the same coating this time imaged in FluoroBrite medium gave the best EPI and UAF photon number values along with a restrained axial distribution, high

in-plane particle density and minimal inter-marker distance of approximately 50 nm. These encouraging results supported two conclusions:

- the optimal PAA gel observation is obtained when coating PAA with a mix of fluorescent markers and ECM protein, and imaging the hydrogel in FluoroBrite medium at 37°C - as it is the temperature that will be prescribed for cell experiments;
- observing the PAA hydrogels in a heated environment did not significantly decrease the observation and localization efficiency of the DONALD setup, which hints at its suitability to be used in live cell contexts.

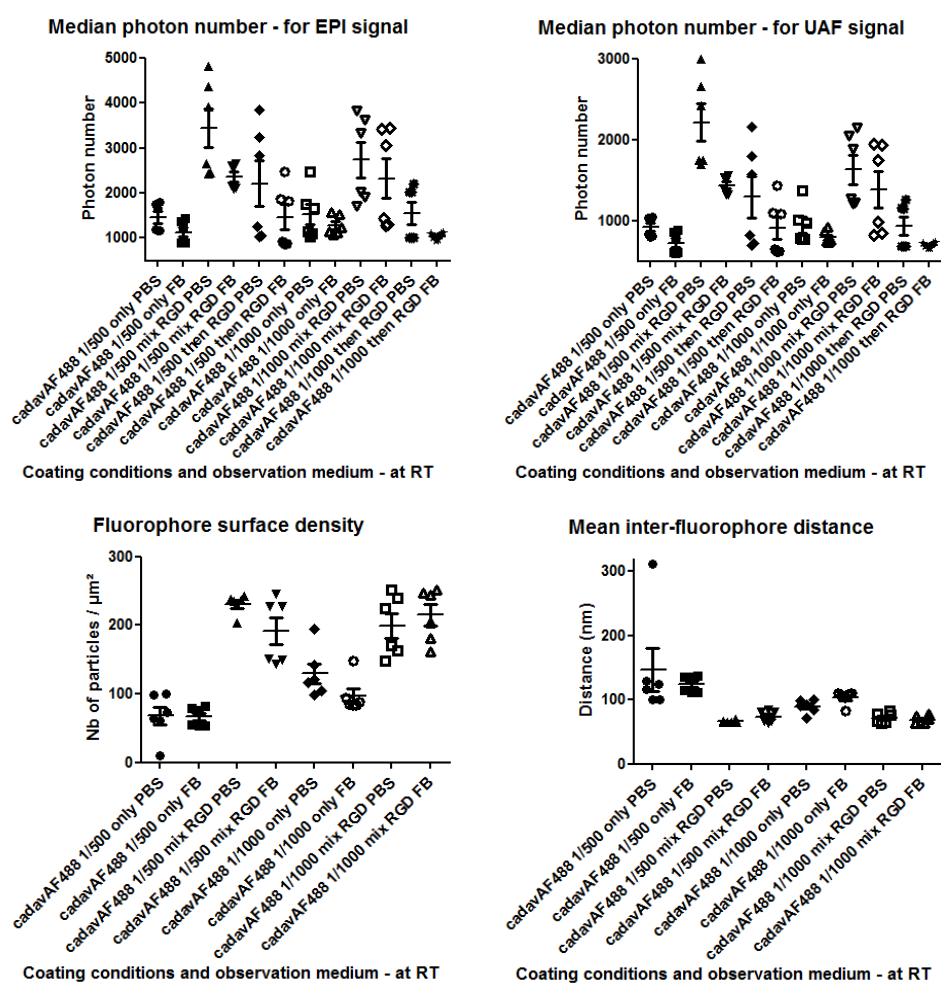


Figure 3.24.: Quantification of useful observables for TFM imaging: fluorescence emission efficiency and fluorescent marker distribution, depending on AF488-coupled cadaverine-coating conditions and observation medium, at room temperature. For the statistics corresponding to each dataset, see Table 3.6 for EPI photon numbers; Table 3.7 for UAF photon numbers; Table 3.8 for fluorescent marker density; Table 3.9 for mean inter-marker distance

Table 3.6.: Median EPI photon number analysis for observation conditions at room temperature

	Mean	Median	Std Deviation
cadavAF488 1/500 only PBS	1458	1427	311.5
cadavAF488 1/500 only FB	1128	1080	257.2
cadavAF488 1/500 mix RGD PBS	3440	3286	1059
cadavAF488 1/500 mix RGD FB	2368	2363	272.5
cadavAF488 1/500 then RGD PBS	2208	2035	1242
cadavAF488 1/500 then RGD FB	1468	1360	678.5
cadavAF488 1/1000 only PBS	1529	1402	557.1
cadavAF488 1/1000 only FB	1282	1188	219.4
cadavAF488 1/1000 mix RGD PBS	2737	2671	959
cadavAF488 1/1000 mix RGD FB	2324	2248	1093
cadavAF488 1/1000 then RGD PBS	1550	1518	587.7
cadavAF488 1/1000 then RGD FB	1043	1057	81.14

Table 3.7.: Median UAF photon number analysis for observation conditions at room temperature

	Mean	Median	Std Deviation
cadavAF488 1/500 only PBS	919.8	913	119.9
cadavAF488 1/500 only FB	726.5	705	134.1
cadavAF488 1/500 mix RGD PBS	2219	2091	560.2
cadavAF488 1/500 mix RGD FB	1440	1446	106.5
cadavAF488 1/500 then RGD PBS	1298	1199	632.6
cadavAF488 1/500 then RGD FB	914.8	861.5	338.5
cadavAF488 1/1000 only PBS	948.7	877	234.7
cadavAF488 1/1000 only FB	793.7	749	83.07
cadavAF488 1/1000 mix RGD PBS	1636	1586	443.8
cadavAF488 1/1000 mix RGD FB	1383	1366	550.9
cadavAF488 1/1000 then RGD PBS	936.7	918.5	276.9
cadavAF488 1/1000 then RGD FB	695.5	701	30.91

Table 3.8.: Fluorescent marker density (μm^{-2}) analysis for observation conditions at room temperature

	Mean	Median	Std Deviation
cadavAF488 1/500 only PBS	67.83	68.81	32.82
cadavAF488 1/500 only FB	66.46	65.1	13.64
cadavAF488 1/500 mix RGD PBS	230.6	235.8	13.82
cadavAF488 1/500 mix RGD FB	191	189.4	47.3
cadavAF488 1/1000 only PBS	129.4	118.4	34.97
cadavAF488 1/1000 only FB	97.26	86.92	25.28
cadavAF488 1/1000 mix RGD PBS	199.2	197.2	44.19
cadavAF488 1/1000 mix RGD FB	214.9	223.8	38.45

Table 3.9.: Mean inter-marker distance (nm) analysis for observation conditions at room temperature

	Mean	Median	Std Deviation
cadavAF488 1/500 only PBS	147	120.8	81.32
cadavAF488 1/500 only FB	124.3	125.2	12.79
cadavAF488 1/500 mix RGD PBS	65.93	65.13	2.10
cadavAF488 1/500 mix RGD FB	73.79	73.77	9.21
cadavAF488 1/1000 only PBS	89.63	91.9	10.47
cadavAF488 1/1000 only FB	103.1	107.3	10.51
cadavAF488 1/1000 mix RGD PBS	71.98	71.71	8.11
cadavAF488 1/1000 mix RGD FB	68.94	67.04	6.53

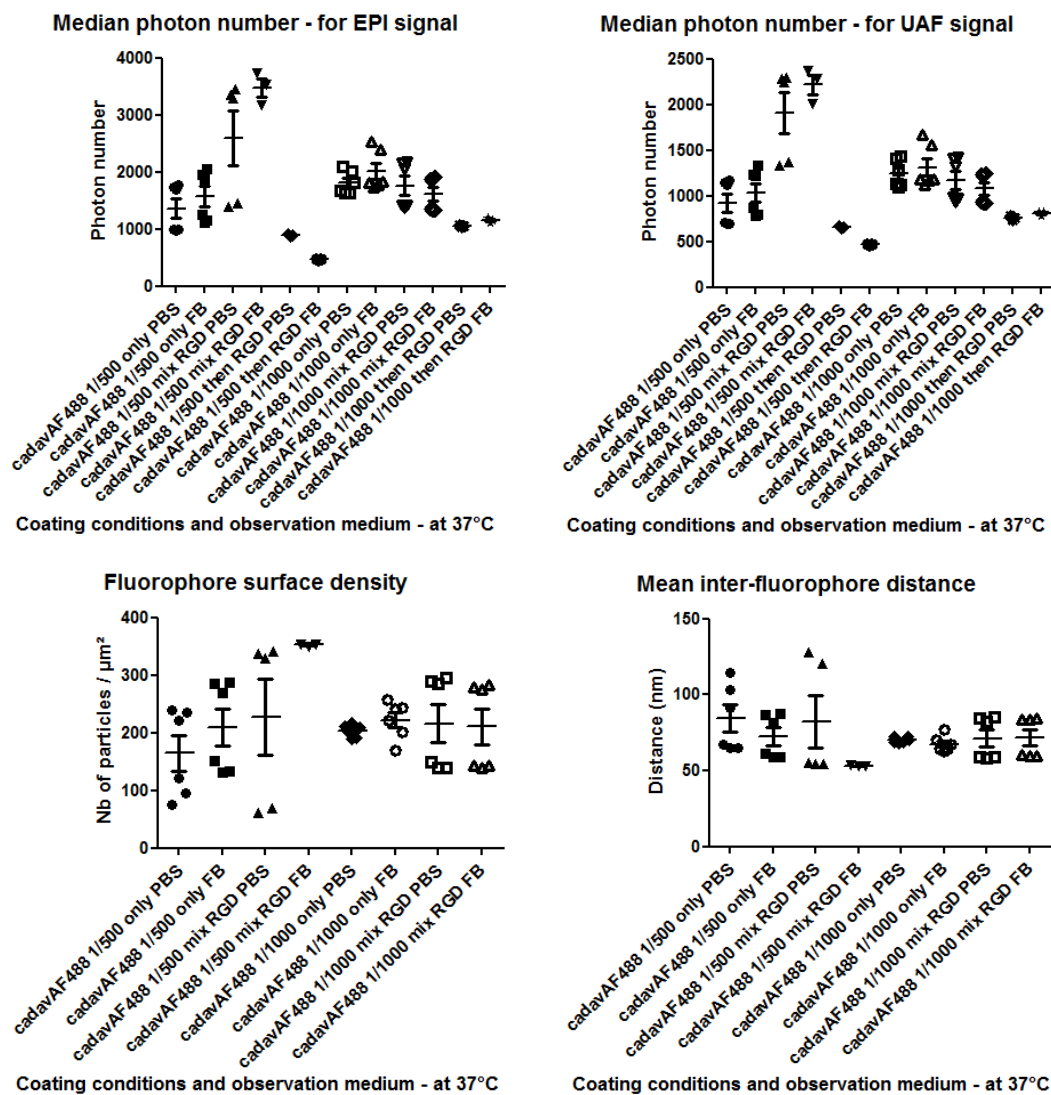


Figure 3.25.: Quantification of useful observables for TFM imaging: fluorescence emission efficiency and fluorescent marker distribution, depending on AF488-coupled cadaverine-coating conditions and observation medium, at 37°C. For the statistics corresponding to each dataset, see Table 3.10 for EPI photon numbers; Table 3.11 for UAF photon numbers; Table 3.12 for fluorescent marker density; Table 3.13 for mean inter-marker distance

Table 3.10.: Median EPI photon number analysis for observation conditions at 37°C

	Mean	Median	Std Deviation
cadavAF488 1/500 only PBS	1360	1345	411.7
cadavAF488 1/500 only FB	1565	1565	437.6
cadavAF488 1/500 mix RGD PBS	2590	3297	1064
cadavAF488 1/500 mix RGD FB	3479	3535	281.7
cadavAF488 1/500 then RGD PBS	896.7	886	22.03
cadavAF488 1/500 then RGD FB	466.7	469	11.68
cadavAF488 1/1000 only PBS	1808	1737	197.4
cadavAF488 1/1000 only FB	2012	1825	348.5
cadavAF488 1/1000 mix RGD PBS	1762	1738	398.3
cadavAF488 1/1000 mix RGD FB	1617	1615	300.6
cadavAF488 1/1000 then RGD PBS	1053	1044	25.32
cadavAF488 1/1000 then RGD FB	1154	1162	36.12

Table 3.11.: Median UAF photon number analysis for observation conditions at 37°C

	Mean	Median	Std Deviation
cadavAF488 1/500 only PBS	920.7	910.5	241.9
cadavAF488 1/500 only FB	1039	1043	245.5
cadavAF488 1/500 mix RGD PBS	1907	2252	507.3
cadavAF488 1/500 mix RGD FB	2217	2282	188.5
cadavAF488 1/500 then RGD PBS	660.3	662	9.61
cadavAF488 1/500 then RGD FB	466.7	469	11.68
cadavAF488 1/1000 only PBS	1248	1210	148.9
cadavAF488 1/1000 only FB	1314	1186	236.2
cadavAF488 1/1000 mix RGD PBS	1172	1156	232.4
cadavAF488 1/1000 mix RGD FB	1080	1080	169.9
cadavAF488 1/1000 then RGD PBS	759.7	747	23.12
cadavAF488 1/1000 then RGD FB	808	816	24.02

Table 3.12.: Fluorescent marker density (μm^{-2}) analysis for observation conditions at $37^{\circ}C$

	Mean	Median	Std Deviation
cadavAF488 1/500 only PBS	164.4	171.4	75.29
cadavAF488 1/500 only FB	209.4	210	78.46
cadavAF488 1/500 mix RGD PBS	227.7	329.3	148.5
cadavAF488 1/500 mix RGD FB	352.8	354	2.16
cadavAF488 1/1000 only PBS	203	205.3	11.15
cadavAF488 1/1000 only FB	222.2	231.4	32.5
cadavAF488 1/1000 mix RGD PBS	216.1	216.9	80.92
cadavAF488 1/1000 mix RGD FB	210.8	209.5	75.38

Table 3.13.: Mean inter-marker distance (nm) analysis for observation conditions at $37^{\circ}C$

	Mean	Median	Std Deviation
cadavAF488 1/500 only PBS	84.28	79.03	21.71
cadavAF488 1/500 only FB	72.45	71.18	14.1
cadavAF488 1/500 mix RGD PBS	82.39	55.1	38.21
cadavAF488 1/500 mix RGD FB	53.24	53.15	0.16
cadavAF488 1/1000 only PBS	70.25	69.8	1.95
cadavAF488 1/1000 only FB	67.58	65.79	5.39
cadavAF488 1/1000 mix RGD PBS	71.3	70.61	13.79
cadavAF488 1/1000 mix RGD FB	71.87	71.86	13.22

First TFM tests

Based on the previous results, exploratory tests were conducted to try and more fully assess the feasibility of a super-resolution TFM experiment with an alpha-version of the developed system. The PAA hydrogel-coated samples were prepared following the same protocol as described in the previous paragraph, and the gel surface was coated with AF488-coupled cadaverine (1/500) mixed with RGD ($10 \mu\text{g}\cdot\text{mL}^{-1}$) overnight. They were then left to soak in serum-deprived FluoroBrite, in the incubator before cell seeding.

3T3 fibroblasts were again used for these experiments, as a cell model presenting focal adhesions which have been shown to apply 3D constraints on deformable substrates (Legant et al., 2013). In order to spot focal adhesion-forming cells when imaging the gel substrates, cells were transfected one day prior to TFM tests using FuGENE HD transfection kit and fluo-tagged viral DNAs. The fluo-tagged viral DNAs used in these tests were Lifeact mCherry and Zyxin RFP, as they stain F-actin or a protein related to focal adhesion, respectively. Transfected cells were trypsinized and resuspended in serum-deprived FluoroBrite medium before seeding on PAA gels. They were left to adhere 15 minutes, before adding serum-supplemented FluoroBrite medium and left to further adhere for an additional 2 hours. The coverslips were mounted in ethanol-sterilized observation chambers, and immersed in warm serum-deprived FluoroBrite DMEM.

Cells were observed with the DONALD setup as follows:

- red fluorescent staining was searched to select one cell to image;
- one light-transmission image was taken of the selected area;
- AF488-coupled cadaverine was imaged with a laser power of 55%, exposure time was set at 50 ms, TIRF depth was fixed at 120 nm and 2500 images were acquired.
- 1 mL of FluoroBrite medium was gently replaced with 0,5% w/v sodium dodecyl sulfate (SDS) solution, and left to lyse cells for 5 minutes;
- another light-transmission snapshot was taken to ensure that the selected cell was well rounded and non-adherent;
- 2500 images of AF488-coupled cadaverine were again acquired with a slightly increased laser power of 60%.

Single molecule images were then pre-processed for super-resolved localization, and analyzed for in-plane displacements with ImageJ plugins analogous to usual TFM acquisitions. The key steps were as follows:

- a stack was created by concatenating the single molecule image acquired after cell removal to the one obtained with a plated cell;
- slices were aligned in the stack using Template matching plugin, with a matching method based on normalized correlation coefficient and without subpixel registration;
- basic iterative particle image velocimetry (PIV) analysis was carried out with PIV plugin, using various PIV interrogation window sizes ranging from 128 to 512 px - on whole images of size 3240*3240 px - and the correlation threshold value set to 0.6;
- PIV post-processing was performed with PIV plugin, with normalized median test (NMT)

and dynamic mean test (DMT) parameters set to default values.

As none of the PIV analyses gave satisfactory results, the same steps were carried out on “static” acquisitions extracted from the various optimal observation condition tests. Yet again, PIV analysis displayed irrelevant and preposterous results. Indeed, it yielded huge displacement values heterogeneously distributed over the whole surface, spanning all directions, even though the two compared images were generated from the same stack, with overlapping data.

Overall, these explorations were still mostly conclusive on some points, and their outcome is summarized in Table 3.14. Thanks to the nano-imprint machine, thin and reproducible coatings of polyacrylamide were deposited on glass coverslips compatible with super-resolution microscopy. Polyacrylamide gels were successfully coated with matrix proteins to allow cells to spread and form adherence structures. However, even if fluorophores compatible with super-resolution microscopy in live conditions were efficiently embedded on the gel surface, their localization in the deformed and relaxed states lacked sufficient axial precision and in-plane distribution similarities in order to estimate cell-induced deformations.

3.2.4. Possible improvement strategies

The first major point worthy of discussing is the obvious lack of statistically relevant dataset for most of the described experiments. Indeed, most of the presented experiments were performed on at most two independent sample preparations. This feat accounts for the purposefully restricted display of statistics computed on experimental results. As this project was assigned to a limited time span, and proved to raise more questions and technical challenges along the way, it was chosen not to pursue it further. However, if it was to be picked up for more thorough explorations, it would be paramount to perform the same previously described tests on multiple independent samples and confirm - or possibly rebut - the established results, so far.

Evaluation of DONALD localization precision in 3D

In-plane localization - Something which was not considered in the previous paragraphs is the addition of a second optical interface to pass through for the emitted fluorescence signals. Indeed, as it has been stated when establishing DONALD detection principle, characterizing both the UAF and SAF signals at the medium-glass interface is the foundation of the acute absolute axial detection (Bourg et al., 2015). Here, the addition of another interface most certainly alters the propagation properties of the emitted fluorescence, and would thus induce required modifications of the PSF characterization parameters, as well as adjustments in segregating EPI and UAF signals. The influence of a slight increase in the observation medium index - to a value of 1.35 - has been tackled in the PhD work of Bourg (Bourg, 2016). It was then stated that localization precision was highly impacted by this shift in optical index value and would ideally require a specific optimization of the DONALD module. However, an estimation of the evolution of the accuracy error value with the emission source depth could help correcting the axial detection of fluorophores in a 1.35 index medium. It would be of the utmost interest to theoretically investigate how propagative and evanes-

Table 3.14.: Synthesis of 3D super-resolution TFM development main challenges and the proposed optimal solution according to this study

Main challenge	Optimal solution proposed	Results
Using an imaging technique allowing for submicron precision in 3D	Imaging with DONALD setup	Localization precision of $15 \times 15 \times 15 \text{ nm}$ according to Bourg's work (Bourg et al., 2015; Bourg, 2016)
Using a deformable material with an optical index as close as possible to that of water $n = 1.33$	Use of polyacrylamide gel as a deformable coating	Measurement of PAA optical index by refractometry $n = 1.35$
Obtaining a flat surface for the deformable material in an unstressed conformation	Shaping polyacrylamide coatings by sandwiching the hydrogel between two glass coverslips + adapting the acrylamide/bis-acrylamide ratio	Measurement of surface roughness with AFM: between 1/200 and 1/50 of ideal thickness for 10kPa PAA
Shaping a 200 nm thick coating of deformable material and a finding reproducible process	Using a nano-imprint machine for the polymerization step and tuning its imprint parameters: volume, time, pressure and temperature	Measurement of PAA coating thickness by profilometry or with DONALD setup: 210 nm
Embedding fluorescent fiducial markers in/on the deformable material	Grafting AF488-coupled cadaverine onto PAA surface <i>via</i> sulfo-SANPAH crosslinking	Observation of satisfactory blinking ability in PBS with DONALD setup
Embedding an ECM protein to promote cell adhesion with fiducial markers in/on the deformable material - for optimal cell adhesion formation	Grafting RGD or fibronectin and AF488-coupled cadaverine at the same time on PAA <i>via</i> sulfo-SANPAH crosslinking	Assessment of cell phenotypes on PAA gels <i>via</i> widefield observation of immunostained samples
Embedding an ECM protein to promote cell adhesion with fiducial markers in/on the deformable material - for optimal observation conditions	Grafting RGD and AF488-coupled cadaverine at the same time on PAA <i>via</i> sulfo-SANPAH crosslinking, observing in FluoroBrite medium at 37°C	Assessment of geometric characteristics of fiducial marker distribution and fluorescence signal quality with DONALD setup

cent wave components are impacted in the presence of two successive step-index interfaces. Then, experimental data ought to be compared to theory predictions in order to establish whether specific alterations to the commercialized DONALD module should be introduced for its application with PAA gel-coated coverslips.

Axial localization - What is more, recent improvements have been implemented to widen the depth range in which localization precision slowly varies with precisions down to 15 nm. The axial localization is performed through a combination of PSF shaping and SAF, which yields absolute axial information over a 1 μm range (Cabriel et al., 2019). Additionally, SAF analysis has also been implemented with more conventional microscopy techniques such as STED. Indeed, STED-SAF implementation benefits from a straightforward gain in axial resolution *via* nanometer axial sectioning, only requires a modification in the detection path of the STED microscope and thus could be widely implemented (Sivankutty et al., 2019). These feat could induce a less strict restriction for the PAA-coating thickness range, while still dependent on the influence of the presence of two optical interfaces.

Assessment of the mechanical properties of PAA thin gels

PAA coating roughness was solely assessed after its shaping *via* the usual sandwich protocol. It would be interesting to probe its surface with AFM after its processing with the nano-imprint machine. Indeed, as it has been noticed in the experimental section, some gels displayed apparent increased “stiffness” or crystallization patterns. Visualization of its surface state would help understanding if such a process alters PAA material properties. These observations could represent key information for further tuning the optimal nano-imprint parameters.

Furthermore, this study also lacked in assessment of the mechanical properties of the PAA coating. Indeed, Young’s modulus value was only discussed when measuring PAA roughness but was then completely overlooked. However, little is known about mechanical behaviors at the submicron scale. They have been explored thanks to adapted nanoindentation methods, mostly in the context of stiffer materials such as crystalline materials (Kulkarni et al., 1996; Sundararajan et al., 2002a; Sundararajan et al., 2002b), fiber epoxy composites (Syed Asif et al., 2001) or polymers (Nowicki et al., 2003). In the specific case of hydrogels, material properties at the submicron scale would be expected to substantially depend on the volumetric organization of polymer chains - their orientation, the order degree of the network-, their length statistical distribution, their crosslinking degree and their water content. Such characteristics could be attainable through Raman spectroscopy analysis (Gupta et al., 1981; Ahern et al., 1988), and would hence require the establishment of a related submicron mechanical model accounting for mesoscale behavior - as the cells would sense the material (Oyen, 2014).

Characterization of blinking illumination in water-based observation media

An issue that was not tackled in this study is the characterization of the blinking temporal pattern of fluorophores. Indeed, AF488-coupled cadaverine was eventually selected due to its high photon number emission and nearly continuous staining of the PAA-surface. The simple fact that so much fluorophores per observed area were seemingly detected confirms their ability to emit fluorescence with a time-varying intensity pattern. However, the characteristics of these oscillations were not assessed, neither was the fact whether one fluorophore was effectively able to be switched on and off a few times. Knowing this feat would further help adjusting the optimal laser exposure time.

Besides, another major fluorescent signal characteristic was not explored during this study: the SNR value associated with the various observation conditions. As it has been stated in the work of Bourg and colleagues, SNR value affects DONALD localization precision (Bourg et al., 2015). It would be essential to carry out further analysis of the available raw data to evaluate SNR values in order to confirm - or refute - the presented choice for fluorophore and observation conditions. Specifically, as noted earlier, given the additional complexity of a second optical interface, SNR value would be expected to drastically impact localization precision.

Visualization of PAA surface after AF488+RGD coating

As it was performed on bare PAA surface, AFM probing of local topography after fluorophore and ECM protein coating would provide valuable insight to the local environment which subsequently seeded cells would probe. Indeed, AF488-coupled cadaverine and RGD peptide differ in size, polarity, chemical affinity and 3D conformation possibilities. It would thus be expected that their grafting on a nanometer rough surface would result in possible enhanced roughness. AFM probing would also reveal whether such coating results in alteration of the material surface geometry, hence adding geometric cues to this artificial cell substrate.

Furthermore, more extensively characterizing the respective surface distributions of AF488-coupled cadaverine and ECM protein would allow for better comprehension of the theoretically attainable spatial rendering of the gel surface on one hand, and of the cell adhesion efficiency on the other hand. Indeed, as integrins require clustering to promote cell adhesion structure formation (Campbell et al., 2011; Huttenlocher et al., 2011) and knowing that the RGD-integrin bond is weaker compared to the full-length ECM protein-integrin bond (Redick et al., 2000), local clustering of RGD could promote cell adhesion and optimize the chances of imaging an adhesion-mediated substrate deformation event (Maheshwari et al., 2000). Additionally, full length protein domains have been shown to differentially mediate cell morphology, cell migration and cell proliferation compared to RGD alone (Fong et al., 2010).

Improving comparison between initial and deformed conformations

It was clearly stated that the early TFM tests were not conclusive at all. Even though FEM simulations predicted PAA surface displacement value theoretically discernable with DONALD module, it

is important to keep in mind that these results could well be overestimated. Indeed, as it was underlined earlier nanoscale mechanical behavior of hydrogels is poorly documented, and assuming that they display the same material properties when shaped in submicron dimensions might prove false. Additionally, most FEM simulation softwares are not provided with microscale mechanical models which could account more faithfully for real material laws at such a reduced scale. Hence the need for establishing a specific submicron mechanical model according to PAA polymer characteristics, as was pointed out earlier.

What is more, there is a major lack of fluorescent marker displacement detection. Indeed, as the number of blinking cycles achieved by a single fluorophore is not known, there is no guarantee of detecting the same fiducial marker both during the stressed configuration and relaxed configuration acquisitions. Also, as was noted in the experimental part, a slight laser power increase was required between the two single molecule imaging steps. This was partly due to an apparent lack of blinking sources after the first exposure, and may attest to the bleaching of most fluorophores before the second exposure. To counter these possible hindrances, two strategies may be considered:

- either infer PAA surface topography for relaxed and stressed configurations according to 3D fluorophore localizations, and extrapolate displacements through comparison of the two 3D function values. This method would then induce a loss in displacement resolution and require that the fluorophore localizations for both acquisitions allowed for the same surface rendering precision;
- or explore the option of fiducial markers tagged with two different fluorophores, of which excitation spectra span completely independent wavelength ranges. This would require first that such fiducial markers can be designed; second that these fluorophores share approximately the same blinking ability and characteristics in water-based observation media. If feasible, this strategy would enable to precisely locate the fiducial markers in both material configurations, with lesser uncertainties about identifying the respective positions of markers on both images;
- or even more ideally, attempt at depositing fiducial markers according to a regular pattern. The geometric characteristics of the lattice would have to be optimized according to the microscopy technique, and the number fluorophores places at the vertices would also require tuning depending on the expected duration of experiments.

3.3. Designing nanoscale 2.5D glass substrates for assessing of macrophage topography sensing

3.3.1. Characterization of cell topography sensing

Cells migrating through various tissue come across various ECM organization. For instance, vessels are composed of amorphous sheets intermittently laden with pits, meshes and grooves (Wagenseil et al., 2009). In contrast, the complex multiscale structure of bone has been described in a previous section of this manuscript 1.1. Similarly, muscle tissue is made up of many muscle bundles, straightly and parallel aligned, that are composed at the microscale of hundreds of aligned fibers. The latter are in turn organized in packaged myofibrils, that are composed of thousands of aligned contractile nanofilaments (Meyer et al., 2011). Hence, cells are submitted to physical environments displaying various order degrees at the micro- and nanoscale, as well as varying topographies. In order to decipher how these geometric characteristics affect cell behaviors, multiple micro- and nanofabrication techniques have been suggested to reproduce ECM features, *via* the fabrication or modification of biocompatible materials. Such biomimetic devices allow to limit the complexity of cell environment to a few physical parameters, so as to discriminate their contribution to subcellular events (Matellan et al., 2019)

ECM topography

Each tissue type display specific 3D structures from the nano- to the microscale, thus presenting cells with multiple topographical variations. Since tissues have different functions, and are exposed to various physical or chemical stimuli and environments, they can be categorized accordingly (Kim et al., 2013):

- protective tissues, such as skin and mucosal lining,
- electroactive tissues like heart or brain,
- shear-stress sensitive tissues, *e.g.* blood vessels,
- mechanosensitive tissues that are bone and tendons

Exploring the complex multidimensional and hierarchical organization of tissues have recently provided valuable insights for the tissue engineering and regenerative medicine field. By focusing on better understanding the interactions between cells and their extracellular environment, the pursuit of generating ideal ECM substitutes may eventually be achieved (Mano, 2015). Indeed, improving the complexity levels with which tissue constructs are generated has been showed to increase the chances for successful grafting (Kelleher et al., 2010; Atala et al., 2012). More specifically, surface topography is one of the most relevant properties of physiological materials to induce and regulate specific cell behavior and tissue development (Norman et al., 2006; Bettinger et al., 2009).

Given the multiscale organizations of both tissues and cell components (Fig. 3.26), cells are not only affected by microscale patterned surfaces, but are also able to sense and respond to nanoscale features (Norman et al., 2006; Martins et al., 2017). ECM provides a wide array of interwoven pro-

teins that provide regulatory topographical cues in addition to chemical cues, which are tissue-specific (Mark et al., 2010; Janson et al., 2015). Thus, the development of patterned substrates provide tailored cell-substrate interactions, and stimulate biological recognition pathways (Craighead et al., 2001; Flemming et al., 1999; Dalby et al., 2003). Exposing cells to various topographical motifs appears crucial to control material-cell interactions, ECM remodeling and cytoskeletal rearrangement, in addition to allow for the precise triggering of cellular responses.

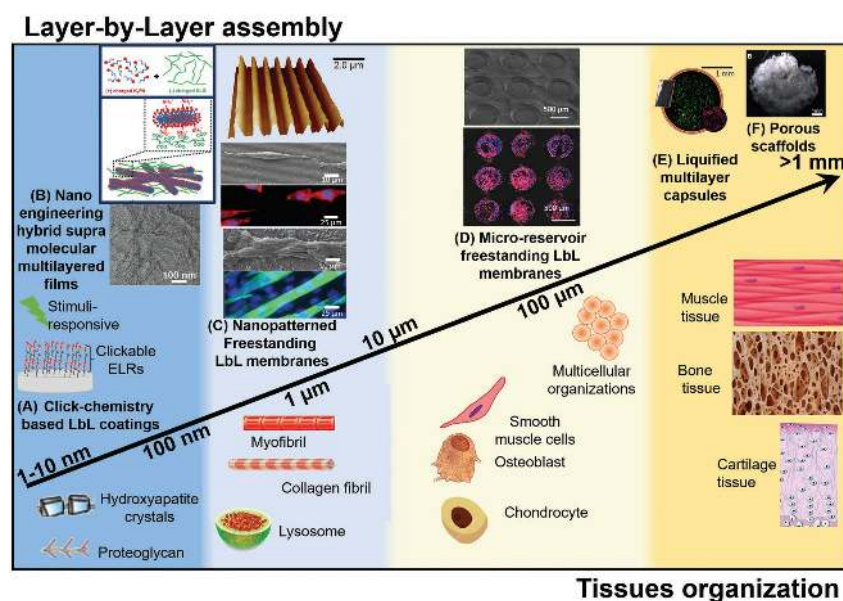


Figure 3.26.: Multiscale hierarchy of different representative tissues and representative synthetic substrates sharing the same topography lengthscale. Adapted from Sousa et al., 2019.

Fabrication techniques to obtain micro- and nano-patterned surfaces

Micro- and nanopatterning consist in producing micro- and nanostructures, respectively, across the surface of a given material. Technological advances in the field of material patterning have recently allowed for the more thorough comprehension of material-cell interactions. Production of ordered as well as randomly distributed topographical features at different length scales have been made possible thanks to available methodologies (Bettinger et al., 2009; Barthes et al., 2014). Bottom-up approaches can be used with different polymers, being a cost-effective way to create well-organized topographies. On the other hand, top-down approaches usually involve the application of external stimuli like heat, UV-exposure, or pressure to produce thin polymer films with specific geometries (Betancourt et al., 2006). Overall, advanced micro- and nanofabrication techniques have been developed with increased resolution and precision, being often combined with different deposition techniques (Qian et al., 2010) (Fig. 3.27).

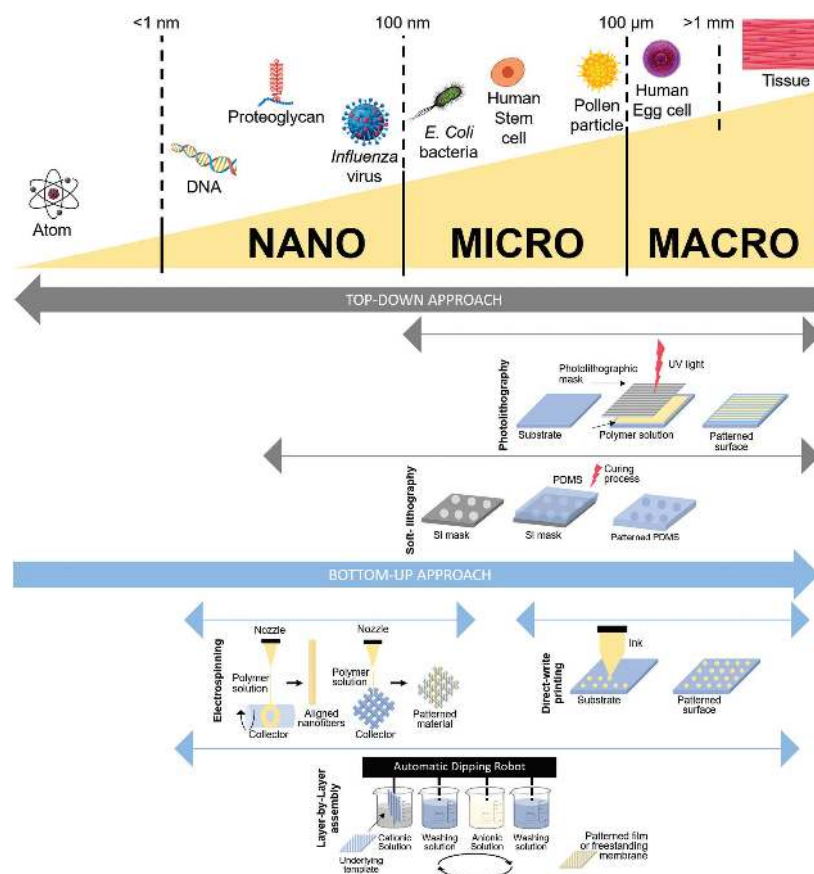


Figure 3.27.: Living systems are organized in different levels, with increasing complexity, as shown in the upper part of the image. Below, the most representative micro- and nanofabrication methods are represented in terms of range resolution and compared with natural systems at different scales of organizational levels. Adapted from Sousa et al., 2019.

Bottom-up approaches

Layer-by-layer - Layer-by-layer technique was first described as a simple and versatile bottom-up method to create multilayer films. Its general concept is based on alternating electrostatic deposition of a wide range of polycation and polyanion species onto a substrate (Decher et al., 1991). It provides high control over physicochemical, morphological and mechanical properties, and offers versatility to coat substrates with bioactive species (Costa et al., 2014; Keeney et al., 2015; Silva et al., 2014). Furthermore, recent protocols have proposed other types of driving forces for the assembly of the films, such as covalent bonding, hydrogen interaction or click chemistry (Borges et al., 2014). This has resulted in an even wider range of materials compatible with the layer-by-layer technique.

Topographical features can be achieved with this technique by constructing the multilayers above a prepatterned sample, or by modification of a layer-by-layer-based film, benefiting from a submicron

fidelity (Sousa et al., 2017; Martins et al., 2017). Moreover, layer-by-layer assembly of 3D bio-based materials above patterned substrates allows for the creation of 3D complex architectures (Khademhosseini et al., 2004).

Electrospinning - Electrospinning is based on the application of a high electric field between a charged polymer solution and a counter electrode, which forces the movement of the solution through a small diameter syringe nozzle, and eventually creates a fiber (Reneker et al., 2008; Lim et al., 2017). Several fibers are then assembled on top of substrates to form fibrous mats covering large surface areas, with varying levels of porosity (Bhardwaj et al., 2010). Moreover, depending on the purpose, the order degree of fiber meshes is easily tunable on a wide length scale, providing with substrates able to mimic natural tissue architectures (Xie et al., 2010).

Colloidal particles - Colloidal particle production has been reported through different techniques, such as suspension-, emulsion-, dispersion- and precipitation-based polymerization, and the preferential materials are usually silica or polystyrene (Dommelen et al., 2018; Kaewsaneha et al., 2013). They can be used as building blocks to form colloidal nanostructured surfaces, particularly *via* self-assembly process (Dommelen et al., 2018; Trujillo et al., 2009). Their wide range of diameter, from 1 *nm* to 100 μm , allows for the generation of complex architectures.

Direct-write or inkjet printing - Direct-write or inkjet printing relies on a printing head to spatially deposit inorganic or organic small molecules, proteins or even cells onto specific areas of substrates (Zhang et al., 2009). While inkjet printing usually produces fluid drops of diameter ranging from 10 to 150 μm , direct-write printing combined with laser-based benefits from an enhanced working resolution, up to 100 *nm*. By controlling the displacement velocity, directionality and modulating the printing duration, such a technique can lead to large 3D freestanding architectures (Accardo et al., 2017).

Micro- and nanocontact printing - Micro- or nanocontact printing is based on pattern transfer from a template to a specific material surface, and consists in a versatile, easy and low-cost method benefiting from submicron accuracy (Ruiz et al., 2007). Other than its use to produce 2D patterned substrates segregating different ECM proteins, it can also be used in the context of creating topographical features. Indeed, 2D patterning of chemical compounds can be used to confine the polymerization of scaffold molecules, which can be further modified, for example through silicification (Yang et al., 2009).

Top-down approaches

Microfluidics - Microfluidic substrates offer a set of fluidic unit operations, designed specifically for their combined use with well-defined motifs, and aiming at miniaturization, automation and parallelization of biochemical processes (Velve-Casquillas et al., 2010). One of the advantages of

this technology is the fact that two or more streams of laminar flow can be generated, connected and managed, providing a unique technology to pattern cells and their environments (Velve-Casquillas et al., 2010; Chen et al., 2009). Indeed, patterning of polymer microscale materials can be achieved through introducing a sheath fluid with a high-speed flow rate, resulting in flat fibers adapting to a pre-existing pattern (Kang et al., 2012). In addition, microfluidics also allow for the dynamic 3D patterning of monolithic structures, thanks to automated deliveries of wash solution and photocurable agents to a photoreactive coating (Cheung et al., 2007).

Photolithography - Photolithography is a widely used and well-documented technique for micro- and nanofabrication, firstly developed for the microelectronic industry. In this technique, a photoreactive material - the photoresist - is coated onto a substrate, typically a silica-based wafer. The selective exposition of only parts of this resist coating is achieved by using a specifically designed chrome mask with micro- or nanoscale features between the light source and the sample. Hence, depending on the polarity of the resist, the regions exposed to ultraviolet (UV) light either polymerize, cross-link or degrade, and the unwanted parts are removed thanks to the treatment with an organic solvent (Desai, 2000; Tran et al., 2017). A wide range of lateral resolutions, spanning from 5 nm to a millimeter, can be achieved by adapting the UV-wavelength for exposure, or the type of mask used (Choi et al., 2003; Pinto et al., 2014).

Photolithography can be used *per se*, or it can be combined with other deposition techniques to alter the surface chemical properties (Shaikh Mohammed et al., 2006). Moreover, substrates obtained through photolithographic process can be either used as such, or as a master mold to produce highly reproducible substrates in softer materials.

Soft lithography - Soft lithography takes advantage of a soft and flexible elastomer material, such as PDMS, to create microscale features on another material surface (Qin et al., 2010). This technique thus involves the production of a master template to emboss the expected structures onto the softer material. Such master templates can be obtained through photolithography, and the creation of curved or nonplanar surfaces with soft lithography allow for overcoming limitations of the mold (Tran et al., 2017).

Applications to decipher topography sensing mechanisms

The distribution of physical and biochemical cues within the 3D space of the ECM is a fundamental factor for the regulation of cellular functions. Indeed, ECM organization sensing controls cell polarization, migration and shape, thus modulating the biochemical cell-matrix interactions and eventually directing cell function. Attempts at mimicking such complex physiological arrangements broadly take two distinct forms: spatial patterning of biochemical cues, and development of 2.5D topographical features - 3D features of negligible size compared to the 2D substrate they are produced on. 2.5D substrate-patterning relies on the afore-mentioned micro- and nano-fabrication techniques, in order to generate grooves, pits or other motifs on cultures substrates (Fig. 3.28). Such approaches

allow for deciphering the mechanisms involved in cell responses to topography, spanning effects on cell proliferation, cell differentiation, cell morphology and polarization (Bettinger et al., 2009). In the context of this study, it is most interesting to focus on the modulation of cell migration and adhesion in the presence of topographic features.

The main mechanisms and their possible effects on cell attachment can be listed as follows:

- alterations in physico-chemical forces *via* an enhancement of the energy barrier first peak;
- cell membrane deformations and subcellular modulations of tension to adapt to its surroundings;
- establishment of local solid-liquid chemical gradients due to entrapment of molecules.

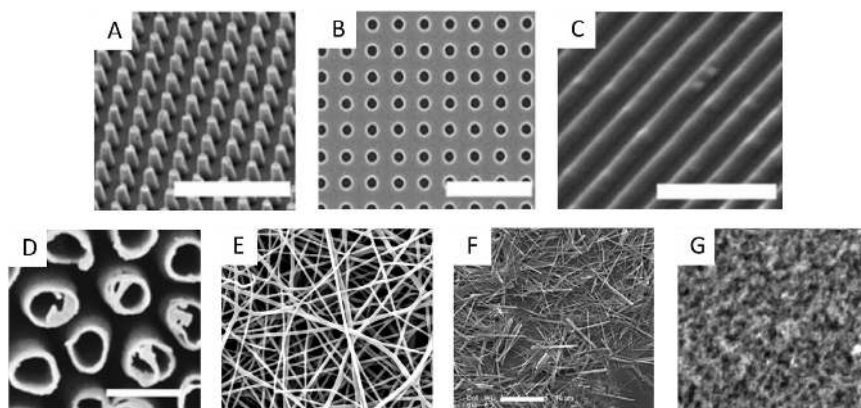


Figure 3.28.: Examples of different type of topographies used to mimic the extracellular matrix of tissues: (A) pillars; (B) pits; (C) grooves/gratings; (D) tubes; (E) fibers; (F) wires and (G) roughness. Adapted from Dobbenga et al., 2016.

Modulating cellular migration - Topotaxis refers to the migration of cells based on the density of topographical cues. Interestingly, the resulting directionality is not universal and has been reported to depend on cell cortical stiffness, hinting at a role for cell deformation during migration (Park et al., 2016; Park et al., 2018). In contrast to previous suggestions, cells may display the capacity to envelop topographic features, instead of just “sitting on a bed of microneedles” (Tan et al., 2003; Saez et al., 2005). Specifically, the ability of the cell surface to deform sufficiently can vary depending on the spacing between the features, the deformability of the plasma membrane and the underlying cytoskeleton (Kim et al., 2010). In the case of topographic features distributed in a spatially graded manner, there may be three distinct observations of cell behavior (Park et al., 2016) (Fig. 3.29):

- if the cell cortex is too stiff, it would not allow for membrane curvature and confine cell contact to the top surface of the topographies;
- on the contrary, cell cortex may be so soft as inducing a complete invasion of the cell in the interspace volume, subsequently increasing the effective area for cell-matrix interactions;

- the degree of penetration into the interspace can vary across the cell length, being maximal in the sparser areas and minimal in the denser areas, and resulting in a general movement away from denser matrix areas (Wolf et al., 2013).

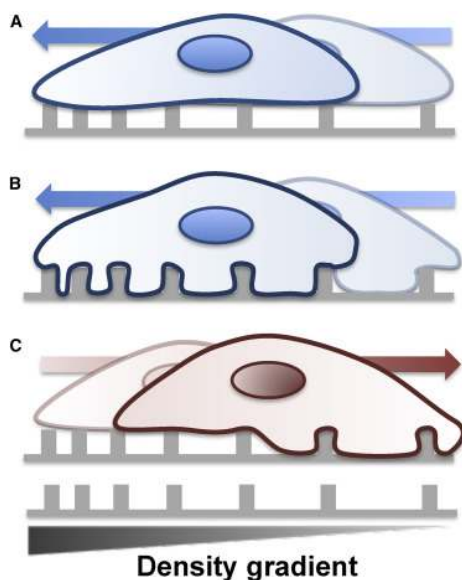


Figure 3.29.: Three scenarios of a cell interfacing with an adhesive substratum containing spatially graded topographic features and the corresponding topotaxis directionality. (A) Stiffer cells show limited interfiber penetration and are guided toward higher-matrix-input areas. (B) Softer cells can penetrate within the topographies, substantially increasing the contact with and input from the extracellular matrix. Topotaxis is toward denser fiber zones. (C) At intermediate cell stiffness, a differential degree of interfiber penetration leading to topotaxis toward sparser fiber zones. Adapted from Park et al., 2018

ECM inputs can in turn affect the effective cortex stiffness, resulting in a feedback effect allowing variations in cell compliance with the topographic features. Indeed, cortical stiffness and deformability have been reported to be controlled by the opposite effects of two signaling pathways: PI3-kinase-dependent enhancement of cortical deformability and protrusive activity; and Rho-associated protein kinase ROCK-dependent increase in cortical stiffness (Fig. 3.30). Of interest, PI3-kinase and the associated Rac1 small GTPase signaling were previously implicated in controlling cell polarity through specification of the cell leading edge for mesenchymal migration (Srinivasan et al., 2003; Xu et al., 2003; Sanz-Moreno et al., 2008; Machacek et al., 2009). On the other hand, ROCK signaling and the associated RhoA small GTPase activity were implicated in cell trailing edge, likely through limiting the protrusive activity and promoting cortical contractility for amoeboid migration (Xu et al., 2003; Machacek et al., 2009; Friedl et al., 2010).

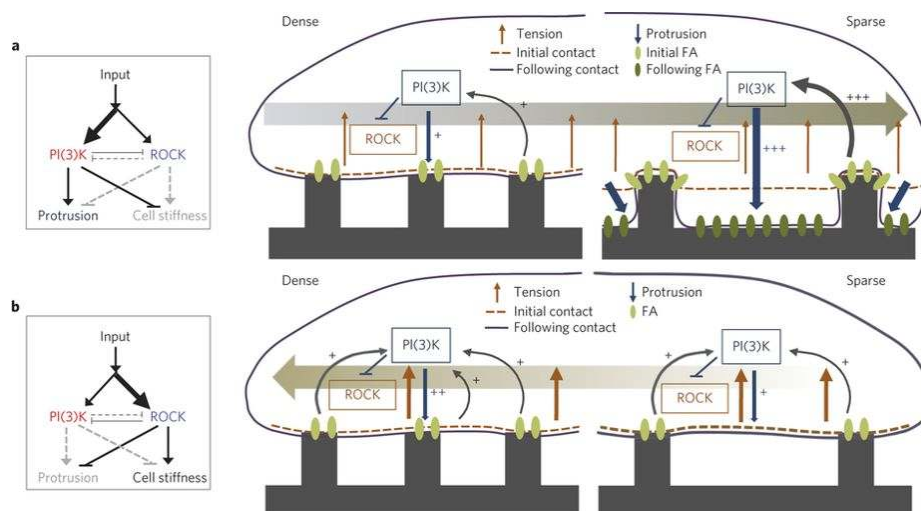


Figure 3.30.: A schematic graphic model of the topotaxis in invasive and non-invasive cells. The directionality of topotactic migration depends on differential conformity of cellular membrane to local topographic structure. The degree of conformity depends on the cell rigidity, which in turn is controlled by the interplay between two ECM-activated signalling pathways: PI(3)K–Akt increasing the degree of conformity and matrix penetration and ROCK–MLCK decreasing the degree of conformity. Adapted from Park et al., 2016.

Modulating cellular adhesion - Substrate height variations in an orderly manner, as opposed to substrate roughness, have been shown to affect cell adhesion. Indeed, human osteoblastic cells cultured on nanoisland topographies displayed enhanced more prominent focal adhesion formation when plated on nanoislands 11 *nm* high, compared to flat surface or higher topographies (Lim et al., 2005). Similar behavior was also reported in fibroblasts and endothelial cells, and the island height was also proposed to modulate both initial and long-term adhesion (Dalby et al., 2004).

Depending on the fabrication method, topographies can either be randomly distributed and display different forms of stripes or scratches (Van den Dries et al., 2012), various levels of roughness (Geblinger et al., 2009; Geblinger et al., 2010; Wittenburg et al., 2014). Or they can display a heightened order parameter at the cell scale (Wójciak-Stothard et al., 1996). In this last case, diverse geometries have been explored such as pillars (Park et al., 2016), lines (Matellan et al., 2019) or wrinkles (Cortizo et al., 2012). Linear ordered motifs have been used to study macrophage adhesion (Wójciak-Stothard et al., 1996) and podosome arrangement (Van den Dries et al., 2012) on 2,5D substrates. Podosome alignment in dendritic cells plated on polystyrene, polymethylmethacrylate or polyethylene naphthalate topographies of height down to approximately 100 *nm* have been observed by Van den Dries *et al.* (Van den Dries et al., 2012).

Micro- and nano-fabrication technological advances now allow to structure surfaces able to mimic submicron ECM geometries *in vitro*. Physico-chemical properties and material stiffness of the substrate are also characteristics of major impact on this adaptability of cell functions. Indeed, the

combination of topographic features with multiple materials have been tested for cell adhesion studies: polymers such as polydimethylsiloxane (PDMS) or polyacrylate (Azatov et al., 2017), metallic materials such as titanium (Ariganello et al., 2018), organic matter like collagen (Cortizo et al., 2012), and borosilicate glass (Van den Dries et al., 2013b).

Particularly considering podosomes, it has been shown that podosomes number and protrusive forces they exert increase with stiffness of the material they are plated on (Labernadie et al., 2014). Van den Dries *et al.* have explored dendritic cells adhesion relative to hydrophilic/hydrophobic properties of various materials - Teflon, borosilicate glass, polystyrene, polyethylene naphthalate, polymethylmethacrylate - and did not observe significant changes in size or podosome number per cell (Van den Dries et al., 2012; Van den Dries et al., 2013b).

Another study also identified a critical spacing of topographic features, which influences cell adhesion. Substrates were generated through 8 nm gold nanodots self-assembly, subsequently coated with RGD and allowing for the binding of a single integrin per dot (Arnold et al., 2004). For a critical dot interspacing of 73 nm, cell attachment was dramatically impaired, supposedly due to the restriction of integrin clustering (Fig. 3.31).

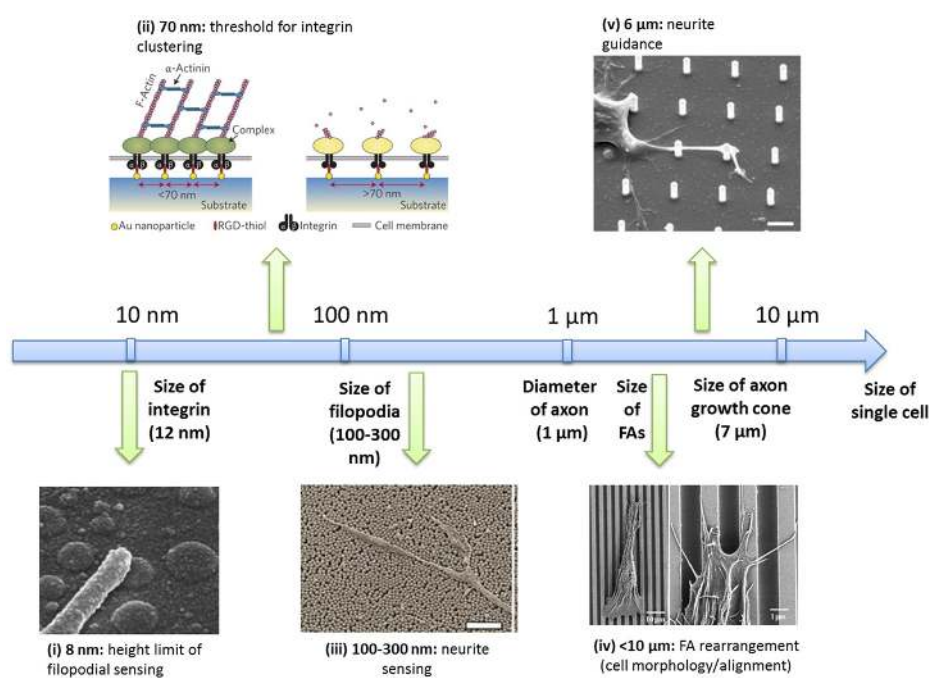


Figure 3.31.: Correlation between size of substratum topography and cellular sensing organelles. Adapted from Nguyen et al., 2016.

While cell-matrix interactions have been extensively studied on traditional 2D surfaces, cells experience *in vivo* complex environments that have various geometric and physical properties. By creating precise surface structures, micro-nano-fabrication represents a powerful tool in understanding cell topographical interactions with topographical features. For instance, the spacing between

mechanical obstacles has been found to be a critical parameter in cell migration (Tan et al., 2001).

Recent developments of strategies to analyze cellular responses substrate topography has allowed for new insights into the cell-microenvironment interactions, especially in terms of cell shape, cytoskeleton organization and focal adhesion remodeling processes (Berry et al., 2004; Frey et al., 2006). As the knowledge concerning how cells detect, move over long time scales and adapt their cytoskeleton or adhesive contacts in a 3D environment is still limited, systematic studies of cell migration and adhesion processes on well-defined topographical substrates appear as a useful tool to tackle these issues. In most of the previously cited examples, the aspect ratio of motifs most often displayed restricted lateral dimensions for barely submicron axial dimensions. However, explorations of the effects of nanoscale axial motif dimensions on cell migration and adhesion could reveal new information of how cell probe physiologically relevant roughness.

The objective of this project is to develop tools aimed at studying how cell adhesion structures sense and react to topographical motifs. So as to tackle this issue, the cell model which has been chosen is human blood monocyte-derived macrophages, and the hypothesis that will be tested is a predominant role of integrins in the event of topography sensing.

3.3.2. Generation of wet-etched glass coverslips to study topography sensing

General outline of this project

This study aims at assessing to which motif height can a detection of ordered grooves be observed. To do so, 2.5D topographical motifs were developed on borosilicate glass coverslips in the shape of lines that are micron sized in width. This geometry allows to easily observe a possible alignment of podosomes with respect to the motifs. The lines are $1 \mu\text{m}$ wide, and separated by a $10 \mu\text{m}$ wide gap. This spacing value is much higher than the mean inter-podosomal distance of $1.77 \mu\text{m}$, measured on 2D surfaces by Proag *et al.* (Proag et al., 2015). Thus, it can be hypothesized that this limits inter-podosomal synchronous effects. This considerable spacing value might also prevent confinement, and allow to discriminate the roles of integrins and membrane tension between two motifs. Indeed, when considering a simply hanging membrane between two pillars, the larger the spacing between the two posts, the lesser the curvature value for the membrane at its central area.

Motif height control for each substrate allows for macrophage adhesion on crenels of height comprised between 10 nm to 200 nm . The possible motif detection processes on such low heights are still to be uncovered.

This height range is targeted at discriminating the different hypotheses on the role of integrins in the adhesion event. Thus, the maximum height has been limited to podosome dimensions, and the minimum height approaches the dimensions of integrins. Another limitation for the minimal height is that the motifs must be detectable apart from local inherent roughness, which should be approximately 10 times lower than the motif height.

So as to keep uniform material properties over the whole surface, and thus discriminate only the

height difference effect, 2.5D topographical motifs were shaped *in situ* directly from the substrate material. Furthermore, no coating of ECM proteins such as fibronectin was deposited over the motifs.

To make these 2.5D motifs, the protocol consisted in a conventional UV-lithography process followed by a wet etching step. Human blood monocyte-derived macrophages were then seeded, left to adhere and fixed on the 2.5D patterned substrates. After immunostaining of F-actin and vinculin, the spatial arrangement of podosomes relative to the crenels was assessed by widefield microscopy observations. The fluorescence images were treated with a dedicated ImageJ macro, which was specifically scripted to uncover a potential influence of the motifs on the localization of podosomes in the presence of nano-scale topographies.

Fabricating and characterizing nano-topographies on glass coverslips

- A conventional UV photolithography process and a wet etching in hydrofluoric acid step were adapted and followed in order to yield nano-topographical motifs on borosilicate glass coverslips. The process parameters were firstly adjusted to the specific requirements of developing nano-topographical motifs on glass coverslips. E-beam lithography technique allows for a higher lateral resolution of approximately 15 nm, but its downsides are that it is costly and slow. Conventional photolithography benefits from its ability to process multiple centimeter-sized samples simultaneously. The etched samples have been characterized by AFM. The optimized version of the various stages of the protocol are schematically represented and summarized in Figure 3.32.

UV photolithography on glass coverslips - Borosilicate glass coverslips of controlled $170 \pm 5 \mu\text{m}$ thickness and of 25 mm diameter were used to make 2.5D crenelated substrates. Coverslips were cleaned in acetone, in deionized water, then in 70% ethanol before being dried with a dinitrogen blower. They were further cleaned by dioxygen plasma exposition for 5 minutes at a power of 800 W and gas flow of 1000 sccm, before chemical vapor deposition of hexamethyldisilazane (HMDS) resist adhesion promoter.

ECI-3012 positive resist was spread on the clean surface by spin-coating for 30 seconds at a speed of $3600 \text{ tr} \cdot \text{min}^{-1}$ and acceleration of $4000 \text{ tr} \cdot \text{s}^{-2}$. Then, the deposited resist was baked before insolation at 90°C for 90 seconds on a hot plate.

Each coverslip was exposed with I-line wavelength UV in a Suss MicroTec MA6 Gen4 mask aligner for 10 seconds, with an exposure dose of $100 \text{ mJ} \cdot \text{cm}^{-2}$ and a power of 30.1 mW. The chrome mask used for this insolation step displays 1 μm wide parallel lines that are 10 μm apart. During UV exposure, it was placed over the coverslips in hard contact mode with a pressure of 4 mbar. Coverslips were then placed on a hot plate set at temperature 110°C for 90 seconds for annealing of the photoresist. So as to reveal the resist motifs, the exposed part of the resist was removed in a bath of MF CD-26 developer solution for approximately 60 seconds. Finally, the coverslips were rinsed with deionized water for 2 minutes, then dried with a dinitrogen blower.

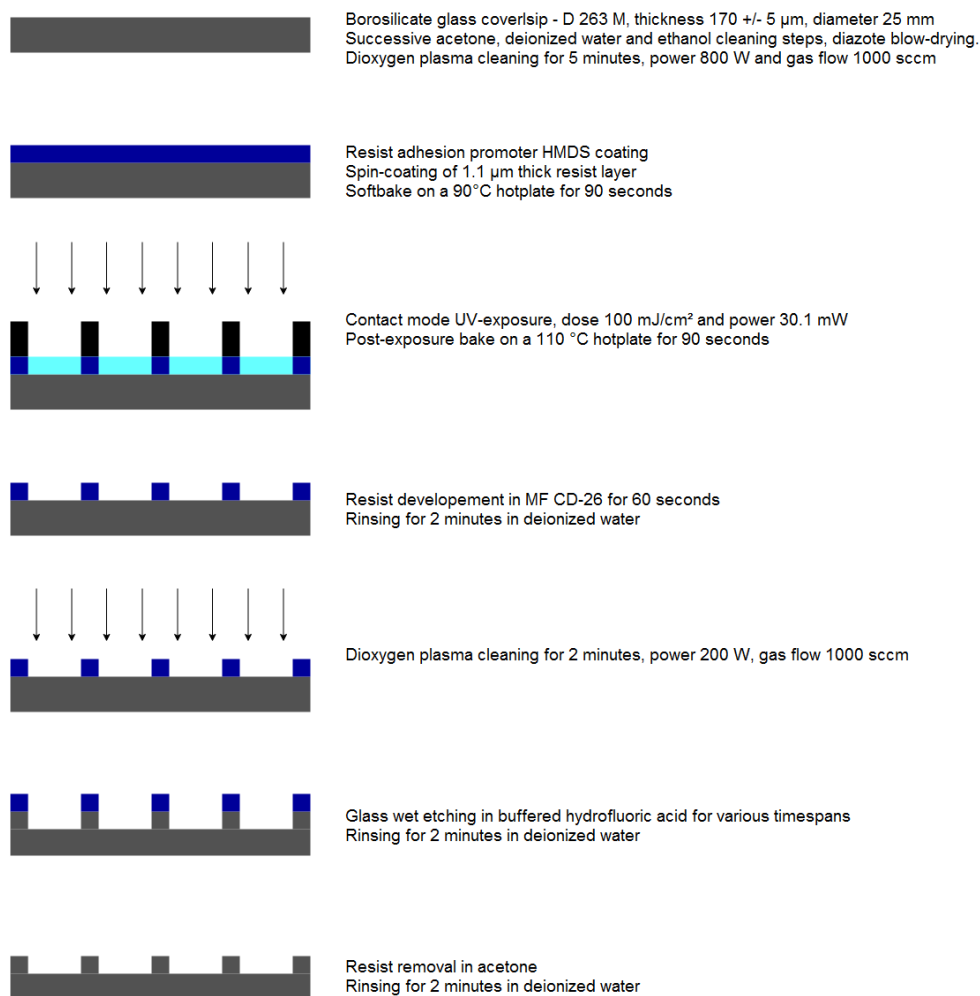


Figure 3.32.: Main steps of the optimized process to fabricate nano-topographies.

Wet etching of the glass - The coverslips were exposed in dioxygen plasma for 2 minutes at a power of 200 W and gas flow of 1000 sccm, in order to remove all resist residues between the motifs and to increase surface hydrophilicity to subsequently facilitate wet etching.

Buffered hydrofluoric acid to a ratio of 7:1 in ammonium fluoride was used to etch glass. Coverslips were statically immersed for 10 to 180 seconds, depending on the targeted height value for topographical motifs. Etching was immediately followed by rinsing with deionized water for 1 minute, then the coverslips were blow-dried with dinitrogen. Etched coverslips were eventually immersed in acetone to dissolve residual resist, and rinsed in deionized water. A final exposition in dioxygen plasma was performed for 2 minutes at a power of 400 W to standardize surface chemistry over the whole samples.

Characterizing etching depth on the samples The various obtained etching depths were characterized thanks to AFM in tapping mode with a RTESPA-525 tip. The probed areas were at least $60 \mu m^2$ and the scanning frequency was lesser than 1.2 Hz. Control parameters such as oscillation amplitude and gains were adjusted depending on motif height for each sample. At least 4 linear motifs were probed for each sample, over a scanning length of $4 \mu m$.

Nanoscope Analysis software was used to analyze the measured data. Motif height measurements were performed with the Step tool, which computes the mean height over all profiles on the image and which yields the corresponding mean height profile. The Roughness tool was used to compute the motif height quadratic mean. This value represents the height standard deviation and describes the squared deviation to the mean height value. It is computed as follows: $R_q = \frac{1}{L} \int_0^L z^2 dl$ with L standing for the total distance over which measured heights are integrated, and z standing for the axial distance between each measure. Mean motif widths were determined thanks to the Width tool as follows: two motif widths were measured at 5% and 95% of the mean motif height respectively.

Seeding, fixing and observing macrophages on crenelated substrates

Human monocytes were isolated from peripheral blood of healthy donors as has been already described in the work of Van Goethem *et al.* (Van Goethem et al., 2010). After 7 days of differentiation in RPMI medium supplemented with recombinant M-CSF, L-glutamine and fetal calf serum (FCS), and in the presence of antibiotics - penicillin and streptomycin -, macrophages were harvested and approximately 10^5 cells were seeded on each 2.5D patterned coverslips, previously sterilized for 2 hours in a dry oven at $180^\circ C$.

The cells were plated for 20 minutes, then FCS-supplemented medium was added and the cells were further left to adhere overnight. They were unroofed thanks to a flow of sterile distilled water supplemented with $10 \mu g.mL^{-1}$ phalloidin and protease inhibitor cocktail, previous to being fixed in paraformaldehyde.

Samples were immunostained with a primary antibody against vinculin, an Alexa Fluor 555-conjugated secondary antibody and Alexa Fluor 488-conjugated phalloidin. Samples were eventually mounted on glass slides in Mowiol DAKO fluorescent mounting medium, and left to solidify overnight.

Fluorescent stainings were observed with a conventional widefield Leica LEITZ DMRB microscope equipped with 63x and 100x oil-immersion objectives and a Photometrics CoolSnap HQ camera, over areas of approximately $0.5*0.5 cm^2$ at the center of each coverslip. In the same regions, the crenel motifs were observed with the same microscope in light transmission mode. Acquisitions of a dozen of cells per coverslip were performed both in light transmission and fluorescence modes sequentially.

Quantifying podosome alignment relative to 2.5D motifs

A dedicated ImageJ macro was developed in order to characterize the influence of the crenels on podosome spatial distribution. As a first approach, F-actin and vinculin intensity variations and the repartition of F-actin fluorescent signal peaks were assessed with respects to motif localization.

The three major macro functionalities are as follows (Fig. 3.33):

- creating a file where all result files are saved;
- creating a merged image of the light transmission and fluorescence images acquired;
- evaluating F-actin, vinculin signal intensity variations and F-actin peak intensity localization depending on the distance to a motif.

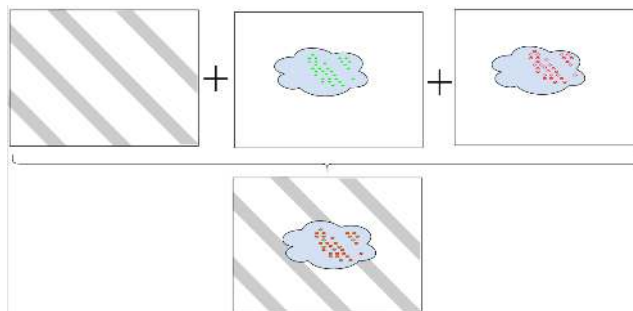


Figure 3.33.: Creation of a merged image to visualize actin-rich cores and ring proteins with epi-fluorescence, with respect to the topographic features observed with light transmission.

Before any analysis on acquisitions, background noise was reduced in F-actin and vinculin staining images thanks to ImageJ Subtract Background function. Images are scanned from top to bottom on a pixel wide line parallel to the motif length, after rotating acquisitions if need be. For each scan line: mean F-actin and vinculin signal intensity, podosome number and cell area are computed. Fluorescence signal intensities and podosome numbers are then divided by the corresponding cell area.

Creating binary masks for localization analyses - Based on the fluorescence images for F-actin and vinculin stainings, various masks were generated (Fig. 3.34). One binary 8-bit mask displays the total area occupied by the plated cell, based on a contour drawn by the user based on the F-actin image. The others are a modification of the original images for F-actin and vinculin staining respectively, with the pixel value arbitrarily set to 0 out of the cell area; or unchanged if the pixel is inside the cell area previously contoured.

The F-actin peak intensity localizations were detected using the ImageJ Find Maxima function, with the threshold value being user-defined according to the quality of the image. This selection resulted in a binary mask associating each peak with one pixel. Finally, the user drew the contours of one motif on the light transmission image to automatically generate a binary mask locating the top of the crenels.

Measuring required data for further analysis - The cell contour binary mask was scanned from top to bottom to evaluate the cell area on the corresponding section (Fig. 3.35). Thus, on each line the following computation was performed: $S_{cell} = \frac{IS}{255}$, where I is the mean intensity along this section and S is the area of the scanning line in pixels. The values were then converted to μm^2 .

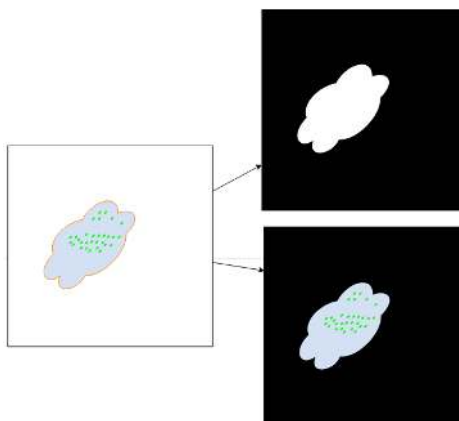


Figure 3.34.: Creation of masks based on actin fluorescence image. The binary mask allows for cell area evaluation. The other mask allows for computing mean actin intensity and podosome numbers.

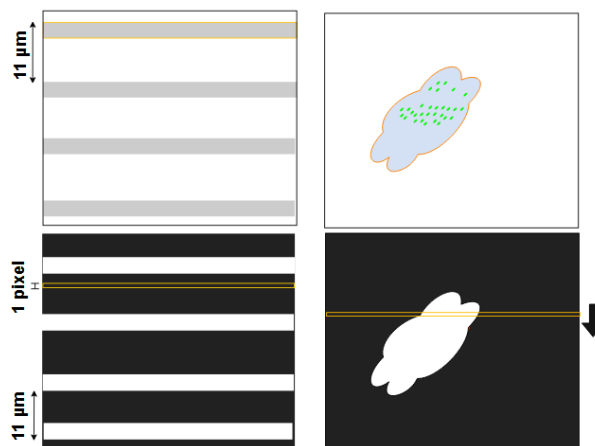


Figure 3.35.: The binary mask allows for cell area evaluation estimation by scanning the image from top to bottom and storing the mean intensity value for each scan line.

Both non-binary masks representing F-actin and vinculin stainings respectively inside the cell area only were scanned similarly. Mean fluorescence signal over the scanning line was computed then divided by the cell area occupied on the corresponding section. The binary mask displaying the localization of podosomes was also scanned. For each scan line, the number of podosomes comprised in this section was computed as follows: $N_{podosomes} = \frac{IS}{255}$, I and S are defined in the same way as just above. The obtained value was finally divided by the cell area occupied on the corresponding section.

3.3.3. Main results

Optimizing topographical motifs fabrication parameters

Photolithography parameters During the first tests, the insolation dose for UV photolithography was set to 200 mJ.cm^{-2} and three development durations of 5, 10 and 20 seconds were tested. Microscopy observations of the etched samples after the 20 second development revealed discontinuous motifs pointing to an issue of resist over-development. As for the 5 and 10 second durations, samples displayed zones where the resist had been lifted off during the etching process. Based on these observations, development speed needed to be modified in order to yield a reproducible and controlled process.

As development speed decreases with the energy dose received by the photoresist during insolation, this parameter was the first to be optimized. Development duration was fixed to 30 seconds, in order to discriminate insolation doses allowing for slower resist development. Three insolation doses were tested: 50, 100 and 150 mJ.cm^{-2} , with the chrome mask being kept close to the samples in hard contact mode. Samples were characterized by wide field microscopy observations of the resist just after development.

For the 150 mJ.cm^{-2} dose, the photoresist displayed discontinuous resist motifs after 30 second development. The sample exposed with a dose of 100 mJ.cm^{-2} showed a light under-development, whereas the one exposed with a dose of 50 mJ.cm^{-2} revealed a more obvious under-development with the motifs being much wider than they should have been (Fig. 3.36).



Figure 3.36.: Optical microscope observation of the center of the coverslip, 10x magnification. The sample was exposed with a dose of 50 mJ.cm^{-2} . Resist motifs appeared wide and under-developed.

Under-developed samples were further immersed in the developer for 20 additional seconds, and were subsequently observed. The sample which had been insolated with a 50 mJ.cm^{-2} dose showed no further improvements of the motif resolution, certainly having received too small an energy dose. However, the resist motifs on the sample exposed with a dose of 100 mJ.cm^{-2} appeared more finely resolved (Fig. 3.37). This insolation dose was selected and applied for the rest of this study.



Figure 3.37.: Optical microscope observation of the center of the coverslip, 10x magnification. The sample was exposed with a dose of 100 mJ.cm^{-2} . Resist motifs appeared more resolved and slightly under-developed.

Multiple samples were then exposed with the same energy dose of 100 mJ.cm^{-2} , and were developed for various durations ranging from 30 to 75 seconds, with a 15 seconds step. The resist motifs were observed both under the light microscope and with a mechanical profilometer. Up to 45 seconds of development, motifs showed an under-developed aspect. Moreover, partial removal of the deposited resist and profilometer measurements revealed the presence of residual resist in between the crenels. The samples that were developed for 60 seconds apparently showed no residual resist detected by profilometer measurements. The motifs that had undergone a 75 second development were discontinuous (Fig. 3.38).

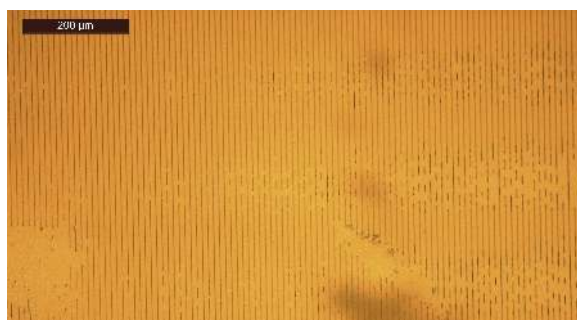


Figure 3.38.: Optical microscope observation of the center of the coverslip, 10x magnification. The sample was exposed with a dose of 100 mJ.cm^{-2} and developed for 75 seconds in CD MF-26. Resist motifs appeared highly discontinuous and over-developed.

The exposition dose of 100 mJ.cm^{-2} combined with a development duration of 60 seconds then appeared to be optimal for the hard contact mode insolation of ECI positive photoresist (Fig. 3.39). Height measurements with the profilometer on the samples that had undergone this same process yielded resist crenel heights ranging from 0.9 to $1.2 \mu\text{m}$. This result was consistent with the clean

room protocol data, which stated that the thickness of ECI photoresist on silica-based substrates should be approximately $1.1 \mu\text{m}$ following the previously described spin coating steps. However, certain samples displayed motif discontinuity under light microscope scrutiny (Fig. 3.40). These in-plane defaults were regularly distributed, which suggested they were due to the fabrication method of the chrome mask rather than created by faults previous to the development step. Indeed, direct observation of the mask confirmed this hypothesis as it showed the same deformations of the linear motifs.



Figure 3.39.: Optical microscope observation of the center of the coverslip, 10x magnification. The sample was exposed with a dose of $100 \text{ mJ}\cdot\text{cm}^{-2}$ and developed for 60 seconds in CD MF-26. Resist motifs appeared well-defined and continuous.

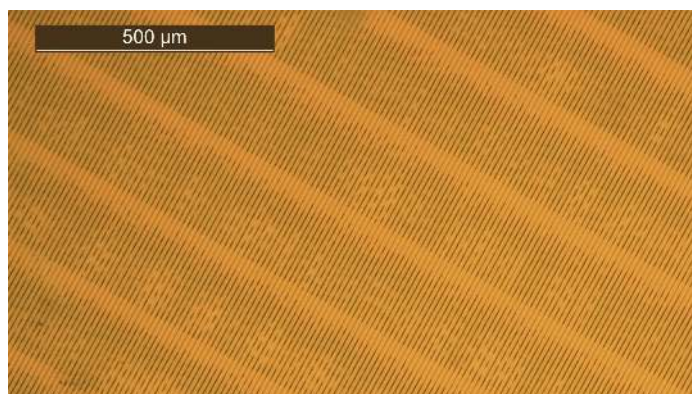


Figure 3.40.: Optical microscope observation of the center of the coverslip, 10x magnification. The sample was exposed with a dose of $100 \text{ mJ}\cdot\text{cm}^{-2}$ in hard contact, and developed for 60 seconds in CD MF-26. Resist motifs discontinuities appeared periodically distributed.

Following the etching of the glass coverslips, flaws were also observed along the motifs. Their general aspect pointed to the presence of residual resist between the crenels. To counter this issue, a dioxygen plasma cleaning stage was added between the resist development and the wet etching.

The plasma parameters were set to a power of 200 W with a gas flow of 1000 sccm for 2 minutes. Furthermore, this additional step allowed for boosting the hydrophilicity of the glass surface, thus facilitating the etching process.

Wet etched substrate characterization - Wet etched crenels obtained after a 90 second immersion in hydrofluoric acid were observed with a scanning electron microscope (SEM). On the approximately 3 mm^2 observed area, motifs appeared to be regularly shaped and distributed (Fig. 3.41).

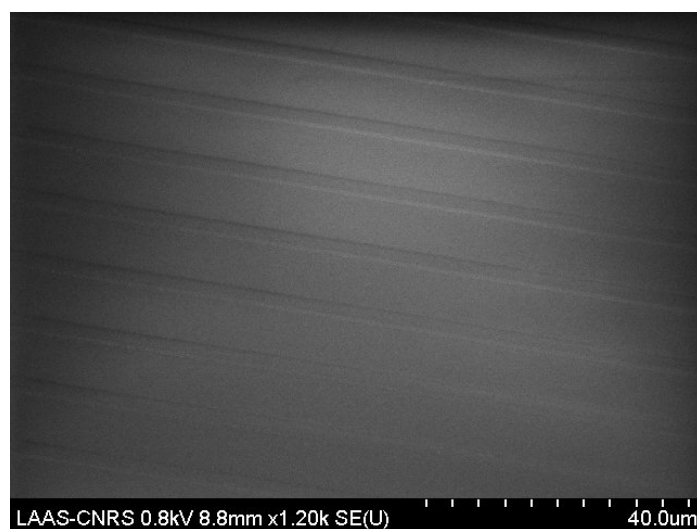


Figure 3.41.: Scanning electron microscopy observation of the topographic features after wet etching. No surface metallisation step was performed. Motifs displayed regular dimensions.

The etching rate was asserted from height measurements. Results are shown in Figure 3.42, for borosilicate glass coverslips etched in buffered hydrofluoric acid (7:1) for immersion times ranging from 10 to 180 seconds. The buffer over acid ratio was selected based on results of various dilution tests. This 7:1 ratio allows a wide range of etching depths, as is well adapted for this exploratory study. Furthermore, etching speed is stabilized with a solution pH that is kept constant over the reaction, which eventually yields reproducible results and enables tuning the exact etching time for a given etching depth. The OriginPro8 software was used in order to linearly fit the etching time *vs.* depth results. The slope gave an etching speed of $62.8 \pm 0.8 \text{ nm} \cdot \text{min}^{-1}$. This value is consistent with the work of Blass *et al.* (Blass et al., 2013) on etching the same material with buffered hydrofluoric acid (7:1).

The etching depths obtained for the various coverslips used in this study are gathered in table 3.15. Mean etching depths ranged from $6.8 \pm 0.4 \text{ nm}$ to $190 \pm 2 \text{ nm}$. All coverslips presented root mean squared roughness (R_q) between motifs ranging from one to two orders of magnitude lesser than the mean motif height. The in-between lines R_q value was comprised between 0.2 nm for an

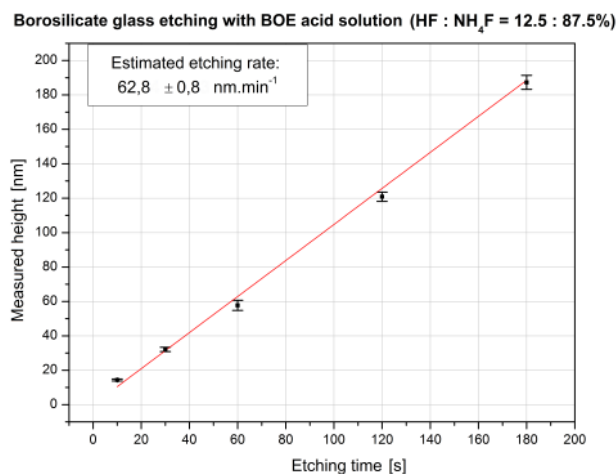


Figure 3.42.: Estimation of the etching rate of borosilicate glass by a buffered hydrofluoric acid (7:1) solution

Table 3.15.: AFM characterization results of etched coverslips subsequently used for cell plating

Mean motif height (<i>nm</i>)	Standard deviation	Roughness R_q (<i>nm</i>)	Motif width ratio between 95% and 5% of height	Mean motif width at 5% of mean height (μm)
6.8	0.8	0.2	0.80	2.3
11.0	0.4	0.2	0.97	1.9
16.5	2.2	0.3	0.87	1.8
31.7	1.2	0.7	0.92	3.0
33.0	0.6	0.3	0.87	2.6
58.1	3.2	0.4	0.80	1.8
116	1.6	0.4	0.63	2.5
190	4.0	1.6	0.57	1.6

etching time of 10 seconds, and went up to 1.6 *nm* for an etching time of 180 seconds. The in-between roughness values were also lesser than at least an order of magnitude compared to the protruding integrin length on the exterior side of the cell membrane of approximately 20 *nm* (Alberts et al., 2002).

The motif width assessed at 95% of their total height was comprised between 1 and 3 μm , which corresponds to the first neighbor distance range for individual podosomes in macrophages (Proag et al., 2015). This dimension should limit the occurring of two podosomes forming side by side on top the motif, in its transverse direction. However, measurements revealed that the motifs displayed highly variable widths. This could be improved by ensuring that the resist motif sides are not tilted after the development step. This could be achieved by further reducing the distance between the sample and the mask during the exposition phase, by opting for vacuum contact instead of hard contact, thus decreasing the lateral UV-light diffusion inside the resist coating. Some processed sub-

strates presented artifacts such as over-etching along a few microns, leading to motif discontinuities. Inhomogeneities in the resist patterning due to over-developing could explain these defects. A typical etching defect is presented in Figure 3.43.

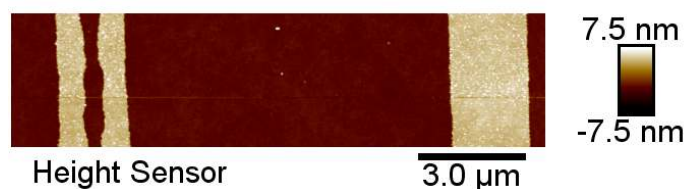


Figure 3.43.: Characteristic aspect of an etching defect observed with AFM tapping mode. The motif appeared irregular, with over-etching at its center.

Influence of the topographical motifs on podosome distribution

Observation of the cell-seeded samples revealed notable effects of the topographies on the spatial distribution of podosomes, for motif heights ranging from $190 \pm 2 \text{ nm}$ to $6.8 \pm 0.4 \text{ nm}$. Different types of observation cases were reported:

- macrophages presenting podosome-enriched areas alternatively with linear podosome-lacking regions, as shown in Figure 3.44. After merging fluorescence images with light transmission image, it appeared that the podosome lacking surfaces corresponded with the top surfaces of the topographies. This segregation effect on podosomes was also noticed in mean density profiles resulting from image analysis with the previously described macro functionalities.
- macrophages displaying a podosome accumulation along the motif length, as shown in Figure 3.45.
- macrophages showing randomly distributed podosomes over the whole cell area. This might occur due to motif defects caused by inhomogeneous resist developing, thus resulting in topography discontinuities.

These observations proved that topographical motifs were able to influence the spatial distribution of adhesion structures at the axial nanoscale, down to a 6 nm crenel height. This distribution change was notably noticed through F-actin peak density differences between the top and the bottom of the motifs, as well as in between the motifs lengths, as summarized in Figure 3.46.

This exploratory study remained quite qualitative, as it considered not more than three characteristic cells plated on the processed coverslips. It ought to be furthered on a greater dataset of cells and processed substrates in order to help decipher prospective statistical trends. These early results still gave rise to potential hypotheses explaining the versatility of observed cell phenotypes:

- topographies were inhomogeneous over the whole observed surfaces, which could demonstrate technological limitations inherent relative to the 2.5D motifs fabrication;
- motif widths displayed non-negligible fluctuations over the surface of the explored regions, and subsequently local plasma membrane curvature varied dramatically at the cell scale;

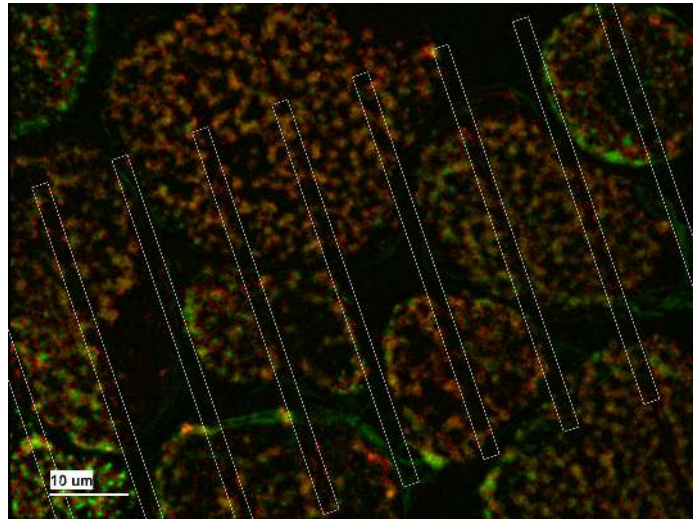


Figure 3.44.: Merged image of actin (green) and vinculin (red) stainings of human macrophages plated on the coverslip displaying 16 nm high topographies. White rectangles show the position of the motifs, as observed with light transmission. Podosomes appeared to preferentially localize between the motifs, and were mostly lacking from the top of topographies.

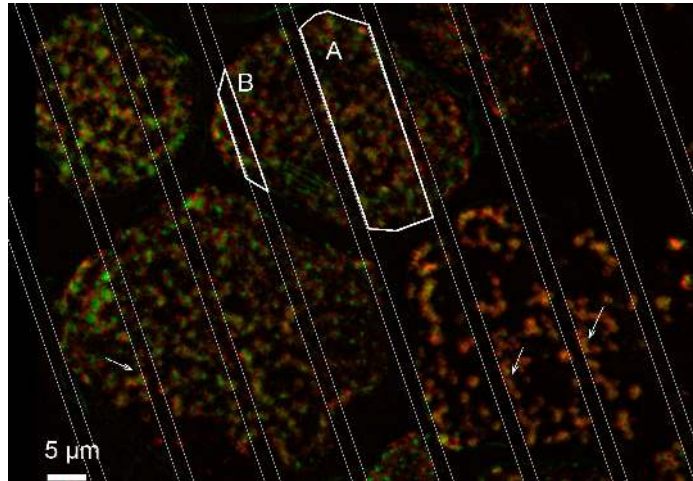


Figure 3.45.: Merged image of actin (green) and vinculin (red) stainings of human macrophages plated on a coverslip displaying 16 nm high topographies. White rectangles show the position of the motifs, as observed with light transmission. Some podosomes appeared to preferentially localize at the edge of motifs (white arrows). Within the same cell, podosome-rich areas (A) coexist with zones exhibiting seldom podosomes.

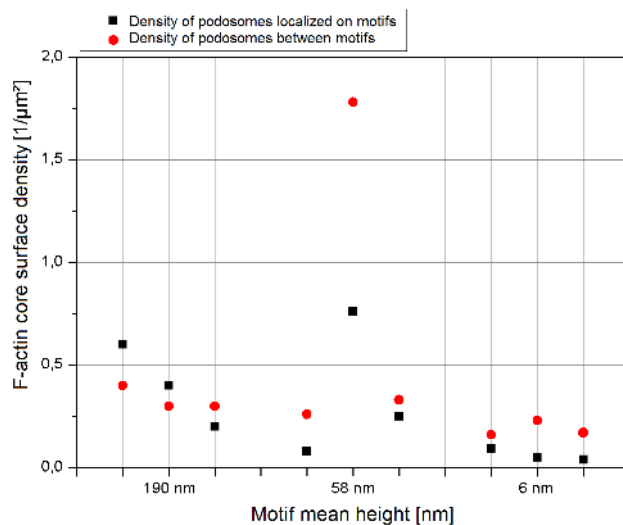


Figure 3.46.: Preferential localization of actin cores relative to the motifs, depending on the topography heights. Black squares represent actin core density on the motifs, and red dots account for actin cores between the topographies. (Each triplet of values stands for one sample with mean motif height specified on the bottom axis.)

- image analyses were conducted based on user-defined contour selections and signal improvement parameters instead of objective signal information;
- macrophages were derived from monocytes of different blood donors, which inherently implied biological diversity of responses such as integrin ratios.

3.3.4. Discussion

Achievements, limits and perspectives

This exploratory project focused on developing nanoscale devices to study podosomes in a topography sensing context, and allowed to establish an optimized protocol for the processing of 2.5D substrates. These shaped coverslips are compatible with future super-resolved microscopy imaging, in particular for the purpose of axially localizing mechanotransduction-involved proteins with respect to the position of crenellations. As early analyses of widefield images showed, podosome spatial distribution appears to be affected by periodic topographical motifs of height as low as a dozen nanometers. However, due to the obvious lack of statistically relevant data, no thorough or objective explanation for the observed discrepancies can be proposed for now.

Regularity and homogeneity of motifs - The major limitation to the motif fabrication method lies in the lack of standardized aspect of the crenels. Indeed, AFM observations revealed

variations in pattern widths and localized over-etched regions a few microns long. What is more, AFM-imaged areas were restricted to a few tens of squared microns. It is hence difficult to quantify motif regularity over the whole substrate surface, or whether these variations could affect cell responses. In order to tackle this issue, it would be interesting to use the same substrates with macrophages derived from different monocyte donors, by removing previously imaged cells completely from the coverslip. Here to limit this uncertainty, several zones confined to approximately 0.5 mm^2 on the middle of the coverslips were characterized with AFM, and a restricted central region was observed with widefield microscopy accordingly.

Scanning electron microscopy (SEM) was also proposed to acquire views of the etched coverslip surface condition. Samples were not metallized and scanned with an acceleration tension lower than 1 kV to minimize charging effects. This microscopy technique could enable the exploration of the entire surface, and the detection of potential etching defects, while ensuring the sample integrity. However, this approach would compulsorily be coupled with AFM motif height and roughness evaluations. An alternative solution to improve crenel standardization is to further reduce the resist developing time, by diluting the developer solution to more finely tune optimal immersion time. This increase in development duration would also benefit from a decrease of the time appreciation relative error, and would thus enhance reproducibility of this protocol stage. Adding hydrochloric acid to the hydrofluoric acid solution could similarly improve surface quality after wet etching. This kind of solution has been commonly used in the context of borosilicate glass etching (Rinke et al., 2017; Iliescu et al., 2005).

Finally, motif in-plane inhomogeneity could be due to the chrome mask fabrication process. It would be interesting to explore whether producing a mask free of defects is a feasible option. Thus, the newly processed mask could additionally display a compartmentalization where various crenel widths and periodicities might be explored.

Data and image analysis - Firstly, a statistically significant study of cell response to topography variations is required in order to conclude on this effect. It would be interesting to assess the percentage of cells showing an organized pattern of individual podosomes compared to cells displaying a random distribution of podosomes, and to characterize the potential organization patterns in the presence of 2.5D motifs. Also, feats worth estimating are the density and geometric parameters of podosomes in the presence of motifs *versus* on a flat surface. These quantifications would be better performed with a more resolved microscopy technique, such as confocal or structured illumination microscopy.

What is more, enhanced microscopy resolution would greatly improve the image analysis process. Indeed, the proposed methodology is but a draft of the potential information extraction attainable with this type of devices. The inter-core distance distributions could be evaluated in the case of podosome pattern-displaying cells, and tessellation tools could also help gaining insight into the specific arrangement of podosomes in the presence of 2.5D motifs. An alignment quantification based on relative orientation between neighbors could also be exploited as has been in previous works (Van den Dries et al., 2012; Meddens et al., 2013). Considering other podosome-associated proteins,

gaining in imaging resolution would allow for more detailed characterization of their rearrangement due to the presence of 2.5D motifs. As for example, potential asymmetry of the vinculin ring could be assessed following the previously published work of Walde *et al.* (Walde et al., 2014). This asymmetry could be representative of a local reorganization of podosomal architecture, or of a possible tilt in its axial orientation due to the topography.

Investigating signaling pathways induced by topography sensing - Analyzing fluorescence signal variation along cross-sections transverse to the motifs would consist in a first basic approach to decipher whether podosomes localize preferentially to the top or bottom edge of the crenellations. However, both podosome core and motif heights are close to classic confocal axial resolution. Imaging cells plated on these 2.5D substrates with super-resolved microscopy technique coupled with a finer axial resolution like DONALD setup (Bourg et al., 2015) would greatly help in solving this question.

For this exploratory study, podosome distribution was assessed at a given time, with cells being fixed after adhering for a few hours. However, it would easily be feasible to follow the successive formation and disassembly cycles of podosomes with live cell imaging. This would bring new insight into how cell topography sensing influence F-actin dynamics. Acquisitions on longer timespans could also shed light on potential cytoskeleton reorganization and migration directionality due to topography variations.

Smoothing the edges of the motifs could also prove to be an interesting alternative to explore how podosomes and the plasma membrane adapt to slope changes. It would also allow for discussing the impact of local membrane curvature on adhesion structure formation, as has been proposed by Van den Dries *et al.* (Linder et al., 2015; Van den Dries et al., 2012). In order to test whether topographical motifs represent diffusion barriers for integrins on cell membrane, single particle tracking (SPT) methods could be applied in the context of the developed 2.5D substrates.

Eventually, the specific role of integrins in potentially directing podosome formation through topography sensing could be addressed considering two major hypotheses:

- local relief induces membrane curvature such that it tends to fit its shape, and thus leads to higher local interaction probability for a specific integrin-ligand pair;
- integrins bump into the relief due to steric hindrance, and are thus activated in a way that stimulates mechanotransduction signaling.

3.4. Discussion

This section presented the very exploratory results of two independent studies on designing new super-resolution microscopy compatible devices.

The proposition of a three-dimensional super-resolved traction force microscopy setup did not completely yield satisfactory results especially considering its ability to give access to adhesion-mediated deformations, and was thus set aside. However, the previously described results could still be used in order to design substrates for mechanosensitivity exploration with super-resolution microscopy techniques. For this purpose, the polyacrylamide gels would not be coated with fluorescent proteins, which would enhance the extracellular matrix protein coating and thus possibly heighten cell adhesion. It would still be required to assess the apparent mechanical properties of the substrates, given the obvious prevalence of the glass coverslip in this “composite” material. And if these mechanosensitivity experiments were to be performed with SAF-analysis nanoscopy techniques (Bourg et al., 2015; Cabriel et al., 2019; Sivankutty et al., 2019), it would be essential that research be conducted on both the influence of the second optical interface on the localization precision, and improvement strategies to counter its expected resolution-loss impact.

The direct shaping of coverslips compatible with super-resolution proved its efficiency in providing submicron crenellations, spanning three orders of magnitude in height. These powerful tools apparently revealed their ability to induce alterations in individual podosome spatial distribution. Hence, they open the way for multiple further analyses. Due to their acute thickness calibration, the etched coverslips are suitable for SAF-analysis nanoscopy with DONALD setup. They could also be beneficial for the study of podosome dynamic behavior on nanoscale topography, as has been done with osteoclasts on non-patterned rough calcite surfaces (Geblinger et al., 2009; Geblinger et al., 2010; Shemesh et al., 2017). Furthermore, as the protocol has been optimized to yield etching depths ranging from a few hundreds to a few nanometers, it would be a potential alternative study to explore the impact of the change in geometry of the motifs, as well as the change of pattern anisotropy degree on cell adhesion. Either way, image analysis strategies would be required to be greatly improved and adapted to higher-resolution acquisition methodologies.

Eventually, it could be imagined to merge both presented protocols to yield substrates on which impacts of simultaneous alterations in mechanical and topographical could be observed. Indeed, an etched coverslip could be used as the inactivated coverslip for the polyacrylamide sandwich process in a nano-imprint machine. This protocol would allow for the production of nanoscale polyacrylamide motifs, of controlled geometry and mechanical properties. What is more, two extracellular matrix protein coating strategies could be implemented: either the whole polyacrylamide and glass surface can be grafted with integrin ligand through complete immersion; or the localization of proteins could be restricted to the top of the polyacrylamide motifs *via* an adapted version of micro-contact printing. Cells adhering on this kind of substrates could then be imaged with super-resolution microscopy setups, and exploration of the nanoscale architecture of their adhesion structure could reveal valuable information on how cells probe their environment.

Conclusions

Discussion about the nanoscale architecture and dynamics of the sealing zone

As seen in the literature review about the sealing zone (1.3), apart from actin, only poor knowledge is available concerning the precise organization of its components. Especially, as this structure is specific to osteoclast adhesion on bone matrix, its characterization during active resorbing activity has been elusive, and is not compatible with classic high-resolution microscopy techniques.

By combining cutting-edge super-resolution techniques and scanning electron microscopy, we were able to report that the sealing zone in human osteoclasts displays the same nanoscale organization of small actin cores nested within a dense network of actin filaments. The morphometric analyses of the core subunits arrangement gave similar results with SEM and RIM techniques, and resulted in slightly different neighbor-to-neighbor distances compared to previous studies on murine osteoclasts (Luxenburg et al., 2007; Anderegg et al., 2011). Dynamic study of actin in actively resorbing cells yielded the first report of actin-related oscillations at the sites of the sealing zone subunits. Specifically, actin core-associated oscillations were showed to be synchronous between close neighbors. In addition, localization of some major actin crosslinker and adhesion plaque proteins revealed that proteins such as vinculin, paxillin and talin were not completely excluded from the inner part of the sealing zone (Lakkakorpi et al., 1993; Babb et al., 1997; Pfaff et al., 2001; Jurdic et al., 2006). This exciting finding shook the usual representation of the sealing zone, and participates in providing a new picture of its nanoscale organization. Combining all our results, we proposed a model where the sealing zone is composed of synchronous islets of actin cores, displaying variable sizes and encircled by adhesion complexes.

This study will hopefully pave the way for further thorough explorations of the sealing zone nanoscale architecture. It could notably participate in providing more detailed information about the localization of key regulators of the sealing zone components, such as Src family kinases involved in the phosphorylation of actin-binding proteins throughout the structure (Lakkakorpi et al., 1999; Pfaff et al., 2001; Szymkiewicz et al., 2004; Heckel et al., 2009; Blangy et al., 2012). Such insights would greatly help in unraveling the mechanisms responsible for actin polymerization/depolymerization within single cores. Therefore, a more comprehensive understanding of the dynamic events occurring at larger scales could also be added to the new model we proposed.

Osteoclasts have been reported to resorb bone in a non-randomly manner, based notably on the mechanical properties of osteons (Pernelle et al., 2017). Their migration process on polymer-based substrates has also been described as involving centrifugal tension coupled with podosome ring expansion (Hu et al., 2011b). In addition, osteoclast migration, establishment of the sealing zone and resorbing activity have also been proposed to be under the regulation of substrate micro- and nanotopography (Geblinger et al., 2010; Geblinger et al., 2011; Shemesh et al., 2015; Shemesh et al., 2017). Apart from these insights, not much is known about the osteoclast specific responses to matrix physical cues, nor about the mechanical properties of the sealing zone.

In the case of the sealing zone, the existence of a local synchrony at the scale of a few actin cores bears mechanical significance when put in perspective with bone resorption activity. Efficient resorption requires a tightly confined environment to drastically decrease the pH. If there existed a global synchrony for actin core oscillations throughout the structure, it would lead to repeated periods during which the confinement efficiency would be lower, and therefore the risk for potential “leaking” would be high. In contrast, it would be expected that a perfectly static system, keeping a steady contact with the matrix during the whole resorption time would be optimal for bone degradation. However, it might be costly for the cell to thus restrict a major pool of its inner components to the accomplishment of one task, while striving at preserving its perfect stability. Energetically speaking, synchrony at the scale of islets might represent the optimal “cost *vs.* efficiency” solution. Modeling this mechanical behavior while taking into account the various signaling cues could consist in a most exciting interdisciplinary research project, and would provide crucial information about the sealing zone.

In human macrophage podosomes, actin oscillations similar to that observed within the sealing zone have been associated with the generation of protruding forces (Labernadie et al., 2014; Proag et al., 2015; Bouissou et al., 2017). This characterization has been facilitated by the development of a new method to assess axial deformations induced by podosomes: protrusion force microscopy (Labernadie et al., 2014; Bouissou et al., 2018). However, applying this technique to the study of osteoclasts did not appear as the best option, as protrusion force microscopy does not allow for measuring planar forces. Nor does it allow for simultaneously visualizing the probed cell structure, which is a pre-requisite for force reconstruction. In this context, part of this PhD work focused on developing a new tool to access 3D estimation of forces applied on 2D substrates. In addition, I also started the development of tools to investigate how the sealing zone probes topography. Eventually, for both these substrate-development projects, the versatility of the aimed outcomes point to their possible use in the general context of cell adhesion, and not only podosome-based structures.

Discussion about the development of substrates for nanoscale investigation of the mechanical properties and topography sensing of adhesion structures

The methodologies described in the third chapter of this manuscript are in line with the recent investigations aiming at unraveling cell-matrix interactions. They were designed in order to simplify the complex system gathering all extracellular matrix cues to only one physical aspect of the problem. Furthermore, their use would allow for a structural approach of adhesion structures in a matrix mimicking context, in addition to the identification of their global regulation by physical cues.

Deformable substrates for super-resolution microscopy

Due to the current lack of techniques allowing for the quantification of cell-exerted forces at the nanoscale and combining evaluation of both in-plane and axial adhesion-induced deformations, we aimed at taking advantage of the available DONALD setup to attempt at bridging the gap in this cell mechanics field.

When considering the development of a new 3D super-resolution traction force microscopy technique, we came across some doubts about the feasibility of such a technique. Indeed, the presence of the polyacrylamide coating induced the presence of an additional optical interface, and how this optical index jump effectively affects the localization precision is yet to be characterized. Moreover, as the target thickness for polyacrylamide coatings did not exceed 200-300 nm, it is unsure whether the forces applied at adhesion sites would be substantial enough to yield measurable displacements of the fiducial markers. Eventually, the use of single molecule localization microscopy to characterize the stressed and relaxed conformations of the gels might not be compatible with the traditional displacement recognition analysis as it is. Therefore, this project requires major advances in the interdisciplinary field of cell mechanics in order to possibly reach completion. However, successful achievements during the conduct of this project opened a new alternative for the use of these thin polyacrylamide coatings. Rather than trying to quantify their deformation induced by adhesion structures, they could make powerful tools for the characterization at the nanoscale of adhesion site architecture in the context of mechanosensing.

Recent explorations focusing on the characterization of cell-exerted forces in fact revealed the increasing use of micro- and nanofabrication techniques to improve the spatial resolution of displacements through the precise deposition of fiducial markers (Bergert et al., 2016). In addition, other techniques relied on label-free strategies to unravel deformations. For example, the protrusion force microscopy technique developed in the lab relies on AFM measurements of the surface topography of a thin film on which macrophage podosomes protrude Labernadie et al., 2014; Bouissou et al., 2018. Other techniques have taken advantage of light reflection in original manners, and inferred cell-exerted forces through the analysis of interferences or the quantification of volume variations (Kim et al., 2016; Kronenberg et al., 2017). However, these setups do not allow for imaging the cell structures involved in the deformation process. Specifically, only rare methods for measuring cell-

exerted forces have also provided insight into the precise architecture of adhesion sites (Morimatsu et al., 2015).

In general, the field of cell mechanics is in dire need of efficient tools benefiting from an easy implementation, and allowing for the simultaneous identification of: global response to matrix mimicking cues, and precise localization of major proteins involved in adhesion structures.

Nanotopographic features for super-resolution microscopy

Again aiming at benefiting from the three-dimensional resolution of DONALD setup, we also explored its possible future application to decipher topography sensing.

Topographic features were implemented on the surface of glass coverslips by direct etching of the material in between protective resist motifs, obtained through photolithography process. Modulating the etching duration allowed for the generation of nanoscale topographies, but they displayed an apparent lack of standardized aspect. Further optimization of the photolithography and wet etching stages would help improving this point. Due to the lack of observations of cells on the crenelated surfaces, only basic image analysis were proposed for the moment. Upon achieving the production of highly reproducible substrates, the etched coverslips would eventually consist in powerful tools to investigate signaling pathways induced by topography sensing at the nanoscale.

Topographic features have been reported to affect various cell functions at a global scale, such as proliferation, migration, differentiation or polarization (Bettinger et al., 2009). These alterations have been reported to depend on subcellular components, namely the actin cytoskeleton and integrins Park et al., 2018. However, the specific role of these components have only been documented in an indirect manner. Specifically, imaging techniques applied in the context of topography sensing studies often do not allow for the precise observation of adhesion sites. This might be partly due to the use of materials with poor optical properties to shape topographies. Therefore, new approaches tackling topography sensing by direct shaping of glass coverslips will pave the way towards the precise comprehension of the specific cell mechanisms involved. Furthermore, parallel advances in micro- and nanofabrication processes allow for improving the complexity of topographic features directly implemented on glass.

Conclusions and perspectives

In conclusion, my PhD work has mainly helped providing new tools and their associated methodology in an ever-improving super-resolution context. These will not only allow for further characterizing the sealing zone in osteoclast at its subunit level with systematic fluorescence microscopy routines and image analysis procedures. They could also eventually consist in powerful turnkey solutions to access the 3D nanoscale localization of key cytoskeletal proteins on flat “control” surfaces, as well as in the context of evaluation of the mechanosensitive properties or topography sensing abilities of any adherent cell type. In order to achieve this comprehensive experimental package, some key experimentations still have yet to be carried out.

Improving knowledge about the sealing zone in osteoclasts

In the short term, the last months of my PhD will be dedicated to the finalization of the results pertaining to the nanoscale characterization of the sealing zone architecture and dynamics. Greater acquisition numbers are required to ensure our study is indeed relevant and provides a faithful account of the reality of the structure. Moreover, acquiring numerous other images could further our knowledge of the sealing zone, and may help us identify different categories of nanoscale organization, *e.g.* due to the global rearrangement during the resorption cycle. We also aim at recording longer time-lapse movies, and with dual color information, visualizing both actin and an adhesion plaque protein to help us decipher the dynamics associated with the core clusters that we observed. It could also be interesting to observe the effects on the local dynamics of various drugs interfering with actin dynamics, or other cytoskeletal components such as microtubules and myosins. Eventually, if time permits, exploring the localization of the major osteoclast integrin $\alpha v\text{-}\beta 3$ would provide most valuable information.

In the long term, it would obviously be most advantageous to benefit from this well-established workflow to thoroughly research other major actin crosslinkers, such as the ones cited in the literature review section 1.3. Their precise localization could therefore be finally uncovered, and a model of the inner dynamics of the sealing zone at the molecular level could be established. In addition, correlative microscopy observations combining RIM and SEM would help identifying their preferential sites of interactions along actin filaments. Ideally, all the proteins localized on fixed samples could also be dynamically recorded along with actin in live cells in order to confirm model assumptions, provided the biochemical tools are available. Furthermore, more biochemically oriented studies could be performed by silencing target proteins in osteoclasts and observe the effects on the sealing zone, and at the nanoscale level on the distribution of their potential partners. In the lab, efficient routines to apply siRNA treatments to human macrophages have already been developed and combined with super-resolution observations. Indeed, they have allowed for the identification of vinculin and paxillin as required for talin extension at the podosome ring (Bouissou et al., 2017). The possible necessity for adjustments in the case of osteoclasts should be evaluated, and the application of the same strategies to osteoclasts would certainly prove to yield valuable information.

Providing new tools for the comprehension of cellular responses to ECM properties

In the short term, concerning the coverslips coated with a thin film of polyacrylamide, their potential use for the study of mechanosensitive properties should be thoroughly asserted. In particular, two points should be explored in priority: whether thin coatings are achievable with the proposed protocol no matter the final material properties of the gel; and whether such devices are effectively efficient to induce significant variations of substrate stiffness, as sensed by cells. Indeed, as the polyacrylamide thickness represents little more than a thousandth of the coverslip thickness, it is expected that cells would not sense the real mechanical properties of the polyacrylamide, but

rather than of a mean material accounting for the superposition. To achieve this exploration, both experimental and *in silico* approaches could be combined. Experimental verification of the effective surface properties can be achieved thanks to AFM measurements on one side. On the other, mechanical modeling and simulations could be performed to predict the efficient rigidity as sensed by cells according to the shape and forces exerted by adhesion structures. Especially, AFM probing results would gather valuable information to precisely tune the model parameters, therefore putting forward results displaying higher fidelity to the real system.

Concerning the etched coverslips, as stated before, the priority should be given to multiplying the experiments in order to yield a statistically relevant and reproducible protocol. Extensive characterization of the samples will help assessing the improvement strategies to produce topographies with sharp and similar profiles all over the observable surface. Then, less ambiguous observations of adhesion structure patterning will be made possible, as the variations would no longer be imputable to variations of motif aspect.

In the long term, optimization of the observation conditions to combine these two substrate types with super-resolution techniques, such as DONALD, need to be assessed. Concerning the substrates for topography sensing, the direct etching of glass coverslips does not induce any optical hindrance, as is the case with the addition of another material. However, the basic workflow for image acquisition will have to be adapted to include the localization of the motif borders, probably still through transmission light imaging. In addition, adhesion structure dynamics in the presence of topographic features could be performed with RIM, on various timescales. This interesting exploration will therefore require the development of a dedicated data analysis procedure.

In the specific case of polyacrylamide-coated coverslips, provided that the two verifications afore mentioned have been fruitful, are “ready to use” *per se*, even if not directly with DONALD technique. Instead, they could be combined with other super-resolution techniques, such as RIM or dSTORM alone, to yield precise in-plane localization of target proteins while awaiting for the adjustments required for efficient axial localization. The 3D super-resolved project could also be picked up where it has been left off, if this modification of the DONALD setup proves feasible. It will still consist in a challenging study, which requires exciting new approaches in various research fields. Therefore, combining acute knowledge from the mechanical, mathematical and microscopy fields might prove successful in helping the completion of this bold project.

Appendices

Appendix A.

Appendix to chapter [2](#)

A.1. Details of the analysis workflow for the geometric characterization of actin cores with RIM technique

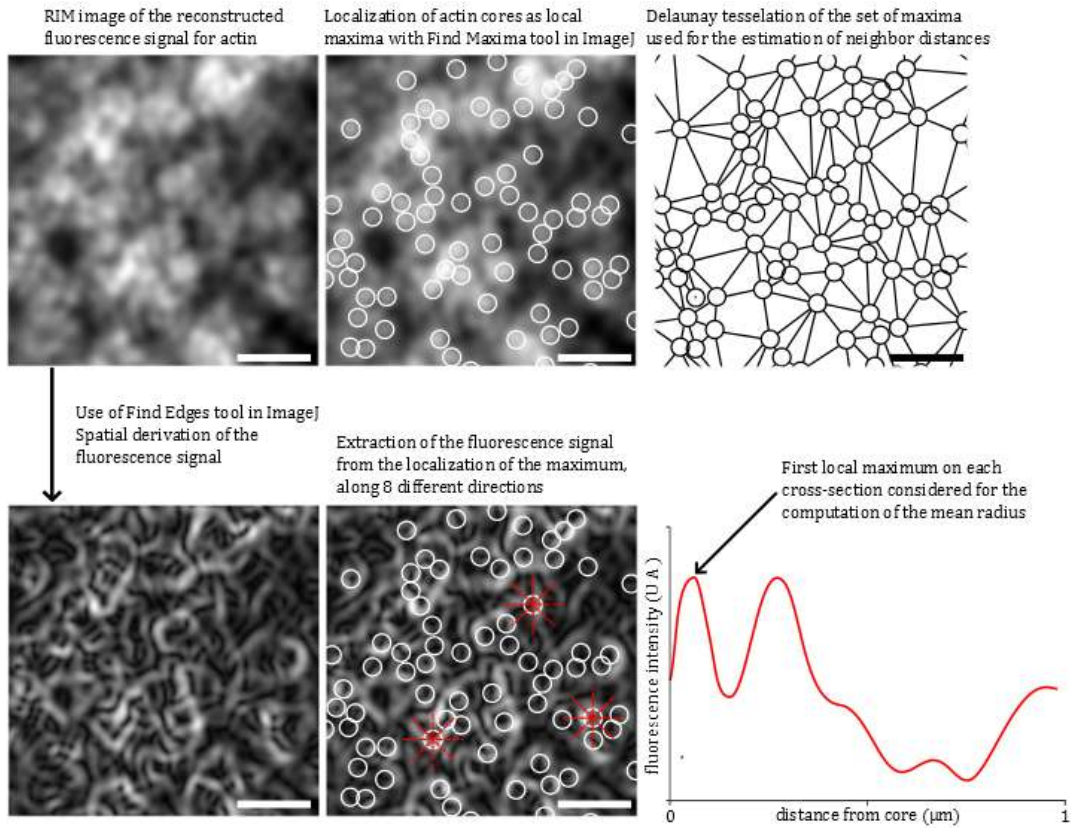


Figure A.1.: Analysis workflow for the geometric characterization of actin cores with RIM technique. When zooming in on a region of a sealing zone, it is observed that actin signal displays numerous local maxima that were localized. The corresponding coordinates were used to estimate the distance between two neighboring maxima, based on Delaunay's tessellation. Then, in order to assess the size of the actin dots, a spatial derivation of the signal was applied and the derived signal was extracted along 8 radii from the center of each dot. On these curves, the first local maximum corresponded to the edge of the actin spot and helped me compute the mean radius for all of them.

A.2. Details of the analysis workflow for the 2D localization of proteins relative to actin cores with RIM technique

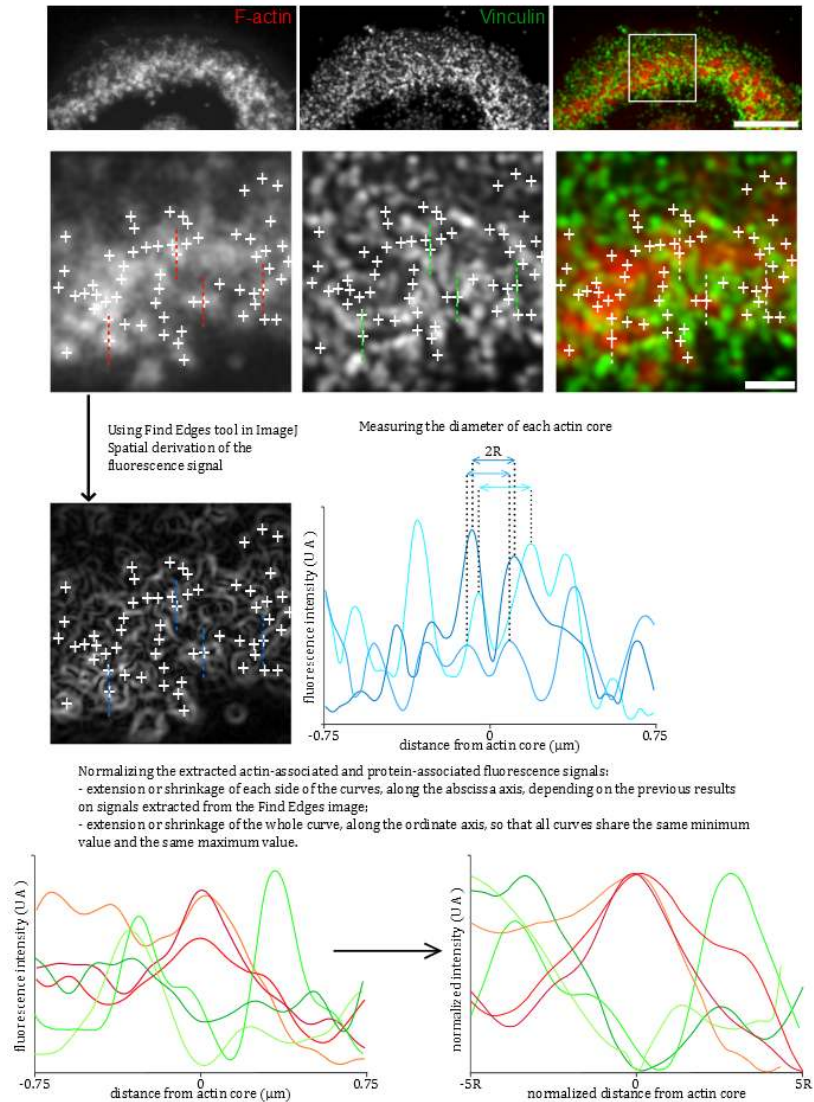


Figure A.2.: Analysis workflow for the 2D localization of proteins relative to actin cores with RIM technique. Similarly as for the evaluation of the size of actin cores, the first step was to extract the coordinates of the cores thanks to the actin staining image. And in the same way, data was also extracted in order to assess the diameter of each core. Then, the local orientation of the sealing zone was evaluated by the user, in order to extract both actin and protein associated signals in the transverse direction. But these curves are not comparable as such, so thanks to the size-related data a normalization protocol was performed on the signals so that they were ready for statistical analysis.

A.3. Details of the analysis workflow for the 3D localization of proteins relative to actin cores with DONALD technique

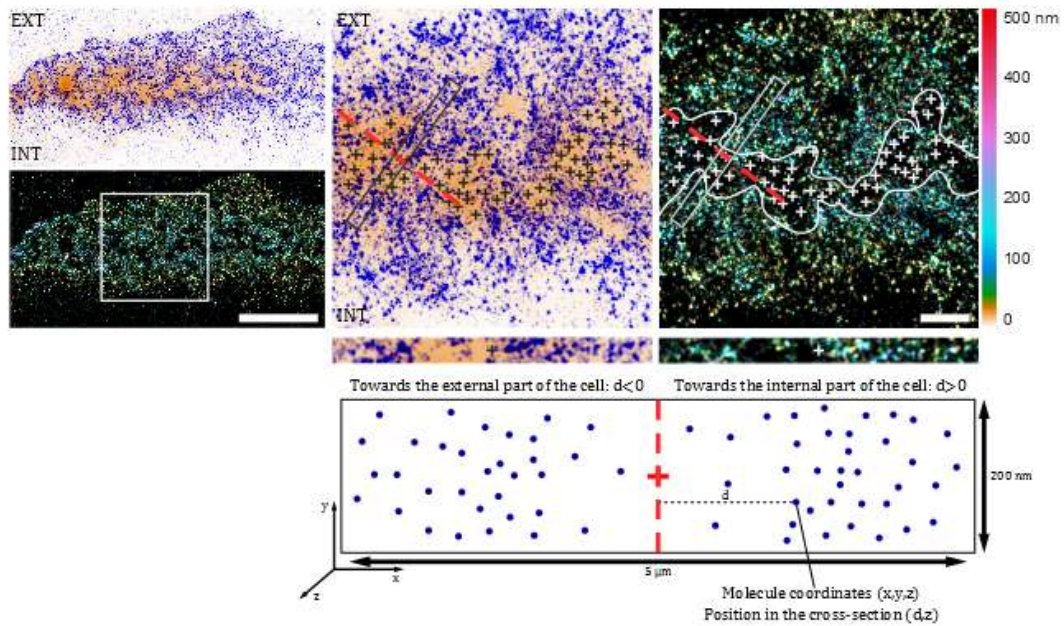


Figure A.3.: Analysis workflow for the 3D localization of proteins relative to actin cores with DONALD technique. When zooming in on a region of the belt, each of the actin cores in the different clusters were located by the user. Then, the general orientation of the cluster was evaluated, and a rectangular region was delimited and centered on an actin core, transverse to the direction of the cluster. Within these cross-sections, molecules were localized depending on their distance to the central axis of the cross-section and their height. Importantly, all molecules situated towards the cell edge were represented on the left, while those towards the interior of the cell are on the right in the associated charts.

A.5. Proposition for the 3D localization of proteins relative to actin cores, and dynamic processes within the sealing zone

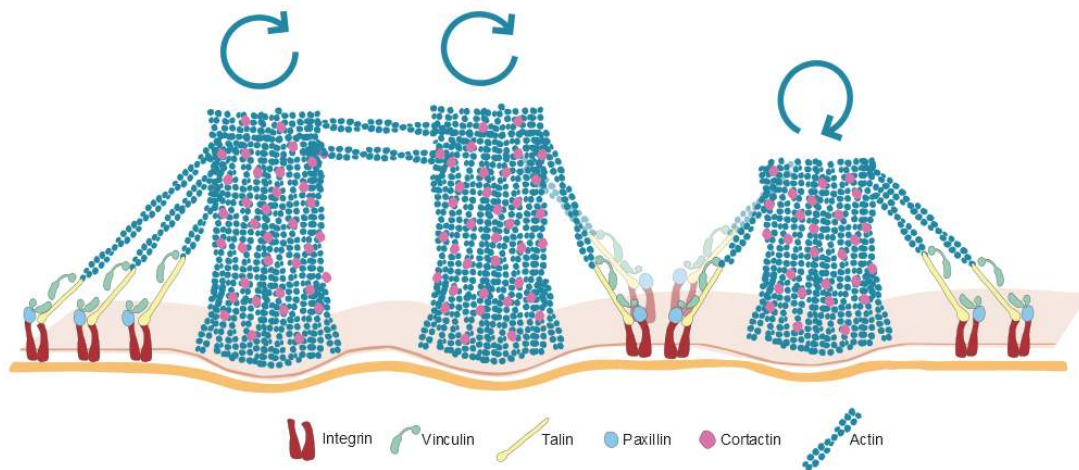


Figure A.5.: Schematics of the proposed dynamics and axial localization of proteins relative to actin cores within a sealing zone. Actin cores are represented as columns of a few hundreds of nanometers high, with a time-fluctuating content of F-actin. Observations also led to think that actin cores within the same cluster were more likely to be connected to each other, compared to two cores within two different clusters. This physical connection might be related to the apparently synchronous behavior that cores tended to display within clusters, with respect to actin content fluctuations. Moreover, actin cores are thought to be connected to the cluster-delimiting integrins *via* tilted actin filaments bound to elongated talin, vinculin and paxillin.

Appendix B.

Appendix: Annex publication

Video Article

Protrusion Force Microscopy: A Method to Quantify Forces Developed by Cell Protrusions

Anaïs Bouissou^{*1}, Amsha Proag^{*1}, Marion Portes¹, Vanessa Soldan², Stéphanie Balor², Christophe Thibault^{3,4}, Christophe Vieu^{3,4}, Isabelle Maridonneau-Parini¹, Renaud Poincloux¹

¹Institut de Pharmacologie et Biologie Structurale, IPBS, Université de Toulouse, CNRS, UPS

²METi

³CNRS, LAAS

⁴Univ de Toulouse, INSA

*These authors contributed equally

Correspondence to: Isabelle Maridonneau-Parini at maridono@ipbs.fr, Renaud Poincloux at Renaud.Poincloux@ipbs.fr

URL: <https://www.jove.com/video/57636>

DOI: [doi:10.3791/57636](https://doi.org/10.3791/57636)

Keywords: Biology, Issue 136, Cell Mechanics, Protrusion Force, Atomic Force Microscopy, Podosome, Macrophage

Date Published: 6/18/2018

Citation: Bouissou, A., Proag, A., Portes, M., Soldan, V., Balor, S., Thibault, C., Vieu, C., Maridonneau-Parini, I., Poincloux, R. Protrusion Force Microscopy: A Method to Quantify Forces Developed by Cell Protrusions. *J. Vis. Exp.* (136), e57636, doi:10.3791/57636 (2018).

Abstract

In numerous biological contexts, animal cells need to interact physically with their environment by developing mechanical forces. Among these, traction forces have been well-characterized, but there is a lack of techniques allowing the measurement of the protrusion forces exerted by cells orthogonally to their substrate. We designed an experimental setup to measure the protrusion forces exerted by adherent cells on their substrate. Cells plated on a compliant Formvar sheet deform this substrate and the resulting topography is mapped by atomic force microscopy (AFM) at the nanometer scale. Force values are then extracted from an analysis of the deformation profile based on the geometry of the protrusive cellular structures. Hence, the forces exerted by the individual protruding units of a living cell can be measured over time. This technique will enable the study of force generation and its regulation in the many cellular processes involving protrusion. Here, we describe its application to measure the protrusive forces generated by podosomes formed by human macrophages.

Video Link

The video component of this article can be found at <https://www.jove.com/video/57636/>

Introduction

Animal cells interact physically with the matrix and the other cells that constitute their environment¹. This is required for them to migrate, internalize bodies, acquire external information, or differentiate. In such processes, the cell must generate mechanical forces and, as numerous studies have shown over the recent years, the ability of a cell to generate forces and probe its environment influences its biological behavior, directing for instance proliferation or differentiation^{2,3}. In turn, the measurement of cellular forces is a major aid to study the regulation of force generation and understand its implication in cell behavior and tissue fate^{4,5}.

Recent years have witnessed the development of numerous techniques to measure the forces that a cell can exert on its environment⁶. The majority of these have been instrumental in revealing the traction forces that cells exert as they pull on mobile probes or a deformable substrate. However, the mechanical forces involved in protrusion into the extracellular environment suffer from a lack of measurement techniques and are to date not well characterized.

To overcome this limitation, we present a method to measure forces exerted orthogonally to the substrate. It consists in plating living cells on a thin elastic sheet that can deform in the orthogonal direction, making it possible to measure substrate deformation by the cells and deduce the forces involved. Substrate topography is measured with nanoscale resolution using atomic force microscopy and the evaluation of forces from deformation relies on the knowledge of the geometry of the protrusive cellular structures^{7,8,9}.

Here, we describe the setup and its application to measure the forces generated by podosomes, protrusive adhesion structures formed by macrophages for their mesenchymal migration in three-dimensional environments^{10,11,12,13,14,15,16,17}. We believe that this technique will advance the understanding of force generation and its regulation in the many cellular processes involving protrusion.

Protocol

1. Preparation of Formvar-Coated Grids

1. Clean electron microscopy grids with pure acetone and dry them on filter paper. Then clean a microscope slide with pure ethanol, wipe with a lens paper and remove dust with a blower.
2. Place an ethanol-cleaned glass slide vertically in the funnel of a film casting device containing a solution of Formvar in the lower part. Cover the top of the funnel.
3. Pump 100 mL of Formvar solution (0.5% in ethylene dichloride) with the atomizer bulb until the level reaches two thirds of the slide.
4. Keep the slide in the solution for 1 min.
5. Open the valve of the device to drain the Formvar solution in a steady stream. A flow rate of 10 to 15 mL/s will yield a Formvar film of 30-80 nm. The thickness of the film is determined by the concentration of the Formvar solution and by the drainage rate.
NOTE: The drainage rate can be controlled by venting the pressure *via* the air-out valve by slowly opening the valve. The faster the drainage, the thicker the film. In practice, because it is difficult to predict the film thickness from the Formvar flow rate, we prepare several batches of Formvar films and control their thickness by AFM (see Step 2).
6. Remove the slide from the chamber and dry it delicately on filter paper to remove any liquid Formvar.
7. Cut out a 20 mm x 50 mm rectangle from the Formvar film with a razor blade.
8. Fill a beaker with clean distilled water and slowly plunge the slide vertically into the water to float off the film: the film should float on the water surface.
9. Place dry acetone-cleaned grids on the film, shiny face up.
10. Place a round glass coverslip (\varnothing 12 mm) onto a few of the grids. This coverslip will serve to measure the film thickness (see Step 2).
11. Cover a microscope slide with a white sticker resized to fit it. Dip the slide vertically at the border of the floating Formvar film until the whole film adheres to the slide. Remove excess water from the slide with filter paper and let it dry at room temperature overnight.

2. Measurement of Film Thickness

1. Cut the Formvar around the coverslip with tweezers to detach it from the slide.
2. Mark the location of the grid under the coverslip with a pen.
3. Cut the Formvar around the marked grid to detach it from the coverslip. There will therefore be a hole in the remaining Formvar sheet, which will allow to measure the film thickness. Cover the coverslip with PBS and place it on a glass slide on the microscope.
4. Mount a silicon nitride cantilever on the AFM glass block, making sure the golden stripe is not covered by the tip of the spring.
NOTE: The sensitivity and spring constant of the cantilever should have previously been calibrated in PBS.
5. Mount the glass block onto the AFM module, and then place the module onto the microscope.
6. Place the Formvar-coated coverslip on the observation chamber and cover it with 500 μ L of PBS.
7. Scan the border of the hole in the Formvar sheet using AFM in contact mode and a 0.5 nN force set point.
8. Use the glass coverslip surface as the reference for height measurements, and evaluate the Formvar thickness as the height of the cross-section (perform at least 10 measurements per Formvar batch).

3. Seeding Cells on Grids

1. Under a sterile hood, put a strip (12 mm x 3 mm) of double-sided adhesive tape on a coverslip.
2. Cut out a Formvar-coated grid with tweezers and put it upside-down on the adhesive strip (only the rim of the grid needs to be attached to the tape). The Formvar film needs to face the coverslip.
3. Put this device in a culture well.
4. Place a 10 μ L droplet of RPMI without FCS containing 10^4 macrophages differentiated from human monocytes¹⁶.
NOTE: Make sure not to touch the grid with the pipette tip to prevent damaging the Formvar coating.
5. Incubate for 30 min (37 °C, 5% CO₂) to let cells adhere.
6. Fill up the well with 2 mL of RPMI containing 10% FCS.
7. Incubate the device for 2 h at 37 °C and 5% CO₂ to let cells adhere before AFM observation.

4. Topography Measurements of Podosome-Induced Deformations

1. Stick two strips of double-sided adhesive tape on a glass bottom Petri dish.
NOTE: The distance between the two strips should be smaller than the grid diameter.
2. Carefully detach the grid plated with macrophages from the adhesive tape.
3. Turn the grid upside-down in order to have the cells facing the glass and stick the grid between the two adhesive strips.
4. Fix the grid with two new strips of double-sided adhesive: the grid will thus be sandwiched between two adhesive strips, leaving the central area of the grid accessible to the AFM tip.
NOTE: Make sure that the grid is well fixed and not twisted; otherwise the AFM cantilever might not be able to approach the Formvar surface.
5. Fill the Petri dish with 2 mL of pre-heated 37 °C culture medium (RPMI with 10% FCS) supplemented with 10 mM HEPES (pH 7.4).
6. Place the culture dish on a 37 °C dish heater.
7. Install the dish heater on the AFM stage.
8. Let the system stabilize at 37 °C.
9. In contact mode with a 0.5 nN force, make a first global image to locate podosomes, and then scan the Formvar topography at 3 Hz with an approximately 20 nm-large pixel.

NOTE: Avoid scanning near the edges of the grid.

Representative Results

The above protocol describes how to prepare the experimental setup to quantify protrusion forces applied by macrophage podosomes on a Formvar substrate. This is achieved using AFM and is illustrated in **Figure 1**.

When analyzing a topographical image of bulges beneath podosomes using the JPK data processing software, a third-degree polynomial fit should be subtracted from each scan line independently. The maximum height of podosome-induced bumps can be assessed by adding a z color scale on the side of the image. After being exported in TIFF format, the topographical image is further analyzed using a dedicated home-made ImageJ macro available online⁸. This macro locates bulges on the corrected height image and yields a force map (**Figure 2**) according to given parameters: Formvar film thickness and podosome ring radius. In addition, the macro also yields a text file with the coordinates, height and computed force value for each detected bulge on the Formvar surface.

This process also applies in the case of time-lapse acquisitions. The macro then tracks each bulge from the middle time point onwards and backwards, requesting user validation if any doubt arises.

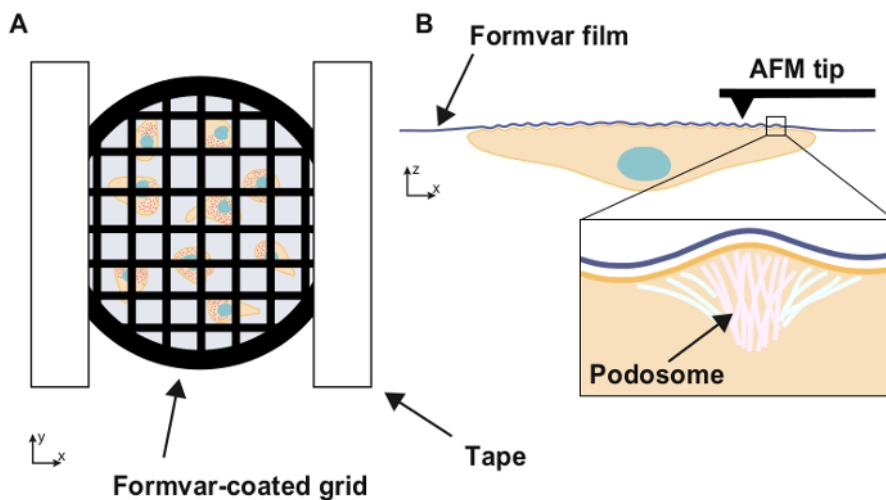


Figure 1: Experimental setup

Schematic illustration of the experimental setup. Cells are seeded on an electron microscopy grid coated with a thin, compliant Formvar film and the grid is placed, cells facing down, inside a Petri dish. When adhering to a substrate, macrophages form submicron highly dynamic adhesion structures called podosomes. The topography of the Formvar film beneath the cells is then imaged using AFM. Podosomes apply forces orthogonal to the substrate, which result in bulges on its surface.

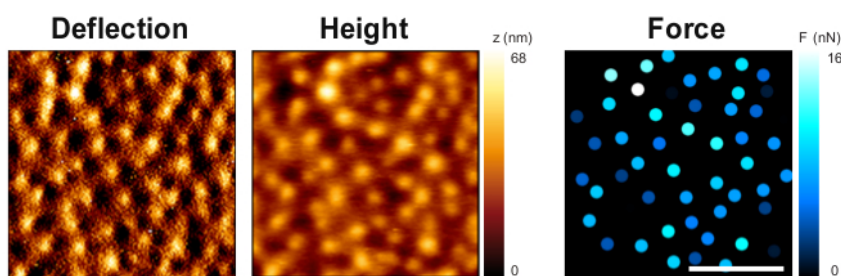


Figure 2: Substrate deformation and forces exerted by podosomes

Topography of the Formvar film on the reverse side of the cells showing deflection (left panel) and height (middle panel, color codes for height). The bulges observed on the film correspond to the deformation by individual podosomes. The force applied by each podosome is evaluated by the model (right panel, each spot corresponds to one podosome and force values are color-coded). Scale bar: 5 μm .

Discussion

Material properties

The choice of the material for the deformable membrane, in our case Formvar, needs to fulfill a few requirements. The material must be transparent to visible light and exhibit limited auto fluorescence to allow observations in bright field and fluorescence microscopy. The roughness of the thin film must be well below 10 nm to avoid any topographical effect on cell adhesion and to allow clear observation of the cell-induced protrusions by AFM imaging. Finally, the stiffness of the membrane, which depends on the Young's modulus and thickness of the material, needs to be high enough to induce the formation of podosomes while keeping some observable deformability for the typical stresses generated at podosome sites which are around 10-100 kPa. Formvar material, prepared in thin films of 30-80 nm is a good compromise between all these

constraints. It is worth noticing that by tuning the thickness of the Formvar membrane, its stiffness can be adjusted to study the mechanosensing properties of podosomes⁷.

Reproducibility and quality of Formvar preparation

Some batches of Formvar present folds on the grid and are therefore unusable: this may be seen beforehand on bright field images. In our experience, we need multiple grids for one condition because sometimes the mounting of the grid is not perfect and the grid moves or gets twisted. The thickness of the Formvar film needs to be adapted to the expected force. The thicker the film, the stiffer it is, but the lower the deformations will be, making observation more difficult. Conversely, the thinner the film, the more fragile it is and the more difficult to manipulate without tearing it.

Influence of the force applied by the cantilever on topography measurements

To obtain a measurement of the film deformation without either affecting the nanomechanical activity of the podosome or deforming the film with the AFM probe, it is crucial to control forces applied during AFM imaging. Indeed, applying excessive force during imaging may lead to an overestimation of the protrusion height and thus of the protrusion force. In other words, there is a need to limit this force far below the stall force of the protruding site. We recommend limiting the applied forces during imaging around to a few hundreds of pico-newtons.

Model for protrusion force evaluation

To convert AFM topographical measurements into force values, it is necessary to define the boundary conditions and to know the spatial configuration of force application. In the case of podosomes, we proposed a model based on the current knowledge of its molecular organisation and verified that this model provided deformation profiles consistent with topographical observations⁸. More precisely, we modeled the dense core of polymerizing vertical actin filaments surrounded by a ring of adhesion proteins as a central module pushing the substrate and a peripheral module pulling on it. Substrate deformation by these two modules acting was determined using finite element simulations, leading to a force-deformation relationship. Thanks to this numerical approach, we characterized the influence of each geometrical parameter on the force-deformation relationship, showing that ring diameter and substrate thickness needed to be measured precisely. The relationship between the height h of a bulge in the substrate and the force F applied by one podosome may be expressed as $F = C_0 E / (1 - \nu^2) e^3 / r^2 h$, where $E = 2.1$ GPa is the Young's modulus of Formvar and $\nu = 0.3$ its Poisson ratio⁷, C_0 is a constant equal to 2.7 and e and r respectively denote film thickness and podosome radius⁸. For each condition, the average value of r was obtained from fluorescence images of podosomes.

Applications of Protrusion Force Microscopy

Protrusion force microscopy was profitably used in macrophages to test the importance of specific proteins on podosome force generation, demonstrate the mechanical role of the podosome ring¹⁸ and reveal spatio-temporal correlations of force generation between close neighbours within the network of podosomes⁹.

Cells have been found to protrude into their environment in several biological processes. Invasive tumor cells use protrusive structures called invadopodia, which are essential to extracellular matrix degradation¹⁹. Lymphocytes have been shown to protrude into endothelial cells during their transcellular diapedesis through the endothelium²⁰. Some instances of cell-cell interaction also rely on cellular protruding structures: this is the case for antigen recognition of T cells on endothelial cells²¹, and for the initiation of cell fusion that leads to multinucleated osteoclasts or to myotubes^{22,23,24}. Finally, internalization processes such as phagocytosis use cellular actin-based structures that project around the target body²⁵. Studying the forces generated by protruding structures will certainly help shed light on the mechanisms at play in these processes.

Disclosures

No conflicts of interest declared.

Acknowledgements

The authors are grateful to Anna Labernadie, Guillaume Charrière and Patrick Delobelle for their initial contribution to this work and to Matthieu Sanchez and Françoise Viala for their help with video filming and editing. This work has been supported by l'Agence Nationale de la Recherche (ANR14-CE11-0020-02), la Fondation pour la Recherche Médicale (FRM DEQ2016 0334894), INSERM Plan Cancer, Fondation Toulouse Cancer and Human Frontier Science Program (RGP0035/2016).

References

1. Discher, D. E., Janmey, P., Wang, Y. L. Tissue Cells Feel and Respond to the Stiffness of Their Substrate. *Science*. **310**, 1139-1143 (2005).
2. Paszek, M. J., *et al.* Tensional Homeostasis and the Malignant Phenotype. *Cancer Cell*. **8**, 241-254 (2005).
3. Engler, A. J., Sen, S., Sweeney, H. L., Discher, D. E. Matrix Elasticity Directs Stem Cell Lineage Specification. *Cell*. **126**, 677-689 (2006).
4. Gilbert, P. M., Weaver, V. M. Cellular Adaptation to Biomechanical Stress across Length Scales in Tissue Homeostasis and Disease. *Seminars in Cell & Developmental Biology*. **67**, 141-152 (2017).
5. Vining, K. H., Mooney, D. J. Mechanical Forces Direct Stem Cell Behaviour in Development and Regeneration. *Nature Reviews Molecular Cell Biology*. (2017).
6. Roca-Cusachs, P., Conte, V., Trepats, X. Quantifying Forces in Cell Biology. *Nature Cell Biology*. **19**, 742-751 (2017).
7. Labernadie, A., *et al.* Protrusion Force Microscopy Reveals Oscillatory Force Generation and Mechanosensing Activity of Human Macrophage Podosomes. *Nature Communications*. **5**, 5343 (2014).

8. Proag, A., *et al.* Working Together: Spatial Synchrony in the Force and Actin Dynamics of Podosome First Neighbors. *ACS Nano*. **9**, 3800-3813 (2015).
9. Proag, A., Bouissou, A., Vieu, C., Maridonneau-Parini, I., Poincloux, R. Evaluation of the Force and Spatial Dynamics of Macrophage Podosomes by Multi-Particle Tracking. *Methods*. **94**, 75-84 (2016).
10. Cougoule, C., *et al.* Three-Dimensional Migration of Macrophages Requires Hck for Podosome Organization and Extracellular Matrix Proteolysis. *Blood*. **115**, 1444-1452 (2010).
11. Cougoule, C., *et al.* Blood Leukocytes and Macrophages of Various Phenotypes Have Distinct Abilities to Form Podosomes and to Migrate in 3d Environments. *European Journal of Cell Biology*. **91**, 938-949 (2012).
12. Guiet, R., *et al.* Macrophage Mesenchymal Migration Requires Podosome Stabilization by Filamin A. *Journal of Biological Chemistry*. **287**, 13051-13062 (2012).
13. Maridonneau-Parini, I. Control of Macrophage 3d Migration: A Therapeutic Challenge to Limit Tissue Infiltration. *Immunology Review*. **262**, 216-231 (2014).
14. Park, H., *et al.* Tyrosine Phosphorylation of Wiskott-Aldrich Syndrome Protein (Wasp) by Hck Regulates Macrophage Function. *Journal of Biological Chemistry*. **289**, 7897-7906 (2014).
15. Van Goethem, E., *et al.* Macrophage Podosomes Go 3d. *European Journal of Cell Biology*. **90**, 224-236 (2011).
16. Van Goethem, E., Poincloux, R., Gauffre, F., Maridonneau-Parini, I., Le Cabec, V. Matrix Architecture Dictates Three-Dimensional Migration Modes of Human Macrophages: Differential Involvement of Proteases and Podosome-Like Structures. *Journal of Immunology*. **184**, 1049-1061 (2010).
17. Verollet, C., *et al.* Hiv-1 Reprograms the Migration of Macrophages. *Blood*. **125**, 1611-1622 (2015).
18. Bouissou, A., *et al.* Podosome Force Generation Machinery: A Local Balance between Protrusion at the Core and Traction at the Ring. *ACS Nano*. **11**, 4028-4040 (2017).
19. Lizarraga, F., *et al.* Diaphanous-Related Formins Are Required for Invadopodia Formation and Invasion of Breast Tumor Cells. *Cancer Research*. **69**, 2792-2800 (2009).
20. Carman, C. V., *et al.* Transcellular Diapedesis Is Initiated by Invasive Podosomes. *Immunity*. **26**, 784-797 (2007).
21. Sage, P. T., *et al.* Antigen Recognition Is Facilitated by Invadosome-Like Protrusions Formed by Memory/Effector T Cells. *Journal of Immunology*. **188**, 3686-3699 (2012).
22. Sens, K. L., *et al.* An Invasive Podosome-Like Structure Promotes Fusion Pore Formation During Myoblast Fusion. *Journal of Cell Biology*. **191**, 1013-1027 (2010).
23. Takito, J., *et al.* The Transient Appearance of Zipper-Like Actin Superstructures During the Fusion of Osteoclasts. *Journal of Cell Science*. **125**, 662-672 (2012).
24. Shilagardi, K., *et al.* Actin-Propelled Invasive Membrane Protrusions Promote Fusogenic Protein Engagement During Cell-Cell Fusion. *Science*. **340**, 359-363 (2013).
25. Freeman, S. A., *et al.* Integrins Form an Expanding Diffusional Barrier That Coordinates Phagocytosis. *Cell*. **164**, 128-140 (2016).

Bibliography

- Abidine, Y., V. M. Laurent, R. Michel, A. Duperray, L. I. Palade, and C. Verdier (2015). “Physical properties of polyacrylamide gels probed by AFM and rheology”. In: *EPL (Europhysics Letters)* 109.3, p. 38003 (cit. on p. 109).
- Accardo, A., M.-C. Blatché, R. Courson, I. Loubinoux, C. Thibault, L. Malaquin, and C. Vieu (2017). “Multiphoton direct laser writing and 3D imaging of polymeric freestanding architectures for cell colonization”. In: *Small* 13.27, p. 1700621 (cit. on p. 150).
- Ahern, A. M. and R. L. Garrell (1988). “Characterization of polyacrylamide gel formation and structure by surface-enhanced Raman spectroscopy”. In: *Langmuir* 4.5, pp. 1162–1168 (cit. on p. 144).
- Akisaka, T. and A. Yoshida (2016). “Ultrastructural analysis of apatite-degrading capability of extended invasive podosomes in resorbing osteoclasts”. In: *Micron* 88, pp. 37–47 (cit. on pp. 41, 69, 81).
- (2019). “Scattered podosomes and podosomes associated with the sealing zone architecture in cultured osteoclasts revealed by cell shearing, quick freezing, and platinum-replica electron microscopy”. In: *Cytoskeleton* (cit. on pp. 41, 51, 62, 66, 69, 70, 81, 82).
- Akisaka, T. and A. Yoshida (2015). “Visualization of structural organization of ventral membranes of sheared-open resorbing osteoclasts attached to apatite pellets”. In: *Cell and tissue research* 360.2, pp. 347–362 (cit. on pp. 41, 42, 58, 62, 69).
- Akisaka, T., H. Yoshida, S. Inoue, and K. Shimizu (2001). “Organization of cytoskeletal F-actin, G-actin, and gelsolin in the adhesion structures in cultured osteoclast”. In: *Journal of Bone and Mineral Research* 16.7, pp. 1248–1255 (cit. on pp. 40, 49).
- Akisaka, T., H. Yoshida, R. Suzuki, and K. Takama (2008). “Adhesion structures and their cytoskeleton-membrane interactions at podosomes of osteoclasts in culture”. In: *Cell and tissue research* 331.3, pp. 625–641 (cit. on pp. 41, 56, 58, 62).
- Alberts, B., A. Johnson, J. Lewis, M. Raff, K. Roberts, and P. Walter (2002). “Integrins”. In: *Molecular Biology of the Cell. 4th edition*. Garland Science (cit. on p. 166).
- (2007). *Molecular biology of the cell: Reference edition*. Garland Science (cit. on pp. 94, 116).
- Albiges-Rizo, C., O. Destaing, B. Fourcade, E. Planus, and M. R. Block (2009). “Actin machinery and mechanosensitivity in invadopodia, podosomes and focal adhesions”. In: *J Cell Sci* 122.17, pp. 3037–3049 (cit. on pp. 29, 30).
- Alvarez-Gonzalez, B., R. Meili, E. Bastounis, R. A. Firtel, J. C. Lasheras, and J. C. del Alamo (2015). “Three-dimensional balance of cortical tension and axial contractility enables fast amoeboid migration”. In: *Biophysical journal* 108.4, pp. 821–832 (cit. on p. 107).
- Ambrose, E. (1956). “A surface contact microscope for the study of cell movements”. In: *Nature* 178.4543, p. 1194 (cit. on p. 113).

- Ambrosi, D. (2006). “Cellular traction as an inverse problem”. In: *SIAM Journal on Applied Mathematics* 66.6, pp. 2049–2060 (cit. on p. 108).
- Ambrosi, D., A. Duperray, V. Peschetola, and C. Verdier (2009). “Traction patterns of tumor cells”. In: *Journal of mathematical biology* 58.1-2, p. 163 (cit. on p. 108).
- Anderegg, F., D. Geblinger, P. Horvath, M. Charnley, M. Textor, L. Addadi, and B. Geiger (2011). “Substrate adhesion regulates sealing zone architecture and dynamics in cultured osteoclasts”. In: *PLoS One* 6.12, e28583 (cit. on pp. 41, 64, 81, 173).
- Aoun, L., P. Weiss, A. Laborde, B. Ducommun, V. Lobjois, and C. Vieu (2014). “Microdevice arrays of high aspect ratio poly (dimethylsiloxane) pillars for the investigation of multicellular tumour spheroid mechanical properties”. In: *Lab on a chip* 14.13, pp. 2344–2353 (cit. on p. 98).
- Aratyn-Schaus, Y., P. W. Oakes, J. Stricker, S. P. Winter, and M. L. Gardel (2010). “Preparation of compliant matrices for quantifying cellular contraction”. In: *JoVE (Journal of Visualized Experiments)* 46, e2173 (cit. on pp. 102, 120).
- Ariganello, M. B., D. G. Bello, A. Rodriguez-Contreras, S. Sadeghi, G. Isola, F. Variola, and A. Nanci (2018). “Surface nanocavitation of titanium modulates macrophage activity”. In: *International journal of nanomedicine* 13, p. 8297 (cit. on p. 155).
- Arnold, M., E. A. Cavalcanti-Adam, R. Glass, J. Blümmel, W. Eck, M. Kantlehner, H. Kessler, and J. P. Spatz (2004). “Activation of integrin function by nanopatterned adhesive interfaces”. In: *ChemPhysChem* 5.3, pp. 383–388 (cit. on p. 155).
- Arron, J. R. and Y. Choi (2000). “Bone versus immune system”. In: *Nature* 408.6812, p. 535 (cit. on p. 17).
- Ascenzi, A., P. Baschieri, and A. Benvenuti (1994). “The torsional properties of single selected osteons”. In: *Journal of Biomechanics* 27.7, pp. 875–884 (cit. on p. 9).
- Ascenzi, A., P. Baschieri, and A. Benvenuti (1990). “The bending properties of single osteons”. In: *Journal of biomechanics* 23.8, pp. 763–771 (cit. on p. 9).
- Ascenzi, A. and E. Bonucci (1967). “The tensile properties of single osteons”. In: *The Anatomical Record* 158.4, pp. 375–386 (cit. on p. 9).
- (1968). “The compressive properties of single osteons”. In: *The Anatomical Record* 161.3, pp. 377–391 (cit. on p. 9).
- Atala, A., F. K. Kasper, and A. G. Mikos (2012). “Engineering complex tissues”. In: *Science translational medicine* 4.160, 160rv12–160rv12 (cit. on p. 147).
- Axelrod, D. (1981). “Cell-substrate contacts illuminated by total internal reflection fluorescence.” In: *The Journal of cell biology* 89.1, pp. 141–145 (cit. on p. 113).
- Azatov, M., X. Sun, A. Suberi, J. T. Fourkas, and A. Upadhyaya (2017). “Topography on a subcellular scale modulates cellular adhesions and actin stress fiber dynamics in tumor associated fibroblasts”. In: *Physical biology* 14.6, p. 065003 (cit. on p. 155).
- Babb, S. G., P. Matsudaira, M. Sato, I. Correia, and S.-S. Lim (1997). “Fimbrin in podosomes of monocyte-derived osteoclasts”. In: *Cell motility and the cytoskeleton* 37.4, pp. 308–325 (cit. on pp. 49, 51, 52, 56, 82, 173).
- Badieirostami, M., M. D. Lew, M. A. Thompson, and W. Moerner (2010). “Three-dimensional localization precision of the double-helix point spread function versus astigmatism and biplane”. In: *Applied physics letters* 97.16, p. 161103 (cit. on p. 113).

- Badowski, C., G. Pawlak, A. Grichine, A. Chabadel, C. Oddou, P. Jurdic, M. Pfaff, C. Albigès-Rizo, and M. R. Block (2008). “Paxillin phosphorylation controls invadopodia/podosomes spatiotemporal organization”. In: *Molecular biology of the cell* 19.2, pp. 633–645 (cit. on pp. 62, 65).
- Balaban, N. Q., U. S. Schwarz, D. Riveline, P. Goichberg, G. Tzur, I. Sabanay, D. Mahalu, S. Safran, A. Bershadsky, L. Addadi, et al. (2001). “Force and focal adhesion assembly: a close relationship studied using elastic micropatterned substrates”. In: *Nature cell biology* 3.5, p. 466 (cit. on p. 97).
- Baldassarre, M., I. Ayala, G. Beznoussenko, G. Giacchetti, L. M. Machesky, A. Luini, and R. Buccione (2006). “Actin dynamics at sites of extracellular matrix degradation”. In: *European journal of cell biology* 85.12, pp. 1217–1231 (cit. on p. 25).
- Balland, M., A. Richert, and F. Gallet (2005). “The dissipative contribution of myosin II in the cytoskeleton dynamics of myoblasts”. In: *European Biophysics Journal* 34.3, pp. 255–261 (cit. on p. 99).
- Bar-Kochba, E., J. Toyjanova, E. Andrews, K.-S. Kim, and C. Franck (2015). “A fast iterative digital volume correlation algorithm for large deformations”. In: *Experimental Mechanics* 55.1, pp. 261–274 (cit. on p. 108).
- Baron, R., L. Neff, D. Louvard, and P. J. Courtoy (1985). “Cell-mediated extracellular acidification and bone resorption: evidence for a low pH in resorbing lacunae and localization of a 100-kD lysosomal membrane protein at the osteoclast ruffled border.” In: *The Journal of cell biology* 101.6, pp. 2210–2222 (cit. on p. 19).
- Barthes, J., H. Ozcelik, M. Hindie, A. Ndreu-Halili, A. Hasan, and N. Vrana (2014). “Cell microenvironment engineering and monitoring for tissue engineering and regenerative medicine: the recent advances BioMed”. In: *Res. Int* 18 (cit. on p. 148).
- Bartl, R. and B. Frisch (2004). “Definition of osteoporosis”. In: *Osteoporosis*. Springer, pp. 24–32 (cit. on p. 17).
- (2009). “Biology of bone”. In: *Osteoporosis*. Springer, pp. 7–28 (cit. on p. 13).
- Basoli, F., S. M. Giannitelli, M. Gori, P. Mozetic, A. Bonfanti, M. Trombetta, and A. Rainer (2018). “Biomechanical characterization at the cell scale: present and prospects”. In: *Frontiers in physiology* 9 (cit. on p. 97).
- Bates, M., B. Huang, G. T. Dempsey, and X. Zhuang (2007). “Multicolor super-resolution imaging with photo-switchable fluorescent probes”. In: *Science* 317.5845, pp. 1749–1753 (cit. on p. 112).
- Batsir, S., B. Geiger, and Z. Kam (2017). “Dynamics of the sealing zone in cultured osteoclasts”. In: *Cytoskeleton* 74.2, pp. 72–81 (cit. on p. 64).
- Bauer, A. L., T. L. Jackson, and Y. Jiang (2009). “Topography of extracellular matrix mediates vascular morphogenesis and migration speeds in angiogenesis”. In: *PLoS computational biology* 5.7, e1000445 (cit. on p. 94).
- Bausch, A. R., U. Hellerer, M. Essler, M. Aepfelbacher, and E. Sackmann (2001). “Rapid stiffening of integrin receptor-actin linkages in endothelial cells stimulated with thrombin: a magnetic bead microrheology study”. In: *Biophysical Journal* 80.6, pp. 2649–2657 (cit. on p. 99).
- Bergeron, S. E., M. Zhu, S. M. Thiem, K. H. Friderici, and P. A. Rubenstein (2010). “Ion-dependent polymerization differences between mammalian β - and γ -nonmuscle actin isoforms”. In: *Journal of Biological Chemistry* 285.21, pp. 16087–16095 (cit. on p. 51).
- Bergert, M., T. Lendenmann, M. Zündel, A. E. Ehret, D. Panozzo, P. Richner, D. K. Kim, S. J. Kress, D. J. Norris, O. Sorkine-Hornung, et al. (2016). “Confocal reference free traction force microscopy”. In: *Nature communications* 7, p. 12814 (cit. on pp. 102, 105, 106, 175).

- Berry, C. C., G. Campbell, A. Spadicino, M. Robertson, and A. S. Curtis (2004). “The influence of microscale topography on fibroblast attachment and motility”. In: *Biomaterials* 25.26, pp. 5781–5788 (cit. on p. 156).
- Betancourt, T. and L. Brannon-Peppas (2006). “Micro-and nanofabrication methods in nanotechnological medical and pharmaceutical devices”. In: *International journal of nanomedicine* 1.4, p. 483 (cit. on p. 148).
- Bettinger, C. J., R. Langer, and J. T. Borenstein (2009). “Engineering substrate topography at the micro-and nanoscale to control cell function”. In: *Angewandte Chemie International Edition* 48.30, pp. 5406–5415 (cit. on pp. 147, 148, 152, 176).
- Betzig, E., G. H. Patterson, R. Sougrat, O. W. Lindwasser, S. Olenych, J. S. Bonifacino, M. W. Davidson, J. Lippincott-Schwartz, and H. F. Hess (2006). “Imaging intracellular fluorescent proteins at nanometer resolution”. In: *Science* 313.5793, pp. 1642–1645 (cit. on p. 111).
- Bhardwaj, N. and S. C. Kundu (2010). “Electrospinning: a fascinating fiber fabrication technique”. In: *Biotechnology advances* 28.3, pp. 325–347 (cit. on p. 150).
- Bhushan, B., J. C. Wyant, and C. L. Koliopoulos (1985). “Measurement of surface topography of magnetic tapes by Mirau interferometry”. In: *Applied Optics* 24.10, pp. 1489–1497 (cit. on p. 114).
- Bhuwania, R., A. Castro-Castro, and S. Linder (2014). “Microtubule acetylation regulates dynamics of KIF1C-powered vesicles and contact of microtubule plus ends with podosomes”. In: *European journal of cell biology* 93.10-12, pp. 424–437 (cit. on pp. 32, 33).
- Bhuwania, R., S. Cornfine, Z. Fang, M. Krüger, E. J. Luna, and S. Linder (2012). “Supervillin couples myosin-dependent contractility to podosomes and enables their turnover”. In: *J Cell Sci* 125.9, pp. 2300–2314 (cit. on pp. 26, 27, 32).
- Binnig, G., C. F. Quate, and C. Gerber (1986). “Atomic force microscope”. In: *Physical review letters* 56.9, p. 930 (cit. on p. 100).
- Binnig, G., H. Rohrer, C. Gerber, and E. Weibel (1982). “Surface studies by scanning tunneling microscopy”. In: *Physical review letters* 49.1, p. 57 (cit. on p. 100).
- Biswas, R. S., D. A. Baker, K. A. Hruska, and M. A. Chellaiiah (2004). “Polyphosphoinositides-dependent regulation of the osteoclast actin cytoskeleton and bone resorption”. In: *BMC cell biology* 5.1, p. 19 (cit. on pp. 49, 51).
- Blair, H. C., S. L. Teitelbaum, R. Ghiselli, and S. Gluck (1989). “Osteoclastic bone resorption by a polarized vacuolar proton pump”. In: *Science* 245.4920, pp. 855–857 (cit. on p. 19).
- Blangy, A. (2017). “Tensins are versatile regulators of Rho GTPase signalling and cell adhesion”. In: *Biology of the Cell* 109.3, pp. 115–126 (cit. on p. 55).
- Blangy, A., H. Touaitahuata, G. Cres, and G. Pawlak (2012). “Cofilin activation during podosome belt formation in osteoclasts”. In: *PLoS One* 7.9, e45909 (cit. on pp. 50, 58, 173).
- Blass, J., O. Köhler, M. Fingerle, C. Müller, and C. Ziegler (2013). “Properties and characteristics of wet (HF) and dry (RIE) etched borosilicate glass”. In: *physica status solidi (a)* 210.5, pp. 988–993 (cit. on p. 165).
- Bloom, R. J., J. P. George, A. Celedon, S. X. Sun, and D. Wirtz (2008). “Mapping local matrix remodeling induced by a migrating tumor cell using three-dimensional multiple-particle tracking”. In: *Biophysical journal* 95.8, pp. 4077–4088 (cit. on p. 108).
- Bo, L. and R. E. Waugh (1989). “Determination of bilayer membrane bending stiffness by tether formation from giant, thin-walled vesicles”. In: *Biophysical Journal* 55.3, pp. 509–517 (cit. on p. 99).

- Bonnelye, E., F. Saltel, A. Chabadel, R. A. Zirngibl, J. E. Aubin, and P. Jurdic (2010). “Involvement of the orphan nuclear estrogen receptor-related receptor α in osteoclast adhesion and transmigration”. In: *Journal of molecular endocrinology* 45.6, pp. 365–377 (cit. on p. 62).
- Borba, V. Z. C. and N. C. P. Mañas (2010). “The use of PTH in the treatment of osteoporosis”. In: *Arquivos Brasileiros de Endocrinologia & Metabologia* 54.2, pp. 213–219 (cit. on p. 16).
- Borges, J. and J. F. Mano (2014). “Molecular interactions driving the layer-by-layer assembly of multilayers”. In: *Chemical reviews* 114.18, pp. 8883–8942 (cit. on p. 149).
- Botvinick, E., V. Venugopalan, J. Shah, L. Liaw, and M. Berns (2004). “Controlled ablation of microtubules using a picosecond laser”. In: *Biophysical journal* 87.6, pp. 4203–4212 (cit. on p. 100).
- Boudou, T., J. Ohayon, Y. Arntz, G. Finet, C. Picart, and P. Tracqui (2006a). “An extended modeling of the micropipette aspiration experiment for the characterization of the Young’s modulus and Poisson’s ratio of adherent thin biological samples: numerical and experimental studies”. In: *Journal of biomechanics* 39.9, pp. 1677–1685 (cit. on p. 109).
- Boudou, T., J. Ohayon, C. Picart, R. I. Pettigrew, and P. Tracqui (2009). “Nonlinear elastic properties of polyacrylamide gels: implications for quantification of cellular forces”. In: *Biorheology* 46.3, pp. 191–205 (cit. on p. 109).
- Boudou, T., J. Ohayon, C. Picart, and P. Tracqui (2006b). “An extended relationship for the characterization of Young’s modulus and Poisson’s ratio of tunable polyacrylamide gels”. In: *Biorheology* 43.6, pp. 721–728 (cit. on p. 109).
- Bouissou, A., A. Proag, N. Bourg, K. Pingris, C. Cabriel, S. Balor, T. Mangeat, C. Thibault, C. Vieu, G. Dupuis, et al. (2017). “Podosome force generation machinery: a local balance between protrusion at the core and traction at the ring”. In: *ACS nano* 11.4, pp. 4028–4040 (cit. on pp. 36, 49, 77, 83, 89, 117, 174, 177).
- Bouissou, A., A. Proag, M. Portes, V. Soldan, S. Balor, C. Thibault, C. Vieu, I. Maridonneau-Parini, and R. Poincloux (2018). “Protrusion Force Microscopy: A Method to Quantify Forces Developed by Cell Protrusions”. In: *JoVE (Journal of Visualized Experiments)* 136, e57636 (cit. on pp. 4, 6, 109, 174, 175).
- Bouma, G., S. O. Burns, and A. J. Thrasher (2009). “Wiskott–Aldrich syndrome: immunodeficiency resulting from defective cell migration and impaired immunostimulatory activation”. In: *Immunobiology* 214.9-10, pp. 778–790 (cit. on p. 28).
- Bourg, N. (May 2016). “Nanoscopie de fluorescence tri-dimensionnelle pour la biologie”. PhD thesis. Université Paris Saclay (cit. on pp. 142, 143).
- Bourg, N., C. Mayet, G. Dupuis, T. Barroca, P. Bon, S. Lécart, E. Fort, and S. Lévêque-Fort (2015). “Direct optical nanoscopy with axially localized detection”. In: *Nature Photonics* 9.9, p. 587 (cit. on pp. 77, 82, 114, 118–120, 123, 142, 143, 145, 171, 172).
- Bowden, E. T., M. Barth, D. Thomas, R. I. Glazer, and S. C. Mueller (1999). “An invasion-related complex of cortactin, paxillin and PKC μ associates with invadopodia at sites of extracellular matrix degradation”. In: *Oncogene* 18.31, p. 4440 (cit. on p. 36).
- Boyce, B. F. and L. Xing (2007). “Biology of RANK, RANKL, and osteoprotegerin”. In: *Arthritis research & therapy* 9.1, S1 (cit. on p. 15).
- Braet, F., C. Rotsch, E. Wisse, and M. Radmacher (1998). “Comparison of fixed and living liver endothelial cells by atomic force microscopy”. In: *Applied Physics A: Materials Science & Processing* 66, S575–S578 (cit. on p. 101).

Bibliography

- Brazier, H., S. Stephens, S. Ory, P. Fort, N. Morrison, and A. Blangy (2006). “Expression profile of RhoGTPases and RhoGEFs during RANKL-stimulated osteoclastogenesis: identification of essential genes in osteoclasts”. In: *Journal of Bone and Mineral Research* 21.9, pp. 1387–1398 (cit. on pp. 53, 54).
- Brugués, J., B. Maugis, J. Casademunt, P. Nassoy, F. Amblard, and P. Sens (2010). “Dynamical organization of the cytoskeletal cortex probed by micropipette aspiration”. In: *Proceedings of the National Academy of Sciences* 107.35, pp. 15415–15420 (cit. on p. 100).
- Bruzzaniti, A. and R. Baron (2006). “Molecular regulation of osteoclast activity”. In: *Reviews in Endocrine and Metabolic Disorders* 7.1-2, pp. 123–139 (cit. on p. 20).
- Bruzzaniti, A., L. Neff, A. Sandoval, L. Du, W. C. Horne, and R. Baron (2009). “Dynamin reduces Pyk2 Y402 phosphorylation and SRC binding in osteoclasts”. In: *Molecular and cellular biology* 29.13, pp. 3644–3656 (cit. on p. 56).
- Bruzzaniti, A., L. Neff, A. Sanjay, W. C. Horne, P. De Camilli, and R. Baron (2005). “Dynamin forms a Src kinase-sensitive complex with Cbl and regulates podosomes and osteoclast activity”. In: *Molecular biology of the cell* 16.7, pp. 3301–3313 (cit. on pp. 56, 60).
- Buckwalter, J., M. Glimcher, R. Cooper, R. Recker, et al. (1995). “Bone biology”. In: *J Bone Joint Surg Am* 77.8, pp. 1256–1275 (cit. on p. 12).
- Bullough, P. G., V. J. Vigorita, and W. F. Enneking (1984). *Atlas of orthopaedic pathology with clinical and radiologic correlations*. Butterworths (cit. on p. 9).
- Burgstaller, G. and M. Gimona (2004). “Actin cytoskeleton remodelling via local inhibition of contractility at discrete microdomains”. In: *Journal of cell science* 117.2, pp. 223–231 (cit. on pp. 23, 32).
- (2005). “Podosome-mediated matrix resorption and cell motility in vascular smooth muscle cells”. In: *American Journal of Physiology-Heart and Circulatory Physiology* 288.6, H3001–H3005 (cit. on p. 23).
- Burns, S., S. J. Hardy, J. Buddle, K. L. Yong, G. E. Jones, and A. J. Thrasher (2004). “Maturation of DC is associated with changes in motile characteristics and adherence”. In: *Cell motility and the cytoskeleton* 57.2, pp. 118–132 (cit. on pp. 23, 25).
- Burridge, K. and K. Wennerberg (2004). “Rho and Rac take center stage”. In: *Cell* 116.2, pp. 167–179 (cit. on p. 53).
- Butler, J. P., I. M. Tolic-Nørrelykke, B. Fabry, and J. J. Fredberg (2002). “Traction fields, moments, and strain energy that cells exert on their surroundings”. In: *American Journal of Physiology-Cell Physiology* 282.3, pp. C595–C605 (cit. on pp. 102, 108).
- Buxboim, A., K. Rajagopal, B. Andre’EX, and D. E. Discher (2010). “How deeply cells feel: methods for thin gels”. In: *Journal of Physics: Condensed Matter* 22.19, p. 194116 (cit. on p. 115).
- Cabriel, C., N. Bourg, P. Jouchet, G. Dupuis, C. Leterrier, A. Baron, M.-A. Badet-Denisot, B. Vauzeilles, E. Fort, and S. Leveque-Fort (2019). “Combining 3D single molecule localization strategies for reproducible bioimaging”. In: *Nature communications* 10.1, p. 1980 (cit. on pp. 83, 144, 172).
- Cai, Y. and M. P. Sheetz (2009). “Force propagation across cells: mechanical coherence of dynamic cytoskeletons”. In: *Current opinion in cell biology* 21.1, pp. 47–50 (cit. on p. 34).
- Calderwood, D. A., I. D. Campbell, and D. R. Critchley (2013). “Talins and kindlins: partners in integrin-mediated adhesion”. In: *Nature reviews Molecular cell biology* 14.8, pp. 503–517 (cit. on p. 43).
- Calle, Y., H.-c. Chou, A. J. Thrasher, and G. E. Jones (2004a). “Wiskott–Aldrich syndrome protein and the cytoskeletal dynamics of dendritic cells”. In: *The Journal of Pathology: A Journal of the Pathological Society of Great Britain and Ireland* 204.4, pp. 460–469 (cit. on pp. 25, 28).

- Calle, Y., G. E. Jones, C. Jagger, K. Fuller, M. P. Blundell, J. Chow, T. Chambers, and A. J. Thrasher (2004b). "WASp deficiency in mice results in failure to form osteoclast sealing zones and defects in bone resorption". In: *Blood* 103.9, pp. 3552–3561 (cit. on pp. 51, 58, 62).
- Campbell, I. D. and M. J. Humphries (2011). "Integrin structure, activation, and interactions". In: *Cold Spring Harbor perspectives in biology* 3.3, a004994 (cit. on p. 145).
- Cao, Y., Y. Wang, S. Sprangers, D. I. Picavet, M. Glogauer, C. A. McCulloch, and V. Everts (2017). "Deletion of adseverin in osteoclasts affects cell structure but not bone metabolism". In: *Calcified tissue international* 101.2, pp. 207–216 (cit. on p. 49).
- Carter, D. R. and W. C. Hayes (1977). "The compressive behavior of bone as a two-phase porous structure." In: *The Journal of bone and joint surgery. American volume* 59.7, pp. 954–962 (cit. on p. 8).
- Cervero, P., M. Himmel, M. Krüger, and S. Linder (2012). "Proteomic analysis of podosome fractions from macrophages reveals similarities to spreading initiation centres". In: *European journal of cell biology* 91.11–12, pp. 908–922 (cit. on p. 23).
- Cervero, P., C. Wiesner, A. Bouissou, R. Poincloux, and S. Linder (2018). "Lymphocyte-specific protein 1 regulates mechanosensory oscillation of podosomes and actin isoform-based actomyosin symmetry breaking". In: *Nature communications* 9.1, p. 515 (cit. on p. 27).
- Chabadel, A., I. Bañon-Rodríguez, D. Cluet, B. B. Rudkin, B. Wehrle-Haller, E. Genot, P. Jurdic, I. M. Anton, and F. Saltel (2007). "CD44 and $\beta 3$ integrin organize two functionally distinct actin-based domains in osteoclasts". In: *Molecular biology of the cell* 18.12, pp. 4899–4910 (cit. on pp. 25, 45–48, 50–52, 58, 69, 82).
- Chambers, T., K. Fuller, J. Darby, J. Pringle, and M. Horton (1986). "Monoclonal antibodies against osteoclasts inhibit bone resorption in vitro." In: *Bone and mineral* 1.2, pp. 127–135 (cit. on p. 43).
- Chellaiah, M., C. Fitzgerald, E. Filardo, D. Cheresch, and K. Hruska (1996a). "Osteopontin activation of c-src in human melanoma cells requires the cytoplasmic domain of the integrin alpha v-subunit". In: *Endocrinology* 137.6, pp. 2432–2440 (cit. on p. 55).
- Chellaiah, M. and K. Hruska (2003a). "The Integrin $\alpha v\beta 3$ and CD44 Regulate the Actions of Osteopontin on Osteoclast Motility". In: *Calcified Tissue International* 72.3, pp. 197–205 (cit. on p. 46).
- Chellaiah, M. A. (2005). "Regulation of actin ring formation by rho GTPases in osteoclasts". In: *Journal of Biological Chemistry* 280.38, pp. 32930–32943 (cit. on pp. 51, 54).
- (2006). "Regulation of podosomes by integrin $\alpha v\beta 3$ and Rho GTPase-facilitated phosphoinositide signaling". In: *European journal of cell biology* 85.3–4, pp. 311–317 (cit. on pp. 48, 49, 53).
- Chellaiah, M. A., R. S. Biswas, S. R. Rittling, D. T. Denhardt, and K. A. Hruska (2003b). "Rho-dependent Rho kinase activation increases CD44 surface expression and bone resorption in osteoclasts". In: *Journal of Biological Chemistry* 278.31, pp. 29086–29097 (cit. on p. 46).
- Chellaiah, M. A., N. Kizer, R. Biswas, U. Alvarez, J. Strauss-Schoenberger, L. Rifas, S. R. Rittling, D. T. Denhardt, and K. A. Hruska (2003c). "Osteopontin deficiency produces osteoclast dysfunction due to reduced CD44 surface expression". In: *Molecular biology of the cell* 14.1, pp. 173–189 (cit. on pp. 46, 60).
- Chellaiah, M. A., T. Ma, and S. Majumdar (2018). "L-plastin phosphorylation regulates the early phase of sealing ring formation by actin bundling process in mouse osteoclasts". In: *Experimental cell research* 372.1, pp. 73–82 (cit. on p. 51).
- Chellaiah, M. A., N. Soga, S. Swanson, S. McAllister, U. Alvarez, D. Wang, S. F. Dowdy, and K. A. Hruska (2000a). "Rho-A is critical for osteoclast podosome organization, motility, and bone resorption". In: *Journal of Biological Chemistry* 275.16, pp. 11993–12002 (cit. on pp. 40, 49, 54, 60).

- Chellaiah, M., C. Fitzgerald, U. Alvarez, and K. Hruska (1998). “c-Src is required for stimulation of gelsolin-associated phosphatidylinositol 3-kinase”. In: *Journal of Biological Chemistry* 273.19, pp. 11908–11916 (cit. on p. 55).
- Chellaiah, M. and K. Hruska (1996b). “Osteopontin stimulates gelsolin-associated phosphoinositide levels and phosphatidylinositol triphosphate-hydroxyl kinase.” In: *Molecular biology of the cell* 7.5, pp. 743–753 (cit. on pp. 50, 52).
- Chellaiah, M., N. Kizer, M. Silva, U. Alvarez, D. Kwiatkowski, and K. A. Hruska (2000b). “Gelsolin deficiency blocks podosome assembly and produces increased bone mass and strength”. In: *The Journal of cell biology* 148.4, pp. 665–678 (cit. on pp. 49, 55, 60).
- Chen, Z., Y. Zhao, W. Wang, and Z. Li (2009). “Microfluidic patterning of nanoparticle monolayer: Mechanism analysis and noncontinuously patterning approach”. In: *2009 4th IEEE International Conference on Nano/Micro Engineered and Molecular Systems*. IEEE, pp. 818–821 (cit. on p. 151).
- Cheung, Y. K., B. M. Gillette, M. Zhong, S. Ramcharan, and S. K. Sia (2007). “Direct patterning of composite biocompatible microstructures using microfluidics”. In: *Lab on a Chip* 7.5, pp. 574–579 (cit. on p. 151).
- Choi, Y.-K., J. Zhu, J. Grunes, J. Bokor, and G. A. Somorjai (2003). “Fabrication of sub-10-nm silicon nanowire arrays by size reduction lithography”. In: *The Journal of Physical Chemistry B* 107.15, pp. 3340–3343 (cit. on p. 151).
- Clark, K., M. Langeslag, B. van Leeuwen, L. Ran, A. G. Ryazanov, C. G. Figdor, W. H. Moolenaar, K. Jalink, and F. N. van Leeuwen (2006). “TRPM7, a novel regulator of actomyosin contractility and cell adhesion”. In: *The EMBO journal* 25.2, pp. 290–301 (cit. on p. 32).
- Clarke, B. (2008). “Normal bone anatomy and physiology”. In: *Clinical journal of the American Society of Nephrology* 3.Supplement 3, S131–S139 (cit. on p. 21).
- Clover, J., R. Dodds, and M. Gowen (1992). “Integrin subunit expression by human osteoblasts and osteoclasts in situ and in culture”. In: *Journal of cell science* 103.1, pp. 267–271 (cit. on pp. 43, 45).
- Cluzel, C., F. Saltel, J. Lussi, F. Paulhe, B. A. Imhof, and B. Wehrle-Haller (2005). “The mechanisms and dynamics of $\alpha\beta3$ integrin clustering in living cells”. In: *J Cell Biol* 171.2, pp. 383–392 (cit. on p. 29).
- Colbert, M.-J., F. Brochard-Wyart, C. Fradin, and K. Dalnoki-Veress (2010). “Squeezing and detachment of living cells”. In: *Biophysical journal* 99.11, pp. 3555–3562 (cit. on p. 99).
- Colin-York, H. E., Y. Javanmardi, L. Barbieri, D. Li, K. Korobchevskaya, Y. Guo, C. Hall, A. Taylor, S. Khuon, G. Sheridan, et al. (2019). “Spatiotemporally Super-resolved Volumetric Traction Force Microscopy”. In: *Nano letters* (cit. on p. 104).
- Colin-York, H., C. Eggeling, and M. Fritzsche (2017). “Dissection of mechanical force in living cells by super-resolved traction force microscopy”. In: *nature protocols* 12.4, p. 783 (cit. on pp. 104, 105, 120).
- Colin-York, H., D. Shrestha, J. H. Felce, D. Waithe, E. Moeendarbary, S. J. Davis, C. Eggeling, and M. Fritzsche (2016). “Super-resolved traction force microscopy (STFM)”. In: *Nano letters* 16.4, pp. 2633–2638 (cit. on pp. 104, 105).
- Collin, O., S. Na, F. Chowdhury, M. Hong, M. E. Shin, F. Wang, and N. Wang (2008). “Self-organized podosomes are dynamic mechanosensors”. In: *Current biology* 18.17, pp. 1288–1294 (cit. on pp. 34, 35, 98).
- Collin, O., P. Tracqui, A. Stephanou, Y. Usson, J. Clément-Lacroix, and E. Planus (2006). “Spatiotemporal dynamics of actin-rich adhesion microdomains: influence of substrate flexibility”. In: *Journal of cell science* 119.9, pp. 1914–1925 (cit. on pp. 32, 34).

- Colombelli, J., A. Besser, H. Kress, E. G. Reynaud, P. Girard, E. Caussinus, U. Haselmann, J. V. Small, U. S. Schwarz, and E. H. Stelzer (2009). “Mechanosensing in actin stress fibers revealed by a close correlation between force and protein localization”. In: *Journal of cell science* 122.10, pp. 1665–1679 (cit. on p. 100).
- Colombelli, J., E. G. Reynaud, and E. H. Stelzer (2007). “Investigating relaxation processes in cells and developing organisms: from cell ablation to cytoskeleton nanosurgery”. In: *Methods in cell biology* 82, pp. 267–291 (cit. on p. 100).
- Conroy, R. (2008). “Force spectroscopy with optical and magnetic tweezers”. In: *Handbook of molecular force spectroscopy*. Springer, pp. 23–96 (cit. on p. 99).
- Cornfine, S., M. Himmel, P. Kopp, K. El Azzouzi, C. Wiesner, M. Krüger, T. Rudel, and S. Linder (2011). “The kinesin KIF9 and reggie/flotillin proteins regulate matrix degradation by macrophage podosomes”. In: *Molecular biology of the cell* 22.2, pp. 202–215 (cit. on p. 33).
- Cortizo, A. M., G. Ruderman, G. Correa, I. G. Mogilner, and E. J. Tolosa (2012). “Effect of surface topography of collagen scaffolds on cytotoxicity and osteoblast differentiation”. In: *Journal of Biomaterials and Tissue Engineering* 2.2, pp. 125–132 (cit. on pp. 154, 155).
- Costa, R. R. and J. F. Mano (2014). “Polyelectrolyte multilayered assemblies in biomedical technologies”. In: *Chemical Society Reviews* 43.10, pp. 3453–3479 (cit. on p. 149).
- Cotter, A. G., C. A. Sabin, S. Simelane, A. Macken, E. Kavanagh, J. J. Brady, G. McCarthy, J. Compston, P. W. Mallon, H. U. S. Group, et al. (2014). “Relative contribution of HIV infection, demographics and body mass index to bone mineral density”. In: *Aids* 28.14, pp. 2051–2060 (cit. on p. 17).
- Cotter, E. J., A. P. Malizia, N. Chew, W. G. Powderly, and P. P. Doran (2007). “HIV proteins regulate bone marker secretion and transcription factor activity in cultured human osteoblasts with consequent potential implications for osteoblast function and development”. In: *AIDS research and human retroviruses* 23.12, pp. 1521–1530 (cit. on p. 17).
- Cougoule, C., V. Le Cabec, R. Poincloux, T. Al Saati, J.-L. Mège, G. Tabouret, C. A. Lowell, N. Laviolette-Malirat, and I. Maridonneau-Parini (2010). “Three-dimensional migration of macrophages requires Hck for podosome organization and extracellular matrix proteolysis”. In: *Blood* 115.7, pp. 1444–1452 (cit. on pp. 27, 37).
- Couret, I. (2004). “Biologie du remodelage osseux”. In: *Médecine nucléaire* 28.2, pp. 57–65 (cit. on p. 12).
- Cowin, S. C. and L. Cardoso (2015). “Blood and interstitial flow in the hierarchical pore space architecture of bone tissue”. In: *Journal of biomechanics* 48.5, pp. 842–854 (cit. on pp. 10, 15).
- Cox, S., E. Rosten, J. Monypenny, T. Jovanovic-Taliman, D. T. Burnette, J. Lippincott-Schwartz, G. E. Jones, and R. Heintzmann (2012). “Bayesian localization microscopy reveals nanoscale podosome dynamics”. In: *Nature methods* 9.2, p. 195 (cit. on p. 25).
- Coxon, F. P. and A. Taylor (2008). “Vesicular trafficking in osteoclasts”. In: *Seminars in cell & developmental biology*. Vol. 19. 5. Elsevier, pp. 424–433 (cit. on p. 11).
- Craighead, H., C. James, and A. Turner (2001). “Chemical and topographical patterning for directed cell attachment”. In: *Current opinion in solid state and materials science* 5.2-3, pp. 177–184 (cit. on p. 148).
- Cretu, A., P. Castagnino, and R. Assoian (2010). “Studying the effects of matrix stiffness on cellular function using acrylamide-based hydrogels”. In: *JoVE (Journal of Visualized Experiments)* 42, e2089 (cit. on p. 102).
- Crippes, B., V. Engleman, S. Settle, J. Delarco, R. Ornberg, M. Helfrich, M. Horton, and G. Nickols (1996). “Antibody to beta3 integrin inhibits osteoclast-mediated bone resorption in the thyroparathyroidectomized rat”. In: *Endocrinology* 137.3, pp. 918–924 (cit. on p. 44).

Bibliography

- Croke, M., F. P. Ross, M. Korhonen, D. A. Williams, W. Zou, and S. L. Teitelbaum (2011). “Rac deletion in osteoclasts causes severe osteopetrosis”. In: *J Cell Sci* 124.22, pp. 3811–3821 (cit. on p. 54).
- Crosby, C. O. and J. Zoldan (2019). “Mimicking the physical cues of the ECM in angiogenic biomaterials”. In: *Regenerative biomaterials* 6.2, pp. 61–73 (cit. on p. 93).
- Dalby, M. J., M. O. Riehle, S. J. Yarwood, C. D. Wilkinson, and A. S. Curtis (2003). “Nucleus alignment and cell signaling in fibroblasts: response to a micro-grooved topography”. In: *Experimental cell research* 284.2, pp. 272–280 (cit. on p. 148).
- Dalby, M., D. Giannaras, M. Riehle, N. Gadegaard, S. Affrossman, and A. Curtis (2004). “Rapid fibroblast adhesion to 27 nm high polymer demixed nano-topography”. In: *Biomaterials* 25.1, pp. 77–83 (cit. on p. 154).
- Dallas, S. L., M. Prideaux, and L. F. Bonewald (2013). “The osteocyte: an endocrine cell. . . and more”. In: *Endocrine reviews* 34.5, pp. 658–690 (cit. on p. 12).
- David-Pfeuty, T. and S. Singer (1980). “Altered distributions of the cytoskeletal proteins vinculin and alpha-actinin in cultured fibroblasts transformed by Rous sarcoma virus”. In: *Proceedings of the National Academy of Sciences* 77.11, pp. 6687–6691 (cit. on p. 23).
- Davies, J., J. Warwick, N. Totty, R. Philp, M. Helfrich, and M. Horton (1989). “The osteoclast functional antigen, implicated in the regulation of bone resorption, is biochemically related to the vitronectin receptor.” In: *The Journal of cell biology* 109.4, pp. 1817–1826 (cit. on p. 43).
- Decher, G., J. Hong, and J. Schmitt (1991). “Buildup of ultrathin multilayer films by a self-assembly process”. In: *Macromolecular Symposia* (cit. on p. 149).
- Deguchi, S., T. S. Matsui, and K. Iio (2011). “The position and size of individual focal adhesions are determined by intracellular stress-dependent positive regulation”. In: *Cytoskeleton* 68.11, pp. 639–651 (cit. on p. 98).
- Deguchi, T., M. H. Alanne, E. Fazeli, K. M. Fagerlund, P. Pennanen, P. Lehenkari, P. E. Hänninen, J. Peltonen, and T. Näreoja (2016). “In vitro model of bone to facilitate measurement of adhesion forces and super-resolution imaging of osteoclasts”. In: *Scientific reports* 6, p. 22585 (cit. on pp. 59, 64, 66).
- Del Alamo, J. C., R. Meili, B. Alonso-Latorre, J. Rodríguez-Rodríguez, A. Aliseda, R. A. Firtel, and J. C. Lasheras (2007). “Spatio-temporal analysis of eukaryotic cell motility by improved force cytometry”. In: *Proceedings of the National Academy of Sciences* 104.33, pp. 13343–13348 (cit. on p. 102).
- Del Álamo, J. C., R. Meili, B. Álvarez-González, B. Alonso-Latorre, E. Bastounis, R. Firtel, and J. C. Lasheras (2013). “Three-dimensional quantification of cellular traction forces and mechanosensing of thin substrata by fourier traction force microscopy”. In: *PloS one* 8.9, e69850 (cit. on pp. 104, 106, 107).
- Delaunay, G. (1953). “Microscope interférentiel A. Mirau pour la mesure du fini des surfaces”. In: *Rev Opt Theor Instrum* 32, pp. 610–614 (cit. on p. 114).
- Dembo, M., T. Oliver, A. Ishihara, and K. Jacobson (1996). “Imaging the traction stresses exerted by locomoting cells with the elastic substratum method”. In: *Biophysical journal* 70.4, pp. 2008–2022 (cit. on p. 101).
- Dembo, M. and Y.-L. Wang (1999). “Stresses at the cell-to-substrate interface during locomotion of fibroblasts”. In: *Biophysical journal* 76.4, pp. 2307–2316 (cit. on pp. 101, 103, 107).
- Dempster, D. W. and H. Zhou (2006). “New concepts in bone remodeling”. In: *Dynamics of Bone and Cartilage Metabolism. Seibel MJ, Robins SP, Bilezikian JP (eds.). Academic Press, San Diego* 22, pp. 377–389 (cit. on p. 12).

- Deng, Z., T. Zink, H.-y. Chen, D. Walters, F.-t. Liu, and G.-y. Liu (2009). “Impact of actin rearrangement and degranulation on the membrane structure of primary mast cells: a combined atomic force and laser scanning confocal microscopy investigation”. In: *Biophysical journal* 96.4, pp. 1629–1639 (cit. on p. 101).
- Desai, T. A. (2000). “Micro-and nanoscale structures for tissue engineering constructs”. In: *Med Eng Phy* 22, pp. 595–606 (cit. on p. 151).
- DeSelm, C. J., B. C. Miller, W. Zou, W. L. Beatty, E. van Meel, Y. Takahata, J. Klumperman, S. A. Tooze, S. L. Teitelbaum, and H. W. Virgin (2011). “Autophagy proteins regulate the secretory component of osteoclastic bone resorption”. In: *Developmental cell* 21.5, pp. 966–974 (cit. on p. 21).
- Desprat, N., A. Richert, J. Simeon, and A. Asnacios (2005). “Creep function of a single living cell”. In: *Biophysical journal* 88.3, pp. 2224–2233 (cit. on p. 100).
- Destaing, O., E. Planus, D. Bouvard, C. Oddou, C. Badowski, V. Bossy, A. Raducanu, B. Fourcade, C. Albiges-Rizo, and M. R. Block (2010). “ β 1A integrin is a master regulator of invadosome organization and function”. In: *Molecular biology of the cell* 21.23, pp. 4108–4119 (cit. on p. 25).
- Destaing, O., F. Saltel, J.-C. Géminard, P. Jurdic, and F. Bard (2003). “Podosomes display actin turnover and dynamic self-organization in osteoclasts expressing actin-green fluorescent protein”. In: *Molecular biology of the cell* 14.2, pp. 407–416 (cit. on pp. 62–64).
- Destaing, O., F. Saltel, B. Gilquin, A. Chabadel, S. Khochbin, S. Ory, and P. Jurdic (2005). “A novel Rho-mDia2-HDAC6 pathway controls podosome patterning through microtubule acetylation in osteoclasts”. In: *Journal of cell science* 118.13, pp. 2901–2911 (cit. on pp. 54, 57).
- Destaing, O., A. Sanjay, C. Itzstein, W. C. Horne, D. Toomre, P. De Camilli, and R. Baron (2008). “The tyrosine kinase activity of c-Src regulates actin dynamics and organization of podosomes in osteoclasts”. In: *Molecular biology of the cell* 19.1, pp. 394–404 (cit. on pp. 27, 55).
- Desvignes, E., A. Bouissou, A. Laborde, T. Mangeat, A. Proag, C. Vieu, C. Thibault, I. Maridonneau-Parini, and R. Poincloux (2018). “Nanoscale forces during confined cell migration”. In: *Nano letters* 18.10, pp. 6326–6333 (cit. on p. 98).
- Dewhirst, F. E., P. P. Stashenko, J. E. Mole, and T. Tsurumachi (1985). “Purification and partial sequence of human osteoclast-activating factor: identity with interleukin 1 beta.” In: *The Journal of Immunology* 135.4, pp. 2562–2568 (cit. on p. 17).
- Dikic, I., G. Tokiwa, S. Lev, S. A. Courtneidge, and J. Schlessinger (1996). “A role for Pyk2 and Src in linking G-protein-coupled receptors with MAP kinase activation”. In: *Nature* 383.6600, p. 547 (cit. on p. 56).
- Dobbenga, S., L. E. Fratila-Apachitei, and A. A. Zadpoor (2016). “Nanopattern-induced osteogenic differentiation of stem cells—A systematic review”. In: *Acta biomaterialia* 46, pp. 3–14 (cit. on p. 152).
- Docheva, D., D. Padula, C. Popov, W. Mutschler, H. Clausen-Schaumann, and M. Schieker (2008). “Researching into the cellular shape, volume and elasticity of mesenchymal stem cells, osteoblasts and osteosarcoma cells by atomic force microscopy”. In: *Journal of cellular and molecular medicine* 12.2, pp. 537–552 (cit. on p. 101).
- Dommelen, R. van, P. Fanzio, and L. Sasso (2018). “Surface self-assembly of colloidal crystals for micro-and nano-patterning”. In: *Advances in colloid and interface science* 251, pp. 97–114 (cit. on p. 150).
- Dong, L. and A. A. Oberai (2017). “Recovery of cellular traction in three-dimensional nonlinear hyperelastic matrices”. In: *Computer Methods in Applied Mechanics and Engineering* 314, pp. 296–313 (cit. on p. 109).
- Dovas, A. and D. Cox (2011). “Signaling networks regulating leukocyte podosome dynamics and function”. In: *Cellular signalling* 23.8, pp. 1225–1234 (cit. on p. 32).

- Dovas, A., J.-C. Gevrey, A. Grossi, H. Park, W. Abou-Kheir, and D. Cox (2009). “Regulation of podosome dynamics by WASp phosphorylation: implication in matrix degradation and chemotaxis in macrophages”. In: *J Cell Sci* 122.21, pp. 3873–3882 (cit. on p. 29).
- Drake, F. H., R. A. Dodds, I. E. James, J. R. Connor, C. Debouck, S. Richardson, E. Lee-Rykaczewski, L. Coleman, D. Rieman, R. Barthlow, et al. (1996). “Cathepsin K, but not cathepsins B, L, or S, is abundantly expressed in human osteoclasts”. In: *Journal of Biological Chemistry* 271.21, pp. 12511–12516 (cit. on p. 20).
- Dreier, M., D. Anselmetti, T. Richmond, U. Dammer, and H.-J. Güntherodt (1994). “Dynamic force microscopy in liquids”. In: *Journal of applied physics* 76.9, pp. 5095–5098 (cit. on p. 101).
- Du Roure, O., A. Saez, A. Buguin, R. H. Austin, P. Chavrier, P. Siberzan, and B. Ladoux (2005). “Force mapping in epithelial cell migration”. In: *Proceedings of the National Academy of Sciences* 102.7, pp. 2390–2395 (cit. on p. 98).
- Duong, L. T., P. T. Lakkakorpi, I. Nakamura, M. Machwate, R. M. Nagy, and G. A. Rodan (1998). “PYK2 in osteoclasts is an adhesion kinase, localized in the sealing zone, activated by ligation of $\alpha v \beta 3$ integrin, and phosphorylated by src kinase.” In: *The Journal of clinical investigation* 102.5, pp. 881–892 (cit. on pp. 45, 49, 56).
- Duong, L. T., P. Lakkakorpi, I. Nakamura, and G. A. Rodan (2000). “Integrins and signaling in osteoclast function”. In: *Matrix Biology* 19.2, pp. 97–105 (cit. on p. 42).
- Duplan, M. B., D. Zalli, S. Stephens, S. Zenger, L. Neff, J. M. Oelkers, F. P. Lai, W. Horne, K. Rottner, and R. Baron (2014). “Microtubule dynamic instability controls podosome patterning in osteoclasts through EB1, cortactin, and Src”. In: *Molecular and cellular biology* 34.1, pp. 16–29 (cit. on pp. 50, 56).
- Enderling, H., N. R. Alexander, E. S. Clark, K. M. Branch, L. Estrada, C. Crooke, J. Jourquin, N. Lobdell, M. H. Zaman, S. A. Guelcher, et al. (2008). “Dependence of invadopodia function on collagen fiber spacing and cross-linking: computational modeling and experimental evidence”. In: *Biophysical journal* 95.5, pp. 2203–2218 (cit. on p. 36).
- Engleman, V. W., G. A. Nickols, F. P. Ross, M. A. Horton, D. W. Griggs, S. L. Settle, P. G. Ruminski, and S. L. Teitelbaum (1997). “A peptidomimetic antagonist of the alpha (v) beta3 integrin inhibits bone resorption in vitro and prevents osteoporosis in vivo.” In: *The Journal of clinical investigation* 99.9, pp. 2284–2292 (cit. on p. 44).
- Eriksen, E. F., D. W. Axelrod, and F. Melsen (1994). *Bone histomorphometry*. Raven Press, pp. 1–12 (cit. on p. 9).
- Evans, E. and W. Rawicz (1990). “Entropy-driven tension and bending elasticity in condensed-fluid membranes”. In: *Physical review letters* 64.17, p. 2094 (cit. on p. 99).
- Evans, E. and A. Yeung (1989). “Apparent viscosity and cortical tension of blood granulocytes determined by micropipet aspiration”. In: *Biophysical journal* 56.1, pp. 151–160 (cit. on p. 100).
- Evans, J. G., I. Correia, O. Krasavina, N. Watson, and P. Matsudaira (2003). “Macrophage podosomes assemble at the leading lamella by growth and fragmentation”. In: *The Journal of cell biology* 161.4, pp. 697–705 (cit. on pp. 24, 30, 32, 36).
- Faccio, R., M. Grano, S. Colucci, A. Villa, G. Giannelli, V. Quaranta, and A. Zallone (2002). “Localization and possible role of two different $\alpha v \beta 3$ integrin conformations in resting and resorbing osteoclasts”. In: *Journal of cell science* 115.14, pp. 2919–2929 (cit. on pp. 44, 45, 53, 60).

- Faccio, R., S. L. Teitelbaum, K. Fujikawa, J. Chappel, A. Zallone, V. L. Tybulewicz, F. P. Ross, and W. Swat (2005). “Vav3 regulates osteoclast function and bone mass”. In: *Nature medicine* 11.3, p. 284 (cit. on pp. 55, 56).
- Fakruddin, J. and J. Laurence (2005). “HIV-1 Vpr enhances production of receptor of activated NF- κ B ligand (RANKL) via potentiation of glucocorticoid receptor activity”. In: *Archives of virology* 150.1, pp. 67–78 (cit. on p. 17).
- Fernández, P., P. A. Pullarkat, and A. Ott (2006). “A master relation defines the nonlinear viscoelasticity of single fibroblasts”. In: *Biophysical journal* 90.10, pp. 3796–3805 (cit. on pp. 8, 100).
- Flemming, R., C. J. Murphy, G. Abrams, S. Goodman, and P. Nealey (1999). “Effects of synthetic micro- and nano-structured surfaces on cell behavior”. In: *Biomaterials* 20.6, pp. 573–588 (cit. on p. 148).
- Flores, M. E., D. Heinegård, F. P. Reinholt, and G. Andersson (1996). “Bone sialoprotein coated on glass and plastic surfaces is recognized by different β 3integrins”. In: *Experimental cell research* 227.1, pp. 40–46 (cit. on p. 43).
- Flores, M. E., M. Norgård, D. Heinegård, F. P. Reinholt, and G. Andersson (1992). “RGD-directed attachment of isolated rat osteoclasts to osteopontin, bone sialoprotein, and fibronectin”. In: *Experimental cell research* 201.2, pp. 526–530 (cit. on p. 43).
- Fong, E. and D. A. Tirrell (2010). “Collective Cell Migration on Artificial Extracellular Matrix Proteins Containing Full-Length Fibronectin Domains”. In: *Advanced Materials* 22.46, pp. 5271–5275 (cit. on p. 145).
- Fort, E. and S. Grébillon (2007). “Surface enhanced fluorescence”. In: *Journal of Physics D: Applied Physics* 41.1, p. 013001 (cit. on p. 119).
- Fort, P. and A. Blangy (2017). “The evolutionary landscape of Dbl-like RhoGEF families: Adapting eukaryotic cells to environmental signals”. In: *Genome biology and evolution* 9.6, pp. 1471–1486 (cit. on p. 54).
- Fournier, M. F., R. Sauser, D. Ambrosi, J.-J. Meister, and A. B. Verkhovsky (2010). “Force transmission in migrating cells”. In: *The Journal of cell biology* 188.2, pp. 287–297 (cit. on p. 96).
- Franck, C., S. Hong, S. Maskarinec, D. Tirrell, and G. Ravichandran (2007). “Three-dimensional full-field measurements of large deformations in soft materials using confocal microscopy and digital volume correlation”. In: *Experimental Mechanics* 47.3, pp. 427–438 (cit. on pp. 107, 108).
- Franck, C., S. A. Maskarinec, D. A. Tirrell, and G. Ravichandran (2011). “Three-dimensional traction force microscopy: a new tool for quantifying cell-matrix interactions”. In: *PloS one* 6.3, e17833 (cit. on pp. 107, 108).
- Frattini, A., P. J. Orchard, C. Sobacchi, S. Giliani, M. Abinun, J. P. Mattsson, D. J. Keeling, A.-K. Andersson, P. Wallbrandt, L. Zecca, et al. (2000). “Defects in TCIRG1 subunit of the vacuolar proton pump are responsible for a subset of human autosomal recessive osteopetrosis”. In: *Nature genetics* 25.3, p. 343 (cit. on p. 19).
- Frey, M. T., I. Y. Tsai, T. P. Russell, S. K. Hanks, and Y.-I. Wang (2006). “Cellular responses to substrate topography: role of myosin II and focal adhesion kinase”. In: *Biophysical journal* 90.10, pp. 3774–3782 (cit. on p. 156).
- Friedl, P. and K. Wolf (2010). “Plasticity of cell migration: a multiscale tuning model”. In: *The Journal of cell biology* 188.1, pp. 11–19 (cit. on p. 153).
- Friedrichs, J., A. Taubenberger, C. M. Franz, and D. J. Muller (2007). “Cellular remodelling of individual collagen fibrils visualized by time-lapse AFM”. In: *Journal of molecular biology* 372.3, pp. 594–607 (cit. on p. 101).

- Frost, H. (1965). “Bone biodynamics”. In: *The American Journal of the Medical Sciences* 249.5 (cit. on p. 12).
- Fu, C., C. Tong, M. Wang, Y. Gao, Y. Zhang, S. Lü, S. Liang, C. Dong, and M. Long (2011). “Determining β 2-integrin and intercellular adhesion molecule 1 binding kinetics in tumor cell adhesion to leukocytes and endothelial cells by a gas-driven micropipette assay”. In: *Journal of Biological Chemistry* 286.40, pp. 34777–34787 (cit. on p. 99).
- Gadea, G. and A. Blangy (2014). “Dock-family exchange factors in cell migration and disease”. In: *European journal of cell biology* 93.10-12, pp. 466–477 (cit. on p. 54).
- Galbraith, C. G., K. M. Yamada, and M. P. Sheetz (2002). “The relationship between force and focal complex development”. In: *J Cell Biol* 159.4, pp. 695–705 (cit. on p. 99).
- Gardel, M. L., F. Nakamura, J. H. Hartwig, J. C. Crocker, T. P. Stossel, and D. A. Weitz (2006a). “Prestressed F-actin networks cross-linked by hinged filamins replicate mechanical properties of cells”. In: *Proceedings of the National Academy of Sciences* 103.6, pp. 1762–1767 (cit. on p. 100).
- Gardel, M., F. Nakamura, J. Hartwig, J. C. Crocker, T. Stossel, and D. Weitz (2006b). “Stress-dependent elasticity of composite actin networks as a model for cell behavior”. In: *Physical review letters* 96.8, p. 088102 (cit. on p. 100).
- Gavazzi, I., M. V. Nermut, and P. C. Marchisio (1989). “Ultrastructure and gold-immunolabelling of cell-substratum adhesions (podosomes) in RSV-transformed BHK cells”. In: *Journal of cell science* 94.1, pp. 85–99 (cit. on p. 24).
- Gawden-Bone, C., M. A. West, V. L. Morrison, A. J. Edgar, S. J. McMillan, B. D. Dill, M. Trost, A. Prescott, S. C. Fagerholm, and C. Watts (2014). “A crucial role for β 2 integrins in podosome formation, dynamics and Toll-like-receptor-signaled disassembly in dendritic cells”. In: *J Cell Sci* 127.19, pp. 4213–4224 (cit. on p. 25).
- Gawden-Bone, C., Z. Zhou, E. King, A. Prescott, C. Watts, and J. Lucocq (2010). “Dendritic cell podosomes are protrusive and invade the extracellular matrix using metalloproteinase MMP-14”. In: *J Cell Sci* 123.9, pp. 1427–1437 (cit. on pp. 24, 27, 31, 32, 36).
- Gdyczynski, C. M., A. Manbachi, S. Hashemi, B. Lashkari, and R. S. C. Cobbold (2014). “On estimating the directionality distribution in pedicle trabecular bone from micro-CT images”. In: *Physiological measurement* 35.12, p. 2415 (cit. on p. 10).
- Geblinger, D., L. Addadi, and B. Geiger (2010). “Nano-topography sensing by osteoclasts”. In: *J Cell Sci* 123.9, pp. 1503–1510 (cit. on pp. 59, 64, 154, 172, 174).
- Geblinger, D., B. Geiger, and L. Addadi (2009). “Surface-induced regulation of podosome organization and dynamics in cultured osteoclasts”. In: *Chembiochem* 10.1, pp. 158–165 (cit. on pp. 41, 59, 63, 64, 69, 154, 172).
- Geblinger, D., C. Zink, N. D. Spencer, L. Addadi, and B. Geiger (2011). “Effects of surface microtopography on the assembly of the osteoclast resorption apparatus”. In: *Journal of the Royal Society Interface* 9.72, pp. 1599–1608 (cit. on pp. 59, 64, 66, 174).
- Georgess, D., M. Mazzorana, J. Terrado, C. Delprat, C. Chamot, R. M. Guasch, I. Pérez-Roger, P. Jurdic, and I. Machuca-Gayet (2014). “Comparative transcriptomics reveals RhoE as a novel regulator of actin dynamics in bone-resorbing osteoclasts”. In: *Molecular biology of the cell* 25.3, pp. 380–396 (cit. on pp. 61, 64).

- Ghajar, C. M., X. Chen, J. W. Harris, V. Suresh, C. C. Hughes, N. L. Jeon, A. J. Putnam, and S. C. George (2008). “The effect of matrix density on the regulation of 3-D capillary morphogenesis”. In: *Biophysical journal* 94.5, pp. 1930–1941 (cit. on p. 94).
- Gibellini, D., E. De Crignis, C. Ponti, L. Cimatti, M. Borderi, M. Tschon, R. Giardino, and M. C. Re (2008). “HIV-1 triggers apoptosis in primary osteoblasts and HOBIT cells through TNF α activation”. In: *Journal of medical virology* 80.9, pp. 1507–1514 (cit. on p. 17).
- Gibson, L. (1985). “The mechanical behaviour of cancellous bone”. In: *Journal of biomechanics* 18.5, pp. 317–328 (cit. on p. 8).
- Gil-Henn, H., O. Destaing, N. A. Sims, K. Aoki, N. Alles, L. Neff, A. Sanjay, A. Bruzzaniti, P. De Camilli, R. Baron, et al. (2007). “Defective microtubule-dependent podosome organization in osteoclasts leads to increased bone density in Pyk2 $^{-/-}$ mice”. In: *The Journal of cell biology* 178.6, pp. 1053–1064 (cit. on pp. 48, 54, 56, 57, 69, 82).
- Gimona, M., R. Buccione, S. A. Courtneidge, and S. Linder (2008). “Assembly and biological role of podosomes and invadopodia”. In: *Current opinion in cell biology* 20.2, pp. 235–241 (cit. on p. 32).
- Glimcher, M. J. (1989). “Mechanism of calcification: Role of collagen fibrils and collagen-phosphoprotein complexes in vitro and in vivo”. In: *The Anatomical Record* 224.2, pp. 139–153 (cit. on p. 10).
- Goetzke, R., J. Franzen, A. Ostrowska, M. Vogt, A. Blaeser, G. Klein, B. Rath, H. Fischer, M. Zenke, and W. Wagner (2018). “Does soft really matter? Differentiation of induced pluripotent stem cells into mesenchymal stromal cells is not influenced by soft hydrogels”. In: *Biomaterials* 156, pp. 147–158 (cit. on p. 93).
- Gohda, J., Y. Ma, Y. Huang, Y. Zhang, L. Gu, Y. Han, T. Li, B. Gao, G. F. Gao, J.-i. Inoue, et al. (2015). “HIV-1 replicates in human osteoclasts and enhances their differentiation in vitro”. In: *Retrovirology* 12.1, p. 12 (cit. on p. 17).
- Goodison, S., V. Urquidi, and D. Tarin (1999). “CD44 cell adhesion molecules.” In: *Molecular Pathology* 52.4, p. 189 (cit. on p. 46).
- Goto, T., H. Maeda, and T. Tanaka (2002). “A selective inhibitor of matrix metalloproteinases inhibits the migration of isolated osteoclasts by increasing the life span of podosomes”. In: *Journal of bone and mineral metabolism* 20.2, pp. 98–105 (cit. on p. 60).
- Gruber, M. F., K. A. Weih, E. J. Boone, P. D. Smith, and K. A. Clouse (1995). “Endogenous macrophage CSF production is associated with viral replication in HIV-1-infected human monocyte-derived macrophages.” In: *The Journal of Immunology* 154.10, pp. 5528–5535 (cit. on p. 17).
- Gruber, R., P. Pietschmann, and M. Peterlik (2008). “Introduction to bone development, remodelling and repair”. In: *Radiology of osteoporosis*. Springer, pp. 1–23 (cit. on pp. 12, 16).
- Gu, Z., J. Kordowska, G. L. Williams, C.-L. A. Wang, and C.-M. Hai (2007). “Erk1/2 MAPK and caldesmon differentially regulate podosome dynamics in A7r5 vascular smooth muscle cells”. In: *Experimental cell research* 313.5, pp. 849–866 (cit. on p. 27).
- Guerra, J. M. (1995). “Super-resolution through illumination by diffraction-born evanescent waves”. In: *Applied physics letters* 66.26, pp. 3555–3557 (cit. on p. 111).
- Guiet, R., R. Poincloux, J. Castandet, L. Marois, A. Labrousse, V. Le Cabec, and I. Maridonneau-Parini (2008). “Hematopoietic cell kinase (Hck) isoforms and phagocyte duties—from signaling and actin reorganization to migration and phagocytosis”. In: *European journal of cell biology* 87.8-9, pp. 527–542 (cit. on p. 27).

Bibliography

- Guiet, R., C. V erollet, I. Lamsoul, C. Cougoule, R. Poincloux, A. Labrousse, D. A. Calderwood, M. Glogauer, P. G. Lutz, and I. Maridonneau-Parini (2012). "Macrophage mesenchymal migration requires podosome stabilization by filamin A". In: *Journal of Biological Chemistry* 287.16, pp. 13051–13062 (cit. on p. 25).
- Gupta, M. K. and R. Bansil (1981). "Laser Raman spectroscopy of polyacrylamide". In: *Journal of Polymer Science: Polymer Physics Edition* 19.2, pp. 353–360 (cit. on p. 144).
- Halleen, J. M., S. L. Alatalo, H. Suominen, S. Cheng, A. J. Janckila, and H. K. V aananen (2000). "Tartrate-resistant acid phosphatase 5b: a novel serum marker of bone resorption". In: *Journal of Bone and Mineral Research* 15.7, pp. 1337–1345 (cit. on p. 15).
- Hamon, L., P. A. Curmi, and D. Pastr e (2010). "High-resolution imaging of microtubules and cytoskeleton structures by atomic force microscopy". In: *Methods in cell biology*. Vol. 95. Elsevier, pp. 157–174 (cit. on p. 101).
- Han, S. J., Y. Oak, A. Groisman, and G. Danuser (2015). "Traction microscopy to identify force modulation in subresolution adhesions". In: *Nature methods* 12.7, p. 653 (cit. on pp. 104, 108).
- Hariharan, P. (2003). *Optical Interferometry, 2e*. Elsevier (cit. on p. 114).
- Harre, U., D. Georgess, H. Bang, A. Bozec, R. Axmann, E. Ossipova, P.-J. Jakobsson, W. Baum, F. Nimmerjahn, E. Szarka, et al. (2012). "Induction of osteoclastogenesis and bone loss by human autoantibodies against citrullinated vimentin". In: *The Journal of clinical investigation* 122.5, pp. 1791–1802 (cit. on p. 17).
- Harris, A. K., P. Wild, and D. Stopak (1980). "Silicone rubber substrata: a new wrinkle in the study of cell locomotion". In: *Science* 208.4440, pp. 177–179 (cit. on p. 101).
- Hartwig, J. H. and P. Shevlin (1986). "The architecture of actin filaments and the ultrastructural location of actin-binding protein in the periphery of lung macrophages." In: *The Journal of cell biology* 103.3, pp. 1007–1020 (cit. on p. 24).
- Hauschka, P., A. Mavrakos, M. Iafrazi, S. Doleman, and M. Klagsbrun (1986). "Growth factors in bone matrix. Isolation of multiple types by affinity chromatography on heparin-Sepharose." In: *Journal of Biological Chemistry* 261.27, pp. 12665–12674 (cit. on p. 16).
- Hayman, A. R., S. J. Jones, A. Boyde, D. Foster, W. H. Colledge, M. B. Carlton, M. J. Evans, and T. M. Cox (1996). "Mice lacking tartrate-resistant acid phosphatase (Acp 5) have disrupted endochondral ossification and mild osteopetrosis". In: *Development* 122.10, pp. 3151–3162 (cit. on p. 15).
- Hecht, E., S. M. Usmani, S. Albrecht, O. H. Wittekindt, P. Dietl, B. Mizaikoff, and C. Kranz (2011). "Atomic force microscopy of microvillous cell surface dynamics at fixed and living alveolar type II cells". In: *Analytical and bioanalytical chemistry* 399.7, pp. 2369–2378 (cit. on p. 101).
- Heckel, T., C. Czupalla, A. I. E. Santo, M. Anitei, M. A. Sanchez-Fernandez, K. Mosch, E. Krause, and B. Hoflack (2009). "Src-dependent repression of ARF6 is required to maintain podosome-rich sealing zones in bone-digesting osteoclasts". In: *Proceedings of the National Academy of Sciences* 106.5, pp. 1451–1456 (cit. on pp. 55, 56, 173).
- Heemskerck, J., R. Rosmalen, R. Janssen-Van, R. Holtslag, D. Teeuw, et al. (1984). "Quantification of viscoelastic effects of polyacrylamide solutions". In: *SPE Enhanced Oil Recovery Symposium*. Society of Petroleum Engineers (cit. on p. 109).
- Helfrich, M., S. Nesbitt, P. Lakkakorpi, M. Barnes, S. Bodary, G. Shankar, W. Mason, D. Mendrick, H. V aananen, and M. Horton (1996). " β 1 integrins and osteoclast function: involvement in collagen recognition and bone resorption". In: *Bone* 19.4, pp. 317–328 (cit. on p. 45).

- Helfrich, M. H., S. A. Nesbitt, E. L. Dorey, and M. A. Horton (1992). "Rat osteoclasts adhere to a wide range of RGD (Arg-Gly-Asp) peptide-containing proteins, including the bone sialoproteins and fibronectin, via a $\beta 3$ integrin". In: *Journal of Bone and Mineral Research* 7.3, pp. 335–343 (cit. on p. 43).
- Hell, S. W. and J. Wichmann (1994). "Breaking the diffraction resolution limit by stimulated emission: stimulated-emission-depletion fluorescence microscopy". In: *Optics letters* 19.11, pp. 780–782 (cit. on p. 111).
- Herant, M. and M. Dembo (2010). "Cytopede: a three-dimensional tool for modeling cell motility on a flat surface". In: *Journal of Computational Biology* 17.12, pp. 1639–1677 (cit. on p. 107).
- Hess, S. T., T. P. Girirajan, and M. D. Mason (2006). "Ultra-high resolution imaging by fluorescence photoactivation localization microscopy". In: *Biophysical journal* 91.11, pp. 4258–4272 (cit. on p. 111).
- Heuser, J. (2000). "The production of 'cell cortices' for light and electron microscopy". In: *Traffic* 1.7, pp. 545–552 (cit. on p. 24).
- Hiregowdara, D., H. Avraham, Y. Fu, R. London, and S. Avraham (1997). "Tyrosine phosphorylation of the related adhesion focal tyrosine kinase in megakaryocytes upon stem cell factor and phorbol myristate acetate stimulation and its association with paxillin". In: *Journal of Biological Chemistry* 272.16, pp. 10804–10810 (cit. on p. 56).
- Hochmuth, R. M. (2000). "Micropipette aspiration of living cells". In: *Journal of biomechanics* 33.1, pp. 15–22 (cit. on p. 99).
- Hodge, J. M., M. A. Kirkland, and G. C. Nicholson (2007). "Multiple roles of M-CSF in human osteoclastogenesis". In: *Journal of cellular biochemistry* 102.3, pp. 759–768 (cit. on p. 15).
- Holliday, L. S., M. R. Bubb, J. Jiang, I. R. Hurst, and J. Zuo (2005). "Interactions between vacuolar H⁺-ATPases and microfilaments in osteoclasts". In: *Journal of bioenergetics and biomembranes* 37.6, pp. 419–423 (cit. on p. 50).
- Hong, J. M., S. L. Teitelbaum, T.-H. Kim, F. P. Ross, S.-Y. Kim, and H.-J. Kim (2011). "Calpain-6, a target molecule of glucocorticoids, regulates osteoclastic bone resorption via cytoskeletal organization and microtubule acetylation". In: *Journal of Bone and Mineral Research* 26.3, pp. 657–665 (cit. on p. 58).
- Horne, W., L. Neff, D. Chatterjee, A. Lomri, J. Levy, and R. Baron (1992). "Osteoclasts express high levels of pp60c-src in association with intracellular membranes." In: *The Journal of cell biology* 119.4, pp. 1003–1013 (cit. on p. 55).
- Horton, J. E., L. G. Raisz, H. A. Simmons, J. J. Oppenheim, and S. E. Mergenhagen (1972). "Bone resorbing activity in supernatant fluid from cultured human peripheral blood leukocytes". In: *Science* 177.4051, pp. 793–795 (cit. on p. 17).
- Horton, M. (1996). "Integrins as therapeutic targets in bone disease." In: *Adhesion receptors as therapeutic targets*. Pp. 223–245 (cit. on p. 43).
- Horton, M. and J. Davies (1989). "Perspectives: adhesion receptors in bone". In: *Journal of Bone and Mineral Research* 4.6, pp. 803–808 (cit. on p. 45).
- Horton, M., M. Taylor, T. Arnett, and M. Helfrich (1991). "Arg-Gly-Asp (RGD) peptides and the anti-vitronectin receptor antibody 23C6 inhibit dentine resorption and cell spreading by osteoclasts". In: *Experimental cell research* 195.2, pp. 368–375 (cit. on p. 44).
- Horton, M. A. (1997). "The $\alpha v \beta 3$ integrin "vitronectin receptor"". In: *The international journal of biochemistry & cell biology* 29.5, pp. 721–725 (cit. on p. 43).
- Horton, M. A., M. A. Nesbit, and M. H. Helfrich (1995). "Interaction of osteopontin with osteoclast integrins." In: *Annals of the New York Academy of Sciences* 760, pp. 190–200 (cit. on pp. 40, 46, 59).

- Hu, S., T. Biben, X. Wang, P. Jurdic, and J.-C. Géminard (2011a). “Internal dynamics of actin structures involved in the cell motility and adhesion: Modeling of the podosomes at the molecular level”. In: *Journal of theoretical biology* 270.1, pp. 25–30 (cit. on p. 65).
- Hu, S., E. Planus, D. Georgess, C. Place, X. Wang, C. Albiges-Rizo, P. Jurdic, and J.-C. Géminard (2011b). “Podosome rings generate forces that drive saltatory osteoclast migration”. In: *Molecular biology of the cell* 22.17, pp. 3120–3126 (cit. on pp. 61, 66, 98, 174).
- Huang, B., W. Wang, M. Bates, and X. Zhuang (2008). “Three-dimensional super-resolution imaging by stochastic optical reconstruction microscopy”. In: *Science* 319.5864, pp. 810–813 (cit. on pp. 112, 113).
- Hultenby, K., F. Reinholt, and D. Heinegård (1993). “Distribution of integrin subunits on rat metaphyseal osteoclasts and osteoblasts.” In: *European journal of cell biology* 62.1, pp. 86–93 (cit. on p. 44).
- Humphries, J. D., A. Byron, and M. J. Humphries (2006). “Integrin ligands at a glance”. In: *Journal of cell science* 119.19, pp. 3901–3903 (cit. on pp. 44, 116).
- Humphries, M. J. (1990). “The molecular basis and specificity of integrin-ligand interactions”. In: *Journal of Cell Science* 97.4, pp. 585–592 (cit. on p. 116).
- Humphries, M. (2000). *Integrin structure* (cit. on p. 95).
- Hur, S. S., Y. Zhao, Y.-S. Li, E. Botvinick, and S. Chien (2009). “Live cells exert 3-dimensional traction forces on their substrata”. In: *Cellular and molecular bioengineering* 2.3, pp. 425–436 (cit. on p. 106).
- Hurst, I. R., J. Zuo, J. Jiang, and L. S. Holliday (2004). “Actin-related protein 2/3 complex is required for actin ring formation”. In: *Journal of Bone and Mineral Research* 19.3, pp. 499–506 (cit. on pp. 50, 51, 69, 83).
- Huttenlocher, A. and A. R. Horwitz (2011). “Integrins in cell migration”. In: *Cold Spring Harbor perspectives in biology* 3.9, a005074 (cit. on p. 145).
- Hynes, R. O. (1992). “Integrins: versatility, modulation, and signaling in cell adhesion”. In: *Cell* 69.1, pp. 11–25 (cit. on p. 42).
- (2002). “Integrins: bidirectional, allosteric signaling machines”. In: *cell* 110.6, pp. 673–687 (cit. on p. 95).
- (2009). “The extracellular matrix: not just pretty fibrils”. In: *Science* 326.5957, pp. 1216–1219 (cit. on p. 95).
- Idier, J., S. Labouesse, M. Allain, P. Liu, S. Bourguignon, and A. Sentenac (2017). “On the superresolution capacity of imagers using unknown speckle illuminations”. In: *IEEE Transactions on Computational Imaging* 4.1, pp. 87–98 (cit. on p. 86).
- Iliescu, C., J. Jing, F. E. Tay, J. Miao, and T. Sun (2005). “Characterization of masking layers for deep wet etching of glass in an improved HF/HCl solution”. In: *Surface and Coatings Technology* 198.1-3, pp. 314–318 (cit. on p. 170).
- Izeddin, I., M. El Beheiry, J. Andilla, D. Ciepielewski, X. Darzacq, and M. Dahan (2012). “PSF shaping using adaptive optics for three-dimensional single-molecule super-resolution imaging and tracking”. In: *Optics express* 20.5, pp. 4957–4967 (cit. on pp. 113, 119, 120).
- Janson, I. A. and A. J. Putnam (2015). “Extracellular matrix elasticity and topography: Material-based cues that affect cell function via conserved mechanisms”. In: *Journal of Biomedical Materials Research Part A* 103.3, pp. 1246–1258 (cit. on p. 148).
- Järveläinen, H., A. Sainio, M. Koulu, T. N. Wight, and R. Penttinen (2009). “Extracellular matrix molecules: potential targets in pharmacotherapy”. In: *Pharmacological reviews* 61.2, pp. 198–223 (cit. on p. 94).
- Jiang, G., G. Giannone, D. R. Critchley, E. Fukumoto, and M. P. Sheetz (2003). “Two-piconewton slip bond between fibronectin and the cytoskeleton depends on talin”. In: *Nature* 424.6946, p. 334 (cit. on p. 99).

- Jiang, H., Y. Wang, A. Viniegra, C. Sima, C. A. McCulloch, and M. Glogauer (2015). “Adseverin plays a role in osteoclast differentiation and periodontal disease-mediated bone loss”. In: *The FASEB Journal* 29.6, pp. 2281–2291 (cit. on p. 49).
- Jilka, R. L. (2003). “Biology of the basic multicellular unit and the pathophysiology of osteoporosis”. In: *Medical and pediatric oncology* 41.3, pp. 182–185 (cit. on p. 12).
- Jones, G. E., D. Zicha, G. A. Dunn, M. Blundell, and A. Thrasher (2002). “Restoration of podosomes and chemotaxis in Wiskott–Aldrich syndrome macrophages following induced expression of WASp”. In: *The international journal of biochemistry & cell biology* 34.7, pp. 806–815 (cit. on p. 28).
- Jones, W. R., H. P. Ting-Beall, G. M. Lee, S. S. Kelley, R. M. Hochmuth, and F. Guilak (1999). “Alterations in the Young’s modulus and volumetric properties of chondrocytes isolated from normal and osteoarthritic human cartilage”. In: *Journal of biomechanics* 32.2, pp. 119–127 (cit. on p. 100).
- Joosten, B., M. Willemse, J. Franssen, A. Cambi, and K. van den Dries (2018). “Super-resolution correlative light and electron microscopy (sr-clem) reveals novel ultrastructural insights into dendritic cell podosomes”. In: *Frontiers in immunology* 9, p. 1908 (cit. on p. 27).
- Jorge-Penas, A., A. Izquierdo-Alvarez, R. Aguilar-Cuenca, M. Vicente-Manzanares, J. M. Garcia-Aznar, H. Van Oosterwyck, E. M. de-Juan-Pardo, C. Ortiz-de-Solorzano, and A. Muñoz-Barrutia (2015). “Free Form Deformation-Based Image Registration Improves Accuracy of Traction Force Microscopy”. In: *PloS one* 10.12, e0144184 (cit. on p. 109).
- Jurdic, P., F. Saltel, A. Chabadel, and O. Destaing (2006). “Podosome and sealing zone: specificity of the osteoclast model”. In: *European journal of cell biology* 85.3-4, pp. 195–202 (cit. on pp. 39, 40, 48, 49, 51, 56, 68, 69, 117, 173).
- Kaewsaneha, C., P. Tangboriboonrat, D. Polpanich, M. Eissa, and A. Elaissari (2013). “Janus colloidal particles: preparation, properties, and biomedical applications”. In: *ACS applied materials & interfaces* 5.6, pp. 1857–1869 (cit. on p. 150).
- Kanehisa, J., T. Yamanaka, S. Doi, K. Turksen, J. Heersche, J. Aubin, and H. Takeuchi (1990). “A band of F-actin containing podosomes is involved in bone resorption by osteoclasts”. In: *Bone* 11.4, pp. 287–293 (cit. on pp. 39, 58, 60, 64, 68).
- Kanehisa, J., T. Izumo, M. Takeuchi, T. Yamanaka, T. Fujii, and H. Takeuchi (1991). “In vitro bone resorption by isolated multinucleated giant cells from giant cell tumour of bone: light and electron microscopic study”. In: *Virchows Archiv A* 419.4, pp. 327–338 (cit. on p. 39).
- Kang, E., Y. Y. Choi, S.-K. Chae, J.-H. Moon, J.-Y. Chang, and S.-H. Lee (2012). “Microfluidic spinning of flat alginate fibers with grooves for cell-aligning scaffolds”. In: *Advanced materials* 24.31, pp. 4271–4277 (cit. on p. 151).
- Kaverina, I., O. Krylyshkina, and J. V. Small (1999). “Microtubule targeting of substrate contacts promotes their relaxation and dissociation”. In: *The Journal of cell biology* 146.5, pp. 1033–1044 (cit. on p. 56).
- Kaverina, I., T. E. Stradal, and M. Gimona (2003). “Podosome formation in cultured A7r5 vascular smooth muscle cells requires Arp2/3-dependent de-novo actin polymerization at discrete microdomains”. In: *Journal of cell science* 116.24, pp. 4915–4924 (cit. on p. 24).
- Kaya, M. and H. Higuchi (2010). “Nonlinear elasticity and an 8-nm working stroke of single myosin molecules in myofilaments”. In: *Science* 329.5992, pp. 686–689 (cit. on p. 99).
- Keeney, M., X. Jiang, M. Yamane, M. Lee, S. Goodman, and F. Yang (2015). “Nanocoating for biomolecule delivery using layer-by-layer self-assembly”. In: *Journal of Materials Chemistry B* 3.45, pp. 8757–8770 (cit. on p. 149).

- Kelleher, C. M. and J. P. Vacanti (2010). “Engineering extracellular matrix through nanotechnology”. In: *Journal of the Royal Society Interface* 7.suppl_6, S717–S729 (cit. on p. 147).
- Khademhosseini, A., K. Y. Suh, J. M. Yang, G. Eng, J. Yeh, S. Levenberg, and R. Langer (2004). “Layer-by-layer deposition of hyaluronic acid and poly-L-lysine for patterned cell co-cultures”. In: *Biomaterials* 25.17, pp. 3583–3592 (cit. on p. 150).
- Khurana, J. S. and L. A. Fitzpatrick (2009). “Osteoporosis and metabolic bone disease”. In: *Bone Pathology*. Springer, pp. 217–237 (cit. on pp. 11, 12).
- Kim, D.-H., E. A. Lipke, P. Kim, R. Cheong, S. Thompson, M. Delannoy, K.-Y. Suh, L. Tung, and A. Levchenko (2010). “Nanoscale cues regulate the structure and function of macroscopic cardiac tissue constructs”. In: *Proceedings of the National Academy of Sciences* 107.2, pp. 565–570 (cit. on p. 152).
- Kim, H. N., A. Jiao, N. S. Hwang, M. S. Kim, D.-H. Kim, K.-Y. Suh, et al. (2013). “Nanotopography-guided tissue engineering and regenerative medicine”. In: *Advanced drug delivery reviews* 65.4, pp. 536–558 (cit. on p. 147).
- Kim, H. and C. A. McCulloch (2011). “Filamin A mediates interactions between cytoskeletal proteins that control cell adhesion”. In: *FEBS letters* 585.1, pp. 18–22 (cit. on p. 25).
- Kim, J., C. A. Jones, N. S. Groves, and B. Sun (2016). “Three-dimensional reflectance traction microscopy”. In: *PloS one* 11.6, e0156797 (cit. on p. 175).
- King, K. L., J. J. D’Anza, S. Bodary, R. Pitti, M. Siegel, R. A. Lazarus, M. S. Dennis, R. G. Hammonds JR, and S. C. Kukreja (1994). “Effects of kistrin on bone resorption in vitro and serum calcium in vivo”. In: *Journal of Bone and Mineral Research* 9.3, pp. 381–387 (cit. on p. 44).
- Kini, U. and B. Nandeesh (2012). “Physiology of bone formation, remodeling, and metabolism”. In: *Radiionuclide and hybrid bone imaging*. Springer, pp. 29–57 (cit. on p. 12).
- Kirkbride, K. C., B. H. Sung, S. Sinha, and A. M. Weaver (2011). “Cortactin: a multifunctional regulator of cellular invasiveness”. In: *Cell adhesion & migration* 5.2, pp. 187–198 (cit. on p. 24).
- Kirshner, H., F. Aguet, D. Sage, and M. Unser (2013). “3-D PSF fitting for fluorescence microscopy: implementation and localization application”. In: *Journal of microscopy* 249.1, pp. 13–25 (cit. on p. 86).
- Kitazawa, R. and S. Kitazawa (2002). “Vitamin D3 augments osteoclastogenesis via vitamin D-responsive element of mouse RANKL gene promoter”. In: *Biochemical and biophysical research communications* 290.2, pp. 650–655 (cit. on p. 16).
- Kodera, N., D. Yamamoto, R. Ishikawa, and T. Ando (2010). “Video imaging of walking myosin V by high-speed atomic force microscopy”. In: *Nature* 468.7320, p. 72 (cit. on p. 101).
- Komori, T. (2010). “Regulation of bone development and extracellular matrix protein genes by RUNX2”. In: *Cell and tissue research* 339.1, p. 189 (cit. on p. 16).
- Kopp, P., R. Lammers, M. Aepfelbacher, G. Woehlke, T. Rudel, N. Machuy, W. Steffen, and S. Linder (2006). “The kinesin KIF1C and microtubule plus ends regulate podosome dynamics in macrophages”. In: *Molecular biology of the cell* 17.6, pp. 2811–2823 (cit. on pp. 30, 32).
- Kornak, U., D. Kasper, M. R. Bösl, E. Kaiser, M. Schweizer, A. Schulz, W. Friedrich, G. Delling, and T. J. Jentsch (2001). “Loss of the ClC-7 chloride channel leads to osteopetrosis in mice and man”. In: *Cell* 104.2, pp. 205–215 (cit. on p. 19).
- Kress, H., E. H. Stelzer, D. Holzer, F. Buss, G. Griffiths, and A. Rohrbach (2007). “Filopodia act as phagocytic tentacles and pull with discrete steps and a load-dependent velocity”. In: *Proceedings of the National Academy of Sciences* 104.28, pp. 11633–11638 (cit. on p. 99).

- Krits, I., R. Wysolmerski, L. Holliday, and B. Lee (2002). “Differential localization of myosin II isoforms in resting and activated osteoclasts”. In: *Calcified tissue international* 71.6, pp. 530–538 (cit. on pp. 40, 52).
- Kronenberg, N. M., P. Liehm, A. Steude, J. A. Knipper, J. G. Berger, G. Scarcelli, K. Franze, S. J. Powis, and M. C. Gather (2017). “Long-term imaging of cellular forces with high precision by elastic resonator interference stress microscopy”. In: *Nature cell biology* 19.7, p. 864 (cit. on p. 175).
- Krylyshkina, O., K. I. Anderson, I. Kaverina, I. Upmann, D. J. Manstein, J. V. Small, and D. K. Toomre (2003). “Nanometer targeting of microtubules to focal adhesions”. In: *The Journal of cell biology* 161.5, pp. 853–859 (cit. on p. 56).
- Kuhn-Spearing, L., C. Rey, H.-M. Kim, and M. J. Glimcher (1996). “Carbonated apatite nanocrystals of bone”. In: *Synthesis and processing of nanocrystalline powder* (cit. on p. 10).
- Kulkarni, A. H., P. Ghosh, A. Seetharaman, P. Kondaiah, and N. Gundiah (2018). “Traction cytometry: regularization in the Fourier approach and comparisons with finite element method”. In: *Soft matter* 14.23, pp. 4687–4695 (cit. on p. 108).
- Kulkarni, A. V. and B. Bhushan (1996). “Nanoscale mechanical property measurements using modified atomic force microscopy”. In: *Thin Solid Films* 290, pp. 206–210 (cit. on p. 144).
- Kumar, K., M. E. Andrews, V. Jayashankar, A. K. Mishra, and S. Suresh (2010). “Measurement of viscoelastic properties of polyacrylamide-based tissue-mimicking phantoms for ultrasound elastography applications”. In: *IEEE Transactions on Instrumentation and Measurement* 59.5, pp. 1224–1232 (cit. on p. 109).
- Kumar, S., I. Z. Maxwell, A. Heisterkamp, T. R. Polte, T. P. Lele, M. Salanga, E. Mazur, and D. E. Ingber (2006). “Viscoelastic retraction of single living stress fibers and its impact on cell shape, cytoskeletal organization, and extracellular matrix mechanics”. In: *Biophysical journal* 90.10, pp. 3762–3773 (cit. on p. 100).
- Labernadie, A., A. Bouissou, P. Delobelle, S. Balor, R. Voituriez, A. Proag, I. Fourquaux, C. Thibault, C. Vieu, R. Poincloux, et al. (2014). “Protrusion force microscopy reveals oscillatory force generation and mechanosensing activity of human macrophage podosomes”. In: *Nature communications* 5, p. 5343 (cit. on pp. 26, 31, 32, 34, 36, 81, 82, 92, 109, 117, 155, 174, 175).
- Labernadie, A., C. Thibault, C. Vieu, I. Maridonneau-Parini, and G. M. Charrière (2010). “Dynamics of podosome stiffness revealed by atomic force microscopy”. In: *Proceedings of the National Academy of Sciences* 107.49, pp. 21016–21021 (cit. on pp. 23, 34).
- Lagache, T., A. Grassart, S. Dallongeville, O. Faklaris, N. Sauvonnet, A. Dufour, L. Danglot, and J.-C. Olivo-Marin (2018). “Mapping molecular assemblies with fluorescence microscopy and object-based spatial statistics”. In: *Nature communications* 9.1, p. 698 (cit. on p. 87).
- Lakkakorpi, P. T., I. Nakamura, R. M. Nagy, J. T. Parsons, G. A. Rodan, and L. T. Duong (1999). “Stable Association of PYK2 and p130Cas in Osteoclasts and Their Co-localization in the Sealing Zone”. In: *Journal of Biological Chemistry* 274.8, pp. 4900–4907 (cit. on pp. 40, 48, 56, 59, 69, 173).
- Lakkakorpi, P. T. and H. K. Väänänen (1996). “Cytoskeletal changes in osteoclasts during the resorption cycle”. In: *Microscopy research and technique* 33.2, pp. 171–181 (cit. on pp. 39, 48, 56, 58, 69, 75).
- Lakkakorpi, P. T. and K. H. Väänänen (1991a). “Kinetics of the osteoclast cytoskeleton during the resorption cycle in vitro”. In: *Journal of Bone and Mineral Research* 6.8, pp. 817–826 (cit. on pp. 39, 56, 62).
- Lakkakorpi, P., M. Helfrich, M. Horton, and H. Vaananen (1993). “Spatial organization of microfilaments and vitronectin receptor, $\alpha\beta_3$, in osteoclasts. A study using confocal laser scanning microscopy”. In: *Journal of Cell Science* 104.3, pp. 663–670 (cit. on pp. 39, 44, 48, 49, 69, 75, 82, 173).

- Lakkakorpi, P., M. Horton, M. Helfrich, E. Karhukorpi, and H. Väänänen (1991b). “Vitronectin receptor has a role in bone resorption but does not mediate tight sealing zone attachment of osteoclasts to the bone surface.” In: *The Journal of cell biology* 115.4, pp. 1179–1186 (cit. on pp. 39, 44).
- Lakkakorpi, P., I. Nakamura, M. Young, L. Lipfert, G. Rodan, and L. Duong (2001). “Abnormal localisation and hyperclustering of $\alpha v\beta 3$ integrins and associated proteins in Src-deficient or tyrphostin A9-treated osteoclasts”. In: *Journal of cell science* 114.1, pp. 149–160 (cit. on pp. 44, 48, 55, 56, 59, 69, 82).
- Lakkakorpi, P. and H. Väänänen (1990). “Calcitonin, prostaglandin E2, and dibutyryl cyclic adenosine 3', 5'-monophosphate disperse the specific microfilament structure in resorbing osteoclasts.” In: *Journal of Histochemistry & Cytochemistry* 38.10, pp. 1487–1493 (cit. on pp. 48, 49).
- Lakkakorpi, P., G. Wesolowski, Z. Zimolo, G. Rodan, and S. Rodan (1997). “Phosphatidylinositol 3-kinase association with the osteoclast cytoskeleton, and its involvement in osteoclast attachment and spreading”. In: *Experimental cell research* 237.2, pp. 296–306 (cit. on pp. 54, 55, 57).
- Landis, W. (1995). “The strength of a calcified tissue depends in part on the molecular structure and organization of its constituent mineral crystals in their organic matrix”. In: *Bone* 16.5, pp. 533–544 (cit. on p. 8).
- Le Digabel, J., M. Ghibaudo, L. Trichet, A. Richert, and B. Ladoux (2010). “Microfabricated substrates as a tool to study cell mechanotransduction”. In: *Medical & biological engineering & computing* 48.10, pp. 965–976 (cit. on p. 98).
- Le Grimellec, C., E. Lesniewska, M.-C. Giocondi, E. Finot, V. Vié, and J.-P. Goudonnet (1998). “Imaging of the surface of living cells by low-force contact-mode atomic force microscopy”. In: *Biophysical journal* 75.2, pp. 695–703 (cit. on p. 101).
- Legant, W. R., C. K. Choi, J. S. Miller, L. Shao, L. Gao, E. Betzig, and C. S. Chen (2013). “Multidimensional traction force microscopy reveals out-of-plane rotational moments about focal adhesions”. In: *Proceedings of the National Academy of Sciences* 110.3, pp. 881–886 (cit. on pp. 107, 109, 141).
- Legant, W. R., J. S. Miller, B. L. Blakely, D. M. Cohen, G. M. Genin, and C. S. Chen (2010). “Measurement of mechanical tractions exerted by cells in three-dimensional matrices”. In: *Nature methods* 7.12, p. 969 (cit. on pp. 103, 108).
- Li, B. and J. H.-C. Wang (2010). “Application of sensing techniques to cellular force measurement”. In: *Sensors* 10.11, pp. 9948–9962 (cit. on p. 98).
- Lim, C. T. et al. (2017). “Nanofiber technology: current status and emerging developments”. In: *Progress in Polymer Science* 70, pp. 1–17 (cit. on p. 150).
- Lim, J. Y., J. C. Hansen, C. A. Siedlecki, J. Runt, and H. J. Donahue (2005). “Human foetal osteoblastic cell response to polymer-demixed nanotopographic interfaces”. In: *Journal of the Royal Society Interface* 2.2, pp. 97–108 (cit. on p. 154).
- Linder, S. (2007). “The matrix corroded: podosomes and invadopodia in extracellular matrix degradation”. In: *Trends in cell biology* 17.3, pp. 107–117 (cit. on p. 29).
- (2009). “Invadosomes at a glance”. In: *J Cell Sci* 122.17, pp. 3009–3013 (cit. on p. 23).
- Linder, S. and M. Aepfelbacher (2003). “Podosomes: adhesion hot-spots of invasive cells”. In: *Trends in cell biology* 13.7, pp. 376–385 (cit. on pp. 25, 27).
- Linder, S., H. Higgs, K. Hüfner, K. Schwarz, U. Pannicke, and M. Aepfelbacher (2000a). “The polarization defect of Wiskott-Aldrich syndrome macrophages is linked to dislocalization of the Arp2/3 complex”. In: *The Journal of Immunology* 165.1, pp. 221–225 (cit. on pp. 23, 25, 27, 28).

Bibliography

- Linder, S., K. Hufner, U. Wintergerst, and M. Aepfelbacher (2000b). “Microtubule-dependent formation of podosomal adhesion structures in primary human macrophages”. In: *Journal of cell science* 113.23, pp. 4165–4176 (cit. on pp. 23, 54).
- Linder, S. and P. Kopp (2005). “Podosomes at a glance”. In: *Journal of cell science* 118.10, pp. 2079–2082 (cit. on pp. 32, 36).
- Linder, S., D. Nelson, M. Weiss, and M. Aepfelbacher (1999). “Wiskott-Aldrich syndrome protein regulates podosomes in primary human macrophages”. In: *Proceedings of the National Academy of Sciences* 96.17, pp. 9648–9653 (cit. on p. 27).
- Linder, S. and C. Wiesner (2015). “Tools of the trade: podosomes as multipurpose organelles of monocytic cells”. In: *Cellular and molecular life sciences* 72.1, pp. 121–135 (cit. on pp. 21, 24, 35, 37, 171).
- Linder, S., C. Wiesner, and M. Himmel (2011). “Degrading devices: invadosomes in proteolytic cell invasion”. In: *Annual review of cell and developmental biology* 27, pp. 185–211 (cit. on p. 32).
- Linnik, V. (1933). “Simple interferometer for the investigation of optical systems.” In: *C. R. Acad. Sci. USSR* 1, pp. 208–210 (cit. on p. 114).
- Litvinov, R. I., H. Shuman, J. S. Bennett, and J. W. Weisel (2002). “Binding strength and activation state of single fibrinogen-integrin pairs on living cells”. In: *Proceedings of the National Academy of Sciences* 99.11, pp. 7426–7431 (cit. on p. 99).
- Liu, W., J. Hainfeld, and R. Powell (2002). “Combined Alexa-488 and Nanogold Antibody Probes”. In: *Microscopy and Microanalysis* 8.S02, pp. 1030–1031 (cit. on p. 128).
- Lizárraga, F., R. Poincloux, M. Romao, G. Montagnac, G. Le Dez, I. Bonne, G. Rigaiil, G. Raposo, and P. Chavrier (2009). “Diaphanous-related formins are required for invadopodia formation and invasion of breast tumor cells”. In: *Cancer research* 69.7, pp. 2792–2800 (cit. on p. 36).
- Longo, M. L. and H. V. Ly (2007). “Micropipet aspiration for measuring elastic properties of lipid bilayers”. In: *Methods in Membrane Lipids*. Springer, pp. 421–437 (cit. on p. 99).
- López-Fagundo, C., E. Bar-Kochba, L. L. Livi, D. Hoffman-Kim, and C. Franck (2014). “Three-dimensional traction forces of Schwann cells on compliant substrates”. In: *Journal of The Royal Society Interface* 11.97, p. 20140247 (cit. on p. 107).
- Luxenburg, C., L. Addadi, and B. Geiger (2006a). “The molecular dynamics of osteoclast adhesions”. In: *European journal of cell biology* 85.3-4, pp. 203–211 (cit. on p. 48).
- Luxenburg, C., D. Geblinger, E. Klein, K. Anderson, D. Hanein, B. Geiger, and L. Addadi (2007). “The architecture of the adhesive apparatus of cultured osteoclasts: from podosome formation to sealing zone assembly”. In: *PLoS one* 2.1, e179 (cit. on pp. 40, 41, 48, 62, 69, 70, 81, 173).
- Luxenburg, C., J. T. Parsons, L. Addadi, and B. Geiger (2006b). “Involvement of the Src-cortactin pathway in podosome formation and turnover during polarization of cultured osteoclasts”. In: *Journal of cell science* 119.23, pp. 4878–4888 (cit. on p. 62).
- Luxenburg, C., S. Winograd-Katz, L. Addadi, and B. Geiger (2012). “Involvement of actin polymerization in podosome dynamics”. In: *J Cell Sci* 125.7, pp. 1666–1672 (cit. on pp. 31, 64).
- Lyubchenko, Y. L. (2011). “Preparation of DNA and nucleoprotein samples for AFM imaging”. In: *Micron* 42.2, pp. 196–206 (cit. on p. 101).
- Ma, T., K. Sadashivaiah, and M. A. Chellaiah (2010). “Regulation of sealing ring formation by L-plastin and cortactin in osteoclasts”. In: *Journal of Biological Chemistry* 285.39, pp. 29911–29924 (cit. on pp. 45, 50, 51, 56, 61, 63, 69, 82).

- Ma, Y., D. Li, Z. J. Smith, D. Li, and K. Chu (2018). “Structured illumination microscopy with interleaved reconstruction (SIMILR)”. In: *Journal of biophotonics* 11.2, e201700090 (cit. on p. 87).
- Machacek, M., L. Hodgson, C. Welch, H. Elliott, O. Pertz, P. Nalbant, A. Abell, G. L. Johnson, K. M. Hahn, and G. Danuser (2009). “Coordination of Rho GTPase activities during cell protrusion”. In: *Nature* 461.7260, p. 99 (cit. on p. 153).
- Maheshwari, G., G. Brown, D. A. Lauffenburger, A. Wells, and L. G. Griffith (2000). “Cell adhesion and motility depend on nanoscale RGD clustering”. In: *J Cell Sci* 113.10, pp. 1677–1686 (cit. on p. 145).
- Mak, M., C. A. Reinhart-King, and D. Erickson (2013). “Elucidating mechanical transition effects of invading cancer cells with a subnucleus-scaled microfluidic serial dimensional modulation device”. In: *Lab on a Chip* 13.3, pp. 340–348 (cit. on p. 100).
- Mangeat, T. and *et al.* (in preparation). “Random Illumination Microscopy (RIM) democratizes nanoscale resolution from single cells to thick, scattering organisms”. In: (cit. on pp. 70, 86).
- Mano, J. F. (2015). “Designing biomaterials for tissue engineering based on the deconstruction of the native cellular environment”. In: *Materials Letters* 141, pp. 198–202 (cit. on p. 147).
- Marchisio, P., D. Cirillo, L. Naldini, M. Primavera, A. Teti, and A. Zamboni-Zallone (1984). “Cell-substratum interaction of cultured avian osteoclasts is mediated by specific adhesion structures.” In: *The Journal of cell biology* 99.5, pp. 1696–1705 (cit. on pp. 39, 48, 51, 52, 58).
- Marie, P. J. and M. Kassem (2011). “Osteoblasts in osteoporosis: past, emerging, and future anabolic targets”. In: *European Journal of Endocrinology* 165.1, pp. 1–10 (cit. on p. 17).
- Mark, K. von der, J. Park, S. Bauer, and P. Schmuki (2010). “Nanoscale engineering of biomimetic surfaces: cues from the extracellular matrix”. In: *Cell and tissue research* 339.1, p. 131 (cit. on p. 148).
- Martens, J. C. and M. Radmacher (2008). “Softening of the actin cytoskeleton by inhibition of myosin II”. In: *Pflügers Archiv-European Journal of Physiology* 456.1, pp. 95–100 (cit. on p. 101).
- Marti, O., B. Drake, and P. Hansma (1987). “Atomic force microscopy of liquid-covered surfaces: Atomic resolution images”. In: *Applied Physics Letters* 51.7, pp. 484–486 (cit. on p. 101).
- Martiel, J.-L., A. Leal, L. Kurzawa, M. Balland, I. Wang, T. Vignaud, Q. Tseng, and M. Théry (2015). “Measurement of cell traction forces with ImageJ”. In: *Methods in cell biology*. Vol. 125. Elsevier, pp. 269–287 (cit. on p. 108).
- Martins, N. I., M. P. Sousa, C. A. Custódio, V. C. Pinto, P. J. Sousa, G. Minas, F. Cleymand, and J. F. Mano (2017). “Multilayered membranes with tuned well arrays to be used as regenerative patches”. In: *Acta biomaterialia* 57, pp. 313–323 (cit. on pp. 147, 150).
- Marvin, M. (1961). *Microscopy apparatus*. US Patent 3,013,467 (cit. on p. 112).
- Marzia, M., R. Chiusaroli, L. Neff, N.-Y. Kim, A. H. Chishti, R. Baron, and W. C. Horne (2006). “Calpain is required for normal osteoclast function and is down-regulated by calcitonin”. In: *Journal of Biological Chemistry* 281.14, pp. 9745–9754 (cit. on p. 52).
- Masarachia, P., M. Yamamoto, G. Rodan, and L. Duong (1995). “Co-localization of the vitronectin receptor $\alpha v \beta 3$ and echistatin in osteoclasts during bone resorption in vivo”. In: *Journal of Bone and Mineral Research* 10, S1647 (cit. on p. 44).
- Maskarinec, S. A., C. Franck, D. A. Tirrell, and G. Ravichandran (2009). “Quantifying cellular traction forces in three dimensions”. In: *Proceedings of the National Academy of Sciences* 106.52, pp. 22108–22113 (cit. on pp. 107, 108).
- Matellan, C. and E. Armando (2019). “Engineering the cellular mechanical microenvironment—from bulk mechanics to the nanoscale”. In: *J Cell Sci* 132.9, jcs229013 (cit. on pp. 147, 154).

Bibliography

- Matsumoto, T., Y. Nagase, J. Hirose, N. Tokuyama, T. Yasui, Y. Kadono, K. Ueki, T. Kadowaki, K. Nakamura, and S. Tanaka (2013). “Regulation of bone resorption and sealing zone formation in osteoclasts occurs through protein kinase b-mediated microtubule stabilization”. In: *Journal of Bone and Mineral Research* 28.5, pp. 1191–1202 (cit. on p. 57).
- McInnes, I. B. and G. Schett (2011). “The pathogenesis of rheumatoid arthritis”. In: *New England Journal of Medicine* 365.23, pp. 2205–2219 (cit. on p. 17).
- McMichael, B. K., P. Kotadiya, T. Singh, L. S. Holliday, and B. S. Lee (2006). “Tropomyosin isoforms localize to distinct microfilament populations in osteoclasts”. In: *Bone* 39.4, pp. 694–705 (cit. on pp. 49, 50).
- McMichael, B. K., R. E. Cheney, and B. S. Lee (2010a). “Myosin X regulates sealing zone patterning in osteoclasts through linkage of podosomes and microtubules”. In: *Journal of Biological Chemistry* 285.13, pp. 9506–9515 (cit. on pp. 52, 57, 58, 64).
- McMichael, B. K. and B. S. Lee (2008). “Tropomyosin 4 regulates adhesion structures and resorptive capacity in osteoclasts”. In: *Experimental cell research* 314.3, pp. 564–573 (cit. on pp. 50, 52, 82).
- McMichael, B. K., S. M. Meyer, and B. S. Lee (2010b). “c-Src-mediated phosphorylation of thyroid hormone receptor-interacting protein 6 (TRIP6) promotes osteoclast sealing zone formation”. In: *Journal of Biological Chemistry* 285.34, pp. 26641–26651 (cit. on p. 55).
- McMichael, B. K., K. F. Scherer, N. C. Franklin, and B. S. Lee (2014). “The RhoGAP activity of myosin IXB is critical for osteoclast podosome patterning, motility, and resorptive capacity”. In: *PloS one* 9.1, e87402 (cit. on pp. 52, 54, 55).
- Medalia, O., M. Beck, M. Ecke, I. Weber, R. Neujahr, W. Baumeister, and G. Gerisch (2007). “Organization of actin networks in intact filopodia”. In: *Current biology* 17.1, pp. 79–84 (cit. on p. 25).
- Meddens, M. B., E. Pandzic, J. A. Slotman, D. Guillet, B. Joosten, S. Mennens, L. M. Paardekooper, A. B. Houtsmuller, K. Van Den Dries, P. W. Wiseman, et al. (2016). “Actomyosin-dependent dynamic spatial patterns of cytoskeletal components drive mesoscale podosome organization”. In: *Nature communications* 7, p. 13127 (cit. on p. 32).
- Meddens, M. B., B. Rieger, C. G. Figdor, A. Cambi, and K. Van Den Dries (2013). “Automated podosome identification and characterization in fluorescence microscopy images”. In: *Microscopy and microanalysis* 19.1, pp. 180–189 (cit. on p. 170).
- Merrild, D. M., D. C. Pirapaharan, C. M. Andreasen, P. Kjærsgaard-Andersen, A. M. Møller, M. Ding, J.-M. Delaissé, and K. Søb (2015). “Pit-and trench-forming osteoclasts: a distinction that matters”. In: *Bone research* 3, p. 15032 (cit. on pp. 22, 62).
- Mersich, A. T., M. R. Miller, H. Chkourko, and S. D. Blystone (2010). “The formin FRL1 (FMNL1) is an essential component of macrophage podosomes”. In: *Cytoskeleton* 67.9, pp. 573–585 (cit. on pp. 27, 29).
- Meyer, G. A. and R. L. Lieber (2011). “Elucidation of extracellular matrix mechanics from muscle fibers and fiber bundles”. In: *Journal of biomechanics* 44.4, pp. 771–773 (cit. on p. 147).
- Mitrossilis, D., J. Fouchard, D. Pereira, F. Postic, A. Richert, M. Saint-Jean, and A. Asnacios (2010). “Real-time single-cell response to stiffness”. In: *Proceedings of the National Academy of Sciences* 107.38, pp. 16518–16523 (cit. on p. 100).
- Mizuno, A., N. Amizuka, K. Irie, A. Murakami, N. Fujise, T. Kanno, Y. Sato, N. Nakagawa, H. Yasuda, S.-i. Mochizuki, et al. (1998). “Severe osteoporosis in mice lacking osteoclastogenesis inhibitory factor/osteoprotegerin”. In: *Biochemical and biophysical research communications* 247.3, pp. 610–615 (cit. on p. 15).

- Mohan, S. and D. J. Baylink (1991). “Bone growth factors.” In: *Clinical orthopaedics and related research* 263, pp. 30–48 (cit. on p. 16).
- Möller, C., M. Allen, V. Elings, A. Engel, and D. J. Müller (1999). “Tapping-mode atomic force microscopy produces faithful high-resolution images of protein surfaces”. In: *Biophysical journal* 77.2, pp. 1150–1158 (cit. on p. 101).
- Moon, J. J., M. S. Hahn, I. Kim, B. A. Nsiah, and J. L. West (2008). “Micropatterning of poly (ethylene glycol) diacrylate hydrogels with biomolecules to regulate and guide endothelial morphogenesis”. In: *Tissue Engineering Part A* 15.3, pp. 579–585 (cit. on p. 95).
- Moore, S. W., N. Biais, and M. P. Sheetz (2009). “Traction on immobilized netrin-1 is sufficient to reorient axons”. In: *Science* 325.5937, pp. 166–166 (cit. on p. 99).
- Moreau, V., F. Tatin, C. Varon, and E. Génot (2003). “Actin can reorganize into podosomes in aortic endothelial cells, a process controlled by Cdc42 and RhoA”. In: *Molecular and cellular biology* 23.19, pp. 6809–6822 (cit. on p. 23).
- Moreno-Herrero, F., J. Colchero, and A. Baro (2003). “DNA height in scanning force microscopy”. In: *Ultramicroscopy* 96.2, pp. 167–174 (cit. on p. 101).
- Morimatsu, M., A. H. Mekhdjian, A. C. Chang, S. J. Tan, and A. R. Dunn (2015). “Visualizing the interior architecture of focal adhesions with high-resolution traction maps”. In: *Nano letters* 15.4, pp. 2220–2228 (cit. on p. 176).
- Mulari, M. T., H. Zhao, P. T. Lakkakorpi, and H. K. Väänänen (2003). “Osteoclast ruffled border has distinct subdomains for secretion and degraded matrix uptake”. In: *Traffic* 4.2, pp. 113–125 (cit. on pp. 11, 19).
- Müller, D. J., H. Janovjak, T. Lehto, L. Kuerschner, and K. Anderson (2002). “Observing structure, function and assembly of single proteins by AFM”. In: *Progress in biophysics and molecular biology* 79.1-3, pp. 1–43 (cit. on p. 101).
- Mundy, G. R., L. G. Raisz, R. A. Cooper, G. P. Schechter, and S. E. Salmon (1974). “Evidence for the secretion of an osteoclast stimulating factor in myeloma”. In: *New England Journal of Medicine* 291.20, pp. 1041–1046 (cit. on p. 17).
- Munoz, J. J. (2016). “Non-regularised inverse finite element analysis for 3D traction force microscopy”. In: *International Journal of Numerical Analysis and Modeling* 13.5, pp. 763–781 (cit. on p. 108).
- Nakahara, H., S. C. Mueller, M. Nomizu, Y. Yamada, Y. Yeh, and W.-T. Chen (1998). “Activation of $\beta 1$ integrin signaling stimulates tyrosine phosphorylation of p190 RhoGAP and membrane-protrusive activities at invadopodia”. In: *Journal of Biological Chemistry* 273.1, pp. 9–12 (cit. on p. 25).
- Nakamura, I., J. Gailit, and T. Sasaki (1996). “Osteoclast integrin $\alpha V \beta 3$ is present in the clear zone and contributes to cellular polarization”. In: *Cell and tissue research* 286.3, pp. 507–515 (cit. on p. 44).
- Nakamura, I., M. F. Pilkington, P. T. Lakkakorpi, L. Lipfert, S. M. Sims, S. J. Dixon, G. A. Rodan, and L. T. Duong (1999). “Role of $\alpha v \beta 3$ integrin in osteoclast migration and formation of the sealing zone”. In: *J Cell Sci* 112.22, pp. 3985–3993 (cit. on pp. 44, 58).
- Nakashima, K., X. Zhou, G. Kunkel, Z. Zhang, J. M. Deng, R. R. Behringer, and B. De Crombrughe (2002). “The novel zinc finger-containing transcription factor osterix is required for osteoblast differentiation and bone formation”. In: *Cell* 108.1, pp. 17–29 (cit. on p. 16).
- Nakashima, T. and H. Takayanagi (2011). “New regulation mechanisms of osteoclast differentiation”. In: *Annals of the New York Academy of Sciences* 1240.1, E13–E18 (cit. on p. 12).
- Nam, S., J. Lee, D. G. Brownfield, and O. Chaudhuri (2016). “Viscoplasticity enables mechanical remodeling of matrix by cells”. In: *Biophysical journal* 111.10, pp. 2296–2308 (cit. on p. 93).

- Neff, L., M. Amling, S. Tanaka, J. Gailit, and R. Baron (1996). “Both the αv and $\beta 3$ integrin subunits are present in the sealing zone of resorbing osteoclasts”. In: *Journal of Bone and Mineral Research* 11, S290 (cit. on p. 44).
- Nesbitt, S., A. Nesbit, M. Helfrich, and M. Horton (1993). “Biochemical characterization of human osteoclast integrins. Osteoclasts express alpha v beta 3, alpha 2 beta 1, and alpha v beta 1 integrins.” In: *Journal of Biological Chemistry* 268.22, pp. 16737–16745 (cit. on p. 45).
- Neuman, K. C. and A. Nagy (2008). “Single-molecule force spectroscopy: optical tweezers, magnetic tweezers and atomic force microscopy”. In: *Nature methods* 5.6, p. 491 (cit. on p. 99).
- Nguyen, A. T., S. R. Sathe, and E. K. Yim (2016). “From nano to micro: topographical scale and its impact on cell adhesion, morphology and contact guidance”. In: *Journal of Physics: Condensed Matter* 28.18, p. 183001 (cit. on p. 155).
- Norman, J. J. and T. A. Desai (2006). “Methods for fabrication of nanoscale topography for tissue engineering scaffolds”. In: *Annals of biomedical engineering* 34.1, pp. 89–101 (cit. on p. 147).
- Novack, D. V. and R. Faccio (2011). “Osteoclast motility: putting the brakes on bone resorption”. In: *Ageing research reviews* 10.1, pp. 54–61 (cit. on p. 22).
- Nowicki, M., A. Richter, B. Wolf, and H. Kaczmarek (2003). “Nanoscale mechanical properties of polymers irradiated by UV”. In: *Polymer* 44.21, pp. 6599–6606 (cit. on p. 144).
- O’Brien, C. A., T. Nakashima, and H. Takayanagi (2013). “Osteocyte control of osteoclastogenesis”. In: *Bone* 54.2, pp. 258–263 (cit. on p. 12).
- Oberleithner, H., C. Riethmüller, H. Schillers, G. A. MacGregor, H. E. de Wardener, and M. Hausberg (2007). “Plasma sodium stiffens vascular endothelium and reduces nitric oxide release”. In: *Proceedings of the National Academy of Sciences* 104.41, pp. 16281–16286 (cit. on p. 101).
- Ochoa, G.-C., V. I. Slepnev, L. Neff, N. Ringstad, K. Takei, L. Daniell, W. Kim, H. Cao, M. McNiven, R. Baron, et al. (2000). “A functional link between dynamin and the actin cytoskeleton at podosomes”. In: *The Journal of cell biology* 150.2, pp. 377–390 (cit. on pp. 40, 50, 56, 82).
- Odgaard, A., J. Kabel, B. van Rietbergen, M. Dalstra, and R. Huiskes (1997). “Fabric and elastic principal directions of cancellous bone are closely related”. In: *Journal of biomechanics* 30.5, pp. 487–495 (cit. on p. 8).
- Okumura, S., T. Mizoguchi, N. Sato, M. Yamaki, Y. Kobayashi, H. Yamauchi, H. Ozawa, N. Udagawa, and N. Takahashi (2006). “Coordination of microtubules and the actin cytoskeleton is important in osteoclast function, but calcitonin disrupts sealing zones without affecting microtubule networks”. In: *Bone* 39.4, pp. 684–693 (cit. on pp. 56, 58).
- Olbrich, K., W. Rawicz, D. Needham, and E. Evans (2000). “Water permeability and mechanical strength of polyunsaturated lipid bilayers”. In: *Biophysical journal* 79.1, pp. 321–327 (cit. on p. 99).
- Oliviero, O., M. Ventre, and P. Netti (2012). “Functional porous hydrogels to study angiogenesis under the effect of controlled release of vascular endothelial growth factor”. In: *Acta biomaterialia* 8.9, pp. 3294–3301 (cit. on p. 116).
- Olivo-Marin, J.-C. (2002). “Extraction of spots in biological images using multiscale products”. In: *Pattern recognition* 35.9, pp. 1989–1996 (cit. on p. 87).
- Orimo, H. (2010). “The mechanism of mineralization and the role of alkaline phosphatase in health and disease”. In: *Journal of Nippon Medical School* 77.1, pp. 4–12 (cit. on p. 15).

- Ory, S., H. Brazier, G. Pawlak, and A. Blangy (2008). “Rho GTPases in osteoclasts: orchestrators of podosome arrangement”. In: *European journal of cell biology* 87.8-9, pp. 469–477 (cit. on pp. 49, 53, 62, 69).
- Osiak, A.-E., G. Zenner, and S. Linder (2005). “Subconfluent endothelial cells form podosomes downstream of cytokine and RhoGTPase signaling”. In: *Experimental cell research* 307.2, pp. 342–353 (cit. on pp. 24, 37).
- Owen, R. and G. C. Reilly (2018). “In vitro models of bone remodelling and associated disorders”. In: *Frontiers in bioengineering and biotechnology* 6 (cit. on p. 14).
- Oyen, M. (2014). “Mechanical characterisation of hydrogel materials”. In: *International Materials Reviews* 59.1, pp. 44–59 (cit. on p. 144).
- Paiva, K. B. and J. M. Granjeiro (2017). “Matrix metalloproteinases in bone resorption, remodeling, and repair”. In: *Progress in molecular biology and translational science*. Vol. 148. Elsevier, pp. 203–303 (cit. on pp. 12, 20).
- Palacio, J., A. Jorge-Peñas, A. Muñoz-Barrutia, C. Ortiz-de-Solorzano, E. de Juan-Pardo, and J. M. García-Aznar (2013). “Numerical estimation of 3D mechanical forces exerted by cells on non-linear materials”. In: *Journal of biomechanics* 46.1, pp. 50–55 (cit. on p. 109).
- Panzer, L., L. Trübe, M. Klose, B. Joosten, J. Slotman, A. Cambi, and S. Linder (2016). “The formins FHOD1 and INF2 regulate inter- and intra-structural contractility of podosomes”. In: *J Cell Sci* 129.2, pp. 298–313 (cit. on pp. 27, 29).
- Parfitt, A. (2002). “Targeted and nontargeted bone remodeling: relationship to basic multicellular unit origination and progression”. In: *Bone* 1.30, pp. 5–7 (cit. on p. 21).
- Park, J., D.-H. Kim, H.-N. Kim, C. J. Wang, M. K. Kwak, E. Hur, K.-Y. Suh, S. S. An, and A. Levchenko (2016). “Directed migration of cancer cells guided by the graded texture of the underlying matrix”. In: *Nature materials* 15.7, p. 792 (cit. on pp. 152, 154).
- Park, J., D.-H. Kim, and A. Levchenko (2018). “Topotaxis: a new mechanism of directed cell migration in topographic ECM gradients”. In: *Biophysical journal* 114.6, pp. 1257–1263 (cit. on pp. 152, 153, 176).
- Pavani, S. R. P., M. A. Thompson, J. S. Biteen, S. J. Lord, N. Liu, R. J. Twieg, R. Piestun, and W. Moerner (2009). “Three-dimensional, single-molecule fluorescence imaging beyond the diffraction limit by using a double-helix point spread function”. In: *Proceedings of the National Academy of Sciences* 106.9, pp. 2995–2999 (cit. on p. 113).
- Pelham Jr, R. J. and Y.-L. Wang (1998). “Cell locomotion and focal adhesions are regulated by the mechanical properties of the substrate”. In: *The Biological Bulletin* 194.3, pp. 348–350 (cit. on p. 92).
- (1999). “High resolution detection of mechanical forces exerted by locomoting fibroblasts on the substrate”. In: *Molecular biology of the cell* 10.4, pp. 935–945 (cit. on p. 92).
- Pelham, R. J. and Y.-l. Wang (1997). “Cell locomotion and focal adhesions are regulated by substrate flexibility”. In: *Proceedings of the National Academy of Sciences* 94.25, pp. 13661–13665 (cit. on p. 92).
- Pernelle, K., L. Imbert, C. Bossier, J. Auregan, M. Cruel, A. Ogier, P. Jurdic, and T. Hoc (2017). “Microscale mechanical and mineral heterogeneity of human cortical bone governs osteoclast activity”. In: *Bone* 94, pp. 42–49 (cit. on p. 174).
- Pfaff, M. and P. Jurdic (2001). “Podosomes in osteoclast-like cells: structural analysis and cooperative roles of paxillin, proline-rich tyrosine kinase 2 (Pyk2) and integrin $\alpha v \beta 3$ ”. In: *Journal of cell science* 114.15, pp. 2775–2786 (cit. on pp. 44, 46, 48–50, 52, 56, 59, 69, 82, 83, 173).

- Pfeilschifter, J. and G. R. Mundy (1987). “Modulation of type beta transforming growth factor activity in bone cultures by osteotropic hormones”. In: *Proceedings of the National Academy of Sciences* 84.7, pp. 2024–2028 (cit. on p. 16).
- Pinto, V., P. Sousa, V. Cardoso, and G. Minas (2014). “Optimized SU-8 processing for low-cost microstructures fabrication without cleanroom facilities”. In: *Micromachines* 5.3, pp. 738–755 (cit. on p. 151).
- Plodinec, M., M. Loparic, and U. Aebi (2010). “Imaging fibroblast cells using atomic force microscopy (AFM).” In: *Cold Spring Harbor Protocols* 2010.10, pdb-prot5500 (cit. on p. 101).
- Plotnikov, S. V., A. M. Pasapera, B. Sabass, and C. M. Waterman (2012). “Force fluctuations within focal adhesions mediate ECM-rigidity sensing to guide directed cell migration”. In: *Cell* 151.7, pp. 1513–1527 (cit. on p. 105).
- Plotnikov, S. V., B. Sabass, U. S. Schwarz, and C. M. Waterman (2014). “High-resolution traction force microscopy”. In: *Methods in cell biology*. Vol. 123. Elsevier, pp. 367–394 (cit. on pp. 104, 105, 108).
- Plow, E. F., T. A. Haas, L. Zhang, J. Loftus, and J. W. Smith (2000). “Ligand binding to integrins”. In: *Journal of Biological Chemistry* 275.29, pp. 21785–21788 (cit. on p. 116).
- Poincloux, R., C. Vincent, A. Labrousse, J. Castandet, M. Rigo, C. Cougoule, C. Bordier, V. Le Cabec, and I. Maridonneau-Parini (2006). “Re-arrangements of podosome structures are observed when Hck is activated in myeloid cells”. In: *European journal of cell biology* 85.3-4, pp. 327–332 (cit. on p. 37).
- Ponta, H., L. Sherman, and P. A. Herrlich (2003). “CD44: from adhesion molecules to signalling regulators”. In: *Nature reviews Molecular cell biology* 4.1, p. 33 (cit. on p. 46).
- Proag, A., A. Bouissou, T. Mangeat, R. Voituriez, P. Delobelle, C. Thibault, C. Vieu, I. Maridonneau-Parini, and R. Poincloux (2015). “Working together: spatial synchrony in the force and actin dynamics of podosome first neighbors”. In: *ACS nano* 9.4, pp. 3800–3813 (cit. on pp. 23, 29, 31, 36, 73, 81, 109, 117, 156, 166, 174).
- Proag, A., A. Bouissou, C. Vieu, I. Maridonneau-Parini, and R. Poincloux (2016). “Evaluation of the force and spatial dynamics of macrophage podosomes by multi-particle tracking”. In: *Methods* 94, pp. 75–84 (cit. on pp. 26, 29, 31, 82, 117).
- Puig-De-Morales, M., M. Grabulosa, J. Alcaraz, J. Mullol, G. N. Maksym, J. J. Fredberg, and D. Navajas (2001). “Measurement of cell microrheology by magnetic twisting cytometry with frequency domain demodulation”. In: *Journal of Applied Physiology* 91.3, pp. 1152–1159 (cit. on p. 99).
- Pullarkat, P. A., P. A. Fernández, and A. Ott (2007). “Rheological properties of the eukaryotic cell cytoskeleton”. In: *Physics Reports* 449.1-3, pp. 29–53 (cit. on p. 100).
- Qian, T. and Y. Wang (2010). “Micro/nano-fabrication technologies for cell biology”. In: *Medical & biological engineering & computing* 48.10, pp. 1023–1032 (cit. on p. 148).
- Qin, D., Y. Xia, and G. M. Whitesides (2010). “Soft lithography for micro-and nanoscale patterning”. In: *Nature protocols* 5.3, p. 491 (cit. on p. 151).
- Radmacher, M., M. Fritz, C. M. Kacher, J. P. Cleveland, and P. K. Hansma (1996). “Measuring the viscoelastic properties of human platelets with the atomic force microscope”. In: *Biophysical journal* 70.1, pp. 556–567 (cit. on p. 101).
- Rafiq, N. B. M., Y. Nishimura, S. V. Plotnikov, V. Thiagarajan, Z. Zhang, S. Shi, M. Natarajan, V. Viasnoff, P. Kanchanawong, G. E. Jones, et al. (2019). “A mechano-signalling network linking microtubules, myosin IIA filaments and integrin-based adhesions”. In: *Nature materials* 18.6, p. 638 (cit. on p. 33).
- Raftopoulou, M. and A. Hall (2004). “Cell migration: Rho GTPases lead the way”. In: *Developmental biology* 265.1, pp. 23–32 (cit. on p. 53).

Bibliography

- Rape, A., W.-h. Guo, and Y.-l. Wang (2011). “Microtubule depolymerization induces traction force increase through two distinct pathways”. In: *J Cell Sci* 124.24, pp. 4233–4240 (cit. on p. 98).
- Raynaud-Messina, B., L. Bracq, M. Dupont, S. Souriant, S. M. Usmani, A. Proag, K. Pingris, V. Soldan, C. Thibault, F. Capilla, et al. (2018). “Bone degradation machinery of osteoclasts: An HIV-1 target that contributes to bone loss”. In: *Proceedings of the National Academy of Sciences* 115.11, E2556–E2565 (cit. on p. 18).
- Redick, S. D., D. L. Settles, G. Briscoe, and H. P. Erickson (2000). “Defining fibronectin’s cell adhesion synergy site by site-directed mutagenesis”. In: *The Journal of cell biology* 149.2, pp. 521–527 (cit. on p. 145).
- Reinholt, F. P., K. Hultenby, A. Oldberg, and D. Heinegård (1990). “Osteopontin—a possible anchor of osteoclasts to bone.” In: *Proceedings of the National Academy of Sciences of the United States of America* 87.12, p. 4473 (cit. on pp. 15, 44).
- Reneker, D. H. and A. L. Yarin (2008). “Electrospinning jets and polymer nanofibers”. In: *Polymer* 49.10, pp. 2387–2425 (cit. on p. 150).
- Rho, J. Y., R. B. Ashman, and C. H. Turner (1993). “Young’s modulus of trabecular and cortical bone material: ultrasonic and microtensile measurements”. In: *Journal of biomechanics* 26.2, pp. 111–119 (cit. on p. 8).
- Rho, J.-Y., L. Kuhn-Spearing, and P. Zioupos (1998). “Mechanical properties and the hierarchical structure of bone”. In: *Medical engineering & physics* 20.2, pp. 92–102 (cit. on p. 9).
- Ricca, B. L., G. Venugopalan, and D. A. Fletcher (2013). “To pull or be pulled: parsing the multiple modes of mechanotransduction”. In: *Current opinion in cell biology* 25.5, pp. 558–564 (cit. on p. 100).
- Riethmüller, C., T. E. Schäffer, F. Kienberger, W. Stracke, and H. Oberleithner (2007). “Vacuolar structures can be identified by AFM elasticity mapping”. In: *Ultramicroscopy* 107.10-11, pp. 895–901 (cit. on p. 101).
- Rinke, T. and C. Koch (2017). *Photolithography: Basics of Microstructuring*. MicroChemicals. ISBN: 9783981878219. URL: <https://books.google.fr/books?id=mcG5tAEACAAJ> (cit. on p. 170).
- Rio, A. del, R. Perez-Jimenez, R. Liu, P. Roca-Cusachs, J. M. Fernandez, and M. P. Sheetz (2009). “Stretching single talin rod molecules activates vinculin binding”. In: *Science* 323.5914, pp. 638–641 (cit. on p. 99).
- Roca-Cusachs, P., V. Conte, and X. Trepat (2017). “Quantifying forces in cell biology”. In: *Nature cell biology* 19.7, p. 742 (cit. on p. 101).
- Rotsch, C. and M. Radmacher (2000). “Drug-induced changes of cytoskeletal structure and mechanics in fibroblasts: an atomic force microscopy study”. In: *Biophysical journal* 78.1, pp. 520–535 (cit. on p. 101).
- Rozario, T. and D. W. DeSimone (2010). “The extracellular matrix in development and morphogenesis: a dynamic view”. In: *Developmental biology* 341.1, pp. 126–140 (cit. on pp. 92, 94).
- Ruckstuhl, T., J. Enderlein, S. Jung, and S. Seeger (2000). “Forbidden light detection from single molecules”. In: *Analytical chemistry* 72.9, pp. 2117–2123 (cit. on p. 118).
- Ruckstuhl, T., M. Rankl, and S. Seeger (2003). “Highly sensitive biosensing using a supercritical angle fluorescence (SAF) instrument”. In: *Biosensors and Bioelectronics* 18.9, pp. 1193–1199 (cit. on p. 119).
- Ruiz, S. A. and C. S. Chen (2007). “Microcontact printing: A tool to pattern”. In: *Soft Matter* 3.2, pp. 168–177 (cit. on p. 150).
- Rumpler, M., T. Würger, P. Roschger, E. Zwettler, I. Sturmlechner, P. Altmann, P. Fratzl, M. Rogers, and K. Klaushofer (2013). “Osteoclasts on bone and dentin in vitro: mechanism of trail formation and comparison of resorption behavior”. In: *Calcified tissue international* 93.6, pp. 526–539 (cit. on pp. 22, 62).

- Rust, M. J., M. Bates, and X. Zhuang (2006). “Stochastic optical reconstruction microscopy (STORM) provides sub-diffraction-limit image resolution”. In: *Nature methods* 3.10, p. 793 (cit. on p. 112).
- Sabass, B., M. L. Gardel, C. M. Waterman, and U. S. Schwarz (2008). “High resolution traction force microscopy based on experimental and computational advances”. In: *Biophysical journal* 94.1, pp. 207–220 (cit. on pp. 105, 107, 108).
- Saez, A., A. Buguin, P. Silberzan, and B. Ladoux (2005). “Is the mechanical activity of epithelial cells controlled by deformations or forces?” In: *Biophysical journal* 89.6, pp. L52–L54 (cit. on p. 152).
- Sahu, S. N., M. A. Khadeer, B. W. Robertson, S. M. Núñez, G. Bai, and A. Gupta (2007). “Association of leupaxin with Src in osteoclasts”. In: *American Journal of Physiology-Cell Physiology* 292.1, pp. C581–C590 (cit. on p. 55).
- Saltel, F., A. Chabadel, E. Bonnelye, and P. Jurdic (2008). “Actin cytoskeletal organisation in osteoclasts: a model to decipher transmigration and matrix degradation”. In: *European journal of cell biology* 87.8-9, pp. 459–468 (cit. on pp. 22, 37, 49, 52, 55, 62, 63, 69).
- Saltel, F., A. Chabadel, Y. Zhao, M.-H. Lafage-Proust, P. Clézardin, P. Jurdic, and E. Bonnelye (2006). “Transmigration: a new property of mature multinucleated osteoclasts”. In: *Journal of bone and mineral research* 21.12, pp. 1913–1923 (cit. on p. 62).
- Saltel, F., O. Destaing, F. Bard, D. Eichert, and P. Jurdic (2004). “Apatite-mediated actin dynamics in resorbing osteoclasts”. In: *Molecular biology of the cell* 15.12, pp. 5231–5241 (cit. on pp. 54, 59, 63, 64, 69).
- Samanna, V., T. Ma, T. Mak, M. Rogers, and M. Chellaiah (2007). “Actin polymerization modulates CD44 surface expression, MMP-9 activation, and osteoclast function”. In: *Journal of cellular physiology* 213.3, pp. 710–720 (cit. on pp. 46, 60).
- Samori, B., G. Siligardi, C. Quagliariello, A. L. Weisenhorn, J. Vesenska, and C. J. Bustamante (1993). “Chirality of DNA supercoiling assigned by scanning force microscopy.” In: *Proceedings of the National Academy of Sciences* 90.8, pp. 3598–3601 (cit. on p. 101).
- Sanchez-Fernandez, M. A., A. Gallois, T. Riedl, P. Jurdic, and B. Hoflack (2008). “Osteoclasts control osteoblast chemotaxis via PDGF-BB/PDGF receptor beta signaling”. In: *PLoS one* 3.10, e3537 (cit. on p. 12).
- Santos, A., A. D. Bakker, and J. Klein-Nulend (2009). “The role of osteocytes in bone mechanotransduction”. In: *Osteoporosis international* 20.6, pp. 1027–1031 (cit. on p. 12).
- Sanz-Moreno, V., G. Gadea, J. Ahn, H. Paterson, P. Marra, S. Pinner, E. Sahai, and C. J. Marshall (2008). “Rac activation and inactivation control plasticity of tumor cell movement”. In: *Cell* 135.3, pp. 510–523 (cit. on p. 153).
- Sato, M., M. Sardana, W. Grasser, V. Garsky, J. Murray, and R. Gould (1990). “Echistatin is a potent inhibitor of bone resorption in culture.” In: *The Journal of Cell Biology* 111.4, pp. 1713–1723 (cit. on p. 44).
- Schachtner, H., S. D. Calaminus, S. G. Thomas, and L. M. Machesky (2013). “Podosomes in adhesion, migration, mechanosensing and matrix remodeling”. In: *Cytoskeleton* 70.10, pp. 572–589 (cit. on pp. 26, 28).
- Schaefer, L. and R. M. Schaefer (2010). “Proteoglycans: from structural compounds to signaling molecules”. In: *Cell and tissue research* 339.1, p. 237 (cit. on p. 94).
- Schenk, R. K., D. Spiro, and J. Wiener (1967). “Cartilage resorption in the tibial epiphyseal plate of growing rats”. In: *The Journal of cell biology* 34.1, pp. 275–291 (cit. on p. 39).

- Schermelleh, L., A. Ferrand, T. Huser, C. Eggeling, M. Sauer, O. Biehlmaier, and G. P. Drummen (2019). “Super-resolution microscopy demystified”. In: *Nature cell biology* 21.1, p. 72 (cit. on pp. 110, 115).
- Schett, G. and E. Gravallesse (2012). “Bone erosion in rheumatoid arthritis: mechanisms, diagnosis and treatment”. In: *Nature Reviews Rheumatology* 8.11, p. 656 (cit. on pp. 17, 18).
- Schmidt, S., I. Nakchbandi, R. Ruppert, N. Kawelke, M. W. Hess, K. Pfaller, P. Jurdic, R. Fässler, and M. Moser (2011). “Kindlin-3-mediated signaling from multiple integrin classes is required for osteoclast-mediated bone resorption”. In: *The Journal of cell biology* 192.5, pp. 883–897 (cit. on p. 46).
- Schneider, S. W., P. Pagel, C. Rotsch, T. Danker, H. Oberleithner, M. Radmacher, and A. Schwab (2000). “Volume dynamics in migrating epithelial cells measured with atomic force microscopy”. In: *Pflügers Archiv* 439.3, pp. 297–303 (cit. on p. 101).
- Schoen, I., W. Hu, E. Klotzsch, and V. Vogel (2010). “Probing cellular traction forces by micropillar arrays: contribution of substrate warping to pillar deflection”. In: *Nano letters* 10.5, pp. 1823–1830 (cit. on p. 98).
- Schoenenberger, C.-A. and J. H. Hoh (1994). “Slow cellular dynamics in MDCK and R5 cells monitored by time-lapse atomic force microscopy”. In: *Biophysical journal* 67.2, pp. 929–936 (cit. on p. 101).
- Seals, D. F., E. F. Azucena Jr, I. Pass, L. Tesfay, R. Gordon, M. Woodrow, J. H. Resau, and S. A. Courtneidge (2005). “The adaptor protein Tks5/Fish is required for podosome formation and function, and for the protease-driven invasion of cancer cells”. In: *Cancer cell* 7.2, pp. 155–165 (cit. on p. 25).
- Shaikh Mohammed, J., M. A. DeCoster, and M. J. McShane (2006). “Fabrication of interdigitated micropatterns of self-assembled polymer nanofilms containing cell-adhesive materials”. In: *Langmuir* 22.6, pp. 2738–2746 (cit. on p. 151).
- Shamloo, A. and S. C. Heilshorn (2010). “Matrix density mediates polarization and lumen formation of endothelial sprouts in VEGF gradients”. In: *Lab on a Chip* 10.22, pp. 3061–3068 (cit. on p. 94).
- Shamloo, A., N. Mohammadaliha, S. C. Heilshorn, and A. L. Bauer (2016). “A comparative study of collagen matrix density effect on endothelial sprout formation using experimental and computational approaches”. In: *Annals of biomedical engineering* 44.4, pp. 929–941 (cit. on p. 94).
- Sharonov, A. and R. M. Hochstrasser (2006). “Wide-field subdiffraction imaging by accumulated binding of diffusing probes”. In: *Proceedings of the National Academy of Sciences* 103.50, pp. 18911–18916 (cit. on p. 112).
- Shemesh, M., L. Addadi, and B. Geiger (2017). “Surface microtopography modulates sealing zone development in osteoclasts cultured on bone”. In: *Journal of The Royal Society Interface* 14.127, p. 20160958 (cit. on pp. 59, 60, 64, 66, 172, 174).
- Shemesh, M., S. Addadi, Y. Milstein, B. Geiger, and L. Addadi (2015). “Study of osteoclast adhesion to cortical bone surfaces: a correlative microscopy approach for concomitant imaging of cellular dynamics and surface modifications”. In: *ACS applied materials & interfaces* 8.24, pp. 14932–14943 (cit. on pp. 59, 66, 174).
- Shevde, N. K., L. A. Plum, M. Clagett-Dame, H. Yamamoto, J. W. Pike, and H. F. DeLuca (2002). “A potent analog of $1\alpha, 25$ -dihydroxyvitamin D3 selectively induces bone formation”. In: *Proceedings of the National Academy of Sciences* 99.21, pp. 13487–13491 (cit. on p. 16).
- Shtengel, G., J. A. Galbraith, C. G. Galbraith, J. Lippincott-Schwartz, J. M. Gillette, S. Manley, R. Sougrat, C. M. Waterman, P. Kanchanawong, M. W. Davidson, et al. (2009). “Interferometric fluorescent super-resolution microscopy resolves 3D cellular ultrastructure”. In: *Proceedings of the National Academy of Sciences* 106.9, pp. 3125–3130 (cit. on p. 114).

- Shyu, J.-F., C. Shih, C.-Y. Tseng, C.-H. Lin, D.-T. Sun, H.-T. Liu, H.-C. Tsung, T.-H. Chen, and R.-B. Lu (2007). “Calcitonin induces podosome disassembly and detachment of osteoclasts by modulating Pyk2 and Src activities”. In: *Bone* 40.5, pp. 1329–1342 (cit. on pp. 59, 62).
- Siddiqui, J. A. and N. C. Partridge (2016). “Physiological bone remodeling: systemic regulation and growth factor involvement”. In: *Physiology* 31.3, pp. 233–245 (cit. on p. 16).
- Silva, J. M., A. R. C. Duarte, S. G. Caridade, C. Picart, R. L. Reis, and J. F. Mano (2014). “Tailored free-standing multilayered membranes based on chitosan and alginate”. In: *Biomacromolecules* 15.10, pp. 3817–3826 (cit. on p. 149).
- Sims, N. A. and T. J. Martin (2014). “Coupling the activities of bone formation and resorption: a multitude of signals within the basic multicellular unit”. In: *BoneKey reports* 3 (cit. on pp. 12, 21).
- Sivankutty, S., I. C. Hernández, N. Bourg, G. Dupuis, and S. Lévêque-Fort (2019). “Supercritical angle fluorescence for enhanced axial sectioning in STED microscopy”. In: *Methods* (cit. on pp. 144, 172).
- Sly, W. S., M. P. Whyte, V. Sundaram, R. E. Tashian, D. Hewett-Emmett, P. Guibaud, M. Vainsel, H. J. Baluarte, A. Gruskin, M. Al-Mosawi, et al. (1985). “Carbonic anhydrase II deficiency in 12 families with the autosomal recessive syndrome of osteopetrosis with renal tubular acidosis and cerebral calcification”. In: *New England Journal of Medicine* 313.3, pp. 139–145 (cit. on p. 19).
- Smith, M. L., D. Gourdon, W. C. Little, K. E. Kubow, R. A. Eguiluz, S. Luna-Morris, and V. Vogel (2007). “Force-induced unfolding of fibronectin in the extracellular matrix of living cells”. In: *PLoS biology* 5.10, e268 (cit. on p. 95).
- Søe, K. and J.-M. Delaissé (2017). “Time-lapse reveals that osteoclasts can move across the bone surface while resorbing”. In: *J Cell Sci* 130.12, pp. 2026–2035 (cit. on pp. 22, 62, 64).
- Song, M.-K., Z. H. Lee, and H.-H. Kim (2015). “Adseverin mediates RANKL-induced osteoclastogenesis by regulating NFATc1”. In: *Experimental & molecular medicine* 47.12, e199 (cit. on p. 49).
- Soriano, P., C. Montgomery, R. Geske, and A. Bradley (1991). “Targeted disruption of the c-src proto-oncogene leads to osteopetrosis in mice”. In: *Cell* 64.4, pp. 693–702 (cit. on p. 55).
- Sousa, M. P., E. Arab-Tehrany, F. Cleymand, and J. F. Mano (2019). “Surface Micro-and Nanoengineering: Applications of Layer-by-Layer Technology as a Versatile Tool to Control Cellular Behavior”. In: *Small*, p. 1901228 (cit. on pp. 148, 149).
- Sousa, M. P., S. G. Caridade, and J. F. Mano (2017). “Control of Cell Alignment and Morphology by Redesigning ECM-Mimetic Nanotopography on Multilayer Membranes”. In: *Advanced healthcare materials* 6.15, p. 1601462 (cit. on p. 150).
- Soysa, N. S. and N. Alles (2016). “Osteoclast function and bone-resorbing activity: an overview”. In: *Biochemical and biophysical research communications* 476.3, pp. 115–120 (cit. on pp. 20, 47, 53, 68).
- Sprangers, S. and V. Everts (2017). “Molecular pathways of cell-mediated degradation of fibrillar collagen”. In: *Matrix Biology* (cit. on p. 15).
- Srinivasan, S., F. Wang, S. Glavas, A. Ott, F. Hofmann, K. Aktories, D. Kalman, and H. R. Bourne (2003). “Rac and Cdc42 play distinct roles in regulating PI (3, 4, 5) P3 and polarity during neutrophil chemotaxis”. In: *J Cell Biol* 160.3, pp. 375–385 (cit. on p. 153).
- Staszowska, A. D., P. Fox-Roberts, E. Foxall, G. E. Jones, and S. Cox (2017). “Investigation of podosome ring protein arrangement using localization microscopy images”. In: *Methods* 115, pp. 9–16 (cit. on p. 23).
- Steenblock, C., T. Heckel, C. Czupalla, A. I. E. Santo, C. Niehage, M. Sztacho, and B. Hoflack (2014). “The Cdc42 guanine nucleotide exchange factor FGD6 coordinates cell polarity and endosomal membrane recycling in osteoclasts”. In: *Journal of Biological Chemistry* 289.26, pp. 18347–18359 (cit. on pp. 52, 55).

- Stellwagen, N. C. (1998). “Apparent pore size of polyacrylamide gels: Comparison of gels cast and run in Tris-acetate-EDTA and Tris-borate-EDTA buffers”. In: *Electrophoresis* 19.10, pp. 1542–1547 (cit. on p. 122).
- Stricker, J., Y. Aratyn-Schaus, P. W. Oakes, and M. L. Gardel (2011). “Spatiotemporal constraints on the force-dependent growth of focal adhesions”. In: *Biophysical journal* 100.12, pp. 2883–2893 (cit. on pp. 97, 98).
- Stricker, J., B. Sabass, U. S. Schwarz, and M. L. Gardel (2010). “Optimization of traction force microscopy for micron-sized focal adhesions”. In: *Journal of Physics: Condensed Matter* 22.19, p. 194104 (cit. on p. 97).
- Style, R. W., R. Boltynskiy, G. K. German, C. Hyland, C. W. MacMinn, A. F. Mertz, L. A. Wilen, Y. Xu, and E. R. Dufresne (2014). “Traction force microscopy in physics and biology”. In: *Soft matter* 10.23, pp. 4047–4055 (cit. on pp. 102, 103, 108).
- Sundararajan, S. and B. Bhushan (2002a). “Development of AFM-based techniques to measure mechanical properties of nanoscale structures”. In: *Sensors and actuators A: Physical* 101.3, pp. 338–351 (cit. on p. 144).
- Sundararajan, S., B. Bhushan, T. Namazu, and Y. Isono (2002b). “Mechanical property measurements of nanoscale structures using an atomic force microscope”. In: *Ultramicroscopy* 91.1-4, pp. 111–118 (cit. on p. 144).
- Syed Asif, S., K. Wahl, R. Colton, and O. Warren (2001). “Quantitative imaging of nanoscale mechanical properties using hybrid nanoindentation and force modulation”. In: *Journal of Applied Physics* 90.3, pp. 1192–1200 (cit. on p. 144).
- Szabó, B., D. Selmeczi, Z. Környei, E. Madarász, and N. Rozlosnik (2002). “Atomic force microscopy of height fluctuations of fibroblast cells”. In: *Physical Review E* 65.4, p. 041910 (cit. on p. 101).
- Szewczyk, K. A., K. Fuller, and T. J. Chambers (2013). “Distinctive subdomains in the resorbing surface of osteoclasts”. In: *PLoS One* 8.3, e60285 (cit. on p. 38).
- Szymkiewicz, I., O. Destaing, P. Jurdic, and I. Dikic (2004). “SH3P2 in complex with Cbl and Src”. In: *FEBS letters* 565.1-3, pp. 33–38 (cit. on pp. 55, 173).
- Takahashi, N., N. Udagawa, S. Tanaka, H. Murakami, I. Owan, T. Tamura, and T. Suda (1994). “Postmitotic osteoclast precursors are mononuclear cells which express macrophage-associated phenotypes”. In: *Developmental biology* 163.1, pp. 212–221 (cit. on p. 45).
- Takigawa, T., Y. Morino, K. Urayama, and T. Masuda (1996). “Poisson’s ratio of polyacrylamide (PAAm) gels”. In: *Polymer Gels and Networks* 4.1, pp. 1–5 (cit. on p. 109).
- Tan, J., H. Shen, and W. M. Saltzman (2001). “Micron-scale positioning of features influences the rate of polymorphonuclear leukocyte migration”. In: *Biophysical Journal* 81.5, pp. 2569–2579 (cit. on p. 156).
- Tan, J. L., J. Tien, D. M. Pirone, D. S. Gray, K. Bhadriraju, and C. S. Chen (2003). “Cells lying on a bed of microneedles: an approach to isolate mechanical force”. In: *Proceedings of the National Academy of Sciences* 100.4, pp. 1484–1489 (cit. on pp. 98, 152).
- Tanaka-Kamioka, K., H. Kamioka, H. Ris, and S.-S. Lim (1998). “Osteocyte shape is dependent on actin filaments and osteocyte processes are unique actin-rich projections”. In: *Journal of Bone and Mineral Research* 13.10, pp. 1555–1568 (cit. on p. 12).
- Tanaka, S., M. Amling, L. Neff, A. Peyman, E. Uhlmann, J. B. Levy, and R. Baron (1996). “c-Cbl is downstream of c-Src in a signalling pathway necessary for bone resorption”. In: *Nature* 383.6600, p. 528 (cit. on p. 55).

- Tanaka, S., N. Takahashi, N. Udagawa, T. Sasaki, Y. Fukui, T. Kurokawa, and T. Suda (1992). “Osteoclasts express high levels of p60c-src, preferentially on ruffled border membranes”. In: *FEBS letters* 313.1, pp. 85–89 (cit. on p. 55).
- Tanner, K., A. Boudreau, M. J. Bissell, and S. Kumar (2010). “Dissecting regional variations in stress fiber mechanics in living cells with laser nanosurgery”. In: *Biophysical journal* 99.9, pp. 2775–2783 (cit. on p. 100).
- Tcherkezian, J. and N. Lamarche-Vane (2007). “Current knowledge of the large RhoGAP family of proteins”. In: *Biology of the Cell* 99.2, pp. 67–86 (cit. on p. 54).
- Tehrani, S., R. Faccio, I. Chandrasekar, F. P. Ross, and J. A. Cooper (2006). “Cortactin has an essential and specific role in osteoclast actin assembly”. In: *Molecular biology of the cell* 17.7, pp. 2882–2895 (cit. on pp. 50, 51, 56, 58, 69, 82).
- Teitelbaum, S. L. (2007). “Osteoclasts: what do they do and how do they do it?” In: *The American journal of pathology* 170.2, pp. 427–435 (cit. on p. 68).
- (2011). “The osteoclast and its unique cytoskeleton”. In: *Annals of the New York Academy of Sciences* 1240.1, pp. 14–17 (cit. on p. 19).
- Teitelbaum, S. L., M. M. Tondravi, and F. P. Ross (1997). “Osteoclasts, macrophages, and the molecular mechanisms of bone resorption”. In: *Journal of leukocyte biology* 61.4, pp. 381–388 (cit. on p. 45).
- Teti, A., M. Grano, A. Carano, S. Colucci, and A. Z. Zamboni (1989). “Immunolocalization of β 3 subunit of integrins in osteoclast membrane.” In: *Bollettino della Societa italiana di biologia sperimentale* 65.11, pp. 1031–1037 (cit. on pp. 44, 49).
- Teti, A., P. C. Marchisio, and A. Z. Zallone (1991). “Clear zone in osteoclast function: role of podosomes in regulation of bone-resorbing activity”. In: *American Journal of Physiology-Cell Physiology* 261.1, pp. C1–C7 (cit. on pp. 19, 39, 49, 68).
- Tezuka, K.-i., S. Takeshita, Y. Hakeda, M. Kumegawa, R. Kikuno, and T. Hashimoto-Gotoh (1990). “Isolation of mouse and human cDNA clones encoding a protein expressed specifically in osteoblasts and brain tissues”. In: *Biochemical and biophysical research communications* 173.1, pp. 246–251 (cit. on p. 12).
- Théry, M. and M. Piel (2009). “Adhesive micropatterns for cells: a microcontact printing protocol”. In: *Cold Spring Harbor Protocols* 2009.7, pdb-prot5255 (cit. on p. 98).
- Tolic-Nørrelykke, I. M., J. P. Butler, J. Chen, and N. Wang (2002). “Spatial and temporal traction response in human airway smooth muscle cells”. In: *American Journal of Physiology-Cell Physiology* 283.4, pp. C1254–C1266 (cit. on p. 103).
- Touaitahuata, H., A. Morel, S. Urbach, J. Mateos-Langerak, S. de Rossi, and A. Blangy (2016). “Tensin 3 is a new partner of Dock5 that controls osteoclast podosome organization and activity”. In: *J Cell Sci* 129.18, pp. 3449–3461 (cit. on pp. 48, 49, 55, 66).
- Touaitahuata, H., E. Planus, C. Albiges-Rizo, A. Blangy, and G. Pawlak (2013). “Podosomes are dispensable for osteoclast differentiation and migration”. In: *European journal of cell biology* 92.4-5, pp. 139–149 (cit. on p. 61).
- Toyjanova, J., E. Bar-Kochba, C. López-Fagundo, J. Reichner, D. Hoffman-Kim, and C. Franck (2014a). “High resolution, large deformation 3D traction force microscopy”. In: *PloS one* 9.4, e90976 (cit. on p. 107).
- Toyjanova, J., E. Hannen, E. Bar-Kochba, E. M. Darling, D. L. Henann, and C. Franck (2014b). “3D Viscoelastic traction force microscopy”. In: *Soft matter* 10.40, pp. 8095–8106 (cit. on p. 109).

- Tran, K. T. and T. D. Nguyen (2017). “Lithography-based methods to manufacture biomaterials at small scales”. In: *Journal of Science: Advanced Materials and Devices* 2.1, pp. 1–14 (cit. on p. 151).
- Trepap, X., M. R. Wasserman, T. E. Angelini, E. Millet, D. A. Weitz, J. P. Butler, and J. J. Fredberg (2009). “Physical forces during collective cell migration”. In: *Nature physics* 5.6, p. 426 (cit. on p. 102).
- Trujillo, N. J., S. H. Baxamusa, and K. K. Gleason (2009). “Grafted functional polymer nanostructures patterned bottom-up by colloidal lithography and initiated chemical vapor deposition (iCVD)”. In: *Chemistry of Materials* 21.4, pp. 742–750 (cit. on p. 150).
- Tse, J. R. and A. J. Engler (2010). “Preparation of hydrogel substrates with tunable mechanical properties”. In: *Current protocols in cell biology* 47.1, pp. 10–16 (cit. on pp. 120, 121).
- Vaananen, H., H. Zhao, M. Mulari, and J. M. Halleen (2000). “The cell biology of osteoclast function”. In: *J Cell Sci* 113.3, pp. 377–381 (cit. on p. 19).
- Van Audenhove, I., N. Debeuf, C. Boucherie, and J. Gettemans (2015). “Fascin actin bundling controls podosome turnover and disassembly while cortactin is involved in podosome assembly by its SH3 domain in THP-1 macrophages and dendritic cells”. In: *Biochimica et Biophysica Acta (BBA)-Molecular Cell Research* 1853.5, pp. 940–952 (cit. on p. 27).
- Van de Linde, S., A. Löschberger, T. Klein, M. Heidbreder, S. Wolter, M. Heilemann, and M. Sauer (2011). “Direct stochastic optical reconstruction microscopy with standard fluorescent probes”. In: *Nature protocols* 6.7, p. 991 (cit. on p. 112).
- Van den Dries, K., L. Nahidiazar, J. A. Slotman, M. B. Meddens, E. Pandzic, B. Joosten, M. Ansems, J. Schouwstra, A. Meijer, and R. Steen (2019). “Modular actin nano-architecture enables podosome protrusion and mechanosensing”. In: *bioRxiv*, p. 583492 (cit. on pp. 26, 32, 75, 83).
- Van den Dries, K., M. Meddens, S. De Keijzer, S. Shekhar, V. Subramaniam, C. G. Figdor, and A. Cambi (2013a). “Interplay between myosin IIA-mediated contractility and actin network integrity orchestrates podosome composition and oscillations”. In: *Nature communications* 4, p. 1412 (cit. on pp. 26, 31, 34, 36).
- Van den Dries, K., S. Schwartz, J. Byars, M. Meddens, M. Bolomini-Vittori, D. Lidke, C. Figdor, K. Lidke, and A. Cambi (2013b). “Dual-color superresolution microscopy reveals nanoscale organization of mechanosensory podosomes”. In: *Molecular biology of the cell* 24.13, pp. 2112–2123 (cit. on pp. 25, 26, 49, 155).
- Van den Dries, K., S. F. van Helden, J. Te Riet, R. Diez-Ahedo, C. Manzo, M. M. Oud, F. N. van Leeuwen, R. Brock, M. F. Garcia-Parajo, A. Cambi, et al. (2012). “Geometry sensing by dendritic cells dictates spatial organization and PGE 2-induced dissolution of podosomes”. In: *Cellular and molecular life sciences* 69.11, pp. 1889–1901 (cit. on pp. 34, 154, 155, 170, 171).
- Van der Flier, A. and A. Sonnenberg (2001). “Function and interactions of integrins”. In: *Cell and tissue research* 305.3, pp. 285–298 (cit. on p. 116).
- Van der Pluijm, G., H. Mouthaan, C. Baas, H. de Groot, S. Papapoulos, and C. Löwik (1994). “Integrins and osteoclastic resorption in three bone organ cultures: differential sensitivity to synthetic Arg-Gly-Asp peptides during osteoclast formation”. In: *Journal of Bone and Mineral Research* 9.7, pp. 1021–1028 (cit. on p. 44).
- Van Goethem, E., R. Guiet, S. Balor, G. M. Charrière, R. Poincloux, A. Labrousse, I. Maridonneau-Parini, and V. Le Cabec (2011). “Macrophage podosomes go 3D”. In: *European journal of cell biology* 90.2-3, pp. 224–236 (cit. on p. 27).
- Van Goethem, E., R. Poincloux, F. Gauffre, I. Maridonneau-Parini, and V. Le Cabec (2010). “Matrix architecture dictates three-dimensional migration modes of human macrophages: differential involvement

Bibliography

- of proteases and podosome-like structures”. In: *The journal of immunology* 184.2, pp. 1049–1061 (cit. on pp. 83, 94, 159).
- Van Helden, S. F., M. M. Oud, B. Joosten, N. Peterse, C. G. Figdor, and F. N. van Leeuwen (2008). “PGE2-mediated podosome loss in dendritic cells is dependent on actomyosin contraction downstream of the RhoA–Rho-kinase axis”. In: *Journal of cell science* 121.7, pp. 1096–1106 (cit. on p. 32).
- Van Rietbergen, B., A. Odgaard, J. Kabel, and R. Huiskes (1996). “Direct mechanics assessment of elastic symmetries and properties of trabecular bone architecture”. In: *Journal of biomechanics* 29.12, pp. 1653–1657 (cit. on p. 8).
- VanWinkle, B. W., M. Snuggs, and M. L. Buja (1995). “Hypoxia-induced alterations in cytoskeleton coincide with collagenase expression in cultured neonatal rat cardiomyocytes”. In: *Journal of molecular and cellular cardiology* 27.12, pp. 2531–2542 (cit. on p. 34).
- Veigel, C. and C. F. Schmidt (2011). “Moving into the cell: single-molecule studies of molecular motors in complex environments”. In: *Nature Reviews Molecular Cell Biology* 12.3, p. 163 (cit. on p. 99).
- Velve-Casquillas, G., M. Le Berre, M. Piel, and P. T. Tran (2010). “Microfluidic tools for cell biological research”. In: *Nano today* 5.1, pp. 28–47 (cit. on pp. 150, 151).
- Vives, V., G. Cres, C. Richard, M. Busson, Y. Ferrandez, A.-G. Planson, M. Zeghouf, J. Cherfils, L. Malaval, and A. Blangy (2015). “Pharmacological inhibition of Dock5 prevents osteolysis by affecting osteoclast podosome organization while preserving bone formation”. In: *Nature communications* 6, p. 6218 (cit. on p. 55).
- Wacker, B. K., S. K. Alford, E. A. Scott, M. D. Thakur, G. D. Longmore, and D. L. Elbert (2008). “Endothelial cell migration on RGD-peptide-containing PEG hydrogels in the presence of sphingosine 1-phosphate”. In: *Biophysical journal* 94.1, pp. 273–285 (cit. on p. 95).
- Wagenseil, J. E. and R. P. Mecham (2009). “Vascular extracellular matrix and arterial mechanics”. In: *Physiological reviews* 89.3, pp. 957–989 (cit. on p. 147).
- Walde, M., J. Monypenny, R. Heintzmann, G. E. Jones, and S. Cox (2014). “Vinculin binding angle in podosomes revealed by high resolution microscopy”. In: *PloS one* 9.2, e88251 (cit. on pp. 25, 171).
- Wang, Y.-L. and R. J. Pelham Jr (1998). “[39] Preparation of a flexible, porous polyacrylamide substrate for mechanical studies of cultured cells”. In: *Methods in enzymology*. Vol. 298. Elsevier, pp. 489–496 (cit. on p. 115).
- Wang, L., D. Mondal, V. F. La Russa, and K. C. Agrawal (2002). “Suppression of clonogenic potential of human bone marrow mesenchymal stem cells by HIV type 1: putative role of HIV type 1 tat protein and inflammatory cytokines”. In: *AIDS research and human retroviruses* 18.13, pp. 917–931 (cit. on p. 17).
- Wang, Y., D. Lebowitz, C. Sun, H. Thang, M. D. Grynblas, and M. Glogauer (2008). “Identifying the relative contributions of Rac1 and Rac2 to osteoclastogenesis”. In: *Journal of Bone and Mineral Research* 23.2, pp. 260–270 (cit. on p. 54).
- Weaver, A. M., J. E. Heuser, A. V. Karginov, W.-l. Lee, J. T. Parsons, and J. A. Cooper (2002). “Interaction of cortactin and N-WASp with Arp2/3 complex”. In: *Current Biology* 12.15, pp. 1270–1278 (cit. on p. 24).
- Weaver, A. M., A. V. Karginov, A. W. Kinley, S. A. Weed, Y. Li, J. T. Parsons, and J. A. Cooper (2001). “Cortactin promotes and stabilizes Arp2/3-induced actin filament network formation”. In: *Current Biology* 11.5, pp. 370–374 (cit. on p. 24).
- Weed, S. A. and J. T. Parsons (2001). “Cortactin: coupling membrane dynamics to cortical actin assembly”. In: *Oncogene* 20.44, p. 6418 (cit. on p. 24).

- Wei, M.-T., A. Zaorski, H. C. Yalcin, J. Wang, M. Hallow, S. N. Ghadiali, A. Chiou, and H. D. Ou-Yang (2008). “A comparative study of living cell micromechanical properties by oscillatory optical tweezers”. In: *Optics express* 16.12, pp. 8594–8603 (cit. on p. 99).
- Weiner, S. and W. Traub (1992). “Bone structure: from angstroms to microns.” In: *The FASEB journal* 6.3, pp. 879–885 (cit. on p. 8).
- Weiss, N. and A. Silberberg (1977). “Inhomogeneity of polyacrylamide gel structure from permeability and viscoelasticity”. In: *British Polymer Journal* 9.2, pp. 144–150 (cit. on p. 109).
- Wheater, P. R. (2006). *Wheater’s functional histology: a text and colour atlas*. Churchill Livingstone, p. 192 (cit. on pp. 9, 14).
- Wiesner, C., J. Faix, M. Himmel, F. Bentzien, and S. Linder (2010). “KIF5B and KIF3A/KIF3B kinesins drive MT1-MMP surface exposure, CD44 shedding, and extracellular matrix degradation in primary macrophages”. In: *Blood* 116.9, pp. 1559–1569 (cit. on pp. 23, 33).
- Wise, S. G. and A. S. Weiss (2009). “Tropoelastin”. In: *The international journal of biochemistry & cell biology* 41.3, pp. 494–497 (cit. on p. 94).
- Wittenburg, G., G. Lauer, S. Oswald, D. Labudde, and C. M. Franz (2014). “Nanoscale topographic changes on sterilized glass surfaces affect cell adhesion and spreading”. In: *Journal of Biomedical Materials Research Part A* 102.8, pp. 2755–2766 (cit. on p. 154).
- Wójciak-Stothard, B., A. Curtis, W. Monaghan, K. Macdonald, and C. Wilkinson (1996). “Guidance and activation of murine macrophages by nanometric scale topography”. In: *Experimental cell research* 223.2, pp. 426–435 (cit. on p. 154).
- Wolf, K., M. Te Lindert, M. Krause, S. Alexander, J. Te Riet, A. L. Willis, R. M. Hoffman, C. G. Figdor, S. J. Weiss, and P. Friedl (2013). “Physical limits of cell migration: control by ECM space and nuclear deformation and tuning by proteolysis and traction force”. In: *J Cell Biol* 201.7, pp. 1069–1084 (cit. on p. 153).
- Wolff, J. (1892). “Das gesetz der transformation der knochen”. In: *A Hirshwald* 1, pp. 1–152 (cit. on p. 8).
- Wood, J. A., N. M. Shah, C. T. McKee, M. L. Hughbanks, S. J. Liliensiek, P. Russell, and C. J. Murphy (2011). “The role of substratum compliance of hydrogels on vascular endothelial cell behavior”. In: *Biomaterials* 32.22, pp. 5056–5064 (cit. on p. 92).
- Xiao, G., H. Cheng, H. Cao, K. Chen, Y. Tu, S. Yu, H. Jiao, S. Yang, H.-J. Im, D. Chen, et al. (2012). “Critical role of filamin-binding LIM protein 1 (FBLP-1)/migfilin in regulation of bone remodeling”. In: *Journal of Biological Chemistry* 287.25, pp. 21450–21460 (cit. on p. 52).
- Xiao, T., J. Takagi, B. S. Collier, J.-H. Wang, and T. A. Springer (2004). “Structural basis for allostery in integrins and binding to fibrinogen-mimetic therapeutics”. In: *Nature* 432.7013, p. 59 (cit. on p. 116).
- Xie, J., X. Li, J. Lipner, C. N. Manning, A. G. Schwartz, S. Thomopoulos, and Y. Xia (2010). ““Aligned-to-random” nanofiber scaffolds for mimicking the structure of the tendon-to-bone insertion site”. In: *Nanoscale* 2.6, pp. 923–926 (cit. on p. 150).
- Xiong, J.-P., T. Stehle, R. Zhang, A. Joachimiak, M. Frech, S. L. Goodman, and M. A. Arnaout (2002). “Crystal structure of the extracellular segment of integrin $\alpha V\beta 3$ in complex with an Arg-Gly-Asp ligand”. In: *Science* 296.5565, pp. 151–155 (cit. on p. 116).
- Xiong, J., M. Onal, R. L. Jilka, R. S. Weinstein, S. C. Manolagas, and C. A. O’Brien (2011). “Matrix-embedded cells control osteoclast formation”. In: *Nature medicine* 17.10, p. 1235 (cit. on p. 12).

Bibliography

- Xu, J., F. Wang, A. Van Keymeulen, P. Herzmark, A. Straight, K. Kelly, Y. Takuwa, N. Sugimoto, T. Mitchison, and H. R. Bourne (2003). “Divergent signals and cytoskeletal assemblies regulate self-organizing polarity in neutrophils”. In: *Cell* 114.2, pp. 201–214 (cit. on p. 153).
- Xu, K., H. P. Babcock, and X. Zhuang (2012). “Dual-objective STORM reveals three-dimensional filament organization in the actin cytoskeleton”. In: *Nature methods* 9.2, p. 185 (cit. on p. 113).
- Xue, C., T. Zhang, X. Xie, Q. Zhang, S. Zhang, B. Zhu, Y. Lin, and X. Cai (2017). “Substrate stiffness regulates arterial-venous differentiation of endothelial progenitor cells via the Ras/Mek pathway”. In: *Biochimica et Biophysica Acta (BBA)-Molecular Cell Research* 1864.10, pp. 1799–1808 (cit. on p. 92).
- Yadav, V. K., F. Oury, K. F. Tanaka, T. Thomas, Y. Wang, S. Cremers, R. Hen, A. Krust, P. Chambon, and G. Karsenty (2011). “Leptin-dependent serotonin control of appetite: temporal specificity, transcriptional regulation, and therapeutic implications”. In: *Journal of Experimental Medicine* 208.1, pp. 41–52 (cit. on p. 11).
- Yamaguchi, H., M. Lorenz, S. Kempiak, C. Sarmiento, S. Coniglio, M. Symons, J. Segall, R. Eddy, H. Miki, T. Takenawa, et al. (2005). “Molecular mechanisms of invadopodium formation: the role of the N-WASP–Arp2/3 complex pathway and cofilin”. In: *The Journal of cell biology* 168.3, pp. 441–452 (cit. on p. 25).
- Yamaguchi, H., F. Pixley, and J. Condeelis (2006). “Invadopodia and podosomes in tumor invasion”. In: *European journal of cell biology* 85.3-4, pp. 213–218 (cit. on p. 37).
- Yamamoto, M., J. E. Fisher, M. Gentile, J. G. Sedor, C.-T. Leu, S. B. Rodan, and G. A. Rodan (1998). “The integrin ligand echistatin prevents bone loss in ovariectomized mice and rats”. In: *Endocrinology* 139.3, pp. 1411–1419 (cit. on p. 44).
- Yang, S. H., K.-B. Lee, B. Kong, J.-H. Kim, H.-S. Kim, and I. S. Choi (2009). “Biomimetic encapsulation of individual cells with silica”. In: *Angewandte Chemie International Edition* 48.48, pp. 9160–9163 (cit. on p. 150).
- Yang, Z., J.-S. Lin, J. Chen, and J. H. Wang (2006). “Determining substrate displacement and cell traction fields—a new approach”. In: *Journal of theoretical biology* 242.3, pp. 607–616 (cit. on p. 108).
- Yeh, Y.-T., R. Serrano, J. François, J.-J. Chiu, Y.-S. J. Li, J. C. Del Álamo, S. Chien, and J. C. Lasheras (2018). “Three-dimensional forces exerted by leukocytes and vascular endothelial cells dynamically facilitate diapedesis”. In: *Proceedings of the National Academy of Sciences* 115.1, pp. 133–138 (cit. on p. 106).
- You, H. X., J. M. Lau, S. Zhang, and L. Yu (2000). “Atomic force microscopy imaging of living cells: a preliminary study of the disruptive effect of the cantilever tip on cell morphology”. In: *Ultramicroscopy* 82.1-4, pp. 297–305 (cit. on p. 101).
- You, L., S. Temiyasathit, P. Lee, C. H. Kim, P. Tummala, W. Yao, W. Kingery, A. M. Malone, R. Y. Kwon, and C. R. Jacobs (2008). “Osteocytes as mechanosensors in the inhibition of bone resorption due to mechanical loading”. In: *Bone* 42.1, pp. 172–179 (cit. on p. 16).
- Zalli, D., L. Neff, K. Nagano, N. Y. Shin, W. Witke, F. Gori, and R. Baron (2016). “The actin-binding protein cofilin and its interaction with cortactin are required for podosome patterning in osteoclasts and bone resorption in vivo and in vitro”. In: *Journal of Bone and Mineral Research* 31.9, pp. 1701–1712 (cit. on pp. 50, 58).
- Zallone, A. Z., A. Teti, M. Primavera, L. Naldini, and P. Marchisio (1983). “Osteoclasts and monocytes have similar cytoskeletal structures and adhesion property in vitro.” In: *Journal of anatomy* 137.Pt 1, p. 57 (cit. on pp. 23, 56).

- Zallone, A. Z., A. Teti, M. Gaboli, and P. C. Marchisio (1989). "Beta3 Subunit of Vitronectin Receptor is Present in Osteoclast Adhesion Structures and Not in Other Monocyte-Macrophage Derived Cells". In: *Connective tissue research* 20.1-4, pp. 143–149 (cit. on p. 44).
- Zambonin-Zallone, A., A. Teti, A. Carano, and P. C. Marchisio (1988). "The distribution of podosomes in osteoclasts cultured on bone laminae: effect of retinol". In: *Journal of Bone and Mineral Research* 3.5, pp. 517–523 (cit. on pp. 39, 62, 68).
- Zambonin-Zallone, A., A. Teti, M. Grano, A. Rubinacci, M. Abbadini, M. Gaboli, and P. C. Marchisio (1989). "Immunocytochemical distribution of extracellular matrix receptors in human osteoclasts: A $\beta 3$ integrin is colocalized with vinculin and talin in the podosomes of osteoclastoma giant cells". In: *Experimental cell research* 182.2, pp. 645–652 (cit. on pp. 48, 49).
- Zanger, D. (1998). "Imaging surface and submembranous structures with the atomic force microscope: a study on living cancer cells, fibroblasts and macrophages". In: *Journal of microscopy* 190.3, pp. 328–338 (cit. on p. 101).
- Zhang, D., N. Udagawa, I. Nakamura, H. Murakami, S. Saito, K. Yamasaki, Y. Shibasaki, N. Morii, S. Narumiya, and N. Takahashi (1995). "The small GTP-binding protein, rho p21, is involved in bone resorption by regulating cytoskeletal organization in osteoclasts". In: *Journal of cell science* 108.6, pp. 2285–2292 (cit. on p. 54).
- Zhang, Y., C. Liu, and D. Whalley (2009). "Direct-write techniques for maskless production of microelectronics: A review of current state-of-the-art technologies". In: *2009 International Conference on Electronic Packaging Technology & High Density Packaging*. IEEE, pp. 497–503 (cit. on p. 150).
- Zhao, H., Y. Ito, J. Chappel, N. W. Andrews, S. L. Teitelbaum, and F. P. Ross (2008). "Synaptotagmin VII regulates bone remodeling by modulating osteoclast and osteoblast secretion". In: *Developmental cell* 14.6, pp. 914–925 (cit. on p. 20).
- Zhao, M., H. Zhang, T. F. Robinson, S. M. Factor, E. H. Sonnenblick, and C. Eng (1987). "Profound structural alterations of the extracellular collagen matrix in postischemic dysfunctional ("stunned") but viable myocardium". In: *Journal of the American College of Cardiology* 10.6, pp. 1322–1334 (cit. on p. 34).
- Zhao, X. (2014). "Multi-scale multi-mechanism design of tough hydrogels: building dissipation into stretchy networks". In: *Soft matter* 10.5, pp. 672–687 (cit. on p. 93).
- Zhou, A.-X., J. H. Hartwig, and L. M. Akyürek (2010). "Filamins in cell signaling, transcription and organ development". In: *Trends in cell biology* 20.2, pp. 113–123 (cit. on p. 25).
- Zhu, X., N. Efimova, C. Arnette, S. K. Hanks, and I. Kaverina (2016). "Podosome dynamics and location in vascular smooth muscle cells require CLASP-dependent microtubule bending". In: *Cytoskeleton* 73.6, pp. 300–315 (cit. on p. 32).
- Zou, W., H. Kitaura, J. Reeve, F. Long, V. L. Tybulewicz, S. J. Shattil, M. H. Ginsberg, F. P. Ross, and S. L. Teitelbaum (2007). "Syk, c-Src, the $\alpha v \beta 3$ integrin, and ITAM immunoreceptors, in concert, regulate osteoclastic bone resorption". In: *The Journal of cell biology* 176.6, pp. 877–888 (cit. on p. 55).
- Zündel, M., A. E. Ehret, and E. Mazza (2017). "Factors influencing the determination of cell traction forces". In: *PloS one* 12.2, e0172927 (cit. on p. 104).